Alignment and Spectroscopy of Ultracold Rb$_2$ Molecules

Dissertation

zur Erlangung des akademischen Grades Dr. rer. nat.

der Fakultät für Naturwissenschaften der Universität Ulm

vorgelegt von

Markus Johannes Deiß

geboren am 01.05.1983 in Ehingen (Donau)

27. Mai 2015

ulm university universität uulm

Amtierender Dekan: Prof. Dr. Joachim Ankerhold

Erstgutachter: Prof. Dr. Johannes Hecker Denschlag

Zweitgutachter: Prof. Dr. Alexander Kubanek

Tag der mündlichen Prüfung: 29. Juli 2015

Die Wurzeln der Bildung sind bitter, doch die Früchte sind süß.

Aristoteles

Abstract

In the present thesis I report on experiments with optically trapped, ultracold Rb_2 molecules at temperatures on the order of one microkelvin. It will be shown that the dimers can be prepared in a variety of precisely defined energy eigenstates, where the electronic, rotational, Zeeman and hyperfine structure is fully resolved. This flexibility enables us to investigate a wide range of physical and chemical properties. Here, I want to focus on our results concerning two different aspects:

I. Alignment of the molecular axis. I will demonstrate a novel technique which allows for the determination of the degrees of alignment of a nonpolar molecule with respect to a space-fixed coordinate system. The method relies on measurements of the dynamical polarizability $\alpha(\omega)$ for all three spatial directions and is exemplified by application to spin-polarized ensembles of Rb_2 dimers in specific rotational levels within the vibrational ground state manifold of the lowest triplet potential. Along with these studies, a detailed analysis of $\alpha(\omega)$ is provided. In particular, we are able to derive the dynamical polarizabilities parallel and orthogonal to the molecular axis at a wavelength of 1064.5 nm.

II. Spectroscopy of hyperfine levels. I will present the observation of the hyperfine structure of states with $\Omega = 0^+$ symmetry for the spin-orbit coupled $A^1\Sigma_u^+ - b^3\Pi_u$ complex. Our measured spectra at a magnetic field of about 1000 G exhibit nonequal spacings of the hyperfine levels, unexpected large energy splittings up to more than 100 MHz and a strong variation dependent on the vibrational quantum number. Using a simple model, we explain the overall hyperfine structure as a result of the repulsion between 0^- and 0^+ states, coupled via hyperfine and Zeeman interactions. By fitting our model to the data, we can extract the frequency separation of the 0^- and 0^+ components for each spectrum, a quantity which is spectroscopically not directly accessible starting from any singlet or triplet ground state molecular level.

Zusammenfassung

In der vorliegenden Dissertation beschreibe ich Experimente mit optisch gefangenen, ultrakalten Rb_2 Molekülen bei Temperaturen in der Größenordnung von einem Mikrokelvin. Wie ich zeigen werde, können wir die Moleküle in verschiedenen, energetischen Eigenzuständen präparieren, wobei sowohl die elektronische als auch die Rotations-, Zeeman- und Hyperfeinstruktur vollständig aufgelöst werden. Diese Flexibilität ermöglicht es uns, eine Fülle physikalischer und chemischer Eigenschaften zu untersuchen. Hier werde ich mich auf die Vorstellung von Resultaten konzentrieren, die sich den folgenden zwei Themengebieten zuordnen lassen:

I. Ausrichtung der molekularen Achse. Ich werde eine neuartige Technik demonstrieren, die es erlaubt, die Ausrichtung eines unpolaren Moleküls bezüglich jeder der Achsen eines raumfesten Koordinatensystems zu bestimmen. Die Methode beruht auf der Messung der dynamischen Polarisierbarkeit $\alpha(\omega)$ in allen drei Raumrichtungen und wird am Beispiel von spinpolarisierten Rb_2 Molekülen vorgeführt. Dafür werden spezielle Rotationsniveaus innerhalb des Vibrationsgrundzustands des energetisch am tiefsten gelegenen Triplett-Potentials verwendet. Basierend auf unseren Studien werden detaillierte Informationen über die Größe $\alpha(\omega)$ gewonnen. Insbesondere können wir die Werte der dynamischen Polarisierbarkeiten parallel und orthogonal zur molekularen Achse für eine Wellenlänge von 1064.5 nm ableiten.

II. Spektroskopie von Hyperfeinniveaus. Ich werde die Beobachtung der Hyperfeinstruktur von Zuständen mit $\Omega = 0^+$ Symmetrie des durch Spin-Bahn-Wechselwirkung gekoppelten $A^1\Sigma_u^+ - b^3\Pi_u$ Komplexes präsentieren. Unsere bei einem Magnetfeld von etwa 1000 G gemessenen Spektren sind dadurch gekennzeichnet, dass die Hyperfeinniveaus nicht äquidistant angeordnet sind und dass unerwartet große Abstände bis zu mehr als 100 MHz zwischen ihnen liegen. Ferner treten deutliche Veränderungen in Abhängigkeit von der Vibrationsquantenzahl auf. Mithilfe eines einfachen Modells können wir die Hyperfeinstruktur generell erklären als Resultat der Abstoßung der 0^- und 0^+ Zustände, welche durch Hyperfein- und Zeeman-Wechselwirkung miteinander gekoppelt sind. Für jedes Spektrum ermitteln wir die Frequenzdifferenz Δ der 0^- und 0^+ Komponenten, indem unser Modell an die jeweiligen Daten angefittet wird. Dies stellt ein wichtiges Ergebnis dar, da Δ spektroskopisch nicht direkt zugänglich ist, ausgehend von beliebigen molekularen Energieniveaus des Singulett- oder Triplett-Grundzustands.

Contents

1 Introduction

In order to experimentally investigate the physical and chemical properties of atomic and molecular species, full control over the available degrees of freedom is desired. Besides translation, molecules can also rotate and vibrate and therefore represent much more complex systems than atoms. The capability to access (all) the external and internal degrees of freedom in a deterministic way is the basic element of the field of ultracold molecules which emerged at the end of the last century. Since then, a variety of fascinating experiments have been carried out and many applications have been proposed making use of the attainable extraordinary control. In this introduction, I want to first give an overview of the development of the field before some prospects of ultracold molecules will be mentioned. Then, I will briefly describe the general scheme of the rubidium experiment in Ulm and the types of measurements performed within my PhD. Finally, the last two sections contain an outline of the present work and a list of manuscripts related to this thesis.

1.1 Ultracold molecules - development of a fascinating field

Besides the ultralow temperatures, key features of ultracold molecules experiments are the relatively long possible observation times as they are performed in a trap, the preparation of precisely defined quantum states and the ability to isolate the particles from each other. These properties are the result of a rapid scientific and technological progress that has been taken place in recent years. They are essential for the measurements presented here and achieved in our setup by forming the molecules from an already ultracold sample of atoms, holding them in a 3D optical lattice, and employing coherent molecular state transfer. In view of these aspects, I want to give an overview of some major advancements that made ultracold molecules to the vibrant field of research it is now. Furthermore, I will put my work in the given scientific context.

The creation of an ultracold sample of molecules in the microkelvin regime is a quite involved task since laser cooling (see, e.g., Ref. [1]) cannot be easily applied. In general, cooling cycles are not completely closed and spontaneous decay to other states occurs. Compared to atoms, the additional vibrational and rotational branching of the molecular level structure gives rise to many more undesired transitions. Therefore, in order to obtain sufficient cooling rates a large number of so-called repump lasers that transfer the corresponding populations back into the main cycle is necessary. Nevertheless, laser cooling, respectively magneto-optical trapping of polar dimers was demonstrated for a few, particularly well suited species like SrF [2, 3] or YO [4], lowering the temperature either in 3D or reduced dimensions to typically a few millikelvin. Other methods to produce cold samples of molecules rely, e.g., on elastic collisions

with a buffer gas [5], electrooptical [6, 7] or Stark deceleration techniques [8]. Particularly, in terms of molecular ions, sympathetic cooling of the translational degrees of freedom is feasible in ion traps due to the Coulomb interaction [9]. Moreover, via optical pumping, it was possible to accumulate population in the rovibrational ground state, both for MgH^+ [10] and HD^+ [11].

An alternative, indirect approach to prepare ultracold (neutral) molecular samples is the association of already ultracold atoms. This circumvents the direct cooling of molecules, exploiting the well-established techniques for atoms, which are very efficient as documented by the observation of Bose-Einstein condensation at typically below one microkelvin [12, 13]. Here, reliable and effective methods to form molecules, applicable in the relevant temperature regime, are mandatory. Widely used are photoassociation schemes, where two colliding atoms absorb a photon and form a bound molecule (for further information, I refer to the review article [14]). Based on this association mechanism different diatomic molecular species were successfully prepared in the vibrational (RbCs [15], Cs_2 [16]) or even rovibrational (LiCs [17], KRb [18]) ground state of the lowest electronic potential.

A different method to convert ultracold atoms into molecules relies on magnetic Feshbach resonances [19]. Compared to photoassociation, this technique is characterized by high efficiency and robustness. In brief, a Feshbach resonance occurs, when two colliding atoms are resonantly coupled to a bound molecular level [20]. In the field of ultracold quantum gases, such scattering resonances have been observed for the first time in the year 1998 [21-23]. Since they allow for the control of the interaction of particles, they represent an important tool to manipulate fermionic as well as bosonic atomic ensembles and have a wide range of applications besides magnetoassociation. However, by ramping the magnetic field across such a scattering resonance a weakly bound molecule with a binding energy on the order of tens of $MHz \times h$ can be formed, which was demonstrated for several atomic species (see, e.g., Refs. [24-30]) shortly after the observation of atom-molecule coherence in 2002 [31]. Using magnetic Feshbach resonances a variety of different homo- and heteronuclear diatomic molecules were produced up to now. This approach has turned out to be very successful leading to impressive achievements like the creation of molecular Bose-Einstein condensates [32-34]. In our setup, we create $^{87}Rb_2$ dimers utilizing a Feshbach resonance at a magnetic field of 1007.4 G. The obtained molecules have both singlet as well as triplet character and therefore represent a good starting point for spectroscopic purposes, since many different excited states can be addressed via optical dipole transitions according to selection rules. Moreover, the dimers are nonrotating, which allows for the investigation of levels of low rotational angular momentum. This can strongly complement the research with thermal and thus rotationally excited samples as exemplified by our studies of the spin-orbit coupled $A^1\Sigma_u^+ - b^3\Pi_u$ complex reported here and in Ref. [35], where we have observed unexpected large and irregular hyperfine structures. The gained precise information about level energies was also valuable for the explanation of the population distribution of molecular reaction products after three body recombination of ^{87}Rb atoms, which was recorded by the team of the BaRbI experiment at our institute [36].

As already mentioned, Feshbach molecules are very weakly bound and therefore can be described essentially as atomic pairs. In the context of ultracold chemistry deeply bound molecules are much more of interest. The so-called STIRAP (stimulated Raman adiabatic

passage) technique represents a powerful method to transfer population from one state to another state. First demonstrated in molecular beam experiments, it has become a standard technique in the field of atomic and molecular physics [37, 38]. It relies on a coherent two photon process and is very efficient. Using STIRAP and starting with magnetoassociated Feshbach dimers, rovibrational ground state molecules were prepared in either the lowest singlet (KRb [39], Cs_2 [40], RbCs [41, 42] and NaK [43]) or triplet (KRb [39] and Rb_2 [44]) potential. In addition, coherent transfer of population between different hyperfine levels of the rovibronic ground state manifold of KRb employing a microwave Raman scheme was realized [45]. With respect to the lowest vibrational triplet state of Rb_2, I will show in the present thesis the preparation of molecules in energy levels that exhibit different rotational quantum numbers (see also Ref. [46]) and nuclear spins.

So far, we have convinced ourselves, that, indeed, ultracold samples of dimers in well-defined molecular states can be produced. But what about the control of the interaction between the particles? In general, the ability to either isolate the molecules from each other or let them collide is desired. For this purpose, a tunable, external trapping potential is appropriate. Although demanding, trapping of molecules has been reported even for the millikelvin regime (see, e.g., Refs. [5, 7, 47-49]). However, in terms of most of the molecular beam apparatuses, where vapors or supersonically expanded gases are investigated, there are still no such traps at all and the experiments have to be performed on short timescales, often in a pulsed fashion. In contrast, various, relatively simple techniques to trap ultracold atoms or molecules exist owing to the low temperatures. Among them, optical lattices allow for unique control over the interparticle interaction. They are created by standing light waves which lead to equidistant potential wells according to the ac Stark effect. These arrays of microtraps can be tailored by adjusting the intensities of the laser beams appropriately. Many opportunities arise from the flexibility of the optical lattice approach as has been demonstrated in seminal experiments like the observation of the superfluid to Mott insulator transition [50] or the realization of a Tonks-Girardeau gas [51, 52].

Concerning molecular studies, starting with a deep 3D optical lattice is advantageous, since the ultracold samples can be prepared with no more than a single molecule per lattice site and therefore collisional losses are strongly suppressed [53, 54]. Consequently, long-lived molecular ensembles with lifetimes of several seconds in the trap have been produced (cf. Refs. [40, 55]). In this context, the state- and frequency-dependent, in general anisotropic, dynamical polarizability is an important quantity as it determines the potential depth and the photon scattering rate for a given light field intensity. For instance, in Ref. [44] a laser at 830 nm was used in order to trap Rb_2 molecules. It turned out that this wavelength is unfavorable owing to the large difference of the dynamical polarizabilities between the Feshbach state and the triplet rovibrational ground state which gives rise to a significant loss of the deeply bound molecules on timescales of tens of microseconds after the STIRAP transfer. Hence, we have implemented a 3D optical lattice at 1064.5 nm, where the dimers exhibit lifetimes on the order of seconds both for the Feshbach state and the rovibrational ground state of the lowest triplet potential. Moreover, we have performed a thorough investigation of the molecular dynamical polarizabilities [46, 56] as knowledge about trap depths and scattering rates is a prerequisite

for well controlled experiments.

An ensemble of molecules in a 3D optical lattice is an ideal starting point for chemical reaction studies. By ramping down the potential depths independently in each spatial direction the dimers are allowed to encounter each other in 3D or reduced dimensions. Up to now, measurements of inelastic collisions in terms of ultracold, vibrational ground state molecules have been predominantly carried out with polar KRb in the lowest singlet potential. The dependences of reaction rates on various parameters like the electric dipole moment [57] or the hyperfine state [58] were investigated. Further impressive results were the observations of spin-exchange interactions [59] and the quantum Zeno effect [60], which was also demonstrated with Rb_2 Feshbach molecules beforehand [61]. Recently, some data concerning collisions of RbCs singlet rovibrational ground state molecules in a crossed optical dipole trap, where the magnetic field was varied, were presented [41]. However, when it comes to ultracold chemistry of deeply bound triplet molecules, there is no data available so far. During my PhD, we have started to look into this by investigating inelastic encounters of nonpolar Rb_2 dimers for various molecular states and different collision geometries. Our results including the determination of reaction rates will be discussed in the doctoral thesis of my colleague Björn Drews.

An important aspect in the context of ultracold chemistry is the influence of the relative alignment or orientation of the colliding particles. Such studies require the ability to engineer and measure alignment or orientation. With ultracold molecules, first experimental findings concerning stereodynamics were obtained again with a sample of KRb that was exposed to a dc electrical field [62]. For the case of nonpolar dimers, different techniques to create alignment have to be developed. I will show here the successful preparation of an aligned ensemble of Rb_2 molecules. For this purpose, we exploit the fact that the STIRAP transfer entails a spin polarization of the dimers. In addition, I will demonstrate a novel method to probe the degrees of alignment of the molecular axis with respect to a space-fixed coordinate system using the 3D optical lattice (see also Ref. [46, 63]). The described techniques to control and probe the axis alignment pave the way for the experimental observation of stereochemical processes in the ultracold temperature regime, in particular with respect to nonpolar molecules.

1.2 Prospects of ultracold molecules

For ultracold molecules, many prospects are predicted making use of the unprecedented control over the internal and external degrees of freedom. Since comprehensive overviews are given, e.g., in Refs. [64, 65], a detailed discussion is omitted, here. However, some aspects, specifically relevant with respect to Rb_2 and our experiment will be described in the outlook (chapter 8). The main part of the proposed applications can be divided into the following topics:

- ultracold chemistry (see, e.g., Refs. [66, 67])

- many body physics (see, e.g., Refs. [68, 69])

- high precision spectroscopy (see, e.g., Ref. [70])

- precision measurements of fundamental constants (see, e.g., Refs. [71-74])

- quantum simulation (see, e.g., Refs. [75, 76])

- quantum computation (see, e.g., Refs. [77-79])

This list documents that experiments with ultracold molecules are, respectively will become, important for versatile fields of physics and chemistry.

1.3 The Rb_2 setup in Ulm

Within the rubidium project our aim is to investigate the properties of ultracold $^{87}Rb_2$ molecules. For this purpose an experimental apparatus was designed and built up at the "Institut für Experimentalphysik" in Innsbruck. After running successfully for several years the rubidium project was moved to the "Institut für Quantenmaterie" in Ulm at the end of the year 2009. Unfortunately, the experiment, especially all the laser systems had to be disassembled for the transport from Innsbruck to Ulm. At this stage my colleague Björn Drews and I started with our PhDs and we began to rebuild and improve the system.

In the following, I want to give a short overview of our general experimental scheme. We work with ultracold Rb_2 molecules either in a weakly bound Feshbach state or in the vibrational ground state ($v = 0$) of the lowest triplet potential $a^3\Sigma_u^+$. After being loaded into a magneto-optical trap (MOT), ^{87}Rb atoms are magnetically transferred to a glass cell. Subsequently the sample is cooled by means of forced evaporation until the ultracold temperature regime is reached. We are able to routinely produce Bose-Einstein condensates (BECs). However, the molecule formation is mainly performed with thermal clouds at temperatures of a few µK as this leads to a larger absolute number of dimers. For this purpose a 3D optical lattice is switched on, while the magnetic trap is switched off. Then, by using a magnetic Feshbach resonance and applying a purification scheme a pure ensemble of weakly bound molecules with no more than a single dimer per lattice site is produced. In order to transfer the molecules to the vibrational ground state, we utilize the STIRAP technique which relies on a coherent optical two-photon process. Since we are able to fully resolve the hyperfine, rotational and Zeeman structure, single well-defined quantum levels can be deterministically populated. Both, the Feshbach molecules as well as the deeply bound molecules exhibit lifetimes on the order of seconds within the optical lattice which is plenty of time for experiments.

1.4 Overview of performed experiments

During my PhD we have performed various types of experiments with ultracold $^{87}Rb_2$ molecules. They can mainly be classified into five different groups:

1. **Preparation of molecular states:** We have prepared the molecules in diverse precisely defined energy levels within the vibrational ground state ($v = 0$) of the lowest triplet potential $a^3\Sigma_u^+$. By applying the highly selective STIRAP technique we have been able to unambiguously populate levels with different rotational quantum number R ($R = 0$ and 2), and different nuclear spin I ($I = 1$ and 3).

2. **Measurements of dynamical polarizabilities and determination of the alignment of the molecular axis:** We have investigated the dynamical polarizabilities of nonpolar $^{87}\mathrm{Rb}_2$ dimers for several molecular quantum states utilizing lattice modulation spectroscopy. From the obtained experimental data the degrees of alignment of the molecular axis with respect to a space-fixed coordinate system have been determined. For this purpose we have exploited the fact that the axis alignment is directly reflected in an anisotropy of the dynamical polarizability.

3. **Spectroscopy of the $A - b$ system:** We have studied the spin orbit coupled $A^1\Sigma_u^+ - b^3\Pi_u$ complex by means of one-photon spectroscopy starting with weakly bound Feshbach molecules at a magnetic field of about 1000 G. As a consequence of selection rules, we have addressed only the 0^+ components. However, the observed combined hyperfine and Zeeman structures with respect to 0^+ entail information about the term values of $b^3\Pi_u$ 0^- owing to the spin orbit coupling between 0^+ and 0^- vibrational levels. In this rather indirect way, it has been possible to infer the spectral splittings of the 0^+ and 0^- components.

4. **Inelastic collisions:** We have performed reaction studies of $a^3\Sigma_u^+$ vibrational ground state molecules and Feshbach molecules, respectively. Starting with a deep 3D optical lattice, where the dimers are well separated from each other we have reduced the lattice depth either equally in each direction or just for single directions. Thereby, molecules are allowed to approach each other giving rise to interaction. We have carried out collision experiments for various geometries, i.e., quasi-1D, quasi-2D and quasi-3D structures. Regarding the $v = 0$ molecules, we have investigated the rotational states $R = 0$ and 2 individually, and observed a strongly inelastic behavior, i.e., already in the first or after just a few molecular encounters a chemical reaction occurs. In general, the interpretation of our data is difficult as several loss-mechanisms have to be considered and the system, including the influence of the trap itself, has to be fully understood. Here, our collisional experiments with Feshbach molecules have helped a lot since these dimers can routinely be created and therefore high statistics are possible. Currently, Björn Drews is preparing a manuscript, where we present our measurements of inelastic collisions of the triplet Rb_2 molecules in an array of quasi-1D traps.

5. **Spectroscopy of the c state:** We have studied the $c^3\Sigma_g^+$ state starting either with weakly bound Feshbach molecules or molecules in well-defined levels corresponding to $v = 0$ of $a^3\Sigma_u^+$. From our experiments we have gained information about the $c^3\Sigma_g^+$ as well as the $a^3\Sigma_u^+$ state, in particular on the Zeeman shift of the individual hyperfine levels.

Please note, our findings concerning the aspects mentioned in 4. and 5. of the given list will not be presented here. They will be discussed in detail in the forthcoming doctoral thesis of Björn Drews.

1.5 Outline of the thesis

This thesis is structured as follows:

Chapter 2 gives a short, rather technological survey of the experimental apparatus focusing on the main parts like the vacuum chamber, the coils, laser systems, cameras and the control system.

Chapter 3 describes the basic experimental procedure, i.e., the various steps necessary to prepare pure samples of ultracold Rb_2 molecules in the lowest vibrational level of $a^3\Sigma_u^+$, trapped in an optical lattice. Here, the fundamental techniques are discussed and important parameters are provided.

Chapter 4 presents measurements of the real part of the dynamical polarizability $\alpha(\omega)$ of Rb_2 dimers in the rovibrational ground state of $a^3\Sigma_u^+$. Furthermore, information about the imaginary part of $\alpha(\omega)$ is gained from the observed lifetime of the molecules in the optical lattice. These experimental results are obtained at $\lambda = 1064.5\,\text{nm}$. Theoretical studies of both the lowest singlet $(X^1\Sigma_g^+)$ as well as triplet $(a^3\Sigma_u^+)$ potential for a wide range of wavelengths are provided, including an analytical model that can be used to reproduce the numerically calculated dynamical polarizabilities with respect to all vibrational levels.

Chapter 5 reports on the creation and the probing of alignment of the molecular axis of an ultracold, nonpolar dimer. Here, a novel technique to determine the degrees of alignment with respect to all directions of space is demonstrated. The method relies on measurements of the dynamical polarizabilities utilizing individually the standing light waves of a rectangular 3D optical lattice. Our experiments with Rb_2 show, that for the nonrotating state the molecular axis is randomly oriented, while rotating dimers exhibit characteristic alignment, which is reflected in an anisotropy of $\alpha(\omega)$. As will be exemplified, this fact can be exploited to gain information about unknown molecular states giving rise to spectroscopic applications of the given technique. In addition, from the obtained data, the dynamical polarizabilities parallel and orthogonal to the molecular axis at a wavelength of $1064.5\,\text{nm}$ are derived.

Chapter 6 covers experimental and theoretical investigations of the combined hyperfine and Zeeman structure of the spin-orbit coupled $A^1\Sigma_u^+ - b^3\Pi_u$ complex of Rb_2. Results of one-photon spectroscopy of the 0^+ state starting from the Feshbach level are presented. The measurements show an unexpected wide spreading of the hyperfine spectra for vibrational states with strong triplet character. A simple model reveals a mixing of the 0^+ and 0^- states of $b^3\Pi_u$ induced by cooperative hyperfine and Zeeman interactions to be responsible for the large hyperfine splittings. From simulations, the typical frequency spacings Δ between the 0^+ and 0^- components are inferred. This represents an important aspect of our work, since Δ is not directly accessible in conventional spectroscopy schemes.

Chapter 7 is a reprint of data concerning three body recombination of ^{87}Rb atoms obtained by the BaRbI team at our institute. These experiments are discussed in detail in the doctoral thesis of Arne Härter [80]. In order to explain the recorded population distribution of the molecular reaction products I have performed spectroscopic measurements on Rb_2 dimers in collaboration with my colleague Björn Drews. We precisely determined relevant energy levels within the $A^1\Sigma_u^+ - b^3\Pi_u$ complex and the $c^3\Sigma_g^+$ potential. For the former case, the main results

are largely discussed in chapter 6. However, our data allowed for the assignment of resonances to molecular transitions in the three body recombination studies.

Chapter 8 is dedicated to a short summary and an outline of possible future experiments.

1.6 Publications

The results obtained in the framework of this thesis are, respectively will be presented in the following manuscripts (in chronological order) which have been published as articles, are submitted or already accepted, or are currently in preparation:

1. A. HÄRTER, A. KRÜKOW, M. DEIß, B. DREWS, E. TIEMANN, and J. HECKER DEN-SCHLAG: *Population distribution of product states following three-body recombination in an ultracold atomic gas.* Nat. Phys. 9, 512 (2013).
   (congruent with chapter 7)

   See also "News and Views" article by S. WILLITSCH: *Molecular physics: Ultracold ménage à trois.* Nat. Phys. 9, 461 (2013).

2. M. DEIß, B. DREWS, B. DEISSLER, and J. HECKER DENSCHLAG: *Probing the axis alignment of an ultracold spin-polarized Rb_2 molecule.* Phys. Rev. Lett. 113, 233004 (2014).
   (congruent with chapter 5, except for section 5.9 which contains additional information)

   This article appeared as an "Editors' Suggestion".
   See also "spotlight article" of the American Physical Society by K. WRIGHT: *Making molecules stand to attention.* Available at `http://physics.aps.org/synopsis-for/10.1103/PhysRevLett.113.233004`.

3. M. DEIß, B. DREWS, J. HECKER DENSCHLAG, N. BOULOUFA-MAAFA, R. VEXIAU, and O. DULIEU: *Polarizability of ultracold Rb_2 molecules in the rovibrational ground state of $a\,{}^3\Sigma_u^+$.* arXiv: 1501.03793 (2015). Accepted for publication in New Journal of Physics.
   (congruent with chapter 4)

4. M. DEIß und J. HECKER DENSCHLAG: *Ultrakalte Moleküle in Reih und Glied.* Physik in unserer Zeit 46 (2), 60 (2015).
   (congruent with appendix A.2)

5. M. DEIß, B. DREWS, J. HECKER DENSCHLAG, and E. TIEMANN: *Mixing of 0^+ and 0^- observed in hyperfine and Zeeman structure of ultracold Rb_2 molecules.* arXiv: 1505.00682 (2015).

(congruent with chapter 6, except for section 6.11 which contains additional information)

6. B. Drews, M. Deiß, K. Jachymski, Z. Idziaszek, and J. Hecker Denschlag: *Inelastic collisions of strongly confined triplet Rb₂ molecules.* Manuscript in preparation.

2 Experimental Apparatus

In the context of our experiment, especially vacuum technology, laser technology, microwave and radiofrequency (RF) technology, optics and electronics are of great importance. Furthermore, we have a complex computer control system in order to run the experiment cycle and for analyzing the data delivered by several cameras.

This chapter is devoted to an overview of the main parts of the apparatus. The intention is to provide all informations from a technological point of view, i.e., no measurement results are presented here. For more details, particularly on the vacuum chamber, the coils and the experiment control system, I refer to the theses of Matthias Theis [81], Klaus Winkler [82, 83] and Gregor Thalhammer [84].

2.1 Vacuum chamber

The vacuum apparatus is divided into two main sections (see Fig. 2.1). In the first section, a reservoir provides the ^{87}Rb atoms for the MOT which is directly loaded from the background vapor. The second section is connected to the MOT chamber by a differential pumping stage and contains a glass cell, where the ^{87}Rb$_2$ molecules are produced and the actual experiments take place. Via the differential pumping stage the pressure is lowered from about 10^{-8} mbar in the MOT chamber to $< 10^{-11}$ mbar in the glass cell, which, as another advantage, allows for good optical access due to its exposed position. A detailed description of the vacuum apparatus can be found in [81].

2.2 Coils

With the division of the vacuum apparatus into different regions one problem comes along. It is necessary to transfer the cold atom cloud from the MOT chamber to the glass cell. In our case, this is done by a magnetic transport [85] using 13 pairs of quadrupole coils (see Fig. 2.2). The starting point of the magnetic transport is a quadrupole trap created by the MOT coils. Since the distance of the MOT coils to the next pair of quadrupole coils is too large, we have an additional coil to push the atoms in the direction of the transport line. The current ramps for the quadrupole pairs are designed such that the minimum of the trapping potential is shifted smoothly along the transport line.

When the atoms arrive in the glass cell, we change to a QUIC[1] trap. The magnetic field of the QUIC trap is created by a pair of quadrupole coils and an additional Ioffe coil (see Fig. 2.3).

---

[1]Abbreviation for quadrupole-Ioffe-configuration.
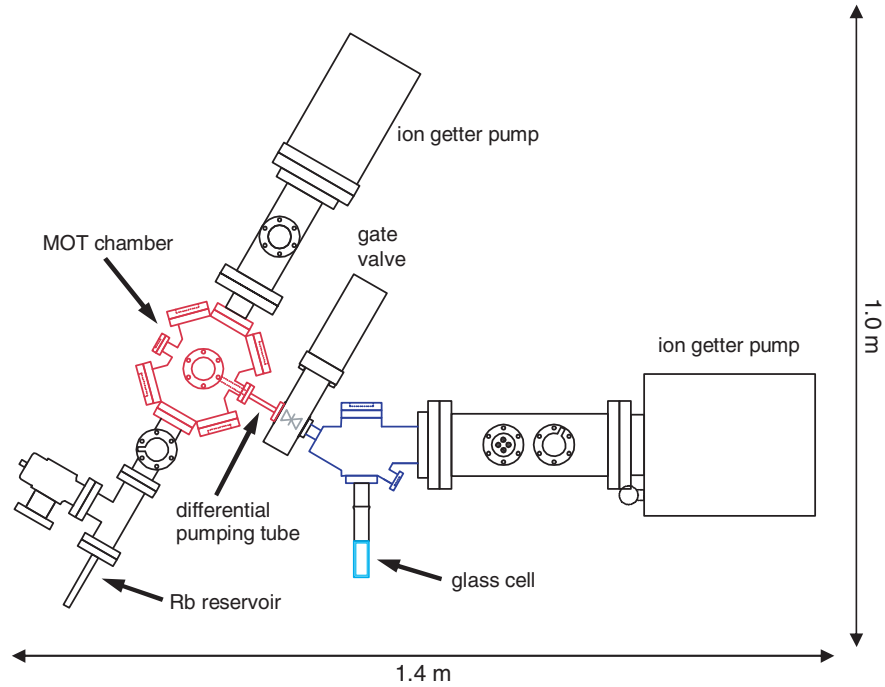
Figure 2.1: Vacuum system. We have two main sections which are connected by a differential pumping stage. First of all, the atoms are trapped in the MOT chamber before they are transferred magnetically into the UHV section where the glass cell is located. The figure is adapted from Ref. [82].

In this trap configuration the main part of the evaporative cooling takes place. Unfortunately, the position of the ultracold atomic cloud in the QUIC trap is displaced by about 6 mm from the center of the quadrupole coils which also create the Feshbach field later on. Since the Feshbach field has to be homogeneous, it is inevitable to shift the atoms back. Most of the coils surrounding the glass cell are involved in this procedure. Among them, especially the levitation coil is important because it is necessary to compensate for the gravitational force while the transfer takes place.

Four power supplies[2] serve as current sources for the coils. This is sufficient since not all the coils are operated at the same time. We use a switch box based on MOSFETs to connect or disconnect the coils from the power supplies during the experimental sequence. The coils are water cooled in order to carry away the dissipated power (for example, the magnetic transport demands currents up to 120 A). In addition, a safety circuit is implemented which switches off all currents if the signal measured by one of the integrated temperature sensors is too high or the water flow is too low for some reason.

For our experiments, stable magnetic fields are of great importance. Especially, the effi-

---

[2]SM 30-100D (two times) and SM 15-200D (two times), Delta Elektronika B.V., Zierikzee, Netherlands.
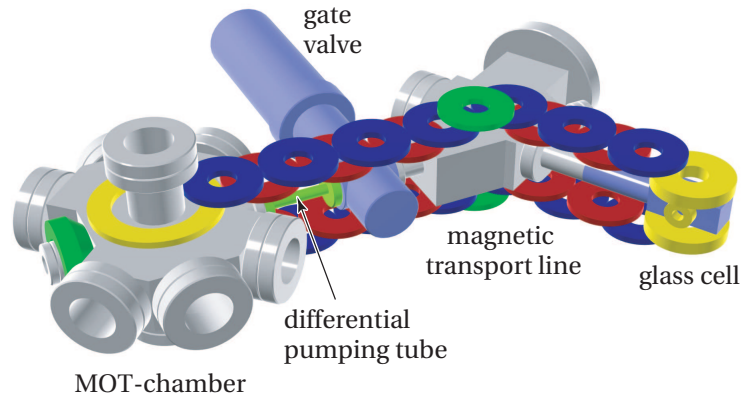
Figure 2.2: Overview of the coils involved in the magnetic transport. On the left hand side one of the MOT coils (yellow) is shown and the coil which is used to push the atoms in the direction of the transport line (green). The yellow coils on the right hand side, which surround the glass cell, are used to create the QUIC trap. In between there are 13 pairs of transport coils (blue, red and green). The figure is adapted from Ref. [82].

ciency of the Feshbach ramping used in order to associate atoms to molecules can be reduced by fluctuations. Thus, a servo loop has been implemented to suppress the noise. We measure the magnetic field created by the quadrupole coils using a current transducer[3]. After A/D conversion the signal is fed in a digital PID controller which acts on the control input of the power supply. By doing so, we achieve a stability of $\pm 5\,\text{mA}$ at a current of $80\,\text{A}$. So the relative magnetic field noise is about 10^{-4}. Further information about the coils, the current control and the safety circuit can be found in [81, 83, 84].

Moreover, a cage of ribbon cables representing pairs of Helmholtz coils in each spatial direction is placed around the MOT chamber (not shown in Fig. 2.2). With these cables we create permanent magnetic offset fields which are used to compensate for the magnetic field of the earth or other time independent stray fields. A similar construction is set up around the glass cell (not shown in Fig. 2.3). Here the currents are adjusted such, that a magnetic field remains in the direction where the transfer of the atoms from the QUIC trap to the center of the quadrupole coils takes place. It turned out that for the experiments in the glass cell the stability of these offset magnetic fields is very crucial, since they have great influence on the evaporative cooling and the spin preparation before the Feshbach ramping. Thus we use very stable power supplies (ES 075-2 from Delta Elektronika B. V.) as current sources.

---

[3]Ultrastab 866, Danfysik A/S, Taastrup, Denmark.
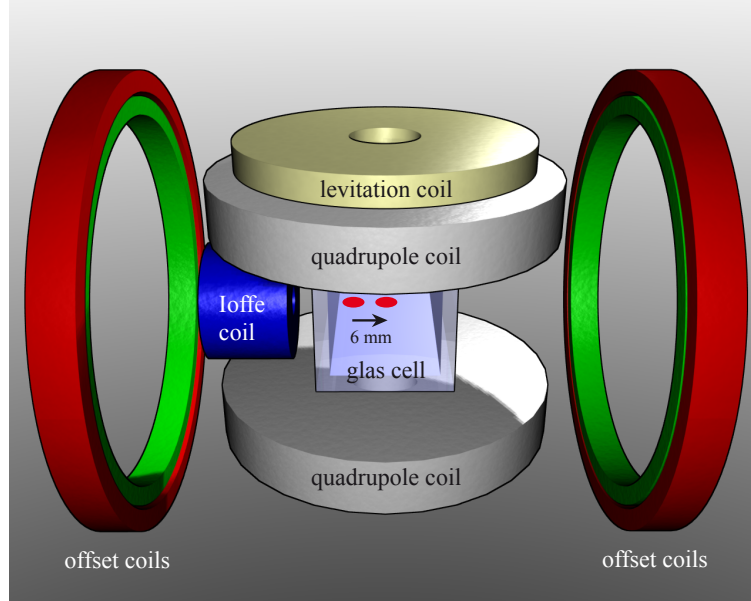
Figure 2.3: Overview of the coils surrounding the glass cell. The quadrupole coils generate the magnetic field for the Feshbach ramping. Together with the Ioffe coil they also create the potential for the QUIC trap. In vertical direction we can produce an inhomogeneous field by the levitation coil which is used for Stern-Gerlach separation of different spins before imaging and for levitation of the atoms during the transfer back to the center of the quadrupole coils. During this transfer the atomic cloud (red ellipse) is shifted by about 6 mm in axial direction, away from the Ioffe coil. Furthermore, we have two pairs of offset coils [big offset coils (red) and small offset coils (green)] in the setup. As a special feature, the big offset coils can be operated in Helmholtz and anti-Helmholtz configuration. The figure is adapted from Ref.[82].

2.3 Laser systems and frequency measurement

In our setup, a lot of different laser systems are employed (see table 2.1). Most of them are frequency-stabilized. The particular locking techniques have been chosen in accordance to the intended applications of the lasers.

In total, the experiment is located on four optical tables. Three of them are used for the generation and frequency stabilization of light, which is then transferred to the vacuum chamber on the experimental table by many polarization maintaining single mode optical fibers. The light is switched on and off by AOMs (acousto optical modulators) and mechanical shutters[4]. We do not have any lasers, AOMs or other shutters directly on the experimental table.

---

[4]Mainly SHT934 from Sunex Inc., Carlsbad, USA.

laser type	model	used wavelength	main application
grating-stabilized diode laser	home built	780 nm	absorption imaging, reference laser
grating-stabilized diode laser	home built	780 nm	laser cooling
grating-stabilized diode laser	home built	780 nm	repump laser
grating-stabilized diode laser	home built	780 nm	purification scheme
tapered amplifier	Toptica BOOSTA	780 nm	laser cooling
grating-stabilized diode laser	Toptica DL pro	993 nm	STIRAP
grating-stabilized diode laser	Toptica DL 100 pro design	1017 nm	STIRAP
grating-stabilized diode laser	Toptica DL 100 L	$985 - 1068$ nm	spectroscopy
diode pumped Nd:YAG	InnoLight Meph. MOPA 25 NE	1064 nm	optical lattice
diode pumped Nd:YAG (frequency-doubled)	Coherent Verdi-V18	532 nm	pump laser for Ti:sapphire lasers
Ti:sapphire ring laser	Coherent 899-01 ring laser	830 nm	optical lattice
Ti:sapphire ring laser	Coherent 899-01 ring laser	1017 nm	spectroscopy
Er:fiber laser system (fs pulse source)	Toptica FFS	1563 nm (center wavelength)	frequency comb

Table 2.1: Overview of all laser systems and their main applications. Please note, the experiments presented in this thesis were predominantly performed using the optical lattice at 1064 nm.

2.3.1 Lasers for atomic transitions at 780 nm

We have four lasers driving different atomic transitions of ^{87}Rb at around $\lambda = 780$ nm[5]. All of them are home built grating-stabilized diode lasers (for details on the design see [86]). The

---

[5]An overview of the optical (and physical) properties of atomic ^{87}Rb is given in Ref. [87].

output power ranges between 50 and 80 mW depending on the laser diode. Each laser is frequency-stabilized but different techniques are used:

- **Imaging laser:** We employ this laser for absorption imaging of atomic clouds at the end of each experimental cycle. It is locked to the $f_a = 2 \rightarrow f_a' = 3$ resonance of the D_2 transition using a small ^{87}Rb vapor cell. Here, f_a denotes the total angular momentum of the atom. We use modulation transfer spectroscopy [84, 88, 89] as locking technique.

- **Cooling laser and purification laser:** The cooling laser provides the cooling light for the MOT. As it has not enough power, it is used to seed a tapered amplifier (TA) in order to achieve high cooling rates. The specified output power of the TA is 1.5 W. On the experimental table we have about 50 mW left in each of the six MOT beams. The purification laser in combination with a microwave is applied to deterministically remove single atoms after the molecule association. For these two lasers the locking scheme is based on a beat with a reference frequency [90]. In both master/slave systems the imaging laser serves as reference. Such beat locks have the great advantage that the frequency of the slave laser can easily be shifted relative to the frequency of the master laser.

- **Repump laser:** At several steps of our experimental sequence, parasitic transitions can occur. As an example I want to mention the MOT cooling cycle, which is not completely closed. Hence, we have an additional laser that enables us to pump population back to a level desired for the respective application. We use a ^{87}Rb vapor cell and employ a technique based on frequency modulation spectroscopy [91] in order to achieve the mandatory frequency stabilization. The laser is locked to the $f_a = 1 \rightarrow f_a' = 1, 2$ crossover of the D_2 transition [84]. Utilizing AOMs the light can be tuned to be resonant either to $f_a = 1 \rightarrow f_a' = 1$ or $f_a = 1 \rightarrow f_a' = 2$.

The frequency stability of all the described laser systems is on the order of < 1 MHz. More information about the applications of the single lasers will be given in chapter 3.

2.3.2 Optical lattice laser

In our setup, molecules are created and manipulated in a 3D optical lattice. After the transport of the experiment to Ulm, we first worked at a wavelength of 830 nm like it was done in Innsbruck. The light was provided by one of the Ti:sapphire lasers pumped by the Verdi-V18[6] [84]. After appropriate adjustment of the ring resonator the system delivered 500 mW of output power at 830 nm when pumped with 6 W. However, as will be discussed in chapter 4 this wavelength is unfavorable for trapping of molecules prepared, e.g., in the rovibrational ground state of the lowest triplet potential. Hence we switched to 1064 nm and now use an InnoLight[7] Mephisto MOPA (master oscillator power amplifier) system for the optical lattice.

---

[6]The Verdi-V18 was used to pump both Ti:sapphire lasers simultaneously. The whole system is from Coherent, Inc., Santa Clara, USA.

[7]InnoLight GmbH, Hannover.

Owing to the different wavelength all the mirrors and lenses guiding the lattice beams on the experimental table to the glass cell had to be replaced.

The MOPA has a spectral linewidth of $1\,\text{kHz}/100\,\text{ms}$ and delivers $25\,\text{W}$ of output power which is divided into three beams directly after the laser. Each beam is switched on and off by an AOM and additionally by a mechanical shutter based on a loudspeaker that allows for moving a nontransparent flag into the beam path employing the voice coil [92]. High power optical fibers[8] are used to guide the three lattice beams to the experimental table. where they first pass optical isolators to avoid damages of the fibers due to the retroreflected beams. At the position of the atoms the single beams have a waist ($1/e^2$ radius) of about $130\,\text{µm}$ and the maximum available power per beam is $3.5\,\text{W}$. For each lattice direction we implemented an intensity stabilization acting on the AOMs. More information about that will be given in section 2.4. It is possible to tune the laser frequency by more than $30\,\text{GHz}$ via the crystal temperature. This can be advantageous in order to avoid or investigate molecular resonance phenomena. However, the range between mode-hops is typically $6 - 8\,\text{GHz}$.

As the MOPA system requires a cooling circuit, we implemented a water chiller[9] that keeps the water temperature permanently at $25°\text{C}$. So, in total we have two cooling water cycles, one for the coils and one for the MOPA. In each of them a safety circuit is integrated. A microcontroller[10] compares the water flow measured at two positions of the water cooling cycle. If there is a leak in between, the difference exceeds a fixed threshold and the water supply is stopped via magnetic valves. At the same time the MOPA laser, respectively the current through the coils is switched off.

2.3.3 Spectroscopy laser

The one-photon spectroscopy is performed with a DL 100L from Toptica[11]. This grating-stabilized laser is tunable between 985 and 1068 nm which enables us to address different interesting molecular potentials. The laser delivers a few mW of optical power at the position of the molecules depending on the chosen wavelength.

In order to perform precision spectroscopy, i.e., measure narrow linewidths the laser has to be frequency-stabilized. For this reason, we implemented a wavelength meter lock (see Sec. 2.3.6) generating a control signal which acts on the piezo tilting the internal grating. The frequency stability is between ± 2 and ± 5 MHz limited by the actualization rate of the WS7. Concerning spectroscopical measurements the wavelength meter lock has some nice features. The frequency can be tuned over the whole mode-hop free range by simply changing the set point. Furthermore, the stabilization is not restricted to a specific frequency range. Hence, it is possible to lock a laser to any frequency provided that the WS7 allows for the measurement of it.

---

[8] PMC-980-9,2-NA008-3-APC/EC-800-P from Schäfter+Kirchhoff GmbH, Hamburg.
[9] P201-16675 from Termotek AG, Baden-Baden.
[10] Arduino Uno.
[11] Toptica Photonics AG, Gräfelfing.

2.3.4 STIRAP lasers

The STIRAP technique is well known as an efficient method to transfer population coherently from one state to another using a Raman transition. In our experiment the method is applied to increase the binding energy of initially prepared weakly bound molecules by more than $7\,\text{THz}$. Two lasers are utilized to couple the initial and the final state in a λ-type three-level system. During a counterintuitive pulse sequence the molecules are kept in a dark superposition state, ending up in the desired level. A more detailed explanation will be given in section 3.9.

For an efficient STIRAP transfer, the two involved lasers have to meet some requirements. The coupling strengths determined by the Rabi frequencies have to be satisfactory. Since the Rabi frequency scales with the square root of the light field intensity this demands sufficient laser powers. In our setup, the STIRAP system is realized by two grating-stabilized diode lasers from Toptica Photonics AG. One of them is operated at about $993.8\,\text{nm}$. It delivers a few mW of optical power at the position of the molecules, which is quite sufficient for the different STIRAP transfers performed during my PhD. The other laser has a maximum output power of $137\,\text{mW}$ at the required wavelength of about $1017.5\,\text{nm}$ yielding roughly $45\,\text{mW}$ at the location of the molecular sample. Concerning intensity, this laser is the bottleneck in our system, i.e., the achievable coupling strength to some specific levels is too low [see Fig. 3.18(b)]. However, for instance, the transfer into the rovibrational triplet ground state works quite well with the available power.

Another prerequisite is the relative phase stability of the two laser beams during the STIRAP sequence. To guarantee the relative phase stability, both lasers are locked to the same optical resonator using a scheme developed by Pound, Drever and Hall (PDH) [93, 94]. For this purpose, we employ a cavity with a free spectral range of $1.5\,\text{GHz}$ and a Finesse $\mathcal{F}$ of about 300 [95].

The resulting laser linewidths have been investigated by a self-heterodyne technique [96]. A detailed discussion of this method including theory aspects can be found in [97] and references therein. In brief, two beams of the same laser are delayed by a time τ_D from each other. They are not correlated anymore if τ_D is longer than the coherence time of the light source. Thus the frequency stability of the laser can be inferred from a beat of the two beams. In order to realize the time delay we couple one of the beams into an optical fiber with a length of $12\,\text{km}$ (see Fig. 2.4), leading to $\tau_D = 58\,\mu\text{s}$ at $\lambda \sim 1000\,\text{nm}$ [98]. So the resolution limit of the interferometer concerning laser linewidths is $\Delta f_{\text{min}} = 1/\tau_D \approx 17\,\text{kHz}$ (FWHM) with respect to the given wavelength.

Figure 2.5 shows self-beat signals of the STIRAP lasers for two different locking parameters recorded with a spectrum analyzer[12]. The measurements in "slow lock" configuration essentially show the frequency fluctuations of the free running laser diodes on small timescales ($\lesssim 100\,\text{ms}$). From fitting the data, we inferred laser linewidths of $\Delta f = 137\,\text{kHz}$ ($1017.5\,\text{nm}$) and $\Delta f = 146\,\text{kHz}$ ($993.8\,\text{nm}$). The "fast lock" is characterized by a shorter integration time and leads to significantly smaller linewidths. We deduced $\Delta f = 39\,\text{kHz}$ for the laser at $1017.5\,\text{nm}$. For the case of the STIRAP laser at $993.8\,\text{nm}$ the linewidth is below the resolution limit of

---

[12]Model MS2718B from Anritsu Corporation, Atsugi, Japan.
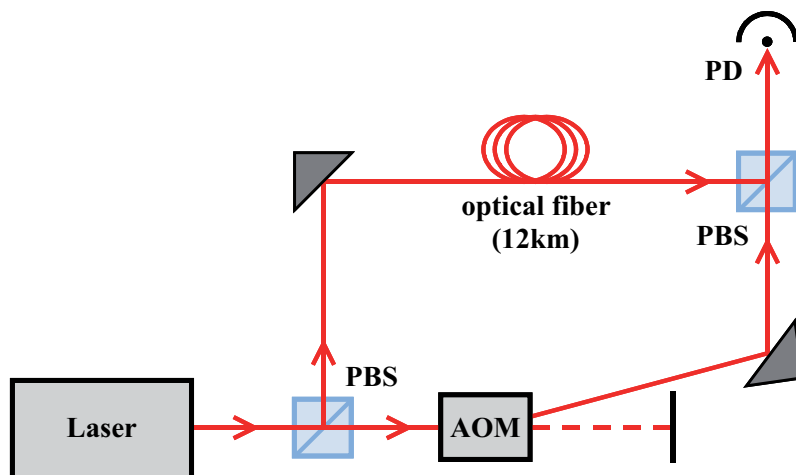
Figure 2.4: Self-heterodyne scheme for laser linewidth measurements. The laser light is divided into two beams. One of them is guided through a 12 km long optical fiber, accumulating a time delay τ_D with respect to the other one. Afterwards the two beams are superimposed and the beat signal is measured using a fast photodiode and a spectrum analyzer. We integrated an AOM in the setup in order to shift the center frequency of the beat away from zero.

$\Delta f_{\min} = 17$ kHz, as indicated by the periodic pattern in Fig. 2.5(c) that occurs, when the two laser beams are correlated. Here, we attribute the achievement of a significantly smaller linewidth to the utilization of a much more elaborate PID controller[13]. In contrast to that, we use a home built PID controller for the locking scheme at 1017.5 nm.

Another essential point is the absolute frequency stability of the lasers, which is mainly affected by thermal drifts of the optical cavity. Since the timescale of such drifts is on the order of minutes or hours, a slow locking scheme is quite sufficient to compensate for that. Thus, we implemented a wavelength meter lock in our setup, as it represents a simple and reliable technique. For this purpose the frequency of the laser at 1017.5 nm, which is already locked to the optical resonator, is measured and compared to the desired value. The control signal then acts on a piezo inside the cavity and changes the resonator length appropriately.

Besides the pivotal relative and absolute frequency stability the locking scheme has to be flexible in terms of frequency tunability. In general, PDH locks are restricted to frequencies which correspond to transmission modes of the optical resonator. However, we have several opportunities to bridge the frequency intervals in between, if necessary. First, both lasers can be shifted simultaneously by the wavelength meter lock controlling the optical resonator length. Furthermore, two AOMs (single pass configuration for the light at 1017.5 nm and double pass configuration for the light at 993.8 nm) allow for the adjustment of the frequencies over ranges of tens of megahertz. So, all frequency combinations of the two lasers are accessible even if

---

[13]Fast Analog Linewidth Control (FALC 110) from Toptica Photonics AG, Gräfelfing.
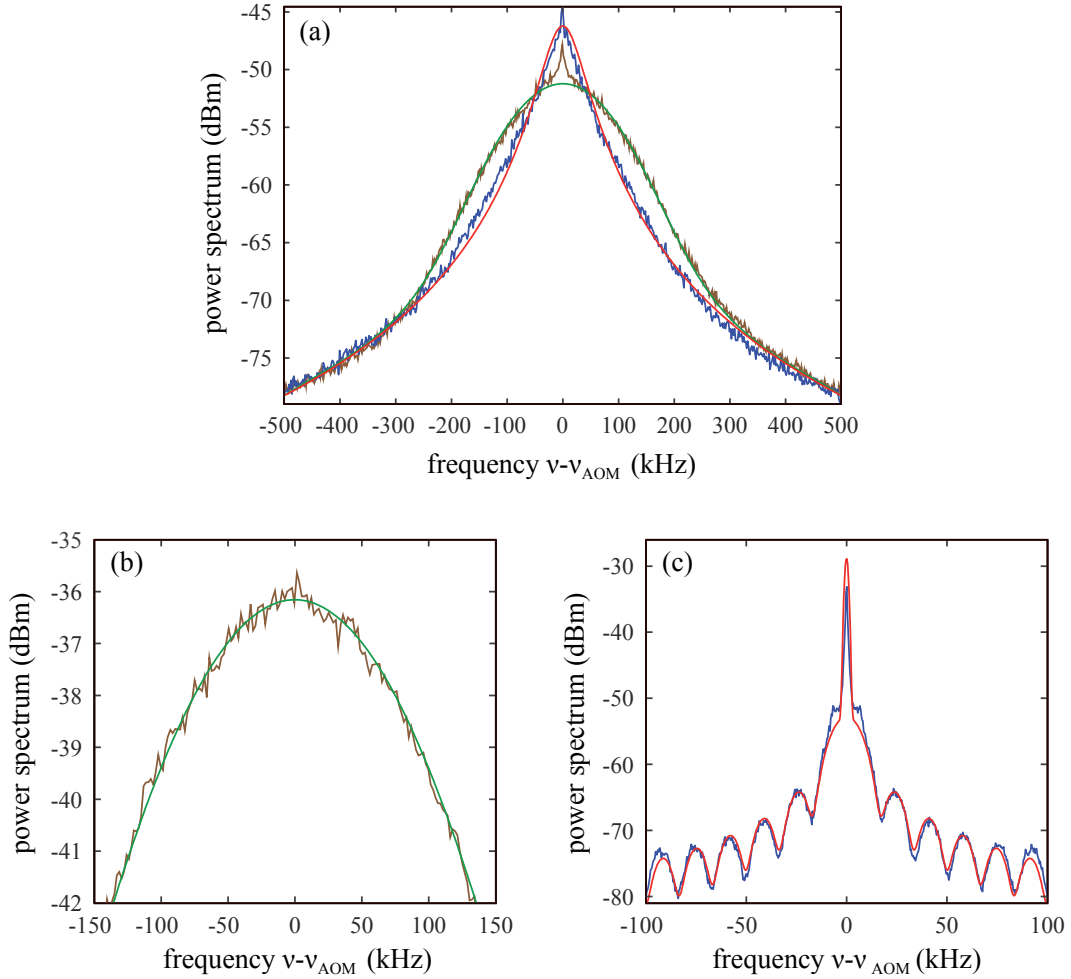
Figure 2.5: Beat signals resulting from self-heterodyne measurements of the STIRAP lasers at 1017.5 nm (a) and 993.8 nm [(b) and (c)]. For each laser, scans corresponding to two different locking configurations ["slow-lock" (brown) and "fast lock" (blue)] are shown. The frequency stabilities are inferred from fits (green and red respectively) assuming a Voigt-like profile of the laser linewidth. In (c) the shape of the beat signal is different from (a) and (b). Here, the periodic structure indicates that the laser linewidth is smaller than the resolution limit of the interferometer.

they are frequency-stabilized.

I want to emphasize that the described scheme is much more convenient than the one previously used, where the cavity was stabilized via a PDH lock to an additional laser, which in turn was stabilized to an atomic ^{87}Rb transition. This change as well as the replacement of the Ti:sapphire laser by the diode laser at 1017.5 nm considerably improved the stability and the repeatability of the STIRAP results.

2.3.5 Frequency comb

Since the development of the frequency comb at the end of the 20th century[14], this technique has brought about a wide range of applications with tremendous impact especially in the field of high precision spectroscopy. Until now, such laser systems have been established as ultrastable frequency references in many quantum optics laboratories all around the world.

In principle, the spectrum of a frequency comb is characterized by narrowband spikes which are arranged in an equidistant pattern. The center frequency ω_n of the n-th tooth is determined by $\omega_n = n\omega_r + \omega_0$ with the repetition frequency ω_r and the offset frequency ω_0.

An Er:fiber laser system (FFS) from Toptica Photonics AG is the key element of our setup. It is an sub 100fs pulse source containing an internal ring resonator which generates a comb-like spectrum with a center wavelength of 1550 nm and a bandwidth of about 80 nm (FWHM). There are two output branches, each delivering ~ 250 mW of light[15]. Subsequent to one of them the light passes a frequency doubling crystal[16] giving rise to a new comb with a center wavelength of about 780 nm, which is the regime of atomic ^{87}Rb transitions. The other path is equipped with a highly nonlinear fiber, which expands the frequency spectrum to a full octave ranging from $1000 - 2100$ nm.

In order to use the Er:fiber laser system as a frequency reference, ω_r and ω_0 have to be stabilized.

- **Repetition frequency:** The repetition frequency ω_r is measured by a photodiode inside the FFS. It can be tuned by changing the length L of the internal ring resonator. An electric motor (coarse tuning) and an piezo serve as control elements for L. By means of a digital phase detector, ω_r is compared to the desired value. Depending on the deviation a PID controller generates an output signal acting on the piezo. In our setup, we use a quartz oscillator[17] with an output frequency of 100 MHz as frequency reference. It is locked to a rubidium frequency standard[18]. Thus, the long term stability of the atomic clock is transferred to the quartz oscillator, which itself is ultrastable on small timescales. Within this scheme, the quality of the reference frequency is very crucial since small fluctuations affect the mode stability of the comb dramatically. For example, a deviation of 1 Hz in the quartz oscillator frequency shifts a single tooth at 1000 nm by about 1 MHz.

- **Offset frequency:** The offset frequency ω_0 can be determined from a beat between the octave-spanning frequency comb $(1000 - 2100$ nm$)$ and its second harmonic generated by a frequency doubling crystal as described in [99] and references therein. In our setup, the offset frequency ω_0 is controlled via the current of the laser diode pumping the erbium doped fiber. The stabilization itself is done similar as for the case of ω_r. A digital phase

---

[14]John L. Hall and Theodor W. Hänsch were awarded with the Nobel prize in 2005 for this achievement.
[15]Note, this value is obtained when measuring the time-averaged power.
[16]Tunable second harmonic generation (T-SHG) unit from Toptica Photonics AG.
[17]Model 501-16843 from Wenzel Associates, Inc., Austin, USA.
[18]Model FS725 from Stanford Research Systems, Inc., Sunnyvale, USA.

detector compares the beat signal to the reference frequency provided by a synthesizer[19] and a PID controller generates an output signal acting on the diode current. Here, the stability of the reference is not so important compared to the corresponding scheme for ω_r, because fluctuations were transferred to the mode profile of the frequency comb without amplification. The lock works quite well as can be inferred from the resulting beat signal linewidth of about 1 Hz. Possibly, the linewidth is even better, since 1 Hz is also the resolution limit of the used spectrum analyzer. In this scheme ω_0 can be tuned in a locked regime simply by changing the output frequency of the synthesizer.

We tested our frequency comb setup by beating single modes with other reference lasers like the Mephisto MOPA system, which has an intrinsic short term frequency stability of about 1 kHz. The resulting linewidths are on the order of a few hundred kHz. Since the noise contributed by ω_0 is ≤ 1 Hz the fluctuations are mainly attributed to a jitter of the repetition frequency. This jitter cannot be compensated for due to the limited bandwidth of the feedback control.

Owing to the instability of the frequency comb, we dropped the plan to stabilize both STIRAP lasers directly to it using beat lock schemes. Nevertheless, the long term stability of the comb is quite good and we decided to use it as a reference for the STIRAP cavity lock. For this purpose, the laser at 1017.5 nm, already stabilized to the optical resonator was beat with one mode of the comb. The measured drift of the beat note compared to a reference frequency provided by a synthesizer was used to realize a slow lock for the cavity. With this setup we were able to perform the STIRAP transfer of molecules. However, after we had implemented the wavelength meter lock, we changed to the configuration described in 2.3.4, since this is much less complex.

A more detailed description of our frequency comb setup including a characterization of all involved locking schemes can be found in [100]. The large jitter of the repetition frequency, that limits the possible applications at the moment can possibly be reduced by improving the current control electronics of the laser diodes.

2.3.6 Measurement of laser frequencies

The ability to measure laser frequencies quite accurately is of great importance in our experiment, especially regarding high precision spectroscopy of molecules or STIRAP transfer. For this purpose we have a WS7 wavelength meter from HighFinesse[20]. In general, if the laser intensity is adequate, the WS7 can determine its frequency on a ms timescale. As we use an eight port multi channel switch the system enables us to measure the frequencies of eight different lasers consecutively within tens of ms.

A very nice feature is the opportunity to implement a very reliable locking scheme making use of the precise frequency measurements and the relatively fast actualization rates of the WS7. The basic idea of such a wavelength meter lock is quite simple. One compares the measured frequency to a desired one. Depending on the deviation from this set point a digital PID controller generates an output signal which is fed back to the laser after conversion to an

---

[19]Model 33250A from Agilent Technologies, Inc., Santa Clara, USA.
[20]HighFinesse GmbH, Tübingen.

analog voltage. The corresponding software was developed by Artjom Krükow and is written in LabVIEW[21]. A limiting factor concerning the achievable frequency stability is given by the actualization rate of the wavelength meter, since a control signal is only generated by the PID when the frequency is measured. This is done in intervals of tens of ms. In the meantime the laser is running freely and can drift. Owing to the multi channel switch it is possible to stabilize eight lasers simultaneously. In our setup the wavelength meter locking technique is applied to the spectroscopy laser and for stabilizing the cavity involved in the STIRAP system (cf. Sec. 2.3.4). More applications are possible. For instance, the frequency of the MOPA laser could easily be tuned using this locking scheme by setting the crystal temperature properly.

The absolute accuracy of the WS7 is specified by the manufacturer to be 60 MHz. We share the WS7 at our institute with the so called BaRbI experiment located at the laboratory next door. One of their lasers is used as calibration reference for the wavelength meter. It is locked to an atomic ^{87}Rb transition yielding a laser frequency stability of <1 MHz. In principle our software enables us to calibrate the WS7 in intervals of seconds and therefore frequency measurements at different times are comparable. It turned out, that the most severe noise source is represented by the fibers guiding the light to the multi channel switch and the wavemeter, respectively. The frequency measurement is affected (due to polarization effects), if the fibers are mechanically stressed or the temperature changes. Whereas the former can be avoided relatively easy, the latter is more challenging. During my PhD we spent a lot of time finding the optimal parameters for the air conditioning system in our laboratory. But it was worth doing it, since we ended up with a stability of $\pm\,0.1$K with respect to the set temperature. So, when looking at the laser used for calibration, we measure a drift of the frequency of about ± 2 MHz over a timescale of hours. This order of magnitude is also confirmed, due to the fact that we are able to resolve molecular transition linewidths below 10 MHz as can be seen in figure 6.3, for example. Such scans typically take 1-2 hours. Note, the frequency stability of the laser used for these measurements is already a few megahertz. Thus the accuracy for relative frequency measurements within several hundred MHz is on the MHz level. Furthermore, we check the positions of the same molecular levels from time to time and do not see jumps of more than ± 10 MHz. This demonstrates the high reproducibility of the wavemeter readings. Spectroscopical measurements with ^{138}Ba$^+$ ions performed in the BaRbI project serve as cross checks leading to the same results even in the UV-regime.

Another important quantity characterizing a wavelength meter is the achievable frequency resolution. For the case of the WS7 the manufacturer specification is 10 MHz. However, measurements with frequency-stabilized lasers and AOMs show that it is possible to resolve frequency shifts of 1 MHz, at least on timescales of minutes.

2.3.7 Geometrical arrangement of the laser beams in the glass cell

For convenience, I want to present an overview of the arrangement of all laser beams relevant for the experiments in the glass cell. The corresponding beam geometry is schematically shown in figure 2.6.

---

[21]National Instruments Corporation, Austin, USA.
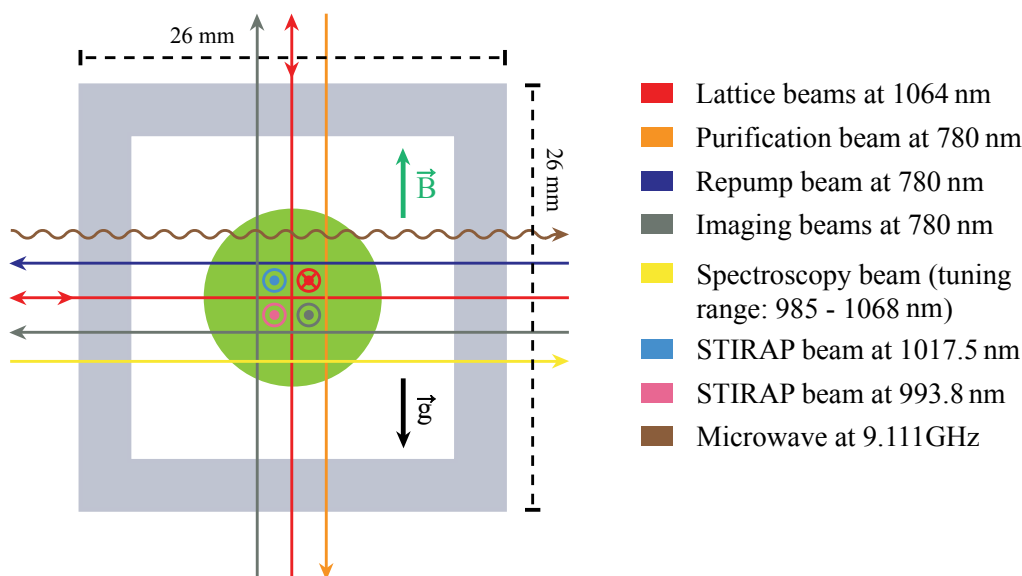
Figure 2.6: Schematic of the laser beam geometry in the glass cell. The dimensions of the glass cell are 26x26x63 mm. Here, a cross section along the short axes is shown. Arrows illustrate all relevant laser beams for our experiments with ultracold molecules that are indicated by the green circle. In addition, the propagation direction of the microwave used in the purification scheme (cf. section 3.8.3) is shown. Each of the laser beams and the microwave irradiate the whole molecular sample, which is not to scale. The quantization axis represented by the direction of the magnetic field $\vec{B}$ points antiparallel to the gravitational force.

2.4 Experiment control and data acquisition

In order to control all the laser beams, magnetic fields, RF and microwave pulses, many different digital and analog signals are necessary. The deterministic interplay of these signals constitutes the experimental sequence. Our control system guarantees the correct succession of all pulses and thus represents a pivotal element of the apparatus. Here, it will be described very briefly. For further information I refer to Ref. [84].

Key element of the experiment control is an ADwin-Gold system[22]. However, the measurement parameters are set by means of a graphic user interface written in LabVIEW. After further processing of some of the data with MATLAB[23], most of the input tables are transferred to the ADwin-Gold system by means of a Python program[24] (some parts are written in C). After completely receiving all necessary parameters for the next experiment cycle, the internal

---

[22]Jäger Computergesteuerte Messtechnik GmbH, Lorsch.
[23]MathWorks, Natick, USA.
[24]In addition, this program also addresses some other devices, like a NI PCI-6534 card and various signal generators.

processor of the ADwin starts and controls the sequence independently. The experiment cycle is synchronized with the 50 Hz power line of the laboratory which improves the reproducibility of the measurements. In principle, the ADwin provides 32 configurable digital input/output ports, two A/D converters for analog input signals and eight analog outputs. Nevertheless, the available number of output ports is insufficient to control the whole experiment. Concerning the digital channels this problem is solved by employing a "port-expander" (see Ref. [84]). Furthermore arbitrary waveform generators are used to create analog signals. In our setup, the required computation time limits the resolution of the ADwin system to 50 µs. For some purposes during the experimental sequence a better time resolution is necessary. To control such fast processes, we utilize a high-speed digital I/O card (PCI-6534 from National Instruments) with a maximum clock rate of 20 MHz.

In general, the overall structure of the experiment control is quite complicated as it has grown over the years. In order to simplify and improve it, we now have an ADwin-Pro II from Jäger Computergesteuerte Messtechnik available. Since this is a modular system, the number of digital and analog channels can be increased easily. At the moment, the ADwin-Pro II is not completely implemented. However, it already controls some of the crucial steps within our sequence, particularly the lattice beams and the STIRAP pulses. We also integrated an digital intensity stabilization for each of the lattice beams. For this purpose, we measure the actual laser beam powers with photo diodes[25]. In the following, I want to consider just one lattice direction, since the basic scheme is the same for the two other ones. The analog signal of the photo diode is fed into the ADwin-Pro II. Subsequently, the deviation from the desired value is measured and depending on that, a digital PID generates an output signal which acts on the RF input power of an AOM and thereby controls the intensity of the lattice beam. Using this setup, we observe remaining intensity fluctuations of less than 0.3%.

At the end of each experiment cycle the measurement results are obtained by absorption imaging (see [101], for example). From these images one can determine the relevant parameters of the atomic cloud like the number of particles, density, size, position etc. Several cameras are employed in our setup. Among them, the most important one is a Luca S[26], which is used to detect atomic signals in the glass cell. By using another two cameras[27], we are able to perform absorption imaging in each lattice direction. This is very convenient, especially for adjusting laser beams to the position of the atomic cloud. One additional Guppy F-38B NIR is available in order to take absorption images of the MOT. The camera software that analyzes the images is programmed in MATLAB (except for the user interface of the Theta camera which is written in LabVIEW).

---

[25]More precisely, the photo diodes are placed behind mirrors and they measure the low power which is transmitted through the coating and the substrate.

[26]EMCCD camera from Andor Technology plc., Belfast, UK.

[27]S285 from THETA SYSTEM Elektronik GmbH, Gröbenzell and Guppy F-38B NIR from Allied Vision Technologies GmbH, Stadtroda.

3 Experimental Methods

In our setup, we perform measurements with ultracold ^{87}Rb$_2$ molecules in precisely defined quantum states. For this purpose, ^{87}Rb atoms are trapped, laser cooled and associated to dimers, which are investigated afterwards. One experiment cycle takes about 35 seconds and is composed by several subsequences:

- Loading of atoms into a MOT with subsequent creation of an optical molasses.

- Spin preparation of atoms in state $|f_a = 1, m_{f_a} = -1\rangle$, where m_{f_a} is the projection of f_a onto the quantization axis.

- Loading of the laser-cooled atoms into a purely magnetic trap (quadrupole trap) and magnetic transport to the glass cell.

- Loading of the atoms into a QUIC trap.

- Evaporative cooling.

- Transfer of the ultracold atom cloud to the center of the quadrupole coils (Feshbach coils).

- Loading of the ultracold atom cloud into a 3D optical lattice.

- Spin preparation of the atoms in state $|f_a = 1, m_{f_a} = +1\rangle$.

- Association of atoms to molecules (dimers) using a magnetic Feshbach resonance.

- Purification of the ensemble, ending up with a pure sample of molecules.

- STIRAP transfer of the weakly bound Feshbach molecules to deeply bound molecules.

- Experiments with deeply bound molecules.

- Reversal of the STIRAP transfer and dissociation of molecules.

- Stern-Gerlach separation of spins.

- Absorption imaging of the atom cloud.

In this chapter the experimental sequence is described, following chronologically the steps just mentioned.

3.1 MOT, optical molasses and spin preparation

The experimental procedure starts in the MOT chamber of the vacuum apparatus (see Fig. 2.1) with the laser cooling of ^{87}Rb atoms. For this purpose, we use pairs of counterpropagating beams in the three spatial directions, i.e., six beams in total with a power of about 50 mW per beam. The cooling light is about 20 MHz red detuned from the $f_a = 2 \rightarrow f'_a = 3$ transition and superimposed by several mW of repumping light ($f_a = 1 \rightarrow f'_a = 2$) in order to close the cooling cycle. In combination with a magnetic quadrupole field, this represents the creation of a MOT. The ^{87}Rb atoms are trapped directly from the background vapor. Subsequent to the MOT loading we perform molasses cooling, i.e., the detuning of the cooling light is increased and the magnetic field is switched off. After that, we end up with $2 - 3 \times 10^9$ atoms at a temperature of about 70 μK. The next step is optical pumping. More precisely the preparation of a spin-polarized ensemble of atoms in state $|f_a = 1, m_{f_a} = -1\rangle$. Therefore, we switch on the push coil (see Fig. 2.2) and generate a magnetic field of several gauss pointing in the direction of the magnetic transport line, in order to define the mandatory quantization axis. Then, a sequence of several light pulses resonant to different atomic transitions around 780 nm is used to transfer as many atoms as possible to the desired state.

3.2 Magnetic transport

After the spin preparation we change to a pure magnetic trap configuration. For this purpose, the MOT coils are switched on again and the current is ramped up until the gradient of the resulting quadrupole field reaches $\partial B_z / \partial z = 13$ G/mm, which is an appropriate value for the following transport. Owing to this procedure, the atomic sample is heated up to about 150 μK. The remaining number of atoms is measured to be $\sim 1 \times 10^9$ and their lifetime τ in the trap is on the order of one second (depending on the adjustable pressure of the ^{87}Rb vapor in the MOT chamber). Then, the atoms are transferred to the glass cell by means of a magnetic transport [85]. In total, a distance of 48 cm including a 120° angle has to be bridged (see Fig. 2.2). By consecutively ramping the currents of neighboring quadrupole coils, the trapping potential is shifted smoothly along the transport line, as described in section 2.2. The overall transfer takes 1.4 s and necessitates current peaks of up to 120 A. In the glass cell, we end up with $\sim 6 \times 10^8$ atoms at a temperature of about $180 - 200$ μK.

3.3 QUIC trap

Subsequent to the magnetic transfer, the atoms are in a quadrupole trap, which is inappropriate in order to perform evaporative cooling down to temperatures typical for Bose-Einstein condensation. Hence, we change to a QUIC trap created by the quadrupole coils and an additional Ioffe coil. First of all, the current of the quadrupole coils is increased such, that the magnetic field gradient reaches $\partial B_z / \partial z = 30$ G/mm. Afterwards, the Ioffe coil is switched on and the current is ramped up slowly (within ~ 1 s) until it equals the current through the quadrupole coils. In this final configuration, the trap frequencies are on the order of 130 Hz in

radial and 15 Hz in axial direction. Owing to the Ioffe coil, the position of the atomic cloud is shifted by about 6 mm with respect to the quadrupole trap. This can be seen in the simulations shown in figure 3.1(a) and (b). Note, an additional offset magnetic field in axial direction is mandatory in order to create an appropriate potential. Otherwise, the atom cloud touches the surface of the glass cell leading to atom losses from the trap. The identification of this problem took quite some time before we produced the first BECs within the rubidium project in Ulm.
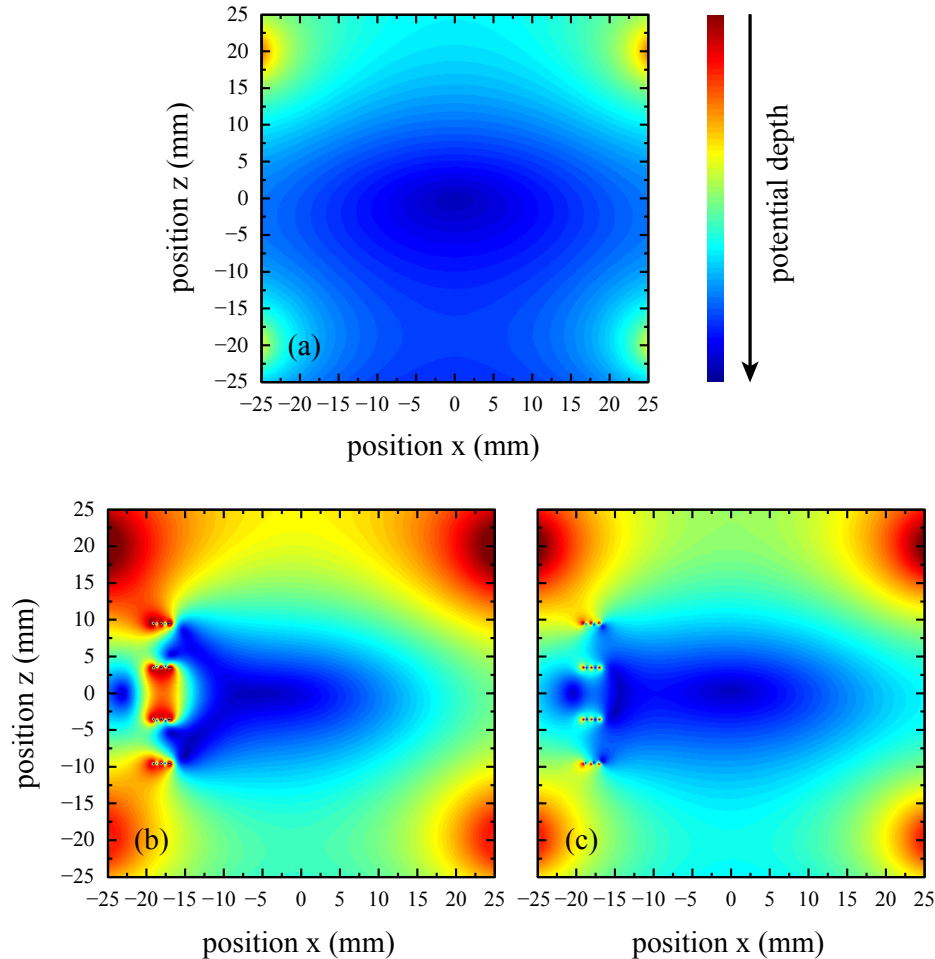
Figure 3.1: Contour plots of trapping potentials. Shown are the results of simulations for the quadrupole trap (a), the QUIC trap (b) and the trap after the transport within the glass cell (c) including all relevant coils and the gravitation. The positions in the vertical direction z and the horizontal (axial) direction x are given with respect to the center of the quadrupole trap. When the Ioffe coil is switched on, the atomic cloud is displaced by about 6 mm along the x axis, as can be seen by comparing (a) and (b). Before the Feshbach field is applied, the atoms are shifted back to zero position [see (c)].

As mentioned above, for the transformation of the traps, the current through the quadrupole coils is increased. During this procedure, the atomic cloud is heated up to about $300\,\mu\mathrm{K}$. Such a high temperature would lead to a huge loss of atoms when changing to the QUIC configuration. Therefore, we already start the evaporative cooling in the steep quadrupole trap. Before the Ioffe coil is switched on, the temperature of the remaining $\sim 1-2\times 10^{8}$ atoms is about $100\,\mu\mathrm{K}$. The transfer efficiency of the atomic cloud is then almost $100\,\%$. Due to the low pressure inside the glass cell, the lifetime τ of the atomic sample is enhanced compared to the values in the MOT chamber. For example, regarding the steep quadrupole trap, we measure $\tau \sim 50\,\mathrm{s}$ for atoms at a temperature of $100\,\mu\mathrm{K}$.

3.4 Evaporative cooling and Bose-Einstein condensation

In this section, I will first of all give some basic formulas concerning Bose-Einstein condensation of a dilute gas in a harmonic trap. A more detailed description can be found, e.g., in Refs. [102, 103]. Afterwards, the experimental realization in our setup using radiofrequency evaporation is presented.

3.4.1 Theoretical description of a BEC

Bose-Einstein condensation is a quantum statistical effect which occurs, when the phase-space density $n\lambda_T^3$ reaches

$$n\lambda_T^3 = \zeta(3/2) \approx 2.612 \ . \tag{3.1}$$

Here, n denotes the spatial atomic density and $\lambda_T = (2\pi\hbar^2/mk_{\mathrm{B}}T)^{3/2}$ the thermal de Broglie wavelength, with T being the temperature and m representing the mass of an atom. Moreover, $\zeta(x)$ is the Riemann zeta function. The critical temperature T_{c} for the phase transition can be written as

$$T_{\mathrm{c}} = \frac{\hbar\bar{\omega}}{k_{\mathrm{B}}}\left(\frac{N}{\zeta(3)}\right)^{1/3} \approx 0.94\frac{\hbar\bar{\omega}}{k_{\mathrm{B}}}N^{1/3} \ , \tag{3.2}$$

where N is the total number of atoms and $\bar{\omega} = (\omega_x\omega_y\omega_z)^{1/3}$ gives the geometric mean of the trapping frequencies. Within mean-field theory, the macroscopic behavior of the condensate confined in an external potential $V_{\mathrm{ext}}(\vec{r})$ can be described by the Gross-Pitaevskii equation

$$i\hbar\frac{\partial}{\partial t}\Phi\left(\vec{r},t\right) = \left(-\frac{\hbar^2\nabla^2}{2m} + V_{\mathrm{ext}}\left(\vec{r}\right) + g|\Phi(\vec{r},t)|^2\right)\Phi\left(\vec{r},t\right) \ . \tag{3.3}$$

The complex-valued classical field $\Phi\left(\vec{r},t\right)$, often referred to as wave function, represents an order parameter, which determines the condensate density, since $n(\vec{r},t) = |\Phi(\vec{r},t)|^2$. Furthermore, the coupling constant $g = 4\pi\hbar^2 a/m$ characterizes the atom-atom interaction and thus is related to the scattering length a. For deriving the time independent case, $\Phi\left(\vec{r},t\right)$ is expressed as $\phi(\vec{r})\exp\left(-i\mu t/\hbar\right)$ using the chemical potential μ, where $\phi(\vec{r})$ is real-valued. According to that,

the Gross-Pitaevskii equation reads

$$\mu\phi(\vec{r}) = \left(-\frac{\hbar^2\nabla^2}{2m} + V_{\text{ext}}(\vec{r}) + g\phi^2(\vec{r})\right)\phi(\vec{r}) \ . \tag{3.4}$$

This equation simplifies drastically in the so called Thomas-Fermi regime, i.e., when the contribution of the kinetic energy term is negligible compared to the interaction energy. With this approximation, Eq. (3.4) can be written as

$$n(\vec{r}) = \phi^2(\vec{r}) = \frac{\mu - V_{\text{ext}}(\vec{r})}{g} \ . \tag{3.5}$$

Therefore, given a harmonic trapping potential, the spatial density is parabolic.

3.4.2 Experimental realization of a BEC

In order to produce a BEC, we perform radiofrequency evaporation, i.e., the atoms are irradiated by an RF field whose frequency is lowered, which leads to a continuous loss of the hottest atoms and thermalization of the remaining sample [104]. For further information on evaporative cooling, I refer to the theoretical description given in Ref. [105]. Starting with 30 MHz, we reduce the frequency to ~ 1 MHz within $10 - 15$ s using a sequence of linear and spline functions. Figure 3.2 shows the phase transition from a cold thermal cloud to a pure BEC[28] of about 1×10^6 atoms with a temperature below 500 nK. Most of the measurements described in this thesis were carried out with ultracold thermal atoms close to condensation as starting point, since this configuration leads to the maximum number of molecules.

3.5 Transport of the atom cloud within the glass cell

In the QUIC configuration, the atoms are displaced by about 6 mm from the center of the quadrupole coils, which create the field for the Feshbach association later on. As this field has to be homogeneous over the dimension of the atomic cloud, it is necessary to transport the atoms back to the center. Hence, the current through the quadrupole coils is decreased and the big offset coils (operated in anti-Helmholtz configuration) are switched on (see also Fig. 2.3). During the transfer, the current of the levitation coil is adjusted properly to compensate for the gravitational force. This is necessary, since the trapping frequencies are lowered to ~ 20 Hz in radial and ~ 7 Hz in axial direction. Furthermore, we employ the last pair of coils of the magnetic transport line for the exact positioning of the atomic sample. In total, the transfer takes about 1 s. A simulation of the resulting trapping potential is shown in Fig. 3.1(c).

---

[28]One of the first BECs of the rubidium experiment in Ulm.
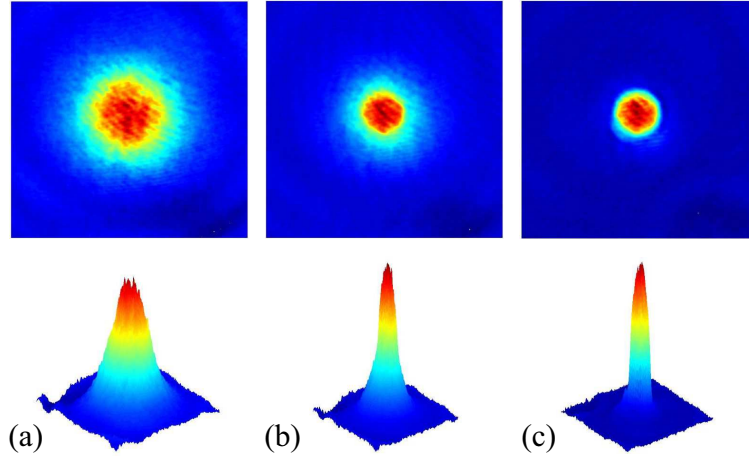
Figure 3.2: Bose-Einstein condensation of ^{87}Rb atoms observed by absorption imaging of the atomic cloud after $15\,\mathrm{ms}$ time of flight. The peak height and the color, respectively, represent the atomic density. From left to right the final value of the RF in the evaporation sequence and thus the temperature is decreased, which gives rise to the phase transition from a thermal cloud (a) to a pure BEC (c). The sharp peak on top of the rather broad distribution in (b) indicates a large fraction of already condensated atoms in the center of the trap surrounded by a cloud of thermal atoms.

3.6 Optical lattice

The molecule formation process and the subsequent manipulations of the dimers are performed within a 3D optical lattice that represents the essential tool for controlling the interparticle separation. If the lattice depth is large enough, the molecules are well isolated from each other, which is called a Mott insulator state. When the depth is lowered, tunneling becomes possible and molecules can collide. By completely switching off one (two) lattice beams, we are able to realize quasi-1D (2D) systems. So, many different interaction regimes and geometries are accessible. In this chapter, I will first provide some basic formulas concerning optical trapping of atoms and molecules. Afterwards, the realization of the optical lattice in our setup is described and characteristic experiments like the diffraction of a BEC, the measurement of the energy-band population and the observation of the superfluid to Mott insulator transition are presented. An overview of this specific field of research can be found in [106].

3.6.1 Optical trapping of atoms and molecules

Here, I want to briefly present the basic idea of optical trapping of particles following the discussion given in Ref. [107]. When an atom is exposed to a linearly polarized, oscillating electric field $\vec{E}(t) = \hat{\varepsilon}E_0\cos(\omega t)$ with amplitude E_0 and unit polarization vector $\hat{\varepsilon}$, a dipole moment $\vec{p}(t) = \alpha(\omega)\vec{E}(t)$ is induced, where $\alpha(\omega)$ denotes the complex-valued, frequency-dependent dy-

namical polarizability. The corresponding dipole interaction potential is fixed by the real part of the polarizability $\text{Re}\{\alpha(\omega)\}$ and reads

$$U = -\frac{1}{2}\langle \vec{p} \cdot \vec{E} \rangle = -\frac{1}{4}\text{Re}\{\alpha(\omega)\}E_0^2 \ . \tag{3.6}$$

Please note, the angular brackets indicate the time average over the rapid oscillating terms. Since $I \propto E_0^2$, the dipole potential is directly linked to the intensity of the electric field. I want to point out that U is attractive, when the sign of $\text{Re}\{\alpha(\omega)\}$ is positive, and repulsive otherwise. In contrast, the imaginary part $\text{Im}\{\alpha(\omega)\}$ is related to the power P_{abs} absorbed by the oscillator from the driving field, according to

$$P_{\text{abs}} = \langle \dot{\vec{p}} \cdot \vec{E} \rangle = \frac{1}{2}\omega\text{Im}\{\alpha(\omega)\}E_0^2 \ . \tag{3.7}$$

Hence, the dynamical polarizability fully characterizes the response of the particle to the electric field.

In principle, molecules can be treated in complete analogy. Nevertheless, the situation is in general more complicated than for atoms, owing to the anisotropic geometric structure. This is reflected into a polarizability tensor $\overleftrightarrow{\alpha}(\omega)$. In our setup, we work with nonpolar dimers and the tensor can be simplified considerably. However, an anisotropic polarizability still remains dependent on the molecular state (see chapter 5).

3.6.2 Realization of the optical lattice

In our setup, the 3D optical lattice at $\lambda = 1064.5$ nm is formed by a superposition of three linearly polarized standing light waves in the x, y, and z directions realized by retroreflected Gaussian beams. The corresponding intensity profile in one dimension reads

$$I(r, z) = 4I_{\text{L}}e^{-\frac{2r^2}{d^2(z)}}\cos^2(k_{\text{L}}z) \ , \tag{3.8}$$

where $r^2 = x^2 + y^2$ and $k_{\text{L}} = 2\pi/\lambda$ denotes the wavenumber of the laser beam. The function

$$d(z) = d_0\sqrt{1 + \left(\frac{z}{z_R}\right)^2} \tag{3.9}$$

gives the $1/e^2$ beam radius depending on the distance z from the focus with the Rayleigh length $z_R = \pi d_0^2/\lambda$. Furthermore, $4I_{\text{L}}$ is the maximum intensity of the standing light wave, which is related to the power P of the laser beam, since $I_{\text{L}} = 2P\pi^{-1}d_0^{-2}$. Inserting the intensity profile of Eq. (3.8) in Eq. (3.6) yields

$$U(r, z) = U_0 e^{-\frac{2r^2}{d^2(z)}}\cos^2(k_{\text{L}}z) \ . \tag{3.10}$$

This interaction potential represents an array of equidistant microtraps separated by the lattice

constant $a = \lambda/2 = 532.25\,\text{nm}$. Usually, the lattice depth U_0 is given in units of recoil energies $E_R = h^2/(2m\lambda^2)$, where h is Planck's constant and m is the mass of the trapped particle.

The polarizations of the three standing light waves in our setup are oriented orthogonal to each other and the optical frequencies are slightly different (on the order of 100 MHz) to avoid interference effects. Thus, the potential of the 3D optical lattice is the sum of three independent terms and reads

$$U_{3\text{D}} = U_{0,x}e^{-\frac{2(y^2+z^2)}{d^2(x)}}\cos^2(k_{\text{L}}x) + U_{0,y}e^{-\frac{2(x^2+z^2)}{d^2(y)}}\cos^2(k_{\text{L}}y) + U_{0,x}e^{-\frac{2(x^2+y^2)}{d^2(z)}}\cos^2(k_{\text{L}}z) \ , \quad (3.11)$$

which gives rise to a crystal-like structure. Correspondingly, a system of parallel tubes (pancakes) is found for the 2D (1D) case.

3.6.3 Diffraction of a BEC by an optical lattice

This subsection is devoted to the sudden loading of a BEC into an optical lattice [108, 109]. More precisely, the BEC is exposed to an optical standing wave for a duration τ, where the light pulse has a rectangular shape. The resulting diffraction patterns can be exploited to adjust the individual lattice beams and to determine the corresponding potential depths. I will first of all give a short theoretical description following Refs. [84, 109]. Afterwards, measurements using either the laser wavelengths of 1064.5 nm or 830.4 nm are presented.

For simplicity, we consider an infinite periodic potential in one dimension, expressed by $U(z) = U_0\cos(k_{\text{L}}z)$. Since atom-atom interactions can be neglected on the timescales relevant here, a single particle treatment is possible and the Hamilton operator reads $H = -\frac{\hbar^2}{2m}\frac{\partial^2}{\partial z^2} + U$. Then, solving the stationary Schrödinger equation results in an energy-band structure (cf. Fig. 4.4, which shows calculations with respect to Rb_2 molecules), in analogy to solid state physics. Accordingly, the eigenstates $|n,q\rangle$ with eigenenergies $E_{n,q}$ are called Bloch states. Here, q denotes the quasimomentum and n is the band index. When expressing the Bloch states in terms of the discrete plane-wave basis $\{|\phi_p\rangle\}$ with momenta $p = q + 2l\hbar k_{\text{L}}$ ($l \in \mathbb{Z}$), one obtains

$$|n,q\rangle = \sum_{l=-\infty}^{\infty} c_{n,q}(l)\,|\phi_{p=q+2l\hbar k_{\text{L}}}\rangle \ . \quad (3.12)$$

We now consider a BEC suddenly loaded into the optical lattice. The initial state of the BEC is described by a plane wave $|\psi(t=0)\rangle = |\phi_q\rangle$. When the optical potential is switched on, the plane wave is projected onto the Bloch states and can be written as

$$|\psi(t=0)\rangle = \sum_{n=0}^{\infty} |n,q\rangle\,\langle n,q|\phi_q\rangle = \sum_{n=0}^{\infty} c_{n,q}^*(0)\,|n,q\rangle \ , \quad (3.13)$$

using Eq. (3.12). Hence, the time evolution of the BEC in the optical lattice is given by

$$|\psi(t)\rangle = \sum_{n=0}^{\infty} c_{n,q}^*(0)e^{-i\frac{E_{n,q}}{\hbar}t}\,|n,q\rangle \ . \quad (3.14)$$

After a time τ the light is abruptly switched off and the state $|\psi(\tau)\rangle$ is projected onto the measurement basis, i.e., onto plane waves again, yielding

$$|\psi(\tau)\rangle = \sum_{l=-\infty}^{\infty} b_q(l) |\phi_{q+2l\hbar k_{\mathrm{L}}}\rangle \tag{3.15}$$

with coefficients

$$b_q(l) = \sum_{n=0}^{\infty} c_{n,q}^*(0) c_{n,q}(l) e^{-i\frac{E_{n,q}}{\hbar}\tau} . \tag{3.16}$$

A free expansion in a time of flight measurement results in the spatial separation of the single plane-wave components and a diffraction pattern is observed. The population of the l-th maximum is determined by $|b_q(l)|^2$. Figure 3.3 shows typical absorption images of the diffraction patterns obtained in a 1D and 2D optical lattice configuration. The maxima $|b_q(l)|^2$ show characteristic oscillations as a function of the pulse time τ, which can be used to determine the lattice depth, in principle. However, we predominantly employed a different method based on lattice modulation spectroscopy (see chapters 4 and 5). This technique is more favorable, when working with molecules in our setup.
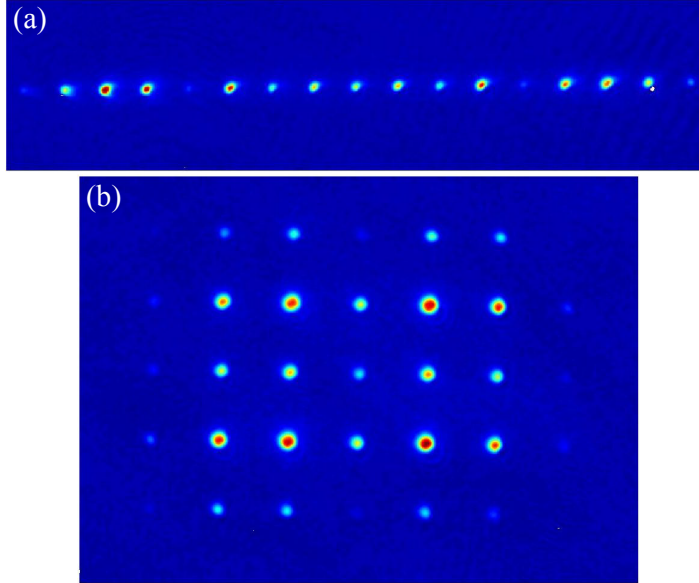
Figure 3.3: Sudden loading of a stationary BEC ($q = 0$) into a 1D (a) and 2D (b) optical lattice, respectively. The atoms are illuminated in the relevant direction(s) for a duration of tens of μs by a light pulse with rectangular shape. After several ms time of flight, the absorption images clearly show a diffraction pattern indicating the plane-wave decomposition of the state. For (a), the lattice wavelength was $\lambda = 1064.5$ nm, while (b) corresponds to a measurement at 830.4 nm.

3.6.4 Adiabatic mapping of the lattice energy-band population

We have seen, that several Bloch bands are populated, if the lattice is switched on all of a sudden. Such a distribution of atoms is disadvantageous regarding the molecule formation and the subsequent experiments described in this thesis. In fact, all the atoms are desired to reside within the lowest Bloch band $n = 0$. This can be achieved by adiabatically ramping up the lattice intensity, which is the case, when the criterion

$$|\langle e, q|\partial H/\partial t|0, q\rangle| \ll |E_{e,q} - E_{0,q}|^2/\hbar \qquad (3.17)$$

is fulfilled [109]. Here, $|n, q\rangle$ denotes the first excitable state. Specifically, for $q = 0$, Eq. (3.17) is satisfied, if $dU_0/dt \ll 16E_R^2/\hbar$, since $|E_{e,q} - E_{0,q}| \geq 4E_R$ for any U_0. In this sense, an adiabatic ramp at $\lambda = 1064.5$ nm to a typical final lattice depth of $12.5E_R$ with respect to ^{87}Rb atoms has to be significantly longer than 60 µs.

   If the lattice is turned off adiabatically, the crystal momentum q is conserved and a Bloch state $|n, q\rangle$ is mapped onto a free particle momentum in the corresponding Brillouin zone n (see, e.g., [110]). Therefore, the population of the n-th energy band can be measured independently. Figure 3.4 shows an absorption image of an atomic cloud adiabatically released from the 3D optical lattice. The atoms in the lowest Bloch band form a cubic structure which corresponds to the momentum interval $-\hbar k_L \leq p \leq \hbar k_L$ in each direction, representing the first Brillouin zone.
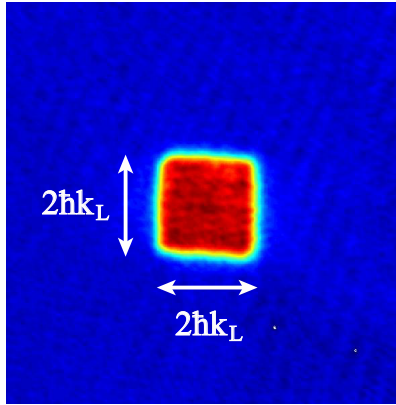
Figure 3.4: Mapping of the Bloch state population onto the free particle momentum distri-
bution. The absorption image is taken after adiabatically ramping down the 3D
optical lattice at $\lambda = 1064.5$ nm with subsequent free expansion of the atomic
cloud. It shows an almost homogeneous filling of the lowest Bloch band, whereas
no populations are found in excited bands.

3.6.5 Superfluid to Mott insulator transition

In the previous section, we have focused on the adiabatic loading of atoms into the 3D optical lattice. Now, the influence of the potential depth will be discussed. More precisely, we consider

the changeover of a weakly interacting quantum gas into a strongly correlated many-body system. This so-called superfluid to Mott insulator phase transition has been predicted in Ref. [111] and experimentally observed with cold bosons in an optical lattice in a seminal work of Greiner *et al.* [50]. For the theoretical description of such systems, atom-atom interactions have to be taken into account, which leads to the famous Bose-Hubbard Hamiltonian [112]

$$\hat{H} = -J \sum_{\langle i,j \rangle} \hat{a}_i^\dagger \hat{a}_j + \frac{1}{2} U \sum_i \hat{n}_i (\hat{n}_i - 1) \ , \tag{3.18}$$

when considering only occupations of the lowest Bloch band. The first term describes the tunneling between adjacent lattice sites i and j, where J denotes the tunnel matrix element and $\hat{a}_i^\dagger$ ($\hat{a}_i$) represents the creation (annihilation) operator for a particle in the potential well i. In contrast to that, the on-site interaction is expressed by the second term with the operator $\hat{n}_i = \hat{a}_i^\dagger \hat{a}_i$ counting the number of bosonic atoms per lattice site i. Here, U corresponds to the repulsion strength of two atoms located in the same potential well. The first, so-called hopping term causes delocalization of the atoms over the entire lattice, whereas the second term of the Bose-Hubbard Hamiltonian gives rise to localization. Hence, the relation U/J, that can be tuned via the lattice depth, determines the fundamental behavior of the atomic ensemble. In the limit of $U/J \ll 1$, the system forms a superfluid phase characterized by an macroscopic wave function. For $U/J \gg 1$, the atoms are prevented from tunneling to neighboring lattice sites, which is referred to as the Mott insulator regime. Owing to the localization, no interference pattern is observed anymore, when suddenly releasing the atoms from the lattice.

In order to observe the superfluid to Mott insulator phase transition, we adiabatically load a BEC into the 3D optical lattice within 250 ms. Note, in contrast to the experiments described in Sec. 3.6.4, adiabaticity here is related to much longer timescales, since the atoms have to redistribute, when the lattice depth is changed. Typical absorption images are shown in Fig. 3.5. For deep optical lattices, the localization of the atoms becomes evident due to the disappearance of the diffraction pattern.

We perform the molecule formation at a potential depth of $12.5 E_R$ with respect to atoms, which approximately corresponds to the threshold concerning the Mott insulator phase. In this regime, atoms of different lattice sites are sufficiently well isolated from each other and collisions are strongly suppressed, which is advantageous for the conversion efficiency to dimers and the lifetime of the molecules.

3.7 Spin preparation

After adiabatically loading the BEC or cold thermal cloud of atoms in spin state $|f_a = 1, m_{f_a} = -1\rangle$ into the 3D optical lattice at $\lambda = 1064.5$ nm, the magnetic trap is slowly turned off. Then, the quantization axis is defined by the direction of the permanent offset magnetic field that stems from the cage of ribbon cables surrounding the glass cell. In order to utilize the Feshbach resonance at $B = 1007.4$ G, we have to prepare the atoms in the high field seeking state $|f_a = 1, m_{f_a} = +1\rangle$. For this purpose, the big offset coils (cf. figure 2.3) are ramped
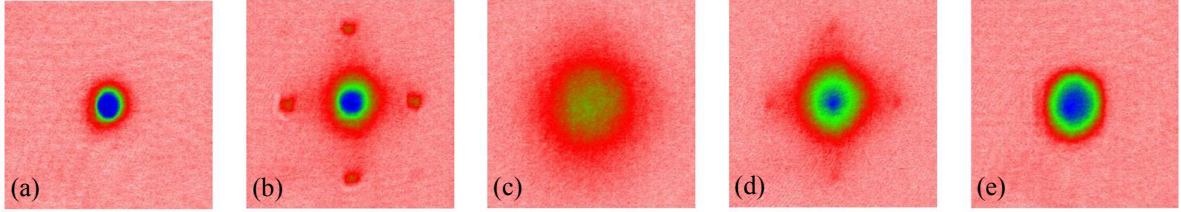
Figure 3.5: Superfluid to Mott insulator phase transition observed with a 3D optical lattice at 830.4 nm. (a) BEC before the lattice is switched on. (b) The lattice depth is adiabatically increased to a final value of $5E_R$ and switched off abruptly. After free expansion of the atoms the absorption image shows a diffraction pattern that characterizes the superfluid phase. (c) If the lattice depth is increased to $15E_R$ the coherence is lost, which is a clear signature for the localization of the atoms. (d) The lattice depth is ramped up to $15E_R$ in analogy to (c) and subsequently ramped down adiabatically to $5E_R$ before it is switched off suddenly. A revival of the interference pattern can be seen, demonstrating the reversibility of the phase transition. (e) After reaching $15E_R$ the lattice is adiabatically ramped down to zero.

up slowly. The corresponding magnetic field points in the opposite direction with respect to the permanent field. Thus, the direction of the quantization axis is reversed. Now, the big offset coils are switched off abruptly, so that the spins cannot follow. Thereby, the atomic state changes from $|f_a = 1, m_{f_a} = -1\rangle$ to $|f_a = 1, m_{f_a} = +1\rangle$ (see also, e.g., [53, 113]). We achieve a preparation efficiency of almost 100%, which can be measured by time of flight absorption imaging, when performing a Stern-Gerlach separation of atomic spin states (cf. section 3.11).

3.8 Feshbach molecules

Feshbach resonances have become a major tool to produce ultracold molecules in recent years. Since a comprehensive overview of the basic concept and the field can be found in [19, 20], I will just give a brief, rather phenomenological description of the molecule formation mechanism here, and then focus onto the experimental realization. At the end of this section, our purification scheme based on an atom-selective microwave transition is presented. The implementation of the Feshbach association and sample purification techniques in our setup was accomplished by the former PhD students Gregor Thalhammer and Klaus Winkler. Using these methods, we are able to prepare pure ensembles of about 3×10^4 ultracold Feshbach molecules showing typical lifetimes on the order of $\sim 1\,\mathrm{s}$ in deep optical lattices at $\lambda = 1064.5\,\mathrm{nm}$.

3.8.1 Molecule formation via a Feshbach resonance

A Feshbach resonance is a scattering feature of two colliding atoms, which are coupled to a bound molecular state. The situation is illustrated in figure 3.6. We consider a pair of colliding
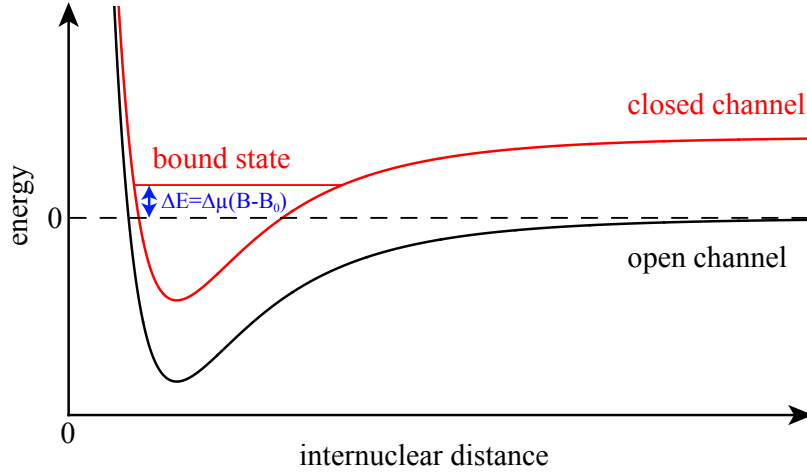
Figure 3.6: Basic principle of a Feshbach resonance. It occurs, when the scattering state of two colliding atoms in the open entrance channel resonantly couples to a bound molecular state of a closed channel. Using a magnetic Feshbach resonance, the energy difference ΔE can be tuned by means of an external magnetic field B.

atoms in the asymptotic limit of large internuclear distances. The corresponding potential represents an energetically open channel sometimes referred to as entrance channel. When a molecular bound state provided by an closed channel potential couples to the scattering state of the atomic pair, it strongly influences the collision properties. Consequently, a Feshbach resonance can be used to tune the scattering length, since the described coupling depends on the energy difference ΔE of the two states. For example, if the magnetic moments with respect to the open and closed channel are different ($\Delta \mu \neq 0$), the Zeeman shift allows for the control of ΔE by means of an applied magnetic field B according to $\Delta E = \Delta \mu (B - B_0)$. Here, B_0 represents the resonant field strength. Such a magnetic Feshbach resonance can be characterized by the s-wave scattering length [20, 114]

$$a(B) = a_{\text{bg}} \left(1 - \frac{\Delta B}{B - B_0} \right) \ , \tag{3.19}$$

where a_{bg} denotes the background scattering length describing the nonresonant regime. The resonance width ΔB is defined by the distance of the zero crossing of $a(B)$ from the resonance position. In analogy, given an optical Feshbach resonance, the coupling of the molecular bound state to the scattering state of the atomic pair can be tuned by a light field [115-117]. However, optical Feshbach resonances will not be discussed in more detail here, as they are not relevant to this work.

For [87]Rb atoms in the prepared spin state $|f = 1, m_f = +1\rangle$, more than 40 Feshbach resonances have been observed in the magnetic field range between $0.5\,\text{G}$ and $1260\,\text{G}$ [118]. Similar to Refs. [30, 54], we use the broadest resonance at $1007.4\,\text{G}$ ($\Delta B = 0.21\,\text{G}$ and $a_{\text{bg}} = 100a_0$ [20],

where a_0 is the Bohr radius) in order to produce molecules. As already mentioned, in our setup, the atoms and also the formed molecules are trapped in an optical lattice. Exemplarily, figure 3.7 depicts the situation for the experimental parameters of Ref. [53], i.e., a potential depth of $35E_R$ at a wavelength of 830 nm. Note, we are currently working with a 3D optical lattice at 1064.5 nm. However, this does not change the basic characteristics. In principle, the location of the Feshbach resonance slightly depends on the vibrational state v with respect to the spherical harmonic trap. We only have to consider $v = 0$ owing to the preparation of the sample in the lowest Bloch band in our setup. By adiabatically ramping down the magnetic field across the Feshbach resonance, a pair of atoms forms a weakly bound molecule. For the case of a linear sweep, the molecule creation probability P can be calculated using a Landau-Zener approach, which yields [19, 53, 119]

$$P = 1 - \exp\left\{ -\frac{2\sqrt{6}\hbar}{ma_{\mathrm{ho}}^3} \left| \frac{a_{\mathrm{bg}}\Delta B}{\dot{B}} \right| \right\} , \qquad (3.20)$$

where $\dot{B}$ is the ramp speed and $a_{\mathrm{ho}} = \sqrt{\hbar/(m\omega_0)}$ represents the harmonic oscillator length.
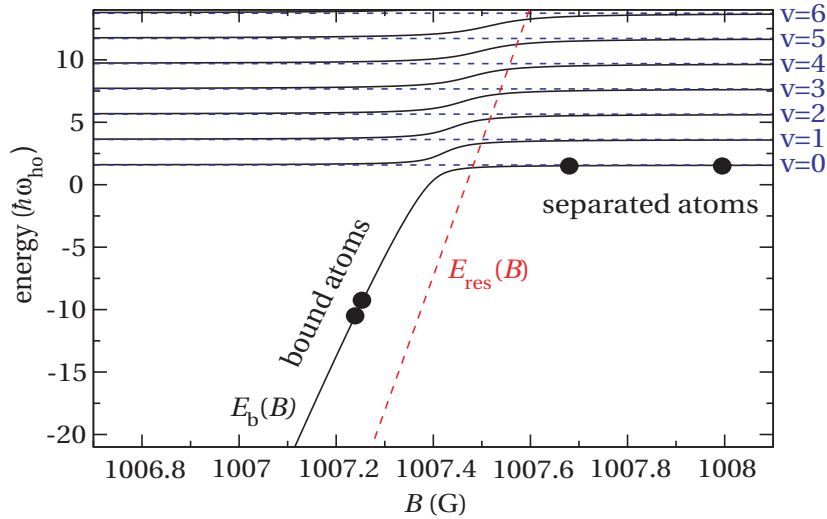
Figure 3.7: Feshbach association of ground state ^{87}Rb atoms in a spherical harmonic trap with an oscillator frequency of $\omega_{\mathrm{ho}} = 2\pi \times 39$ kHz. The dashed lines indicate the vibrational levels ($v = 0, \ldots, 6$) of the harmonic trap (blue) and the bare Feshbach resonance energy $E_{\mathrm{res}}(B)$ (red). Owing to the coupling, the dressed energy levels (solid lines) show avoided crossings. Thus, a pair of atoms in the lowest vibrational state can be associated to a weakly bound molecule by adiabatically ramping down the magnetic field across the resonance at about $B = 1007.4$ G. The figure is adapted from Ref. [19].

3.8.2 Creation of diatomic molecules in the experiment

In our setup, the quadrupole coils operated in Helmholtz configuration are used in order to generate the Feshbach field. Since it has been described in great detail in Refs. [53, 84], I will just briefly present the molecule formation procedure here. First of all, we quickly ramp up the magnetic field to a value slightly above the Feshbach resonance at 1007.4 G, which has essentially no effect on the atoms owing to the fast ramping speed. Afterwards, we adiabatically cross the Feshbach resonance creating weakly bound molecules. I want to emphasize that, due to our active stabilization, the magnetic field has a relative accuracy of about 10^{-4} (cf. section 2.2).

   If a lattice site is filled with three or more atoms, they are lost due to inelastic collisions, when ramping over the Feshbach resonance. The conversion efficiency for doubly occupied lattice sites is more than 90% [53]. In order to get rid of remaining single atoms, we apply a purification scheme, which is described in section 3.8.3. However, starting with $\sim 4 \times 10^5$ atoms in the optical lattice, we typically end up with a pure ensemble of about $2.5 - 3 \times 10^4$ weakly bound molecules. Please note, there is no more than a single molecule per lattice site. Since they cannot be directly observed by our standard absorption imaging, we detect the atom signal after reversing the Feshbach ramping in order to obtain the number of dimers. Figure 3.8 shows the dissociation of molecules evident by the reappearance of the atomic signal after adiabatically crossing the Feshbach resonance at 1007.4 G again. For $B < 1007.4$ G only

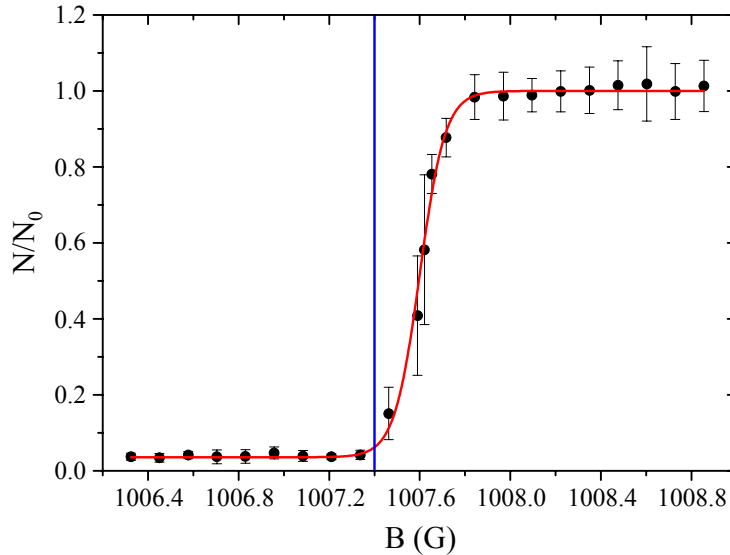Figure 3.8: Dissociation of Feshbach molecules. After the production and purification of the molecule ensemble, the magnetic field is adiabatically increased. The normalized number of atoms N/N_0 is measured as a function of the final value of B. Here, N_0 corresponds to the atom number in the high field asymptotic limit. The Feshbach resonance at 1007.4 G is indicated by the blue vertical line.

small atom numbers are detected, demonstrating the high efficiency of our purification scheme. I want to point out that the actual atom numbers in this regime might even be lower than the values inferred from the absorption images, since, in general, a fit to a vanishing signal is problematic. Small fluctuations resulting from technical imperfections, i.e., artifacts of the imaging can contribute and lead to an overestimation of the atom number. Originally, figure 3.8 was measured as a function of the current through the quadrupole coils. Since, the position of the Feshbach resonance is well known, the magnetic field can be calibrated. We found, that $B = 1007.4$ G corresponds to a current of 79.59 A.

3.8.3 Purification scheme

After the creation of weakly bound dimers, remaining single atoms have to be removed in order to realize the preparation of a pure molecular sample. For this purpose, we apply a purification scheme that relies on a combined microwave and light pulse addressing only atoms [53] (see also [27]). Subsequent to the adiabatic crossing of the Feshbach resonance the magnetic field is set to $B = 1000$ G. Then, the atom-molecule sample is irradiated by a microwave at 9.111 GHz and resonant light driving the transitions illustrated in figure 3.9. Thereby, single atoms are removed from the 3D optical lattice with almost 100% efficiency. Both pulses have a rectangular shape, start at the same time and have durations of 2 ms (microwave) and 3 ms (light), respectively. We use a rectangular waveguide open to one side as antenna. The
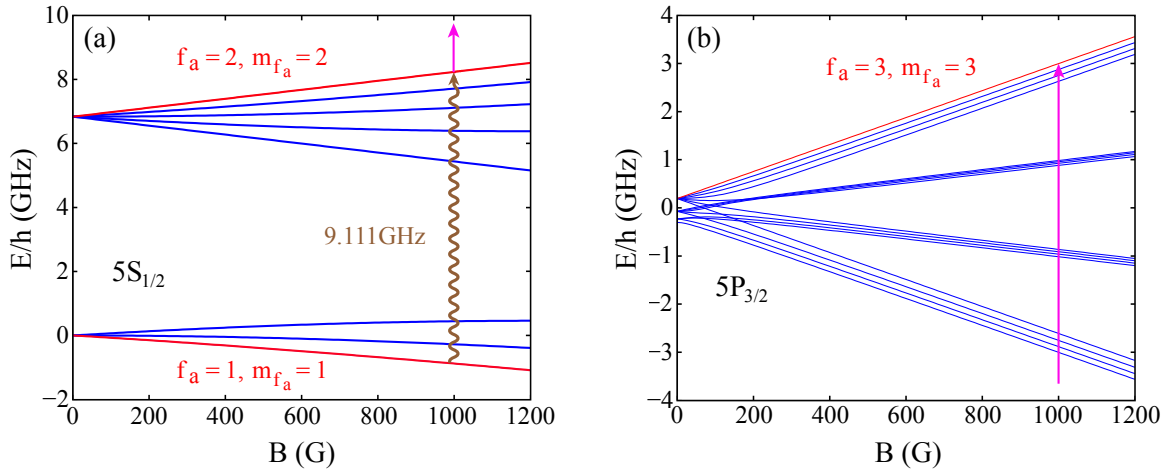
Figure 3.9: Hyperfine and Zeeman structure of atomic ^{87}Rb levels relevant for the purification scheme. (a) By applying a microwave at 9.111 GHz we resonantly drive the transition from $|f_a = 1, m_{f_a} = +1\rangle$ to $|f_a = 2, m_{f_a} = +2\rangle$ within the $5S_{1/2}$ manifold. (b) The light pulse excites the atoms to the $|f_a = 3, m_{f_a} = +3\rangle$ level of the $5P_{3/2}$ state removing the atoms from the lattice owing to the recoil momentum transfer from the scattered photons [27].

microwave is generated by a synthesizer[29] and amplified[30] to a power of 1 W. For the optical transition, the light of the purification laser is used. At $B = 1000$ G the resonance frequency of the $|f_a = 2, m_{f_a} = +2\rangle \leftrightarrow |f_a = 3, m_{f_a} = +3\rangle$ transition is 1402 MHz blue detuned compared to the one at zero magnetic field. We account for this frequency difference in the beat locking scheme described in section 2.3.1.

3.8.4 Lifetimes of Feshbach molecules in the optical lattice

In general, the ability to prepare long-lived molecular samples is advantageous for experimental purposes. It is convenient, if intrinsic losses of particles are negligible on the timescales of the measurements (typically several milliseconds). With respect to a 3D optical lattice, there are mainly two effects which can lead to a decreased number of observed molecules: photon scattering and inelastic collisions. First of all, the lattice light itself can induce transitions to higher excited molecular levels. This can lead to direct losses from the trap due to heating or dissociation processes, where the atoms gain kinetic energy. However, most likely, the excited molecules decay to nonobservable states, i.e., they are possibly still trapped but escape from detection. Since the photon scattering rate is proportional to the square of the electric field amplitude [see equations (4.1) and (4.7)], low laser powers would be advantageous for the lifetime of the molecules. Unfortunately, for low lattice depths, collisional losses come more and more into play owing to increased tunneling of molecules to adjacent lattice sites. A theoretical description of inelastic collisions is an involved topic and requires the precise knowledge of the molecule distribution and the trap geometry. For the special case of a 1D Tonks-Girardeau gas, experiments with ^{87}Rb$_2$ Feshbach molecules were performed, where an inhibition of particle loss in the strong dissipation regime was observed, which represents a manifestation of the quantum Zeno effect [61]. However, we have studied the collisional dynamics in various trap geometries that are not directly comparable to those of Ref. [61]. As mentioned in the introduction (section 1.4) our results concerning this field of research will be presented in the forthcoming doctoral thesis of Björn Drews. Therefore, I restrict the discussion here to a rather phenomenological description of some basic features of the experimental data.

In our setup, the Feshbach association takes place at equal lattice depths of typically $12.5E_R$ in each of the three directions, i.e., the atoms of different potential wells are well isolated from each other. Since the Feshbach dimers have twice the mass and their polarizability is known to be two times the one of a single atom [120], the corresponding lattice depths for the molecules are $50E_R$. For this case, tunneling to adjacent lattice sites is highly suppressed and the main loss mechanism is given by laser induced photon scattering. Then, as can be seen in figure 3.10, the lifetime of a pure molecular sample can be modeled by an exponential law. From the fit, we obtain a $1/e$ decay time of 1.08 s. Please note that due to technical reasons we are limited to a holding time τ_h of about 900 ms in our measurements. When looking at the experimental data for a lattice depth of $10E_R$, we see fast losses of molecules within $\tau_h \lesssim 200$ ms, which we mainly attribute to inelastic collisions owing to tunneling. On

---

[29]N5183A from Agilent Technologies, Inc., Santa Clara, USA.
[30]QPJ-09103030 from QuinStar Technology, Inc., Torrance, USA.
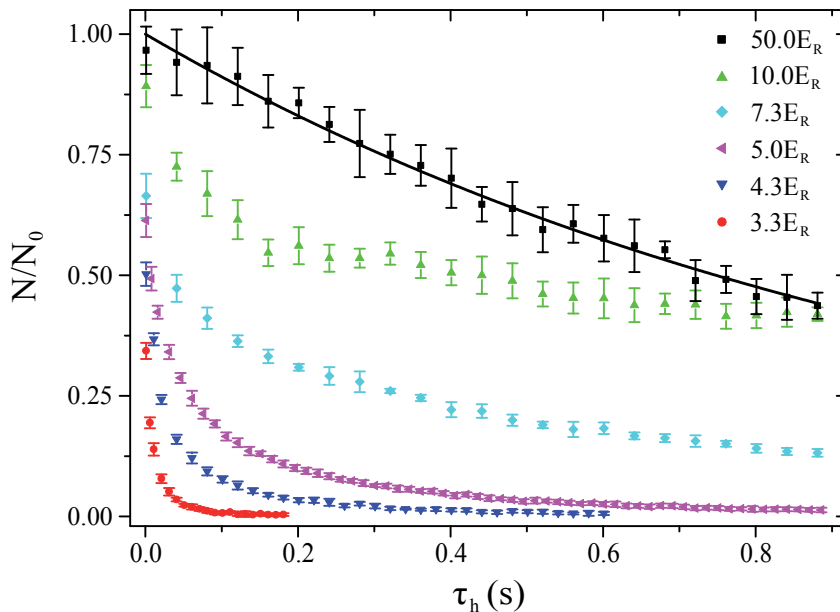
Figure 3.10: Lifetimes of weakly bound Feshbach molecules in a 3D optical lattice. Within 1ms, the initial lattice depth of $50E_R$ is lowered simultaneously in each direction to the value given in the legend. We measured the number N of remaining molecules as a function of the holding time τ_h in the lattice, where $\tau_\mathrm{h} = 0$ represents the moment, when the final depth is reached. The starting point of our measurements is $\tau_\mathrm{h} = 1$ ms. Here, $N_0 = 15940$ represents the number of molecules at $\tau_\mathrm{h} = 0$ obtained by an exponential fit (solid line) for the case, when the lattice is not lowered at all. The corresponding $1/e$ decay time is 1.08 s. Typically, each data point is the average of about 7 repetitions of the experiment except for the scan at $5.0E_R$, where each data point represents the average of 21 repetitions.

longer timescales the decay is much slower. This is reasonable, as the density of molecules is decreased and the collision partners have to tunnel over many lattice sites to find each other. Consequently, for $\tau_\mathrm{h} \gtrsim 200$ ms, similarly to the case of $50E_R$, the losses are mainly determined by laser induced photon scattering. However, the decay curve is not so steep since the laser intensity is by a factor of five less. For even lower lattice depths, inelastic collisions are further increased. In addition, molecules can simply drop out of the lattice, which sets another loss mechanism. Consequently, a complete loss of dimers (within our maximum holding time) is observed for lattice depths $< 5.0E_R$.

Next, we want to study the situation, when one lattice beam is completely switched off giving rise to an array of parallel tubes in the trapping potential. The experimental data for a high background lattice ($50E_R$) corresponding to the remaining two directions is shown in figure 3.11(a). We observe a fast decay within about 5 ms, that we attribute to inelastic collisions within the tubes. Remarkably, a significant fraction of molecules exhibits a much longer
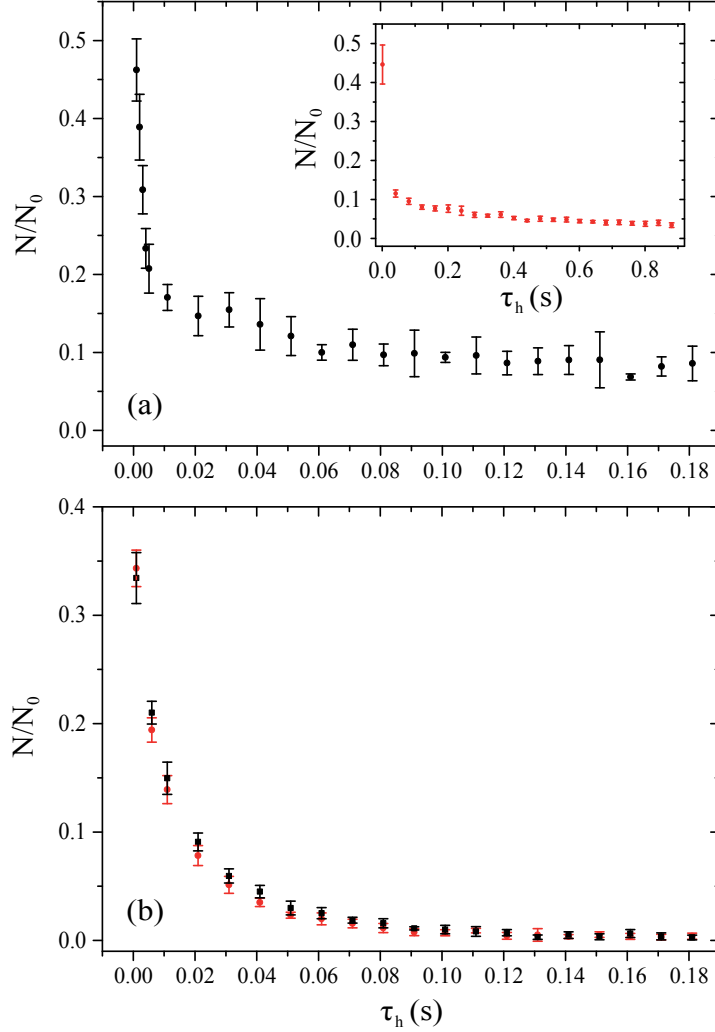
Figure 3.11: Lifetimes of weakly bound Feshbach molecules in a 2D optical lattice. The experimental scheme is identical as for figure 3.10, except that one lattice beam is completely switched off. We used the same normalization factor $N_0 = 15940$, here. (a) Both scans are obtained for final lattice depths of $36.7 E_R$ in the remaining two directions and show the behavior for different timescales. In (b), square plot symbols represent our measurements for a shallow background lattice of $3.3 E_R$. This scan shows no significant difference to the case, when all three lattice directions are set to $3.3 E_R$ (circles). Typically, each data point represents the average of seven repetitions of the experiment.

lifetime, which can be understood as follows. When assuming two body reactions, inelastic collisions can lead to a complete loss, if the tube is occupied by an even number of molecules.

For the case of an odd number, always one molecule remains per tube. The decay of this "offset signal" is then mainly determined by laser induced transitions, i.e., photon scattering. However, for very low lattice depths, where tunneling between adjacent tubes is strongly increased, we do not find any difference compared to the corresponding 3D configuration as can be seen in figure 3.11(b).

3.8.5 Potential curves of Rb_2 molecules and description of the Feshbach state

In order to manipulate and control ultracold molecules, detailed knowledge about their electronic energy structure is pivotal. Figure 3.12 shows potential curves of the $^{87}Rb_2$ dimer. For the experiments described in this thesis, the triplet ground state $a^3\Sigma_u$ is most relevant, since the deeply bound molecules are prepared in this state. Furthermore, we have investigated the $(1)^3\Sigma_g$ manifold and the spin-orbit coupled $(1)^1\Sigma_u - (1)^3\Pi_u$ complex spectroscopically[31].

After the Feshbach association of atoms to weakly bound dimers, the magnetic field is set to $B = 1000$ G, which represents the starting point of most of our experiments. Due to the Zeeman shift and the molecule binding energy (~ 20 MHz $\times h$) the Feshbach state is located 1.748 GHz $\times h$ below the $|f_a = 1, m_{f,a} = +1\rangle + |f_b = 1, m_{f,b} = +1\rangle$ atomic asymptote $(5S_{1/2} + 5S_{1/2})$ at 0 G, with f_a and f_b being the quantum numbers of the total angular momenta of the single atoms. The situation is shown in figure 3.13. I want to point out that the energy corresponding to the given atomic asymptote is 8.543 GHz $\times h$ (calculated, using Eq. (16) of Ref. [87]) less compared to the dissociation limit when hyperfine interaction is ignored.

At the given magnetic field of $B = 1000$ G the Feshbach state has both, singlet as well as triplet character, i.e., it is a mixture of $X^1\Sigma_g$ (16%) and $a^3\Sigma_u$ (84%) (E. Tiemann, private communication). This comes about owing to spin-orbit interaction and is quite convenient as regarding selection rules, transitions to many different molecular quantum states can be realized. Please note, for $B = 1000$ G Hund's coupling case (e) is most appropriate.

Now, we want to first consider the dominant triplet admixture. All vibrational levels $v = 36$ to 40 of $a^3\Sigma_u$ are involved, while the main contributions correspond to $v = 36$ and 40 (cf. Fig. 3.13). These states correlate to

$$|v = 36, (f_a = 2, f_b = 2), f = 2, S = 1, R = 0, F = 2, m_F = 2\rangle$$

and

$$|v = 40, (f_a = 1, f_b = 1), f = 2, S = 1, R = 0, F = 2, m_F = 2\rangle$$

at low magnetic fields (see also Refs. [122, 124]). Here, f denotes the sum of both atomic angular momenta, S is the total electronic spin and R is the mechanical rotation of the atomic pair. Furthermore, F is the total angular momentum and m_F represents its projection onto the quantization axis given by the direction of the magnetic field $\vec{B}$. For $v = 40$, the total nuclear spin I is a mixture of $I = 1$ and 3 with the latter component being dominant. In contrast to that, the vibrational level $v = 36$ has $I = 1$.

The singlet fraction of the Feshbach state is composed by the vibrational levels $v' = 119$

---

[31]Note, in a different notation, $(1)^3\Sigma_g$, $(1)^1\Sigma_u$, and $(1)^3\Pi_u$ correspond to $c^3\Sigma_g$, $A^1\Sigma_u$, and $b^3\Pi_u$, respectively.
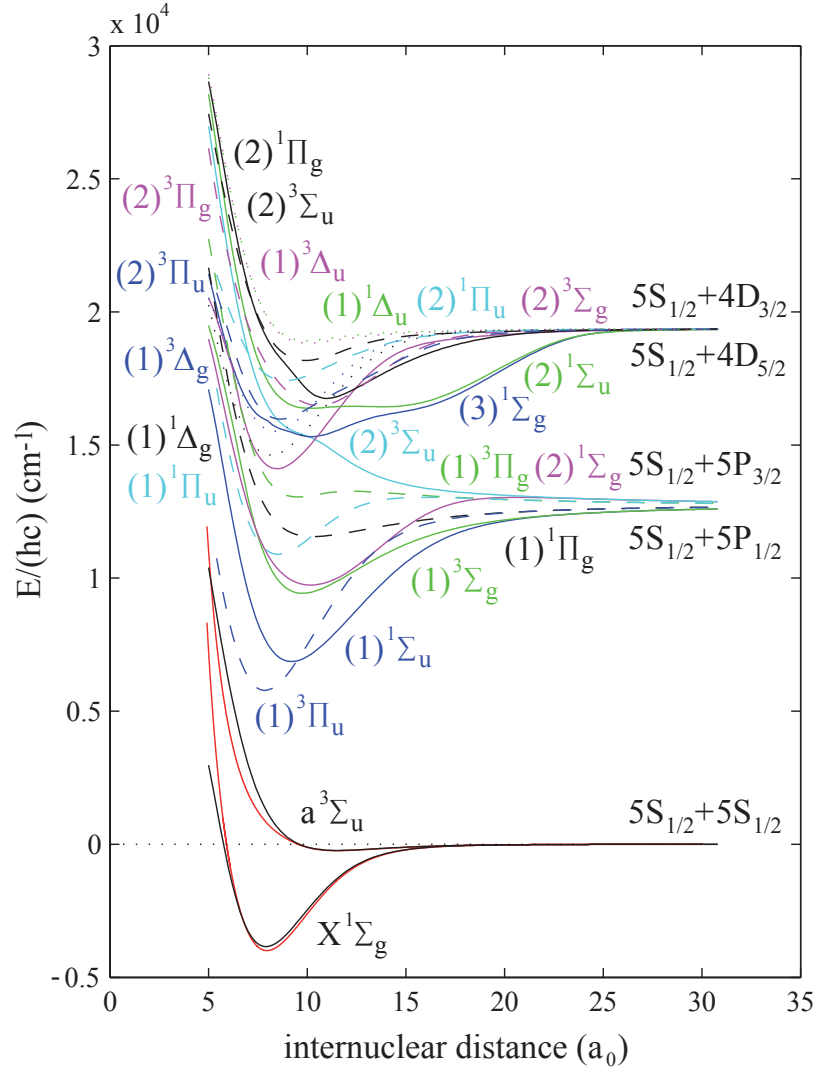
Figure 3.12: Potential energy curves of the $^{87}\text{Rb}_2$ molecule taken from Ref. [121]. The red curves represent the optimized singlet (triplet) ground state potentials of Refs.[122, 123]. Solid lines correspond to Σ potentials and dashed (dotted) lines to Π (Δ) potentials, respectively.

to 124 of $X^1\Sigma_g$. Among them, the main contributions are related to $v' = 120$ and 124. They can be characterized by the quantum numbers $S' = R' = 0$ and $f' = I' = F' = m'_F = 2$.

Unfortunately, the energy level structure of weakly bound Feshbach molecules is very complicated and exhibits many avoided crossings. Thus, it is experimentally very difficult to work at 0 G, which would be nice for some purposes owing to the absence of the Zeeman shift. A feasible solution for this problem is to bridge avoided crossings by adiabatic population
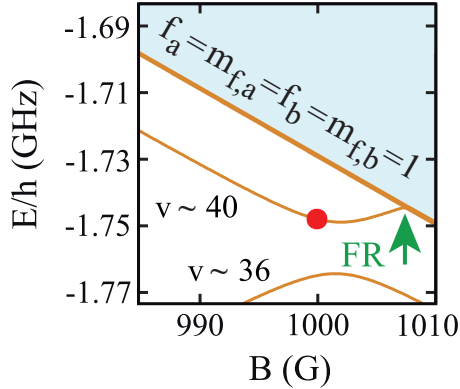
Figure 3.13: Avoided crossing for weakly bound $^{87}\text{Rb}_2$ molecules. The plot shows the level structure as a function of the magnetic field B in the vicinity of the Feshbach resonance at 1007.4 G, which is indicated by the green arrow. After the molecule formation, the magnetic field is set to 1000 G, where the molecular state (red circle) is a mixture of different singlet as well as triplet vibrational levels. The triplet character is dominant with the main contributions corresponding to $v = 36$ and $v = 40$ of $a^3\Sigma_u$. Here, the energy reference is given by the $|f_a = 1, m_{f,a} = +1\rangle + |f_b = 1, m_{f,b} = +1\rangle$ atomic asymptote at $B = 0$ G.

transfer as demonstrated in Ref.[125]. However, this technique will not be described here, since all the measurements concerning weakly bound molecules reported in the present thesis were performed at 1000 G. For the case of the relevant lowest rotational states within the $v = 0$ manifold of $a^3\Sigma_u$, the magnetic field can be tuned over significantly larger ranges without encountering any avoided crossings owing to the less complicated energy level structure.

3.8.6 Repulsively bound atom pairs

In future, working with repulsively bound atom pairs might become interesting. Therefore, I want to briefly present the experimental realization of such an exotic state in our setup using the periodic potential of the optical lattice. Even for repulsive interactions, two atoms form a bound state, if there is no possibility to release the energy in a dissociation process. As the energy band-structure of an optical lattice shows forbidden areas, where no dissipation channels are provided, such systems are ideal testbeds to investigate this effect.

We have created repulsively bound atom pairs following the method described in Ref.[126]. Regarding a quasi-1D geometry (the lattice depth in one direction is significantly lower than in the other two directions) a clear signature of this phenomenon is a bare-like structure of the quasimomentum distribution obtained in a time of flight measurement after releasing the atoms from the lattice. Consequently, for the 2D configuration one observes a maximum in each of the corners of the first Brillouin zone (cf. Fig. 3.14). Further information about repulsively bound atom pairs can be found in [82, 126].
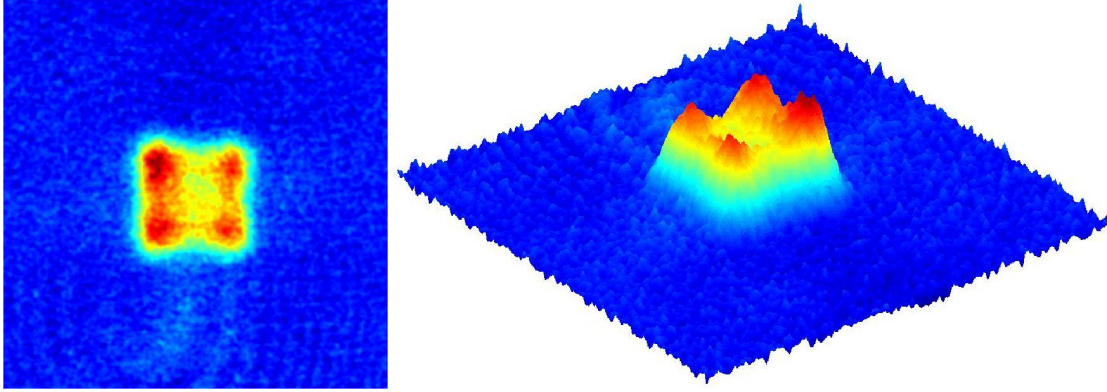
Figure 3.14: Time of flight absorption image of the atomic distribution after release from an optical lattice. The anisotropic distribution within the first Brillouin zone indicates the successful preparation of repulsively bound atom pairs in a 2D configuration.

3.9 STIRAP transfer to the vibrational ground state of the lowest triplet potential

So far, I have described the preparation of very weakly bound molecules. Of course, in the context of ultracold physics and chemistry molecules with high binding energies are also very interesting. The STIRAP technique, first demonstrated in the group of Klaas Bergmann [37], is an efficient method to coherently transfer population from one state to another. Two laser fields are used to keep the molecules in a dark superposition state during the transfer, which strongly suppresses losses due to spontaneous light scattering. Starting with Feshbach dimers, the STIRAP technique has been applied in our setup to prepare lower lying vibrational levels [127] or even the rovibrational ground state [44] of the $a^3\Sigma_u^+$ potential with respect to Rb$_2$. In this thesis, I report on the preparation and investigation of several well-defined molecular quantum states within the $v = 0$ manifold, including different rotational levels ($R = 0$ and 2) and states with different nuclear spin ($I = 1$ and 3).

This section is devoted to a description of the creation of deeply bound molecular ensembles. For this purpose, I will first of all introduce the λ-type three-level system used for STIRAP in our setup. Afterwards, two-photon dark state spectroscopy is presented, since this technique allows for the determination of the relevant transition frequencies. Finally, the experimental pulse sequence is discussed and measured data concerning the successful preparation of various final states are shown. For a theoretical treatment of the STIRAP process, which will not be given in the present work, I refer, e.g., to [38].

3.9.1 STIRAP level scheme and dark state spectroscopy

The STIRAP technique makes use of a stimulated Raman transition involving two light fields, which have to be phase stable relative to each other. Figure 3.15(a) shows the potential energy
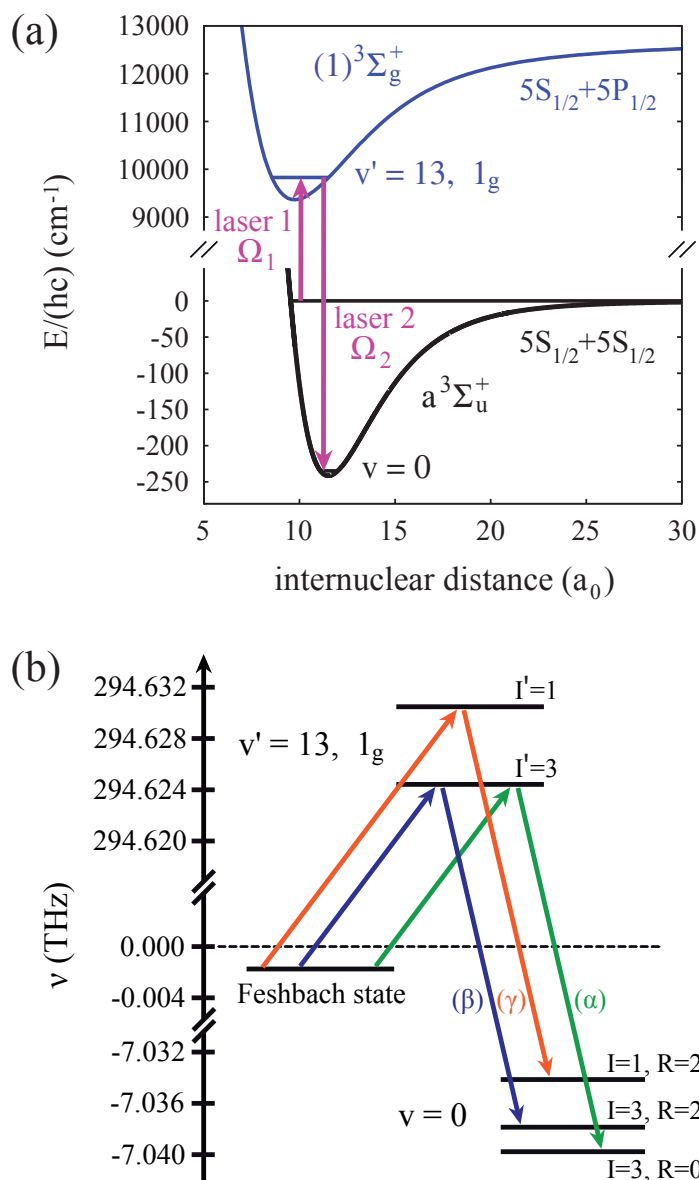
Figure 3.15: STIRAP scheme. (a) Potential energy curves and vibrational levels involved in the STIRAP transfer. The two lasers 1 and 2 induce couplings with Rabi frequencies Ω_1 and Ω_2, respectively. Here, the $(1)^3\Sigma_g^+$ $(a^3\Sigma_u^+)$ potential curve is taken from [121] ([122, 123]). Please note the different scaling of the energy. (b) Relevant levels for STIRAP transfers to different states of the vibrational ground state manifold $(v = 0)$ of $a^3\Sigma_u^+$. Pairs of arrows (α), (β), and (γ) represent the two laser frequencies used to address well-defined final states with quantum numbers $R = 0$ or $R = 2$ and $I = 1$ or $I = 3$. The energy reference is given by the atomic asymptote including the hyperfine splitting as described in section 3.8.5.

curves and vibrational levels relevant for the STIRAP scheme in our setup. Owing to the large binding energy difference of more than $7\,\text{THz} \times h$ between the Feshbach state and the $v = 0$ level manifold, we have to employ two different lasers 1 and 2, that are stabilized to the same cavity in order to guarantee phase stability for sufficiently long timescales (cf. section 2.3.4). Both lasers are resonant to the same intermediate level, sometimes referred to as virtual level, since it is ideally not populated at all during the process. The preparation of any final state of $v = 0$ described in the present work is performed using an intermediate level with 1_g character located in the $v' = 13$ manifold of the excited $(1)^3\Sigma_g^+$ potential.

In principle, a population transfer is possible, if the dipole selection rules allow for a coupling of the intermediate level to both, the initial and the final state. For example, in our setup, the two laser beams are oriented parallel to each other (cf. Fig. 2.6) and their polarizations are such that only π transitions can be induced. Hence, we solely are able to address final states with $m_F = 2$, where m_F is the projection of the total angular momentum F onto the quantization axis. Figure 3.15(b) depicts the three-level systems used for the preparation of different $a^3\Sigma_u^+$ states with $v = 0$. Note, only the quantum numbers for the vibration v, the rotation R and the nuclear spin I are given here, for simplicity. Furthermore, in order to achieve high efficiencies, the coupling strengths, i.e., the Rabi frequencies Ω_1 and Ω_2 have to be sufficiently large. Therefore high laser intensities I_L are beneficial, as $\Omega \propto \sqrt{I_\text{L}}$.

The STIRAP technique necessitates precise knowledge of the relevant transition frequencies. By performing one-photon spectroscopy of the excited $(1)^3\Sigma_g^+$ potential starting with Feshbach molecules, we have been able to pin down the positions of several possible intermediate states. As already mentioned in section 1.4, these results will be presented elsewhere. However, contrary to [124] we have identified levels with a nuclear spin of $I' = 1$, which allows us to access final states with $I = 1$ via STIRAP. The transition frequency from the intermediate level to the deeply bound state can be measured using two-photon dark state spectroscopy as described in Ref. [122], again starting with Feshbach molecules. For this purpose, laser 1 is kept on resonance to the intermediate state while laser 2 is scanned. This Raman-type spectroscopy method relies on the Autler-Townes splitting. In brief, the excitation of molecules by laser 1 constantly induces losses owing to leakage of dimers from the trap or decay to nonobservable molecular states. When laser 2 approaches the resonance, the intermediate level evolves into a dressed state which is not resonant to laser 1 anymore and losses are strongly suppressed. A more detailed description can be found in [128, 129].

As an example, figure 3.16 shows a dark resonance obtained for the rovibrational ground state of the $a^3\Sigma_u^+$ potential. In our sequence, we use rectangular laser pulses for the two-photon spectroscopy. Laser 1 is switched on $0.5\,\text{ms}$ after laser 2. The pulse duration is $2\,\text{ms}$ for laser 2 and $1\,\text{ms}$ with respect to laser 1. Concerning the employed dark state spectroscopy scheme, it is very crucial to adjust the light intensities appropriately. If the coupling strength of laser 1 is too large, losses are dominant and no resonance can be observed. This problem is related to the utilization of rectangular pulses. It could, to some extent, be overcome by ramping the lasers similar to the sequence that will be discussed in the context of the STIRAP transfer (see Fig. 3.17). However, using relatively long rectangular pulses turned out to be convenient for searching dark resonances as they are easy to implement and the resulting transition linewidths
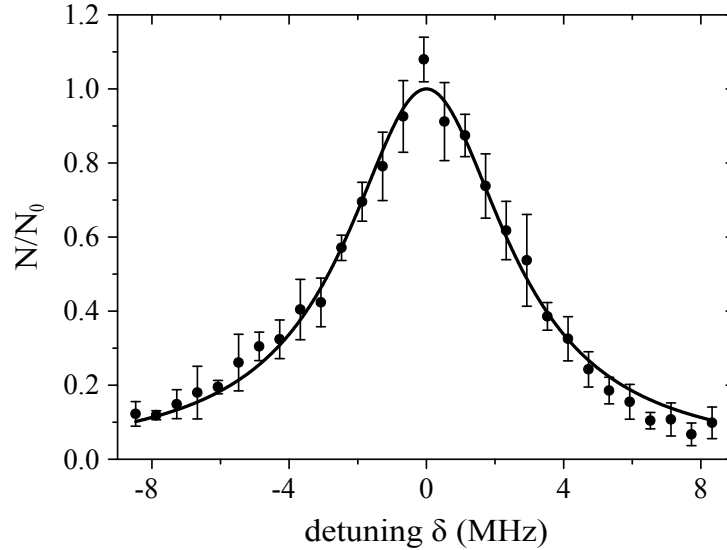
Figure 3.16: Dark resonance. The data points are obtained by two-photon spectroscopy of the rovibrational ground state of the $a^3\Sigma_u^+$ potential. We measured the fraction N/N_0 of molecules as a function of the detuning δ of laser 2. Here, N_0 represents the number of dimers at $\delta = 0$ obtained from a Lorentzian fit (solid curve).

are sufficiently large.

3.9.2 Experimental realization of the STIRAP transfer

The STIRAP transfer of Feshbach molecules to the vibrational ground state of the lowest triplet potential is based on a counterintuitive pulse sequence as shown in figure 3.17. After performing experiments with the deeply bound dimers, we have to reverse the STIRAP and subsequently dissociate the molecules, since only atoms can be detected in our setup. The corresponding pulse sequence is given by the mirror image of the ground state transfer. I want to note that during the time, when only laser 1 is turned on, remaining Feshbach molecules are excited and escape detection owing to loss from the trap or decay to nonobservable states. In this sense, the sample is purified as a consequence of the STIRAP pulse sequence.

Figure 3.18 shows measurements demonstrating the successful preparation of different well-defined molecular levels within the $v = 0$ manifold of the $a^3\Sigma_u^+$ potential. For the case of the rovibrational ground state $(R = 0, I = 3)$, the far-off-resonance signal approaches zero, indicating that all molecules corresponding to the detected atoms must have been in the deeply bound state. In contrast, with respect to $(R = 2, I = 1)$ we observe a significant fraction of molecules remaining in the Feshbach state. As depicted in Fig. 3.15(b), we use a different intermediate level for the transfer to $(R = 2, I = 1)$. Unfortunately, the coupling of the Feshbach state to this level is very low. Hence, the intensity of laser 1 is not sufficient to completely remove all remaining weakly bound molecules within the given irradiation time,
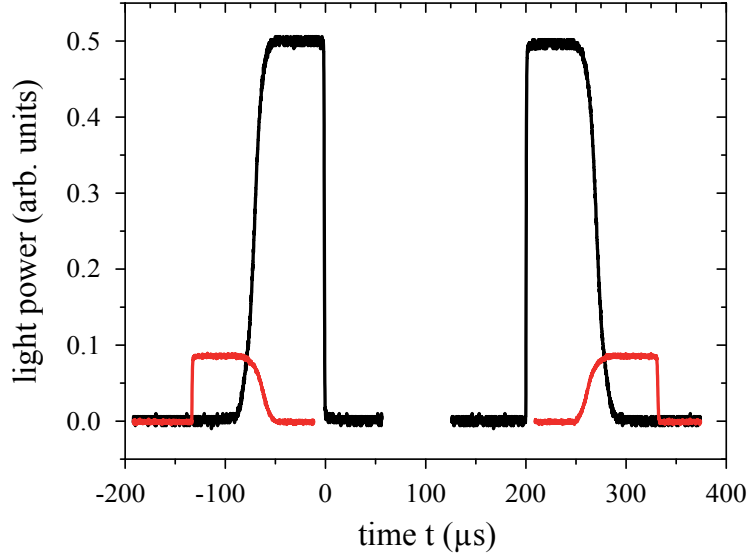
Figure 3.17: Round trip STIRAP pulse sequence. The graph shows the power of the two involved laser beams measured by a photo diode. First of all, the Feshbach molecules are illuminated by laser 2. Then laser 2 is ramped down while laser 1 is ramped up, and the molecules are transferred to a well-defined level of the vibrational ground state of the $a^3\Sigma_u^+$ potential. The second pulse sequence is applied in order to reverse the first STIRAP process (see text). Experiments with deeply bound dimers are performed in the time gap between the two molecular state transfers. This time gap can be varied, but the maximum duration is limited to $\sim 1\,\mathrm{s}$ for technical reasons. I want to note that the intensity of laser 1 is about five times larger than the one of laser 2, which yields appropriate Rabi frequencies, e.g., for addressing the rovibrational ground state.

which causes the offset visible in Fig. 3.18(b). Please note, this problem can simply be overcome by increasing the pulse lengths of laser 1. I want to point out that for the transfer to state $(R = 2,\ I = 3)$ the same intermediate level is employed as for $(R = 0,\ I = 3)$. Consequently, when applying the pulse sequence of Fig. 3.17, we also obtain a pure ensemble of $(R = 2,\ I = 3)$ molecules.

In our setup, the linewidths of the STIRAP resonances are typically on the order of several hundreds of kHz. The data can be simulated using a three-level model based on a master equation approach (see, e.g., Refs. [128, 129]). However, we are mainly interested in the resonance frequency, which is related to the maximum number of deeply bound molecules. Thus, for convenience, we usually fit a Lorentzian to the experimental data since the resulting accuracy is satisfactory[32]. The maximum in figure 3.18(a) corresponds to 1.5×10^4 dimers in the

---

[32]In analogy, the master equation approach would be more appropriate also for the two-photon dark state spectroscopy.
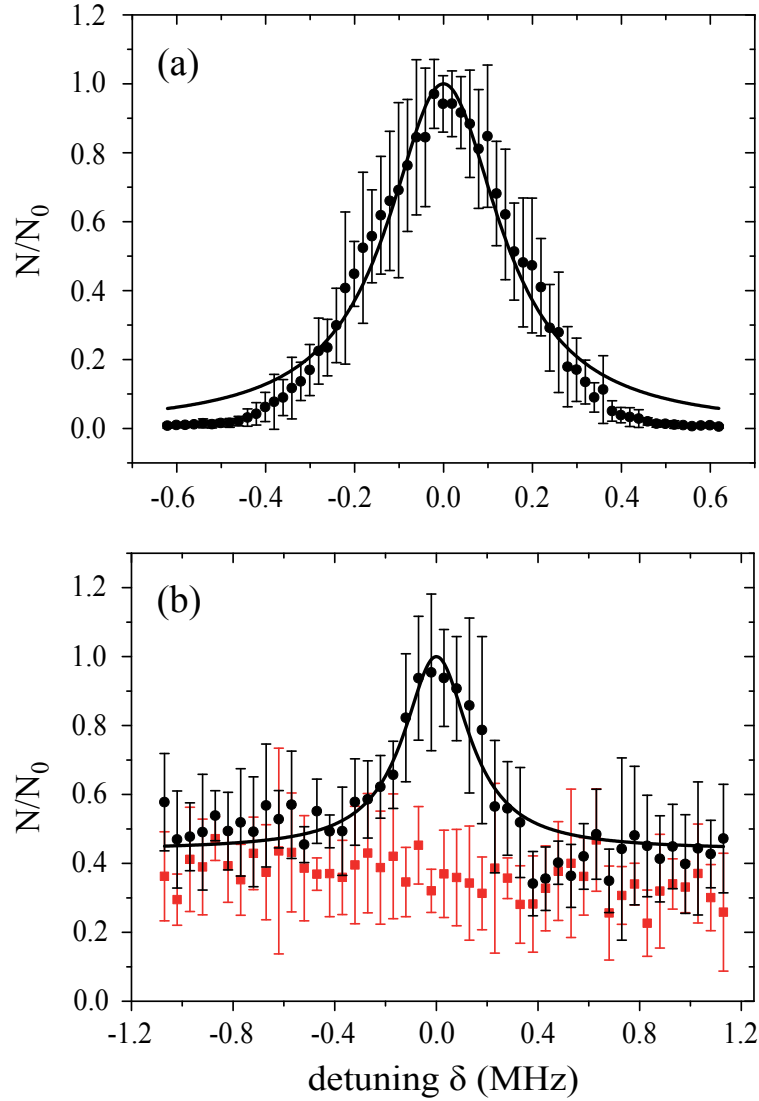
Figure 3.18: STIRAP resonances at a magnetic field of $B = 1000$ G. We performed the population transfers to the levels $R = 0$, $I = 3$ (a) and $R = 2$, $I = 1$ (b) of the $a^3\Sigma_u^+$ vibrational ground state $v = 0$ and back to the Feshbach state according to the sequence depicted in Fig. 3.17. Afterwards, the relative number N/N_0 of dimers was measured as a function of the detuning δ of laser 2, while laser 1 was kept on resonance. Here, N_0 represents the maximum number of molecules obtained from Lorentzian fits (black solid lines). The red square plot symbols in (b) show the observed results, when the second pulse of laser 2 is not applied. This signal and therefore also the offset of the black solid line correspond to remaining Feshbach molecules, which are not transferred at all. Contrary to that, the resonance visible in (a) is characteristic for a pure ensemble of deeply bound dimers.

rovibrational ground state of the $a^3\Sigma_u^+$ potential. This represents about 60% of the number of molecules initially prepared in the Feshbach state. Owing to that, the single STIRAP efficiency is almost 80%, when assuming equal efficiencies for both transfers.

Table 3.1 lists the measured transition frequencies concerning STIRAP transfers to various precisely defined final levels of the $a^3\Sigma_u^+$ vibrational ground state manifold. As we are able to fully resolve the rotational, hyperfine, and Zeeman substructure in the vicinity of the relevant levels, any desired final state can unambiguously be populated. Finally, I want to emphasize that the STIRAP transfer entails spin polarization of the molecules, which gives rise to characteristic alignment of the molecular axis. This will be described in great detail in chapter 5.

final molecular state $(a^3\Sigma_u^+,\, v = 0)$	ν_{L1} [THz]	ν_{L2} [THz]	$\Delta\nu$ [THz]
$R = 0,\, I = 3$	294.62443	301.66248	7.03805
$R = 2,\, I = 3$	294.62443	301.66054	7.03611
$R = 2,\, I = 1$	294.63048	301.66287	7.03239

Table 3.1: STIRAP transition frequencies ν_{L1} and ν_{L2} of the two lasers used for the transfers to different final molecular states within the $v = 0$ manifold of the lowest triplet potential at a magnetic field of $B = 1000$ G. In addition, the frequency difference $\Delta\nu = \nu_{\mathrm{L2}} - \nu_{\mathrm{L1}}$ is provided. Note, $\Delta E = h\Delta\nu$ represents the gain in binding energy with respect to the weakly bound Feshbach molecules. The energy reference is given by the atomic asymptote including the hyperfine splitting as described in section 3.8.5.

3.10 Magnetic field ramping

Here, I will first briefly describe the magnetic field ramping sequence which is applied in our setup in order to create and investigate ultracold molecules. Contrary to Feshbach dimers, for many levels of the $v = 0$ manifold, the magnetic field can be tuned over a large range without encountering avoided crossings. However, we have found that still population transfer between molecular states can occur when B is changed. The underlying mechanism is related to the optical lattice and will be discussed in the second part of this section.

3.10.1 Ramping sequence

For our studies of molecules in well-defined levels of the vibrational ground state of the lowest triplet potential, we generally use the magnetic field ramping sequence shown in figure 3.19. After the STIRAP transfer, the strength of B and the optical lattice depths can be adjusted as intended for the measurements. The experiments with the vibrational ground state molecules, e.g., spectroscopy, the determination of dynamical polarizabilities or investigations of molecular collisions are carried out during the holding time τ_{h}.
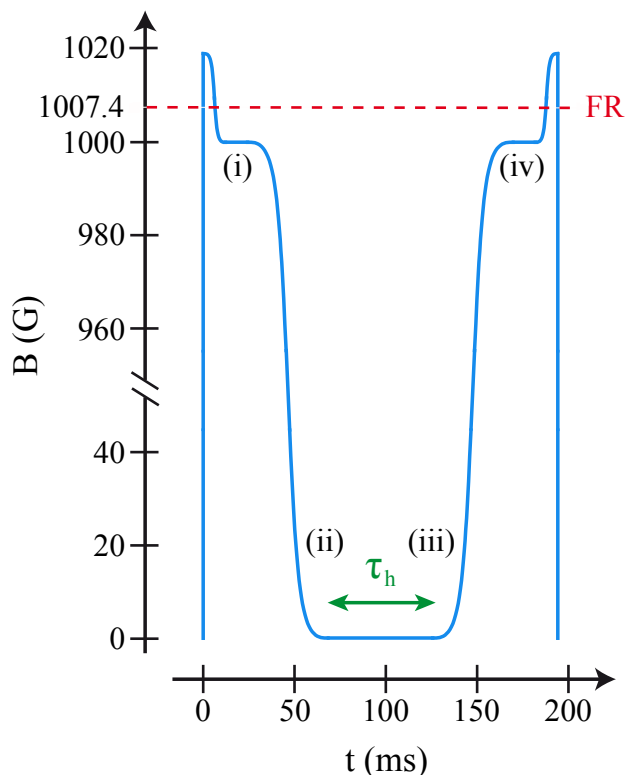
Figure 3.19: Magnetic field ramping sequence. Shown is the magnetic field of the quadrupole coils as a function of the time. The Feshbach resonance (FR) at $B = 1007.4$ G is illustrated by the red dashed line. After producing a pure sample of weakly bound molecules the STIRAP transfer (i) takes place at $B = 999.9$ G. Then, the strength of the magnetic field can be changed, e.g., to $B = 0$ G. Subsequent to that, the lattice depths in each direction are set to the desired values by independently ramping the powers of the lattice beams (ii). During the holding time τ_h, which can be varied, experiments with the vibrational ground state molecules can be performed. Since we are not able to detect the molecules directly, the whole sequence has to be reversed. Therefore the lattice is ramped up again (iii), the magnetic field is set to $B = 999.9$ G and the deeply bound dimers are transferred to the Feshbach state via STIRAP (iv). After dissociating the molecules, the magnetic field is switched off and the atoms are detected by means of absorption imaging.

3.10.2 State transfer induced by decreasing molecular level spacings

When ramping down the magnetic field, different molecular levels can approach the state initially prepared at $B = 1000$ G. For example, figure 3.20(a) shows the energies of the hyperfine levels $m_F = 2$ and $m_F = 1$ corresponding to the rovibrational ground state of the
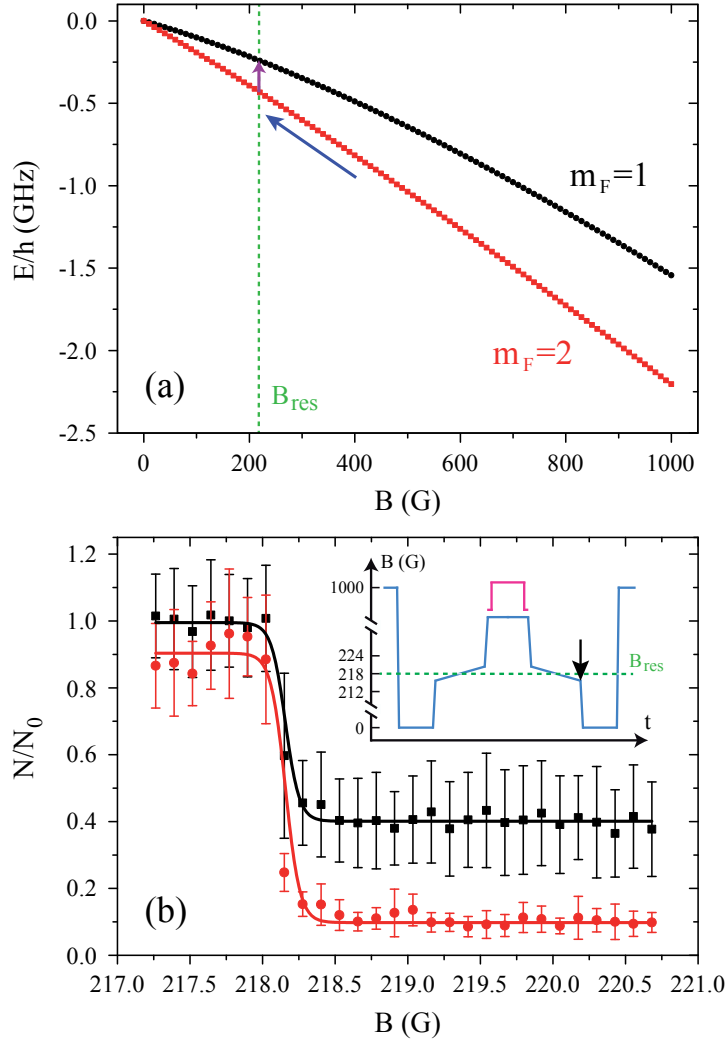
Figure 3.20: Transfer of rovibrational ground state molecules initially prepared in state $m_F = 2$ to the hyperfine level $m_F = 1$. The green dashed lines represent the resonant field B_{res}, where the transition occurs. (a) Energies of the two molecular hyperfine levels as a function of B resulting from coupled channel calculations provided by E. Tiemann. Here, zero energy corresponds to $-7.03583\,\text{THz} \times h$ with respect to the Feshbach state at 1000 G. Blue and purple arrows sketch the state transfer, when B is decreased. (b) Preparation of molecules in state $m_F = 1$ by ramping the magnetic field after the STIRAP process as shown in the inset (see also text). We measured the number N of molecules as a function of B, which was varied at the position indicated by the black arrow. Shown are data obtained either with (red circles) or without (black squares) applying an optical purification scheme (cf. pink rectangular pulse in the inset). The value N_0 corresponds to the low field asymptotic behavior of the black square plot symbols.

$a^3\Sigma_u^+$ potential (i.e., $v = 0$, $S = 0$, $R = 0$, $F = 2$, $I = 3$) as a function of B. By lowering the magnetic field, the energy difference between the two levels decreases. If it matches the relative detuning of two lattice beams a transfer from the initial state $m_F = 2$ to $m_F = 1$ can occur, provided that the polarizations of these lattice beams allow to drive such a transition. Please note, the three standing light waves of the rectangular optical lattice are offset by about 100 MHz relative to each other in order to avoid interference effects. In general, the more complex the molecular level structure is, the more parasitic transitions are possible, leading to a loss in the detected number of dimers at the end of the experiment cycle. I want to recall that, as a consequence of the selectivity of the STIRAP transfer, molecules in a different state than the initially prepared one cannot be observed. Therefore, it is reasonable to choose fast ramping speeds to shorten the coupling times to other molecular levels. Indeed, for the case of the rovibrational ground state, using an appropriate sequence, we are able to decrease the magnetic field down to $B = 0$ G without obtaining any losses.

On the other hand, the magnetic field ramp can be adjusted such, that a transition is driven deterministically. Thus, it is possible to prepare molecular states that are not accessible in our STIRAP scheme owing to selection rules. To make this more clear, we again consider the situation for the rovibrational ground state [cf. figure 3.20(a)]. If the magnetic field is ramped slowly across the resonant value B_{res}, where the two levels $m_F = 2$ and $m_F = 1$ are coupled, the main fraction of molecules can be transferred to the $m_F = 1$ state, when starting with $m_F = 2$. This can be seen from the data points shown in figure 3.20(b), which are obtained by carrying out the magnetic field sequence illustrated in the inset. First of all, B is switched off as fast as possible, which does not affect the molecular state. Subsequently, the magnetic field is set to a value slightly below B_{res}. Then, B is ramped up slowly over the resonance and the molecular quantum state changes to $m_F = 1$ owing to the two-photon process induced by the lattice beams. Afterwards, the magnetic field is increased further to a value, where the levels $m_F = 1$ and $m_F = 2$ are well separated from each other, in order to apply a purification pulse. For this purpose, we use light that resonantly drives the transition from $m_F = 2$ to an excited state in the $(1)^3\Sigma_g^+$ potential, leading to a decay of these molecules to nonobservable states. If B_{res} is slowly crossed for the second time, a revival of molecules in state $m_F = 2$ occurs. This demonstrates, that indeed, the dimers have been in a different molecular state. Consequently, figure 3.20(b) shows the successful preparation of an almost pure ensemble of molecules with $m_F = 1$ in the rovibrational ground state of the $a^3\Sigma_u^+$ potential.

3.11 Stern-Gerlach separation of atomic spins and absorption imaging

In order to detect atoms, we perform standard time of flight absorption imaging as described in Ref. [101]. After free expansion, the atom cloud is illuminated by light of the imaging laser. The light is resonant or slightly detuned (several MHz) with respect to the $f_a = 2 \rightarrow f_a' = 3$ transition (cf. section 2.3.1). Owing to the absorption of photons the atom cloud casts a shadow, which is imaged by a CCD camera. From these images, parameters like the atom

number, density, temperature etc. can be determined. The technique is more efficient, if, in addition, the atoms are illuminated by light of the repump laser. It transfers the atoms back to the initial state and therefore the number of scattered photons during the imaging process is increased.

In most experiments, we apply a magnetic field gradient after the trap is switched off, in order to perform a Stern-Gerlach separation of the present m_{f_a} states. For this purpose, the levitation coil is used. The corresponding inhomogeneous magnetic field leads to a splitting of the atom cloud along the direction of gravitation as the magnetic moment depends on m_{f_a}. For example, figure 3.21 is taken after irradiating the atoms by a microwave pulse driving the transition $|f_a = 1, m_{f_a} = +1\rangle \leftrightarrow |f_a = 2, m_{f_a} = +2\rangle$ in the purification scheme. The small atomic fractions in $|f_a = 1, m_{f_a} = 0\rangle$ and $|f_a = 1, m_{f_a} = -1\rangle$ indicate the high preparation efficiency concerning the initial state $|f_a = 1, m_{f_a} = +1\rangle$. However, for this image, it was intentionally not perfect in order to show all relevant spin states. Generally, the Stern-Gerlach separation is an important tool to check several steps of the overall sequence. Therefore, it is also performed when working with pure ensembles of molecules for monitoring reasons. Once, at this stage, atoms are detected in states different from $|f_a = 1, m_{f_a} = +1\rangle$, the experimental parameters have to be adjusted accordingly.
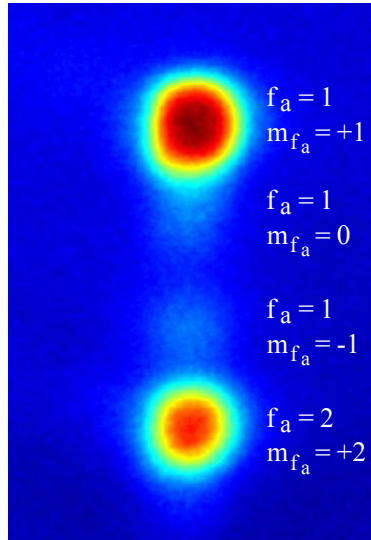
Figure 3.21: Stern-Gerlach separation of different spin states. Shown is a time of flight absorption image taken after applying the microwave pulse of the purification scheme. The individual atom clouds are assigned to the corresponding quantum numbers (f_a, m_{f_a}).

4 Polarizability of Ultracold $\mathrm{Rb_2}$ Molecules in the Rovibrational Ground State of $\mathrm{a^3\Sigma_u^+}$

Markus Deiß, Björn Drews, and Johannes Hecker Denschlag

Institut für Quantenmaterie and Center for Integrated Quantum Science and Technology IQST, Universität Ulm, 89069 Ulm, Germany

Nadia Bouloufa-Maafa, Romain Vexiau, and Olivier Dulieu

Laboratoire Aimé Cotton, Université Paris-Sud, ENS Cachan, Bât. 505, Campus d'Orsay, 91405 Orsay Cedex, France

We study, both theoretically and experimentally, the dynamical polarizability $\alpha(\omega)$ of $\mathrm{Rb_2}$ molecules in the rovibrational ground state of $a^3\Sigma_u^+$. Taking all relevant excited molecular bound states into account, we compute the complex-valued polarizability $\alpha(\omega)$ for wave numbers up to 20000 cm^{-1}. Our calculations are compared to experimental results at 1064.5 nm ($\sim$ 9400 cm^{-1}) as well as at 830.4 nm ($\sim$ 12000 cm^{-1}). Here, we discuss the measurements at 1064.5 nm. The ultracold $\mathrm{Rb_2}$ molecules are trapped in the lowest Bloch band of a 3D optical lattice. Their polarizability is determined by lattice modulation spectroscopy which

measures the potential depth for a given light intensity. Moreover, we investigate the decay of molecules in the optical lattice, where lifetimes of more than 2 s are observed. In addition, the dynamical polarizability for the $X^1\Sigma_g^+$ state is calculated. We provide simple analytical expressions that reproduce the numerical results for $\alpha(\omega)$ for all vibrational levels of $a^3\Sigma_u^+$ as well as $X^1\Sigma_g^+$. Precise knowledge of the molecular polarizability is essential for designing experiments with ultracold molecules as lifetimes and lattice depths are key parameters. Specifically the wavelength at ~ 1064 nm is of interest, since here, ultrastable high power lasers are available.

4.1 Introduction

Owing to the extraordinary control over the internal and external degrees of freedom, ultracold molecules trapped in an optical lattice represent a system with many prospects for studies in ultracold physics and chemistry [64, 66], the realization of molecular condensates [68], precision measurements of fundamental constants [71-74] and quantum computation [77, 78] and simulation [75]. In the recent years, several groups have realized the preparation of optically trapped vibrational ground state ($v = 0$) molecules in either the lowest lying singlet or triplet potential [39-42, 44]. Experiments with these molecules, e.g. ultracold collisions, are typically carried out in optical lattices or optical dipole traps [59, 60, 130]. In these environments, precise knowledge of the dynamical polarizability of molecules is important for well controlled experiments.

The Rb$_2$ molecule is one of the few ultracold molecular species currently available, with which benchmark experiments for nonpolar molecules can be carried out. Here, we investigate the dynamical polarizability $\alpha(\omega)$ of a Rb$_2$ triplet molecule in the lowest rovibrational level of $a^3\Sigma_u^+$. A similar analysis for Cs$_2$ regarding the electronic ground state $X^1\Sigma_g^+$ was previously carried out by Vexiau *et al.* [120]. In addition to calculations of the frequency dependent dynamical polarizability $\alpha(\omega)$, we present measurements of the real part Re$\{\alpha(\omega)\}$ at a wavelength of $\lambda = 1064.5$ nm. The experiments are performed with molecules trapped in the lowest Bloch band of a cubic 3D optical lattice which consists of three standing light waves with polarizations orthogonal to each other. By carrying out modulation spectroscopy on one of the standing light waves, we map out the energy band-structure for various light intensities. From these measurements Re$\{\alpha(\omega)\}$ is determined. Our experimental findings at $\lambda = 1064.5$ nm and also those at 830.4 nm [44] agree well with the calculations. In addition, we experimentally investigate the decay time of the deeply bound molecules in a 3D optical lattice at 1064.5 nm for various lattice depths. Here, lifetimes of more than 2 s are observed. Furthermore, we present numerical results for the dynamical polarizabilities of the rovibronic ground state, i.e., the lowest rovibrational level of the $X^1\Sigma_g^+$ potential. For convenient application of our results, we provide a simple analytical expression and the corresponding effective parameters which can be used to reproduce the dynamical polarizabilities for all vibrational levels of both, the lowest singlet as well as triplet state outside the resonant wavelength regions.

This article is organized as follows. In section 4.2, we give a brief, general introduction

to the dynamical polarizability $\alpha(\omega)$ of a homonuclear diatomic molecule. Sections 4.3 to 4.6 describe the calculations and measurements related to the polarizability of $^{87}\mathrm{Rb}_2$ in the rovibrational ground state of $a^3\Sigma_u^+$, along with a comparison of our results to reference values from literature. In section 4.7 we present calculations of the polarizability for the rovibrational ground state of $X^1\Sigma_g^+$. Afterwards, section 4.8 provides a simple expression which parametrizes the polarizability for all vibrational levels of the lowest singlet as well as triplet state. Tables with the corresponding parameters can be found in the Supplemental Material [131] and in Appendix A.1, respectively.

4.2 Interaction of a diatomic molecule with light

When a nonpolar molecule is subject to a linearly polarized electric field $\vec{E} = \hat{\varepsilon} E_0 \cos(\omega t)$ with amplitude E_0 and unit polarization vector $\hat{\varepsilon}$, a dipole moment $\vec{p} = \overleftrightarrow{\alpha}(\omega)\vec{E}$ is induced. In general, $\overleftrightarrow{\alpha}(\omega)$ is a tensor (see, e.g., [46]). For the sake of simplicity, we restrict ourselves to Hund's case (b) molecules in the lowest rotational level $N = 0$ of the nuclei, for which only the scalar isotropic polarizability $\alpha(\omega)$ is relevant (see, e.g., [44, 46]). Here, $\vec{N} = \vec{L} + \vec{R}$, where $\vec{L}$ denotes the total electronic orbital angular momentum and $\vec{R}$ is the mechanical rotation of the atomic pair. The complex dynamical polarizability characterizes the response of a molecule to the electric field expressed by photon scattering and the ac Stark shift of molecular levels. This shift is directly linked to the dipole interaction potential

$$U = -\langle \vec{p} \cdot \vec{E} \rangle / 2 = -\frac{1}{4}\mathrm{Re}\{\alpha(\omega)\}E_0^2 \tag{4.1}$$

and therefore to the real part of the polarizability $\mathrm{Re}\{\alpha(\omega)\}$ (see, e.g., [107]). In Eq. (4.1), the angled brackets $\langle \ldots \rangle$ indicate time averaging. We note, that the dipole potential is attractive, when the sign of $\mathrm{Re}\{\alpha(\omega)\}$ is positive and repulsive otherwise. The imaginary part of the polarizability $\mathrm{Im}\{\alpha(\omega)\}$ is related to the power P_{abs} absorbed by the oscillator from the driving field, since

$$P_{\mathrm{abs}} = \langle \dot{\vec{p}} \cdot \vec{E} \rangle = \frac{1}{2}\omega \, \mathrm{Im}\{\alpha(\omega)\}E_0^2. \tag{4.2}$$

We calculate the dynamical polarizability $\alpha(\omega)$ following the method described in Ref. [120]. The generic expression of the polarizability for a diatomic molecule in a state $|i\rangle$ is

$$\alpha(\omega) = \frac{2}{\hbar}\sum_f \frac{\omega_{if} - i\frac{\gamma_f}{2}}{\left(\omega_{if} - i\frac{\gamma_f}{2}\right)^2 - \omega^2}\left|\langle f|\vec{d}\cdot\hat{\varepsilon}|i\rangle\right|^2. \tag{4.3}$$

Here, the angled brackets refer to the spatial integration over all internal coordinates of the system. The summation covers all the accessible dipole transitions with frequency ω_{if} and transition electric dipole moment $\vec{d}$ from the initial state $|i\rangle$ to final states $|f\rangle$ with line width γ_f.

4.3 Calculation of $\alpha(\omega)$ for a$^3\Sigma_\mathrm{u}^+$ molecules

4.3.1 Relevant transitions

If the molecule is initially in a vibrational level v_a of the $a^3\Sigma_u^+$ state, all rovibrational levels (including the continuum) of the electronic potentials with $^3\Sigma_g^+$ and $^3\Pi_g$ symmetry need to be accounted for in Eq. (4.3). As $N = 0$ in the initial $a^3\Sigma_u^+$ state, only transitions towards final levels with total angular momentum $J = 0, 1, 2$ must be considered. Here, $\vec{J} = \vec{S} + \vec{N}$, where $\vec{S}$ is the total electronic spin. Therefore, when considering a diatomic molecule it is usual to define two contributions to the isotropic polarizability α: the parallel polarizability $\alpha_\parallel$ along the molecular axis $\hat{Z}$, which is related to d_Z, and the perpendicular polarizability $\alpha_\perp$, which is related to $d_X = d_Y$. In general, $\alpha_\parallel$ involves $^3\Sigma^+ \rightarrow {}^3\Sigma^+$ transitions and $\alpha_\perp$ is related to $^3\Sigma^+ \rightarrow {}^3\Pi$ transitions. One can show that $\alpha = (\alpha_\parallel + 2\alpha_\perp)/3$ (see, e.g., Refs. [46, 120]).

The expression given by Eq. (4.3) deals only with the transitions involving the two valence electrons of Rb$_2$. Following Ref. [132], the contribution to the polarizability of the two Rb$^+$ cores, hereafter referred to as α_c, must be taken into account, and is added to the results of Eq. (4.3). More details about this quantity are discussed in section 4.11.1.

The first step of the calculations is to collect a set of accurate molecular potential energy curves (PECs) and transition electric dipole moments (TEDMs). The $a^3\Sigma_u^+$ PEC is taken from the spectroscopic study of Ref. [133]. For the excited molecular states and the related TEDMs from the $a^3\Sigma_u^+$ state, we use the same data as Refs. [121, 134], which we report in the Supplemental Material [131], for convenience. The PECs are displayed in Fig. 4.1(a), while the TEDMs are drawn in Fig. 4.10 (see section 4.11.2). These data are obtained by the quantum chemistry approach described in details in Ref. [135]. Briefly the Rb$_2$ molecule is considered as two valence electrons moving in the field of the two ionic Rb$^+$ cores, which are represented by a large effective core potential (ECP) including a core polarization potential (CPP) [136, 137]. A full configuration interaction (FCI) is then performed on the two valence electrons, using a large Gaussian basis set [138], with the CIPSI quantum chemistry code developed at Université Paul Sabatier in Toulouse. It is worth mentioning that partial spectroscopic information is available on the $1^3\Sigma_g^+$ [124], the $1^3\Pi_g$ [139] state, and on the $2^3\Pi_g$ state [133], but no complete PEC has been extracted in these studies. As discussed for instance in Refs. [121, 139], the computed PECs are suitable to reproduce the observed data provided that they are slightly shifted in frequency (in terms of $\omega/(2\pi c)$, by at most $100\,\mathrm{cm}^{-1}$). We will estimate in section 4.5 the limited influence of such shifts on the results reported in the present work. Finally, the vibrational wave functions of levels $|i\rangle$ and $|f\rangle$ for the summation are obtained using the Mapped Fourier Grid Hamiltonian representation [140, 141].

4.3.2 Results

The real and imaginary parts of the dynamical polarizability $\alpha_{v_a=0}(\omega)$ of a molecule in the vibrational ground state of the $a^3\Sigma_u^+$ potential are displayed in Fig. 4.1(b) and (c) as functions of the trapping laser frequency. The polarizabilities are expressed in atomic units (a.u.), which can be converted into SI units according to 1 a.u. $= 4\pi\varepsilon_0 a_0^3 = 1.649 \times 10^{-41}\mathrm{Jm^2V^{-2}}$, where
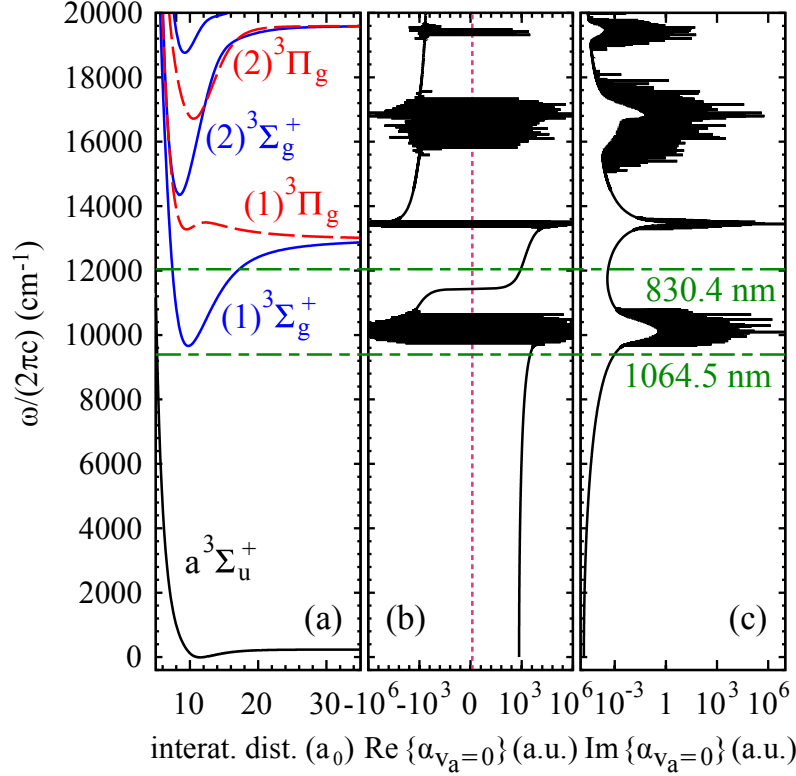
Figure 4.1: (a) $^3\Sigma_g^+$ (solid blue lines) and $^3\Pi_g$ (dashed red lines) potential curves of Rb$_2$ [121, 134]. The $a^3\Sigma_u^+$ potential is drawn in black. In (b) and (c) the real and imaginary parts of the dynamical polarizability $\alpha_{v_a=0}$ of Rb$_2$ molecules in the rovibrational ground level ($v_a = 0$, $R = 0$) of the $a^3\Sigma_u^+$ molecular state are shown as a function of $\omega/(2\pi c)$. The two wavelengths used in the experiments are indicated by dashed horizontal lines. Furthermore, the red dashed vertical line in (b) represents zero polarizability.

a_0 denotes the Bohr radius and ε_0 is the vacuum permittivity. Note, for some applications, e.g., considerations related to the ac Stark shift, units of HzW^{-1}cm^2 (1 a.u. corresponds to 4.6883572×10^2 HzW^{-1}cm^2) are advantageous. The sum in Eq. (4.3) has been truncated to include only the vibrational levels of the four lowest $^3\Sigma_g^+$ states and the three lowest $^3\Pi_g$ states. Furthermore, electric-dipole-forbidden transitions are not considered in the sum, as they would appear as very weak and narrow resonances in the polarizability. The associated molecular data are collected in the Supplemental Material [131]. For simplicity, the natural lifetime $\tau_f = (\gamma_f)^{-1}$ has been fixed to 10 ns ($\gamma_f \approx 2\pi \times 15$ MHz) for all the excited molecular levels.

Strongly oscillating patterns in both Re$\{\alpha_{v_a=0}(\omega)\}$ and Im$\{\alpha_{v_a=0}(\omega)\}$ [see Figs. 4.1(b) and (c), respectively] correspond to frequency ranges of strong absorption which should be disre-

garded for trapping purpose. The real part smoothly increases from the static polarizability $\alpha_{v_a=0}(\omega = 0) = 698.5$ a.u. up to the bottom of the $1^3\Sigma_g^+$ potential well, reaching 3147 a.u. at the wavelength of the trapping laser used in the present experiment (1064.5 nm). In the same region the imaginary part increases from about 10^{-5} a.u. at $\omega = 0$ to 10^{-3} a.u. at the trapping laser frequency which leads to a correspondingly larger photon scattering rate.

It is difficult to provide a well-defined error bar on the theoretical values of the dynamical polarizabilities as their accuracy depends on the considered wavelength. Various causes of global inaccuracies have been analyzed in depth in Ref. [142]. First, the choice of a constant radiative lifetime for all excited levels in Eq. (4.3) influences only the strongly oscillating regions of the polarizability, changing the amplitude of the resonances. We checked that this approximation has no effect in the smoothly varying regions which are relevant for trapping experiments. We verified also that adding a couple of upper electronic states in the sum of Eq. (4.3) contributes to the polarizability for less than 1%. Moreover, the first excited Σ and Π states contribute together for more than 90% to the polarizability. Usually, these are the most well known states either because accurate spectroscopic results are available, or because they are well-determined by quantum chemistry calculations. The accuracy of TEDMs is tedious to analyze as their experimental determination relies on line intensities which are difficult to measure accurately. However, one argument in favor of the accuracy of the TEDMs results when comparing the values obtained from different methods. For instance, in Refs. [143, 144], with respect to various alkali-metal dimers, the TEDMs computed by two different methods are found to agree within 2%. Finally, an indication for the accuracy of the present work is provided by the measurement of the dynamical polarizability for the $v = 0$, $J = 0$ level of the Cs₂ electronic ground state at 1064.5 nm, which is quite far away from the lowest resonant region [120]. The experimentally determined value with respect to $\lambda = 1064.5$ nm is $2.42(15) \times \alpha_{Cs}$ (E. Kirilov and H.-C. Nägerl, private communication), where α_{Cs} is the dynamical polarizability of the Cs atom. This is in remarkable agreement with the computed value of $2.48 \times \alpha_{Cs}$ [120].

4.4 Measurement of $\mathrm{Re}\{\alpha(\omega)\}$ for $\mathrm{a}^3\Sigma_\mathrm{u}^+$

4.4.1 Experimental setup and measurement scheme

The experiments presented in this work are carried out with a pure sample of about 1.5×10^4 ^{87}Rb₂ molecules prepared in the rovibrational ground state of the $a^3\Sigma_u^+$ potential and trapped in a 3D optical lattice. There is no more than a single molecule per lattice site and the temperature of the sample is about $1\,\mu$K. As described in detail in Refs. [44, 46, 53], the molecules are prepared as follows. An ultracold thermal cloud of spin-polarized ^{87}Rb atoms ($f_a = 1$, $m_{f_a} = 1$) is adiabatically loaded into the lowest Bloch band of a 3D optical lattice at a wavelength of $\lambda = 1064.5$ nm. The lattice is formed by a superposition of three linearly polarized standing light waves with polarizations orthogonal to each other, see Fig. 4.2(a). The three lattice beams are derived from the same laser source with a linewidth of a few kHz and have relative intensity fluctuations of less than 10^{-3}. In order to avoid interference effects, the frequencies of the standing waves are offset by about 100 MHz relative to each other. At the

(a)

(b)
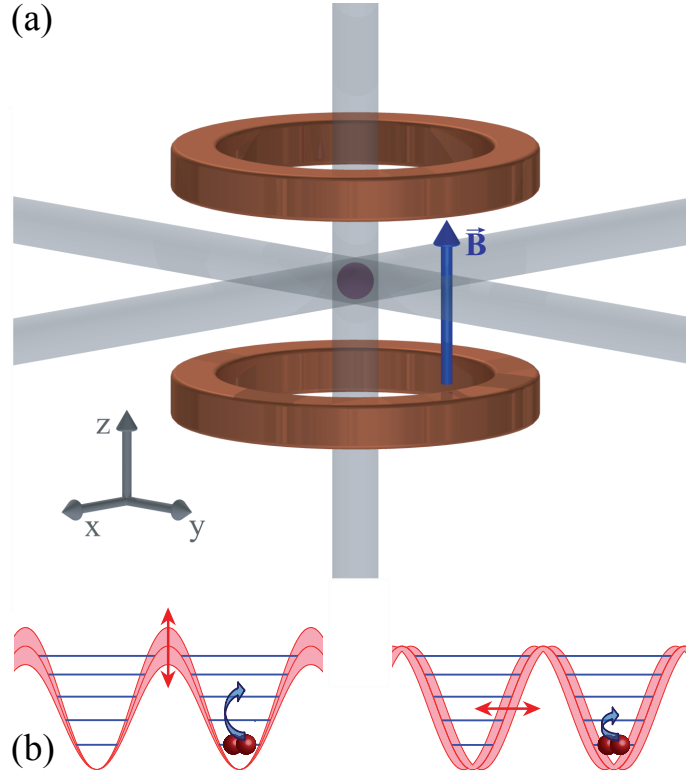
Figure 4.2: (a) Experimental scheme. Three retroreflected laser beams with polarizations orthogonal to each other form a 3D optical lattice. A trapped cloud of Rb_2 molecules is sketched in the intersection of the laser beams. The optical lattice is located between two Helmholtz coils which create a magnetic field $\vec{B}$. In our setup, the direction of $\vec{B}$ represents the quantization axis. (b) Illustration of amplitude (left) and phase (right) modulation spectroscopy.

location of the atomic sample the beam waists ($1/e^2$ radii) are about $130\,\mu\text{m}$ and the maximum available power per beam is about $3.5\,\text{W}$. By slowly crossing the magnetic Feshbach resonance at 1007.4 G we produce weakly bound diatomic molecules. After a purification step which removes remaining atoms, a STIRAP (stimulated Raman adiabatic passage) is performed at 1000 G, transferring the dimers into the rovibrational ground state ($v_a = 0$, $N = 0$, $m_N = 0$) of the $a^3\Sigma_u^+$ potential. Here, m_N is the projection of N on the quantization axis defined by the direction of the magnetic field $\vec{B}$ [cf. Fig. 4.2(a)]. The molecule has positive total parity, total electronic spin $S = 1$, total nuclear spin $I = 3$ and is further characterized by the quantum number $f = 2$ ($\vec{f} = \vec{S} + \vec{I}$). Moreover, the total angular momentum is given by $F = 2$ ($\vec{F} = \vec{f} + \vec{J}$) and its projection is $m_F = 2$. Henceforth, we simply refer to these molecules as "$v_a = 0$ molecules".

According to Eq. (4.1), $\text{Re}\{\alpha(\omega)\} = 4|U|/E_0^2$, i.e., the real part of the dynamical polar-

izability can be determined by measurements of the potential depth $|U|$ and the electric field amplitude E_0 of an optical trap. For the case of a cubic 3D optical lattice with orthogonal polarizations, the trapping potential is given by $V(x, y, z) = \sum_{\beta=x,y,z} V_\beta(\beta)$ where the

$$V_\beta(\beta) = -|U|_\beta \cos^2 (k\beta + \phi_\beta) \qquad (4.4)$$

represent the contributions of the standing waves of directions $\beta = x, y, z$ with $k = 2\pi/\lambda$ being the wave number of the lattice beams. We now only consider the part of the lattice in the vertical z direction since this axis is the only one relevant for the measurements of the potential depth in the present work. Therefore, we define $V_z(z) \equiv V(z)$, $|U|_z \equiv |U|$ and $\phi_z \equiv \phi$. The phase ϕ is a function of the laser wavelength λ because the standing light wave is created by retroreflecting the laser beam from a fixed mirror at position z_m. It is given by $\phi = 4\pi z_m/\lambda$ at $z = 0$.

4.4.2 Lattice modulation spectroscopy

In order to obtain $|U|$, we carry out lattice modulation spectroscopy (see, e.g., [40, 109, 145, 146]). For this, we either modulate $|U|$ by periodically changing the intensity of the standing light wave (amplitude modulation) or we modulate the phase ϕ by periodically changing the laser wavelength λ (phase modulation). Resonant amplitude (phase) modulation drives transitions from the lowest Bloch band ($n = 0$), in which the molecules have been initially prepared, to even (odd)-numbered excited lattice bands [see Fig. 4.2(b)]. This can cause either direct loss from the trap owing to heating (see, e.g., [145]) or molecules in higher lattice bands collide with each other and those of the lowest Bloch band, respectively, resulting in decay to nonobservable states. In consequence, resonant excitation leads to a decreased molecular signal in our measurements.

For amplitude modulation spectroscopy, we modulate the intensity of the lattice laser beam sinusoidally by a few percent. When performing phase modulation spectroscopy, we modulate the laser frequency by a few MHz corresponding to a phase difference on the order of a few 10^{-2} rad as $z_m \sim 0.4$ m. The modulation duration is typically on the order of 1 ms. At the end of each experimental cycle (which takes about 40 s), the remaining number N of molecules is measured. We only find molecules in the lowest Bloch band, not in higher bands. In order to determine the molecule number, we reverse the STIRAP and dissociate the resulting Feshbach dimers by sweeping over the Feshbach resonance. Then, the generated atoms are detected via absorption imaging. By comparing the resonant transition frequencies observed in the modulation spectra to the energy band-structure of the sinusoidal lattice, the lattice depth $|U|$ is deduced. This will be explained in detail further below.

Figure 4.3 shows measured excitation spectra of Feshbach (a) and $v_a = 0$ (b,c) molecules, obtained via amplitude or phase modulation spectroscopy. A single data point typically consists of 5 to 30 repetitions of the experiment (For a given spectrum the number of repetitions is constant). Fig. 4.3(a) as well as (b) exhibit a prominent resonance after amplitude modulation. This resonance is related to a transition from the lowest Bloch band ($n = 0$) to the second excited lattice band ($n = 2$). Spectrum (a) for Feshbach molecules in addition shows a broad
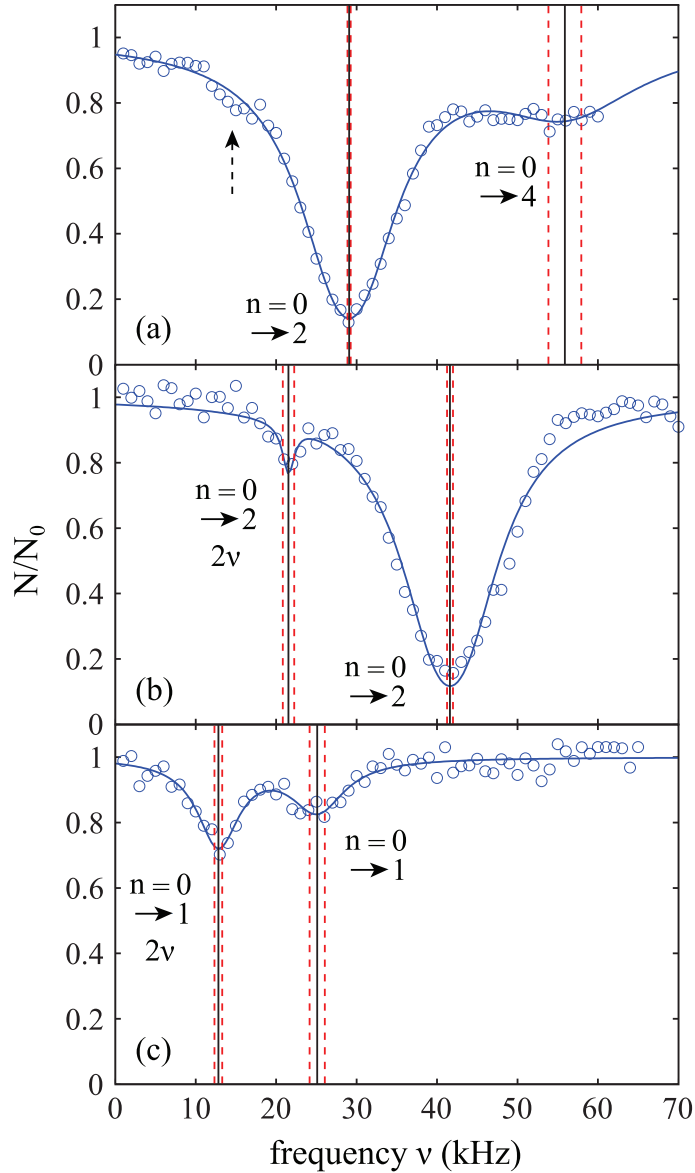
Figure 4.3: Amplitude [(a) and (b)] and phase (c) modulation spectra of weakly bound Feshbach molecules (a) and molecules in the rovibrational ground state of the $a^3\Sigma_u^+$ potential [(b) and (c)]. We measure the fraction of remaining molecules N/N_0 as a function of the modulation frequency ν. The statistical error of each data point is in the range of $\pm(0.05 - 0.15)$. Here, the numbers N_0 are given by the asymptotic limits of Lorentzian fits (solid blue lines). The resulting center frequencies of the resonances are illustrated as black vertical lines, while the red dashed lines indicate the corresponding uncertainties. We note, that the mean intensity of the lattice beam used for modulation in (b) is 30% less than in (a) and (c).

shoulder at around 50 kHz which we attribute to a resonant transition from $n = 0$ to $n = 4$. Due to the large width of this resonance the uncertainty in the determination of its center frequency is relatively large. Spectrum (b) in Fig. 4.3 also features a second resonance dip, but here it is located at about half the frequency of the prominent one. This resonance dip can be assigned to a transition from the lowest Bloch band to the second excited band, involving two identical "quanta" with frequency ν. It is known (see, e.g., [145]) that such subharmonic resonances exist. To be consistent, a similar sub-harmonic resonance dip should be present in Fig. 4.3(a) at about 15kHz (as indicated by the vertical, dashed arrow). Indeed, at that position the data points seem to be systematically below the fit curve with respect to the prominent peak. However, the corresponding signal (if at all) is very weak, partially due to its position at the steep flank of the prominent resonance.

Now, we turn to Fig. 4.3(c), which shows an excitation spectrum after phase modulation for $v_a = 0$ molecules. We observe two resonances of similar strength, both of which we attribute to the transition from $n = 0$ to $n = 1$. The dip at lower frequency is again a subharmonic resonance. Surprisingly, it is stronger than the harmonic one at about 25kHz. We attribute this to a purely technical issue, as the strength of the phase modulation varied with the frequency in our setup. However, we have verified the assignment of the resonances by comparison to the corresponding amplitude modulation spectra.

We calculate the Bloch bands by diagonalizing the Hamilton operator for the lattice in 1D (neglecting gravitation),

$$H = -\frac{\hbar^2}{2m}\frac{\partial^2}{\partial z^2} + V(z) \, , \tag{4.5}$$

which is particularly simple in momentum space (see, e.g., [147]). Here, m is the mass of a molecule, i.e., twice the mass of a ^{87}Rb atom. Figure 4.4 shows the calculated energy eigenvalues as a function of the lattice depth. The energies are given in terms of the recoil energy $E_R = h^2/(2m\lambda^2)$, with h being Planck's constant. As we do not specify the quasimomentum, the energy eigenvalues form bands which are broad for low lattice depths. However, the bands $n = 0$ to $n = 2$ are quite narrow for lattice depths above $\sim 40\, E_R$. This is the regime where we take most of our measurements. Having measured the resonant excitation frequencies after modulation we could in principle use Fig. 4.4 to read off the corresponding lattice depth $|U|$. We refine this method and at the same time check for consistency as follows.

In the experiment we control the lattice depth $|U|$ via the laser beam power P that can be measured using photodiodes. The square to the electrical field E_0^2 is proportional to P. Consequently $|U| \propto P$, i.e., the precise value of $|U|$ is known up to a calibration factor (which depends linearly on the dynamical polarizability). Thus, given a molecular state, we should be able to adjust the calibration factor such that all data obtained for various powers P match the band structure calculation. The measured data points in Fig. 4.4 clearly show that this works quite well, both for deeply bound molecules (red) and Feshbach molecules (blue). In this procedure we do not account for the transitions from $n = 0$ to $n = 4$ owing to the large uncertainties of the corresponding resonances in the excitation spectra. Nevertheless, these data points are shown in the plot for comparison.

In addition to $|U|$, the electrical field amplitude E_0 of the optical lattice has to be deter-
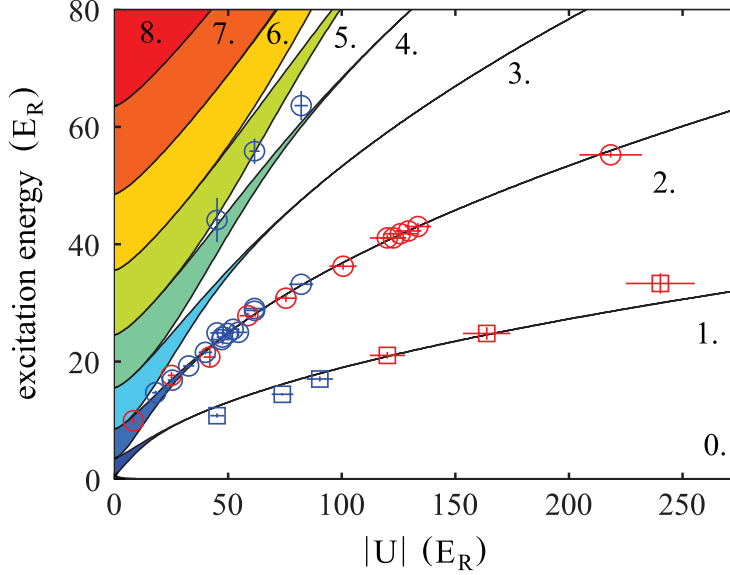
Figure 4.4: Energy band-structure with zero energy corresponding to the center of the lowest Bloch band. Solid lines are calculations for a single lattice direction, where the numbers 1. to 8. give the band index n. The data points are obtained excitation energies for $\lambda = 1064.5$ nm, stemming from amplitude (circles) or phase (squares) modulation spectroscopy. Red (blue) plot symbols indicate measurements for triplet rovibrational ground state (Feshbach) molecules. Here, the experimental results are shown after independently fitting the data for each molecular species to the band-structure calculation. By doing so, we determine the individual calibration factors and therefore the lattice depths $|U|$ (see also text). The horizontal error bars represent the resulting uncertainties of $|U|$, whereas the vertical error bars are given by the uncertainties of the Lorentzian fits in the modulation spectra.

mined in order to infer the dynamical polarizability $\alpha(\omega)$ [see Eq. (4.1)]. We can circumvent this by referencing the measurements on the lattice depth $|U|$ for the molecules in the rovibrational ground state of the $a^3\Sigma_u^+$ potential to similar measurements with Feshbach molecules, of which the polarizability $\alpha_{\mathrm{Fesh}}(\omega)$ is known to be twice the one of a Rb atom $\alpha_{\mathrm{Rb}}(\omega)$ in the electronic ground state [120]. According to Eq. (4.1) the lattice depths $|U_{v_a=0}|$ and $|U_{\mathrm{Fesh}}|$ for the $v_a = 0$ and Feshbach molecules are related by

$$\frac{|U_{v_a=0}|}{|U_{\mathrm{Fesh}}|} = \frac{\mathrm{Re}(\alpha_{v_a=0})}{\mathrm{Re}(\alpha_{\mathrm{Fesh}})} \tag{4.6}$$

for a given lattice beam intensity, i.e., a given E_0.

From our experiments at $\lambda = 1064.5$ nm we obtain $\mathrm{Re}\{\alpha_{v_a=0}\} = (2.5 \pm 0.1) \times \mathrm{Re}\{\alpha_{\mathrm{Fesh}}\}$, whereas $\mathrm{Re}\{\alpha_{v_a=0}\} = (0.1 \pm 0.02) \times \mathrm{Re}\{\alpha_{\mathrm{Fesh}}\}$ was found at $\lambda = 830.4$ nm [44]. Using our

calculated atomic values of 685.8 a.u (1064.5 nm) and 2995.9 a.u (830.4 nm) yields molecular polarizabilities Re$\{\alpha_{v_a=0}\}$ of 3430 ± 140 a.u (1064.5 nm) and 600 ± 120 a.u (830.4 nm), respectively.

4.5 Comparison of results

Table 4.1 shows our measured and calculated polarizabilities along with results of other references. First, it should be noted that our theoretical atomic polarizabilities (including only the $5s - 5p$ and $5s - 6p$ transition frequencies from the NIST database [148] at 828.4 nm and at 1060.1 nm are in good agreement with the ones of Refs. [149, 150] which consider the $5s - 5p$ transition frequency from the NIST database, and *ab initio* values for the frequencies up to the $5s - 8p$ transitions.

We find good agreement between our theoretical (3147 a.u.) and experimental (3430 ± 140 a.u.) results for the molecular polarizability Re$\{\alpha_{v_a=0}\}$ at 1064.5 nm (see table 4.1). In contrast, the agreement for the polarizability at 830.4 nm of our former measurements [44] (600 ± 120 a.u.) with the present calculations (875.8 a.u.) is somewhat poor. In view of this discrepancy we want to estimate the influence of slight shifts of the potential energy curves on the calculations. The potential well depths of the $1^3\Sigma_g^+$ and the $1^3\Pi_g$ states used in the

Species	λ (nm)	Re$\{\alpha\}$ (a.u.)	Ref.
^{87}Rb	828.4	3132 ± 3	[149]
^{87}Rb	828.4	3131.4	tw theo
^{87}Rb	830.4	2995.9	tw theo
^{87}Rb$_2$	830.4	875.8	tw theo
^{87}Rb$_2$	830.4	600 ± 120	[44], using $\alpha_{\rm Rb} = 2995.9$ a.u.
^{87}Rb	1060.1	692.7	tw theo
^{87}Rb	1060.1	693.5 ± 0.9	[150]
^{87}Rb	1064.5	685.8	tw theo
^{87}Rb$_2$	1064.5	3147	tw theo
^{87}Rb$_2$	1064.5	3430 ± 140	tw exp, using $\alpha_{\rm Rb} = 685.8$ a.u.
^{87}Rb$_2$	1064.5	3200 ± 500	[153]
^{87}Rb	∞	318.6 ± 0.6	[155]
^{87}Rb	∞	317.9	tw theo
^{87}Rb$_2$	∞	698.5	tw theo
^{87}Rb$_2$	∞	677.5	[151]

Table 4.1: Measured and calculated polarizabilities Re$\{\alpha\}$ in a.u. for ^{87}Rb atoms and ^{87}Rb$_2$ molecules in the rovibrational ground state of $a^3\Sigma_u^+$. Here, the abbreviations "tw exp (theo)" mean "this work, experimental (theoretical)".

computation are smaller by $72\,\mathrm{cm}^{-1}$ and $51\,\mathrm{cm}^{-1}$ with respect to the experimental determinations of Refs. [124] and [139], respectively. Such shifts would lead to a change in the calculated polarizability of about 10% for the particular wavelengths of 830.4 nm and 1064.5 nm. This sets a range for the uncertainty of the calculated polarizability that arises from the uncertainty of the PECs. Furthermore, in terms of the experiments, we note that in Ref. [44] a different method to determine the dynamical polarizability was used. The polarizability was inferred from the oscillating dynamics of molecular wave packets that occurred when $v = 0$ molecules were suddenly loaded into several Bloch bands of the optical lattice. This leaves potentially room for a systematic discrepancy between the two measurements. With respect to the static polarizability, i.e., $\omega = 0$, the calculations presented in this work give 698.5 a.u. (cf. table 4.1) for the $v_a = 0$ molecules. This value actually agrees well with the one previously reported in Ref. [151], 677.5 a.u., as it was not including the contribution of $\alpha_c \equiv 2 \times \alpha(\mathrm{Rb}^+) = 18.2$ a.u. [152].

Figure 4.5 is a zoom into Fig. 4.1(b) showing the calculated real part of the dynamical polarizability of a $v_a = 0$ molecule (solid black lines). In addition, $\mathrm{Re}\{\alpha(\omega)\}$ for a Feshbach molecule is plotted (dashed red lines), which is given by twice the atomic polarizability. The two wavelengths used in our experiments (830.4 nm and 1064.5 nm) are indicated as vertical green dashed lines. Outside the resonant and therefore lossy regions in Fig. 4.5 (vertical black bands) the two polarizability curves never cross. Thus, there is no so-called "magic" wavelength, where the ac Stark shift of the two molecular states caused by the trapping light is equal. Such state-insensitive trapping conditions can be beneficial, e.g., when converting Feshbach molecules to
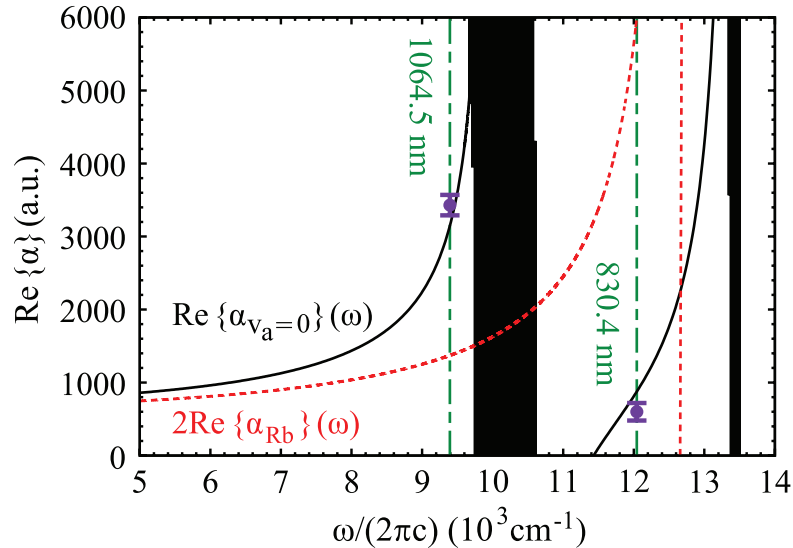

Figure 4.5: Real parts of the dynamical polarizabilities of triplet rovibrational ground state molecules (solid black lines) and Feshbach molecules (dashed red lines). The circles represent the experimental results given in table 4.1 with the corresponding wavelengths indicated by green dashed vertical lines.

deeply bound states. Specifically, in Ref. [44], owing to the large difference of the dynamical polarizabilities at $\lambda = 830.4\,$nm, the STIRAP transfer of Rb$_2$ from the Feshbach level to $v_a = 0$ populated several lattice bands.

We have again studied this issue in this work and find that population of higher lattice bands can be suppressed even in the absence of a magic wavelength when working with deep lattices. At $\lambda = 1064.5$ nm there is still a factor of 2.5 difference in polarizability between Feshbach and $v_a = 0$ molecules. For an initial (final) lattice depth of 50 E_R (125 E_R) at 1064.5 nm a calculation of the wave function overlap for the Bloch states shows that still 97% of the population stays in the lowest Bloch band after the STIRAP. In addition, we are able to energetically resolve the lattice bands during STIRAP as $n = 0$ and $n = 2$ are separated by about 40 kHz at $|U| = 125\,E_R$ (cf. Fig. 4.4). This strongly increases the selectivity of the transition (see, e.g., [156]). Indeed, in our experiments we do not observe any significant population of higher bands.

As can be seen in Fig. 4.5, the absolute dynamical polarizability of the triplet rovibrational ground state molecules at 1064.5 nm is about four times larger than at 830.4 nm. This is convenient since it results in a four times deeper interaction potential at the same laser intensity. For longer wavelengths than 1064.5 nm, Fig. 4.5 reveals, that the dynamical polarizabilities of $v_a = 0$ molecules and Feshbach molecules approach each other. Hence working at even longer wavelengths than 1064.5 nm might be advantageous for some applications.

4.6 Lifetime of the molecules

According to Eq. (4.2), the imaginary part of the dynamical polarizability, Im$\{\alpha\}$, is linked to the light power absorbed by a molecule, P_{abs}, which in turn can be expressed in terms of the photon scattering rate $\Gamma_{\mathrm{sc}} = \hbar^{-1}\omega^{-1}P_{\mathrm{abs}}$ [107]. Using this and Eq. (4.1), Γ_{sc} can be written as

$$\Gamma_{\mathrm{sc}} = -\frac{2U}{\hbar}\frac{\mathrm{Im}\{\alpha(\omega)\}}{\mathrm{Re}\{\alpha(\omega)\}} \; . \tag{4.7}$$

For a 3D optical lattice with equal lattice depths $|U|$ in each direction the scattering rate is given by $\Gamma_{\mathrm{sc}}^{3\mathrm{D}} = 3\Gamma_{\mathrm{sc}}$. As an example, we consider the case of $|U| = 50E_R$ at $\lambda = 1064.5$nm. Then, the corresponding values for the polarizability obtained in the present work, Im $(\alpha) = 0.96{\times}10^{-3}$a.u and Re$\{\alpha\} = 3430$ a.u., yield $\Gamma_{\mathrm{sc}} = 0.18\,\mathrm{s}^{-1}$. Note, this calculation only accounts for an ideal optical lattice. As there is always background light that does not contribute to the lattice, the estimated value for the scattering rate represents just a lower bound. Once a photon is absorbed, the molecule is excited and typically decays to a nonobservable state. Assuming excitation to be the only loss-mechanism a lifetime $\tau = 1.9$s of the $v_a = 0$ molecules is expected in a 50 E_R deep 3D optical lattice at 1064.5 nm.

We experimentally investigate the lifetimes of the molecules in the rovibrational ground state of $a^3\Sigma_u^+$ by varying the holding time t_{h} in the lattice. Figure 4.6 shows lifetime measurements of $v_a = 0$ molecules for various potential depths $|U|$, which are adjusted to be equal in each direction. Applying an exponential fit, we obtain a $1/e$ decay time τ of more than 2 s for
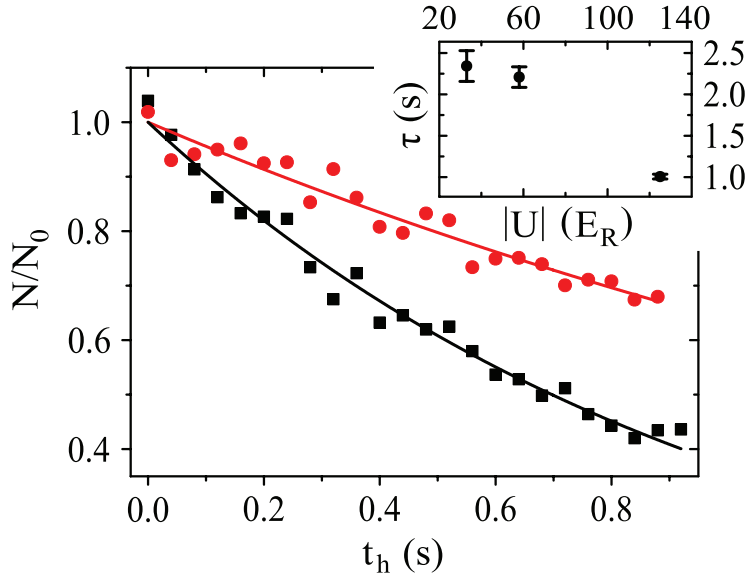
Figure 4.6: Decay of triplet rovibrational ground state molecules trapped in a 3D optical lattice at 1064.5nm with equal potential depths $|U|$ in each direction. Shown is the fraction of remaining molecules N/N_0 as a function of the holding time t_h in the lattice. Square plot symbols (red circles) correspond to a lattice depth of $125\,E_R$ ($58\,E_R$). Each data set typically consists of 10 to 15 repetitions of the experiment, where the statistical error of a data point is on the order of ± 0.1. Solid lines are exponential fits to the data. Here, N_0 is given by the values of these fits at $t_h = 0$ s. In general, the absolute molecule numbers N_0 are about 1.5×10^4. The inset depicts the resulting $1/e$ decay times for various lattice depths.

both our measurements at $|U| = 33\,E_R$ and $|U| = 58\,E_R$.

In order to estimate possible loss induced by inelastic molecular collisions, we calculate the tunneling rates Γ_tu between adjacent lattice sites within the lowest Bloch band ($n = 0$). When considering a lattice depth of $33\,E_R$ ($58\,E_R$) one obtains $\Gamma_\text{tu} = 2.37\,\text{s}^{-1}$ ($\Gamma_\text{tu} = 0.09\,\text{s}^{-1}$). In our setup at most 20% of the lattice sites are occupied in the region of highest molecule density. Thus, for $|U| = 33\,E_R$ decay due to collisions cannot be neglected, whereas for $|U| = 58\,E_R$ and beyond the only relevant loss mechanism is photon scattering. For such deep lattices, the lifetime τ scales directly inversely with the lattice depth $|U|$. We confirm this for the measurements at $|U_1| = 58\,E_R$ and $|U_2| = 125\,E_R$, since the ratio of the lifetimes $\tau_1/\tau_2 = 2.20$ is close to $|U_2|/|U_1| = 2.16$.

4.7 Polarizability of $\text{X}^1\Sigma_g^+$ molecules

As the agreement between calculations and measurements for the triplet molecules is in general good, we also provide calculations for the singlet ground state of $^{87}\text{Rb}_2$. Using the same

approach as above (see also [120]), we compute the dynamical polarizability $\alpha_{v_X=0}(\omega)$, i.e., with respect to the $v_X = 0$, $J = N = 0$ level. The $X^1\Sigma_g^+$ PEC has been derived from spectroscopic data of Ref. [122]. The $A^1\Sigma_u^+$ and the $b^3\Pi_u$ PECs and the related spin-orbit coupling between those two states are taken from Ref. [157]. The PECs for all the other states and for the TEDMs are taken from the computations reported in Refs. [121, 134]. Again, the sum in Eq. (4.3) has been truncated to include only the levels of the four lowest $^1\Sigma_u^+$ states and the three lowest $^1\Pi_u$ states. The natural lifetime of the excited levels has been fixed at 10 ns. Results are presented in Fig. 4.7, showing that two magic wavelengths can be identified at 990.1 nm and 1047.2 nm. The latter is located close to the region of strong absorption resonances and consequently, from the imaginary part [cf. Fig. 4.7(b)], the photon scattering rate at 1047.2 nm is expected to be about four times larger than at 990.1 nm.

4.8 Parametrization of the polarizability

4.8.1 Rovibrational ground state of a$^3\Sigma_u^+$

In general, using figures (e.g., Figs. 4.1 and 4.7) to read off the dynamical polarizabilities at specific wavelengths is cumbersome. Therefore, we provide here a simple analytical fitfunction and parameters that allow for reproducing the numerical results with respect to nonresonant wavelength regimes. In the infrared and optical domain we are studying, the main contributions to the polarizability of the X (a) state outside of resonances come from the transitions towards the first excited $^{1(3)}\Sigma^+$ state and the first $^{1(3)}\Pi$ state. Thus we attempt to model the polarizability by reducing those transitions to a single effective transition towards each of the two different symmetries. The approximate real part of the polarizability is expressed as

$$\alpha_{\text{eff}}(\omega) = \frac{2\omega_\Sigma}{\hbar(\omega_\Sigma^2 - \omega^2)}d_\Sigma^2 + \frac{2\omega_\Pi}{\hbar(\omega_\Pi^2 - \omega^2)}d_\Pi^2 + \alpha_c \tag{4.8}$$

with ω_Σ (resp. ω_Π) the effective transition frequencies and d_Σ (resp. d_Π) the corresponding effective dipole moments. We have isolated in this expression the core polarizability α_c as its frequency dependence is much weaker than the one of the terms coming from valence electron excitation (see section 4.11.1). The imaginary part of the polarizability is neglected since the model is designed for the ranges outside the resonant regions.

We extract the effective parameters from a fit to the full numerical results using Eq. (4.8). The results with respect to the $a^3\Sigma_u^+$ and $X^1\Sigma_g^+$ rovibrational ground state are shown in Fig. 4.8. For the triplet case, data points with frequencies close to resonances, i.e., from $\omega/(2\pi c) = 9527$ cm^{-1} to 11018 cm^{-1} and above 13173 cm^{-1}, are excluded from the fit. We obtain $\omega_\Sigma/(2\pi c) = 10112.33$ cm^{-1}, $d_\Sigma = 2.792881$ a.u., $\omega_\Pi/(2\pi c) = 13481.32$ cm^{-1} and $d_\Pi = 3.211023$ a.u. Note, in terms of dipole moments, atomic units can be converted into SI units according to 1 a.u. $= ea_0 = 8.478 \times 10^{-30}$ Ams. Using these parameters, the effective polarizability reproduces the numerical results in the fitted region to within a relative root
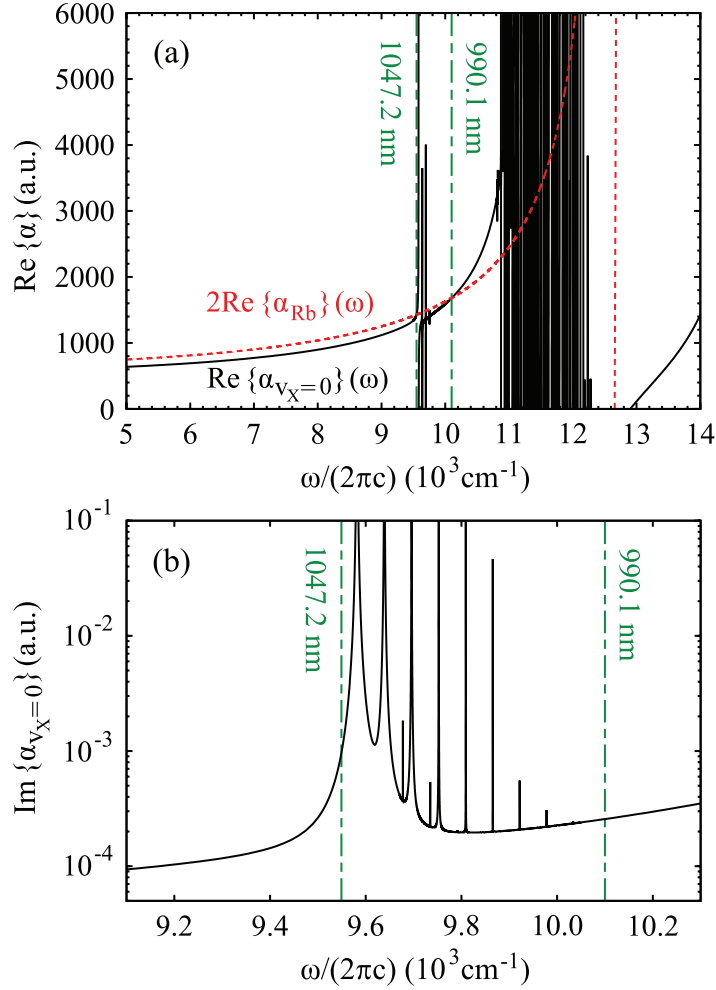
Figure 4.7: Real part (a) and imaginary part (b) of the dynamical polarizability of ^{87}Rb$_2$ $X^1\Sigma_g^+$ molecules in their $v_X = 0$, $N = 0$ level. In (a), for comparison, also the numerical results corresponding to $2\mathrm{Re}\{\alpha_{\mathrm{Rb}}\}$ are shown (red dashed line), representing the real part of the dynamical polarizability of Feshbach molecules. Two magic wavelengths, where both polarizabilities are equal, are obtained and indicated by vertical dashed lines.

mean square value (rRMS) of around 1% [see Fig. 4.8(a)]. The rRMS value is defined by

$$\mathrm{rRMS} = \sqrt{\sum_{i=1}^{M} \frac{1}{M} \left(\frac{\alpha_{\mathrm{eff}}(\omega_i) - \alpha(\omega_i)}{\alpha(\omega_i)} \right)^2} \tag{4.9}$$

with $\alpha(\omega_i)$ being the numerical values, and $\alpha_{\mathrm{eff}}(\omega_i)$ the fitted ones. Here, M is the number of
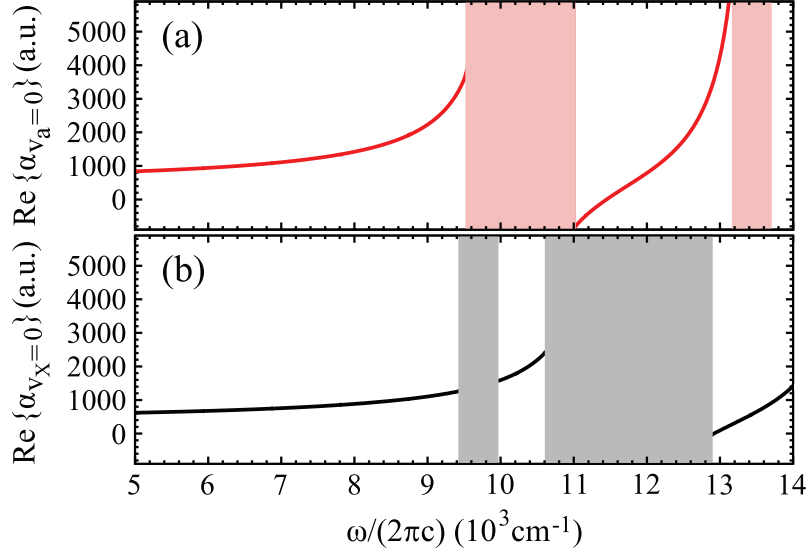
Figure 4.8: Analytical fits of the dynamical polarizabilities of the $a^3\Sigma_u^+$ molecule in $v_a = 0$, $N = 0$ (a), and of the $X^1\Sigma_g^+$ molecule in $v_X = 0$, $N = 0$ (b). Frequency ranges excluded from the fits are indicated as shaded areas. At the scale of the figure, the original curves and the fitted curves are indistinguishable.

considered values ω_i, which depends on the vibrational level as the resonant frequency regions excluded from the fit vary. We point out that if we take the transition dipole moment d_Z (resp. $d_X = d_Y$) at the equilibrium distance of the $a^3\Sigma_u^+$ state and multiply it by the appropriate Hönl-London factor ($1/\sqrt{3}$ for $\Sigma^+ - \Sigma^+$ transition and $\sqrt{2/3}$ for $\Sigma^+ - \Pi$ transition), we get the value 2.767 a.u. (resp. 3.142 a.u.), very close to the effective dipole moment found above. Moreover, the effective transition frequencies correspond roughly to the average frequencies of transitions with favorable Franck-Condon factor.

4.8.2 Rovibrational ground state of $\mathbf{X^1\Sigma_g^+}$

A similar fit can be performed for the dynamical polarizability of $X^1\Sigma_g^+$ molecules in the $(v_X = 0, N = 0)$ level [Fig.4.8(b)]. Frequency domains from $\omega/(2\pi c) = 9432\,\text{cm}^{-1}$ to $9960\,\text{cm}^{-1}$, from $10613\,\text{cm}^{-1}$ to $12890\,\text{cm}^{-1}$ and above $14736\,\text{cm}^{-1}$, corresponding to resonances towards the $b^3\Pi_u$, $A^1\Sigma_u^+$ and $B^1\Pi_u$ excited states, respectively, were excluded from the fit. We omitted to account for levels of the $b^3\Pi_u$ state as they have a very small singlet character. Then, the fit to the numerically calculated dynamical polarizability yields $\omega_\Sigma/(2\pi c) = 11450.31\,\text{cm}^{-1}$, $d_\Sigma = 2.647731$ a.u., $\omega_\Pi/(2\pi c) = 15019.57\,\text{cm}^{-1}$ and $d_\Pi = 2.965774$ a.u. Again, we point out that the effective transition dipole moments obtained are very close to the electronic transition dipole moments taken at equilibrium distance multiplied by the Hönl-London factors, i.e., 2.613 a.u. and 2.959 a.u., respectively. Here, the rRMS of the fit is 0.5%.

4.8.3 Excited vibrational states

Both, the frequency domains with good Franck-Condon factors and transition dipole moments depend significantly on the initial vibrational level. This is reflected in the variation of the effective parameters when we perform an individual fit for each vibrational level (with $N = 0$) of the $a^3\Sigma_u^+$ ($v_a = 0$ to 40) and $X^1\Sigma_g^+$ ($v_X = 0$ to 124) states. The corresponding parameters, which can be used to reproduce the dynamical polarizabilities in the nonresonant frequency domains, are reported in the Supplemental Material [131] and Appendix A.1. Figure 4.9 shows the resulting rRMS values as a function of the vibrational level with respect to the lowest triplet and singlet state.

Using the ansatz of Eq. (4.8) gives a poor result for most excited vibrational levels of the $a^3\Sigma_u^+$ potential with an rRMS exceeding 4% in the range of $v_a = 2$ to 27. This behavior is related to the fact that Franck-Condon factors mainly depend on the amplitude of the excited wave function around both the inner and the outer classical turning points of the initial vibrational level studied. The shape of the $a^3\Sigma_u^+$ potential is quite different compared to the relevant excited states. Consequently, the inner turning point region of a given vibrational level v_a will induce couplings to levels of excited molecular states with energies strongly different from those related to couplings induced by the outer turning point region. This effect mainly
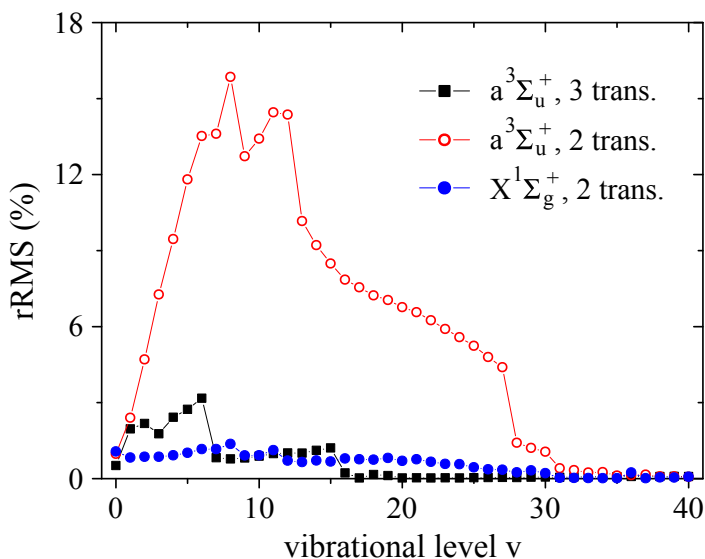
Figure 4.9: Relative root mean square (rRMS) values of the analytical fits to the numerically calculated dynamical polarizabilities. Blue closed (red open) circles correspond to fit results obtained with the "two-effective-transitions" ansatz for the vibrational levels v_a of $a^3\Sigma_u^+$ (v_X of $X^1\Sigma_g^+$), whereas the black closed squares stem from fits including a third effective transition to represent the dynamical polarizabilities with respect to v_a, which significantly increases the accuracy (see text). The rRMS values for $v_X > 40$ do not exceed 0.1% (not shown here).

occurs for the excited $^3\Sigma_g^+$ potential wells as they are deep. Instead, the depth of the $^3\Pi_g$ potential is not sufficient to create such a variation.

Thus we added one more transition term to the ansatz of Eq. (4.8) in order to account for both the inner and outer part of the $a^3\Sigma_u^+$-$^3\Sigma_g^+$ transitions in the model. This reduced significantly the rRMS of the effective polarizabilities of the v_a levels (see Fig. 4.9). We want to emphasize that such an interpretation gives a reasonable physical picture for most levels. However, for some levels like the deeply bound ones or those close to the dissociation limits, the three-effective-transition model is somewhat artificial and the effective parameters should be taken only as numerical parameters needed to easily obtain the corresponding polarizability.

4.9 Conclusion

We have studied the dynamical polarizability of the $^{87}Rb_2$ molecule in the rovibrational ground state of the $a^3\Sigma_u^+$ potential. Calculations of both, the real and imaginary part are provided and we measured $Re\{\alpha(\omega)\}$ at $\lambda = 1064.5$nm. Our experimental and theoretical findings show good agreement. From our computed value of $Im\{\alpha(\omega)\}$ at this wavelength, we expect trapping times of the molecules on the order of seconds for lattice depths around $50\,E_R$, which was confirmed by our observations. We also have investigated theoretically the dynamical polarizability of the singlet ground state $X^1\Sigma_g^+$. These results are interesting for future STIRAP transfer of Rb_2 to the corresponding rovibronic ground state. Furthermore, we have introduced a simple analytical expression to parametrize the dynamical polarizabilities for all levels of both, $a^3\Sigma_u^+$ and $X^1\Sigma_g^+$ states. By fitting this expression to the numerical results, we have extracted effective parameters, which can be used to reproduce $Re\{\alpha(\omega)\}$ of a given vibrational state with high fidelity. The precise knowledge of the dynamical polarizability enables accurate control of optical dipole potentials and therefore is of importance for future experiments with deeply bound Rb_2 molecules.

4.10 Acknowledgements

4.11 Additional information on the core polarizability and the transition electric dipole moments

4.11.1 Polarizability of the Rb^+ core

As the two ionic Rb^+ cores are only weakly perturbing each other, we consider the molecular core polarizability as twice the atomic Rb^+ polarizability. First, we calculate the atomic
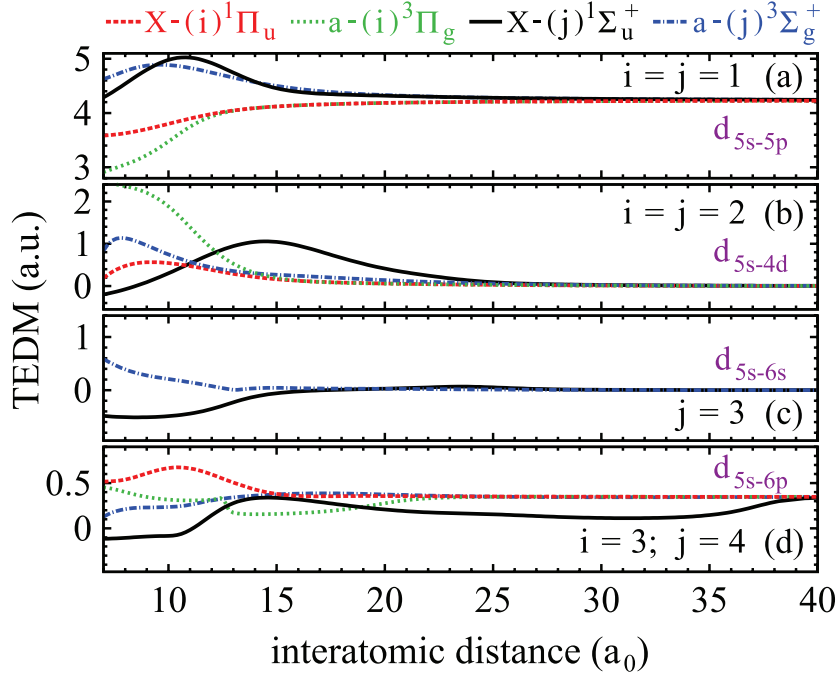
Figure 4.10: Computed transition electric dipole moments (TEDMs) for the main transitions from the $a^3\Sigma_u^+$ and the $X^1\Sigma_g^+$ states to the states correlated to the $5s+5p$ dissociation limit (a), the $5s+4d$ dissociation limit (b), the $5s+6s$ dissociation limit (c), and the $5s+6p$ dissociation limit (d). The individual curves can be assigned to the corresponding transitions as indicated on top of the graph using the numbers i and j. At large distances the TEDMs converge towards d_{5s-nl} which is equal to the atomic TEDMs multiplied by $\sqrt{2}$ (see text).

polarizabilities at imaginary frequencies $\alpha_{\mathrm{Rb}}(i\omega)$ [158], which includes only the contribution of the valence electron. We subtract them from the values of Ref. [132], where the resulting differences represent the contribution of the core electrons, and thus the Rb^+ polarizability. Following Ref. [132] this estimate assumes that the influence of the valence electrons on the core polarizability is negligible.

We use an ansatz similar to the one of Eq. (4.8) to model the core polarizability with two effective transitions. This yields the effective frequencies $\omega/(2\pi c) = 165912\ \mathrm{cm}^{-1}$ and $362918\ \mathrm{cm}^{-1}$, and the effective dipole moments 2.72799 a.u. and 1.40119 a.u. We note that these two transition frequencies are on the order of magnitude of the main transition in Rb^+ and Rb^{2+}, respectively. The core polarizability is a small contribution slowly varying from 17.9 a.u. at vanishing frequency up to 18.1 a.u. in the optical domain relevant here. For the static case, we can compare the result or our calculations to the value of 18.2 a.u. reported in Ref. [152] and find good agreement.

4.11.2 Transition electric dipole moments

For the sake of completeness we show in figure 4.10 the transition electric dipole moments included in the calculations of the dynamical polarizabilities as functions of the internuclear distances. The corresponding numerical values are given in the Supplemental Material [131]. Some of the data with respect to the lowest transitions have already been reported in Refs.[121, 134]. The largest TEDMs in the range of the PECs concern the first excited Σ^+ and Π potentials [see Fig. 4.10(a)]. At large distances the molecular excited electronic wave functions become close to the form $[\phi_{5s}(1)\phi_{nl}(2) \pm \phi_{5s}(2)\phi_{nl}(1)]/\sqrt{2}$ and therefore the TEDMs converge towards d_{5s-nl}, which is equal to the atomic TEDMs multiplied by $\sqrt{2}$. We find $d_{5s-5p} = 4.23$ a.u. and $d_{5s-6p} = 0.347$ a.u., in excellent agreement with the values extracted from the NIST database [148] (4.226 a.u. and 0.3531 a.u.), obtained by averaging the TEDMs corresponding to $5s-np_{1/2}$ and $5s-np_{3/2}$ for $n = 5$ and 6, respectively. This confirms the good quality of the present representations of the atomic electronic wave functions.

5 Probing the Axis Alignment of an Ultracold Spin-Polarized $\mathrm{Rb_2}$ Molecule

Markus Deiß, Björn Drews, Benjamin Deissler, and Johannes Hecker Denschlag

Institut für Quantenmaterie and Center for Integrated Quantum Science and Technology IQST, Universität Ulm, 89069 Ulm, Germany

We present a novel method for probing the alignment of the molecular axis of an ultracold, nonpolar dimer. These results are obtained using diatomic $^{87}\mathrm{Rb_2}$ molecules in the vibrational ground state of the lowest triplet potential $a^3\Sigma_u^+$ trapped in a 3D optical lattice. We measure the molecular polarizabilities, which are directly linked to the alignment, along each of the x, y, and z directions of the lab coordinate system. By preparing the molecules in various, precisely defined rotational quantum states we can control the degree of alignment of the molecular axis with high precision over a large range. Furthermore, we derive the dynamical polarizabilities for a laser wavelength of 1064.5 nm parallel and orthogonal to the molecular axis of the dimer, $\alpha_{\parallel} = (8.9 \pm 0.9) \times 10^3$ a.u. and $\alpha_{\perp} = (0.9 \pm 0.4) \times 10^3$ a.u., respectively. Our findings highlight that the depth of an optical lattice strongly depends on the rotational state of the molecule which has to be considered in collision experiments. The present work paves the way for reaction studies between aligned molecules in the ultracold temperature regime.

5.1 Introduction

In molecular physics and chemistry, control over alignment or orientation of the molecular axis in the laboratory frame is often essential for understanding reaction processes and molecular

structures (see, e.g., Refs. [159-163]). Currently, such experiments are typically carried out with molecular beams in a pulsed fashion, where the alignment or orientation is achieved by state selection with hexapole fields, optical preparation techniques, or exposure to strong ac or dc electric or magnetic fields (see, e.g., Refs. [159, 164-167]). In general, the alignment of the molecular axis is measured via photodissociation, where the angular dependence of the fragments with respect to the laser polarization is measured.

A different approach entails working with optically trapped, ultracold molecular ensembles [66]. Such systems allow for extraordinary control over the internal and external degrees of freedom including the tailoring of the trapping potential and the preparation of molecules in precisely defined quantum states. Here, novel experimental regimes can be reached featuring ultralow-energy collisions and possible interaction times up to many seconds. Further prospects are reaction studies in reduced dimensions and selective investigations of few-body collisions by controlling the number of aligned particles per trapping site. Hence, ultracold molecules will strongly complement the research with molecular beams.

In terms of orientation, the first experiments with ultracold molecules were performed in 2011 where polar KRb molecules were exposed to a dc electric field [62]. Afterwards, their anisotropic polarizability was investigated in a 1D optical lattice of which the polarization was rotated [168].

In this Letter, we demonstrate a novel method to determine the alignment of the molecular axis. This method can be readily implemented in typical ultracold-molecule setups. It relies on the fact that the axis alignment is directly reflected in an anisotropy of the molecular polarizability. The molecules are trapped in a cubic 3D optical lattice with orthogonal polarizations. For each lattice beam, we measure the potential depth for a given light intensity from which we infer the dynamical polarizabilities in the three directions of space and therefore the alignment of the molecular axis. As an application, we briefly show how this technique can be used to spectroscopically investigate unknown molecular states.

Our experiments are performed with ultracold Rb$_2$ molecules in the vibrational ground state of the $a^3\Sigma_u^+$ potential. The molecular ensemble is held in a 3D optical lattice at $1064.5\,\text{nm}$ with trapping times of several seconds. There is no more than a single molecule per lattice site. We are able to prepare a variety of precisely defined molecular energy eigenstates, where the rotational, Zeeman, and hyperfine structure is fully resolved. Consequently, hyperfine depolarization [169, 170] plays no role. The Rb$_2$ molecules are 100% spin polarized. The spin polarization directly determines the molecular axis alignment, which is the quantity that we measure in our experiment. Although no forced alignment via electric or magnetic fields is employed, sizeable degrees of alignment of the molecular axis are readily achieved. Furthermore, the alignment persists as long as a quantization axis is defined, in our case by an external magnetic field.

5.2 Theoretical description

When a nonpolar molecule is exposed to a linearly polarized, oscillating electric field $\vec{E}(t) = \hat{\varepsilon} E_0 \cos(\omega t)$ with amplitude E_0 and unit polarization vector $\hat{\varepsilon}$, a dipole potential $U = -\hat{\varepsilon} \cdot$

$(\overleftrightarrow{\alpha}\hat{\varepsilon})E_0^2/4$ is induced. In a Cartesian coordinate system of which one axis is pointing along the molecular axis the polarizability tensor $\overleftrightarrow{\alpha}$ of a dimer is diagonal and its components have two values $\alpha_\parallel$ and $\alpha_\perp$ for the directions parallel and perpendicular to the molecular axis. U can then be written as $U = -(\alpha_\parallel E_\parallel^2 + \alpha_\perp E_\perp^2)/4$ where $E_\parallel$ and $E_\perp$ are the corresponding components of the electric field amplitude. We describe the orientation of the molecular axis by a unit vector $\vec{A} = (A_x, A_y, A_z) = (\sin\theta\cos\phi, \sin\theta\sin\phi, \cos\theta)$, see Fig. 5.1(a). Using $E_\parallel^2 = (\hat{\varepsilon} \cdot \vec{A})^2 E_0^2$ and $E_\perp^2 = E_0^2 - E_\parallel^2$ the potential becomes $U = -\left[\alpha_\parallel (\hat{\varepsilon} \cdot \vec{A})^2 + \alpha_\perp [1 - (\hat{\varepsilon} \cdot \vec{A})^2]\right] E_0^2/4$. In a quantum mechanical treatment $(\hat{\varepsilon} \cdot \vec{A})^2$ is replaced by its expectation value $\langle (\hat{\varepsilon} \cdot \vec{A})^2 \rangle$. Using electric fields with amplitudes $E_{0,i}$ and polarizations $\hat{\varepsilon}_i$ that point in each of the directions $(i = x, y, z)$ of the lab coordinate system we measure the molecular polarizabilities

$$\alpha^{(i)} = \frac{4|U_i|}{E_{0,i}^2} \; , \tag{5.1}$$

where

$$\alpha^{(i)} = \langle A_i^2 \rangle \alpha_\parallel + (1 - \langle A_i^2 \rangle)\alpha_\perp \; . \tag{5.2}$$

The quantity $\langle A_i^2 \rangle$ defines the degree of alignment of the molecular axis with respect to the direction $\hat{\varepsilon}_i$. For nonaligned molecules, all $\langle A_i^2 \rangle$ are equal to $1/3$. Clearly, by measuring the polarizability $\alpha^{(i)}$ we can directly determine $\langle A_i^2 \rangle$ once $\alpha_\parallel$ and $\alpha_\perp$ are known.

For the $a^3\Sigma_u^+$ state of Rb$_2$ the dynamics of the molecular axis are well described by the wave function of a quantum rotor, of which the Hamiltonian is essentially given by $\vec{R}^2$ with $\vec{R}$ being the operator for nuclear rotation[33]. Especially for magnetic fields larger than $100\,\mathrm{G}$, we can in general safely ignore coupling of $\vec{R}$ to any other spins or angular momenta. Therefore R and its projection m_R onto the quantization axis in the z direction are the only relevant quantum numbers to describe the angular distribution of the molecular axis, turning the Rb$_2$ molecule into a simple and fundamental system to study alignment. Consequently, the eigenstates of the axial motion are the spherical harmonics $Y_{R,m_R}(\theta, \phi) \equiv |R, m_R\rangle$. The degree of alignment of the molecular axis with respect to the x, y, and z directions can be calculated as

$$\langle A_i^2 \rangle = \int |Y_{R,m_R}|^2 A_i^2 \; \sin(\theta)d\theta d\phi \; . \tag{5.3}$$

Figure 5.1(b) shows polar plots of $|Y_{R,m_R}|^2$ corresponding to relevant rotational states. For $|R = 0, m_R = 0\rangle$ the axis direction is isotropic in space, indicating a nonaligned molecule. In contrast, the axis direction is anisotropic for $|2, 0\rangle$ and $|2, \pm 2\rangle$, which is directly reflected in degrees of alignment different from $1/3$.

---

[33]Interestingly, J $(\vec{J} = \vec{R} + \vec{S})$ is in general not a good quantum number for Rb$_2$ in state $a^3\Sigma_u^+$ because the electron spin $\vec{S}$ is only weakly coupled to $\vec{R}$ via second-order spin-orbit interaction but strongly to the nuclear spin $\vec{I}$ via hyperfine interaction [122]. Thus f $(\vec{f} = \vec{S} + \vec{I})$ is good. The weak spin-orbit interaction tends to couple $\vec{f}$ and $\vec{R}$ to form the total angular momentum $\vec{F}$, but already a small Zeeman interaction due to a B field of a few tens of gauss leads again to decoupling, especially for deeply bound molecules.
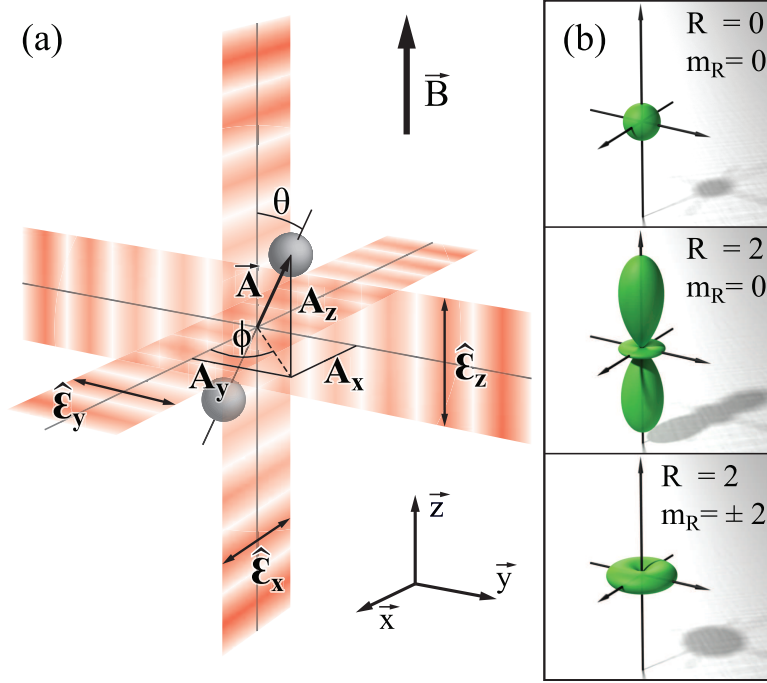
Figure 5.1: (a) Schematic of the experiment. Three laser beams with linear polarizations $\hat{\varepsilon}_i$ orthogonal to each other form a 3D optical lattice. The axis of a diatomic molecule is given by $\vec{A}$. The magnetic field $\vec{B}$ points in the z direction and represents the quantization axis. (b) Polar plots of $|Y_{R,m_R}(\theta, \phi)|^2$ for states $|R, m_R\rangle = |0, 0\rangle$, $|2, 0\rangle$, $|2, \pm 2\rangle$.

5.3 Experimental setup

Our experimental setup and the molecule preparation has been described in detail in Ref. [44]. In brief, an ultracold thermal ensemble of spin-polarized ^{87}Rb atoms ($f_a = 1, m_{f_a} = 1$) is loaded into a 3D optical lattice and converted into Feshbach molecules at a magnetic field of $B = 1007.4$ G. Each Feshbach molecule is nonrotating and has magnetic quantum number $m_F = 2$ of total angular momentum $\vec{F}$. The total nuclear spin is a superposition of components $I = 1, 2, 3$. Using an optical two-photon process [stimulated Raman adiabatic passage (STIRAP)] at $B = 1000$ G, we transfer the molecules to the vibrational ground state of the $a^3\Sigma_u^+$ potential, ending up with a pure ensemble of 1.5×10^4 molecules at a temperature of about $1\,\mu$K. As we use π-polarized light, $m_F = 2$ does not change. The intermediate STIRAP level is located in the $c^3\Sigma_g^+$ potential, has quantum number $I = 3$, and is a mixture of different R. Concerning the final level we choose to populate either one of the well-defined states $|R, m_R\rangle = |0, 0\rangle$ or $|2, 0\rangle$, which are separated by about 1.9 GHz (see Ref. [122]) by setting the relative detuning of the STIRAP lasers. Both levels have quantum numbers $I = 3$ and $f = 2$ ($\vec{f} = \vec{S} + \vec{I}$), where $\vec{S}$ denotes the total electronic spin. Compared to molecular beam setups, the STIRAP pulse

in ultracold atoms or molecules experiments is orders of magnitude longer (typically tens of microseconds). It therefore can usually resolve any molecular substructure and unambiguously populate any quantum state as long as the selection rules allow for it.

The molecules reside within the lowest Bloch band of the optical lattice, which consists of a superposition of three linearly polarized standing light waves in the x, y, and z directions with polarizations orthogonal to each other, see Fig. 5.1(a). Each lattice beam has a wavelength of $\lambda = 1064.5$ nm, a linewidth of a few kilohertz, and relative intensity fluctuations of less than 10^{-3}. In order to avoid interference effects, the frequencies of the standing waves are offset by about 100 MHz relative to each other. At the location of the atomic sample, the waists ($1/e^2$ radii) of the lattice beams are about 130 µm and the maximum available power per beam is about 3.5 W.

5.4 Determination of the molecular polarizabilities

We now independently determine the three molecular polarizabilities $\alpha^{(i)}(i = x, y, z)$, which, according to Eq. (5.2), are directly linked to the degrees of molecular alignment $\langle A_i^2 \rangle$. Using Eq. (5.1), we need a measurement of both the lattice depth U_i and the field amplitude $E_{0,i}$. In order to measure U_i we consider a lattice beam with polarization $\hat{\varepsilon}_i$ (see Fig. 5.1). We perform modulation spectroscopy [40, 109] in which the intensity of this lattice beam is sinusoidally modulated by a few percent for a time of 10 modulation periods. A resonant modulation frequency drives transitions from the lowest Bloch band to the second excited band [see inset in Fig. 5.2(c)] giving rise to losses. At the end of each experimental cycle, the fraction N/N_0 of molecules remaining is measured. For this purpose, the atom signal is detected via absorption imaging after reversing the STIRAP and dissociating the molecules using a magnetic field sweep across the Feshbach resonance. By comparing the resonant transition frequency to a band-structure calculation of the sinusoidal lattice, the lattice depth U is determined.

Figure 5.2 shows excitation spectra after modulation for vibrational ground state molecules in states $|0,0\rangle$ and $|2,0\rangle$ as well as for weakly bound Feshbach molecules at a magnetic field of $B = 1000$ G. For each measurement, we determine the center of the excitation resonance using a Lorentzian fit. For technical reasons the modulation strength varied between the three lattice directions (6%, 5%, and 2% peak-to-peak intensity modulation for $\hat{\varepsilon}_x$, $\hat{\varepsilon}_y$, and $\hat{\varepsilon}_z$, respectively), leading to different depths of the resonances. We have checked that this variation does not affect the resonance positions. As the light field amplitudes $E_{0,i}$ for the three lattice directions are similar, we observe that for nonrotating molecules in $|0,0\rangle$ [Fig. 5.2(a)], the resonant excitation frequencies in the three different modulation directions are also very similar. For the case of $|2,0\rangle$ [Fig. 5.2(b)], however, the lattice depth for $\hat{\varepsilon}_z$ polarization is much higher than for $\hat{\varepsilon}_x$ and $\hat{\varepsilon}_y$, indicating an alignment of molecules along the z direction.

In order to precisely determine the electric field amplitudes $E_{0,i}$ we perform lattice modulation measurements with weakly bound Feshbach molecules for the same experimental parameters as for deeply bound molecules [Fig.5.2(c)]. In this way, the polarizability can be determined independently of the exact beam parameters. We use $\alpha_{\text{Rb+Rb}}^{(i)} = 4|U_i|/E_{0,i}^2$ and the fact that the polarizability of Feshbach molecules, $\alpha_{\text{Rb+Rb}}$, is isotropic and known to be twice the atomic
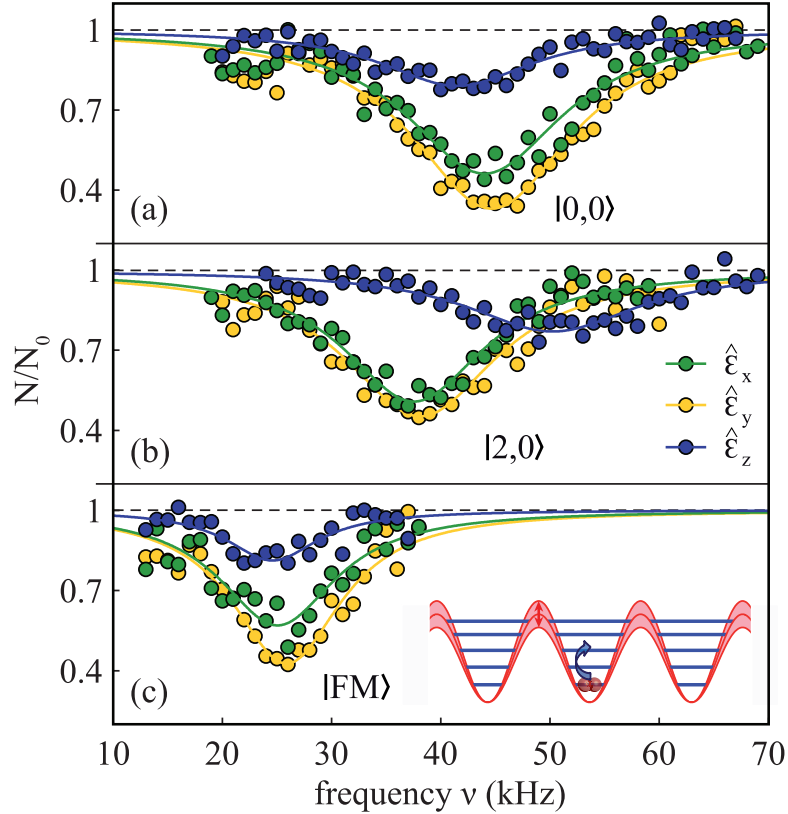
Figure 5.2: Modulation spectroscopy. The general scheme is sketched in the inset in (c) illustrating the resonant modulation of the lattice depth in one direction. The data show resonances for molecules in states $|0,0\rangle$ (a) and $|2,0\rangle$ (b), as well as for Feshbach molecules $|\text{FM}\rangle$ (c) at $B = 1000$ G. We measured the fraction of remaining molecules N/N_0 as a function of the modulation frequency ν for the three different lattice directions. Here, $\hat{\varepsilon}_x$, $\hat{\varepsilon}_y$, and $\hat{\varepsilon}_z$ indicate the electric field of which the amplitude has been modulated [cf. Fig. 5.1(a)]. Each data point is the average of between five and 25 repetitions of the experiment (for a given molecular state and direction i the number of repetitions is constant). The statistical error of each data point is typically $\pm(0.05 - 0.15)$. Solid lines correspond to Lorentzian fits.

polarizability $\alpha_{\text{Rb}} = (693.5 \pm 0.9)$ a.u. [149]. Here, 1 a.u. $= 4\pi\varepsilon_0 a_0^3 = 1.649 \times 10^{-41}$ Jm^{2}V^{-2}, where a_0 denotes the Bohr radius and ε_0 is the vacuum permittivity. As can be seen from the obtained excitation resonances [Fig. 5.2(c)], the absolute lattice depth and thus the electric field amplitude slightly varies in the three directions. Of course, according to Eq. (5.1), this variation drops out when determining the polarizabilities of the deeply bound molecules.

Figure 5.3 shows measured polarizabilities $\alpha^{(i)}$ of molecules initially prepared in state $|0,0\rangle$ or $|2,0\rangle$ at $B = 1000$ G. After production we adiabatically lower the magnetic field from $B =$
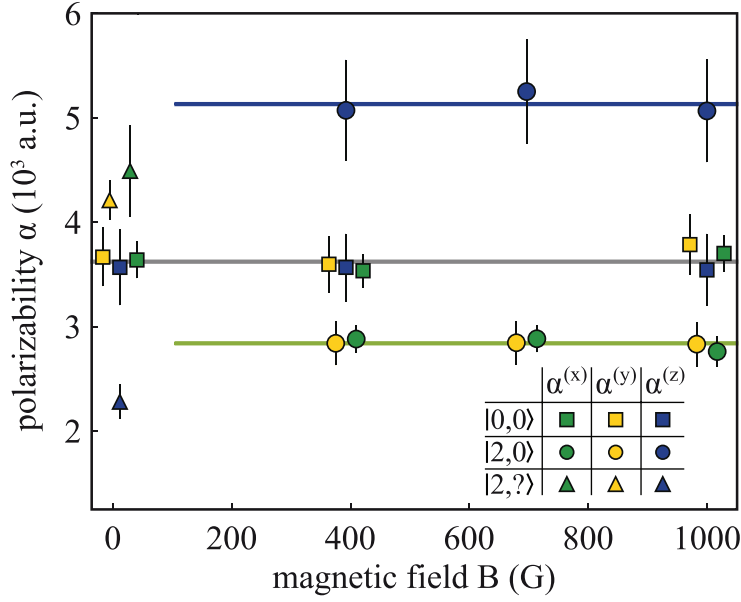
Figure 5.3: Polarizabilities $\alpha^{(i)}(i=x,y,z)$ of the Rb$_2$ triplet molecules for the rotational states $|R=0, m_R=0\rangle$ (squares), $|2,0\rangle$ (circles), and an unknown state $|2,?\rangle$ (triangles) for different magnetic fields $B = 1000$ G, 700 G, 400 G, and about 10 G. For better visibility overlapping data points are shifted slightly with respect to each other in the horizontal direction. The error bars are given by the uncertainty of the Lorentzian fits in the amplitude modulation spectra (cf. Fig. 5.2). Horizontal lines indicate the mean values of the measured polarizabilities for the states $|0,0\rangle$ and $|2,0\rangle$.

1000 G to 700 G, 400 G, and about 10 G. At each B field we measure $\alpha^{(i)}$ in all three directions. As already seen in Fig. 5.2(a) the nonrotating state $|0,0\rangle$ exhibits an isotropic polarizability $\alpha^{(i)}$. This isotropy is reflected in the spherical symmetry of the rotational wave function for the molecular axis, $Y_{0,0}$, which is simply a constant. Correspondingly, the calculated expectation value $\langle A_i^2 \rangle$ is 1/3 for all directions. Thus, Eq. (5.2) simplifies to the useful relation $3\alpha^{(i)} = \alpha_\parallel + 2\alpha_\perp$.

Next, we study $\alpha^{(i)}$ for state $|2,0\rangle$ down to $B = 400$ G. As already observed in Fig. 5.2(b) there is a clear anisotropy of $\alpha^{(i)}$. The polarizabilities in the x and y directions are identical, but differ from the one in the z direction. We check for the consistency of the measurements. From Eq. (5.2) and $\langle A_x^2 \rangle + \langle A_y^2 \rangle + \langle A_z^2 \rangle = 1$ follows $\sum_i \alpha^{(i)} = \alpha_\parallel + 2\alpha_\perp$, which should be equal to $3\alpha^{(i)}$ of state $|0,0\rangle$. Our experimental data fulfill this relation to within 1%. The fact that the polarizability $\alpha^{(i)}$ is independent of B both for $|0,0\rangle$ and $|2,0\rangle$ highlights that the alignment of the molecular axis is not forced by the magnetic field. It merely sets the direction of the quantization axis, stabilizing the spin polarization of the molecules.

We can use the measurements of $\alpha^{(i)}$ for state $|2,0\rangle = Y_{2,0}(\theta,\phi)$ to determine $\alpha_\parallel$ and

$\alpha_\perp$ from Eq. (5.2). Using Eq. (5.3) we calculate $\langle A_x^2 \rangle = \langle A_y^2 \rangle = 0.2381$ and $\langle A_z^2 \rangle = 0.5238$ [cf. Fig. 5.1(b)]. We obtain a set of two independent equations (the equations for the x and y directions are nominally identical), which can be uniquely solved, resulting in $\alpha_\parallel = (8.9 \pm 0.9) \times 10^3$ a.u. and $\alpha_\perp = (0.9 \pm 0.4) \times 10^3$ a.u. These values are in good agreement with *ab initio* calculations, which give $\alpha_\parallel = (7.5 \pm 1.2) \times 10^3$ a.u. and $\alpha_\perp = (1.0 \pm 0.1) \times 10^3$ a.u. (M. Tomza and R. Moszyński (private communication), [154]). The large difference of $\alpha_\parallel$ and $\alpha_\perp$ can be explained as mainly arising from the different lattice laser detuning with respect to the relevant electronic transitions[34].

5.5 Using the method to gain information about unknown quantum states

The novel method to probe the alignment of the molecular axis can be used to gain information about unknown quantum states and therefore has possible future applications in spectroscopy. As an example, we now look at the data points (triangles) at 10 G. Although these data are also obtained by first preparing state $|2, 0\rangle$ at 1000 G and subsequently ramping down the B field, they look quite different from the ones at 400, 700, or 1000 G discussed previously. All polarizabilities change considerably and $\alpha^{(z)}$ is now smaller than $\alpha^{(x)}$ and $\alpha^{(y)}$, but the sum rule $\sum_i \alpha^{(i)} = \alpha_\parallel + 2\alpha_\perp$ still holds. Apparently the molecular quantum state undergoes a drastic change at low B fields when sweeping the magnetic field. Since $\alpha_\parallel$ and $\alpha_\perp$ are known, we can directly extract the degrees of alignment from the measured polarizabilities $\alpha^{(i)}$ according to Eq. (5.2). From a simultaneous fit, assuming $\langle A_x^2 \rangle = \langle A_y^2 \rangle$ and using the normalization $\langle A_x^2 \rangle + \langle A_y^2 \rangle + \langle A_z^2 \rangle = 1$, we obtain $\langle A_{x,y}^2 \rangle = 0.42$ and $\langle A_z^2 \rangle = 0.16$. Coupled channel calculations show that in the direct vicinity of the initial state $|2, 0\rangle$ ($f = 2$, $I = 3$, $S = 1$) only rotational levels with $R = 2$ are present (E. Tiemann, private communication). The measured values closely match the calculated degrees of alignment $\langle A_{x,y}^2 \rangle = 0.4286$ and $\langle A_z^2 \rangle = 0.1429$ of the states $|2, \pm 2\rangle$, whereas no agreement is found for $|2, \pm 1\rangle$ ($\langle A_{x,y}^2 \rangle = 0.2857$ and $\langle A_z^2 \rangle = 0.4286$). How the change in the molecular quantum state comes about is currently still an open question and necessitates further investigation.

5.6 Conclusion

In conclusion, we have studied the axis alignment of trapped, ultracold, nonpolar molecules in two predetermined rotational quantum states. For this purpose, we introduced a novel method that relies on the measurement of the polarizability of the molecules along the three spatial axes. Furthermore, we have demonstrated how to apply this method to spectroscopically investigate unknown molecular quantum states.

We have verified that sizeable alignment or antialignment (i.e., $\langle A_i^2 \rangle < 1/3$) of the

---

[34]See Supplemental Material of [46] given in section 5.8 and at `http://link.aps.org/supplemental/10.1103/PhysRevLett.113.233004`, respectively, which includes potential energy curves from Ref. [121], for a qualitative explanation of the large difference of the molecular polarizabilities $\alpha_\parallel$ and $\alpha_\perp$.

molecular axis can be achieved with spin polarized samples even without any alignment forces. We determined the dynamic polarizabilities $\alpha_{\parallel} = (8.9 \pm 0.9) \times 10^3$ a.u. and $\alpha_{\perp} = (0.9 \pm 0.4) \times 10^3$ a.u. for the Rb$_2$ vibrational ground state of the $a^3\Sigma_u^+$ potential at a wavelength of 1064.5nm. The fact that $\alpha_{\parallel}$ and $\alpha_{\perp}$ are so different implies that the lattice depth strongly depends on the rotational level. This can be used for filtering, i.e., state selection of molecules. The ability to prepare well-defined rotational states and the successful probing of their alignment paves the way for collisional studies of stereochemical processes. Indeed, we are currently investigating collisions between aligned molecules in a quasi-1D geometry.

5.7 Acknowledgements

5.8 Supplemental Material

Owing to selection rules for π- and σ-transitions, $\alpha_{\parallel}$ ($\alpha_{\perp}$) is linked to $\Sigma-\Sigma$ ($\Sigma-\Pi$) transitions. As can be seen from Fig. 5.4, the detuning of our lattice laser from the Franck-Condon point on the $d^3\Pi_g$ potential curve is about 6 times larger than from that of the $c^3\Sigma_g^+$ potential curve, explaining the large difference of $\alpha_{\parallel}$ and $\alpha_{\perp}$ to first order.
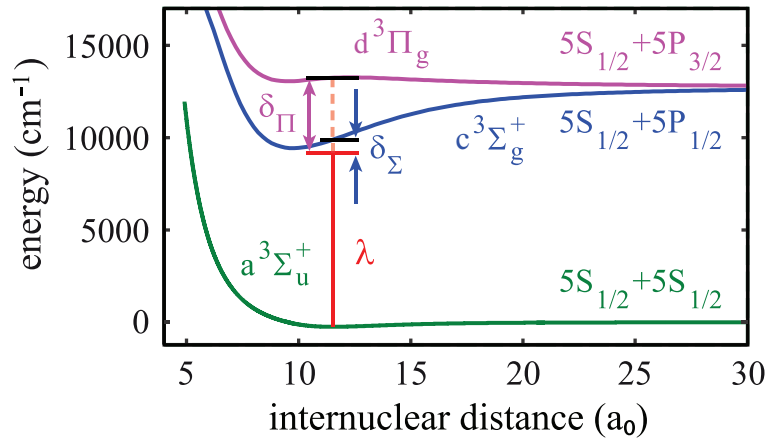
Figure 5.4: Detunings δ_Σ and δ_Π of the lattice laser at $\lambda = 1064.5$nm from the two most relevant transitions, $a^3\Sigma_u^+ - c^3\Sigma_g^+$ and $a^3\Sigma_u^+ - d^3\Pi_g$, that determine the polarizabilities $\alpha_{\parallel}$ and $\alpha_{\perp}$, respectively. The energy reference is given by the asymptote of the $a^3\Sigma_u^+$ potential. The potential curves are taken from [121].

5.9 Additional information concerning small magnetic fields

As described in section 5.5, for the rotationally excited state $R = 2$, we observe a change of the molecular quantum number m_R when decreasing the magnetic field to a low value of about 10 G. In view of the question how this comes about, I want to discuss two aspects in the following, albeit a final statement is not possible at the moment.

First of all, I want to point out a technical issue concerning the ramping of the magnetic field down to very low values. In our setup, B is generated by the two quadrupole coils (cf. Fig. 2.3) operated in Helmholtz configuration and points antiparallel to the gravitational force. By adjusting the current I_{QC} through these coils appropriately, B is set to the desired value. Unfortunately, we also have a permanent offset magnetic field of several gauss, which approximately points orthogonal to the field of the quadrupole coils (see also section 2.2). Hence, the quantization axis changes by about 90°, when I_{QC} approaches zero. However, the used ramping speed is so low, that all angular momenta of the molecule should adiabatically follow the magnetic field direction, i.e., they should not change their relative orientation with respect to the quantization axis. Therefore, one has to relabel the lattice directions for comparing results obtained with high and low magnetic fields. Nevertheless, it seems to be unlikely that the described effect leads to the observed change of the quantum number m_R.

As the necessity of the offset magnetic field is related to the QUIC trap and the spin preparation (see sections 2.2 and 3.3), it could be turned off once the atoms are associated to Feshbach molecules. Thus, this rather technical problem might in principle be overcome by programming the power supplies responsible for the offset field accordingly. At the moment, these power supplies are not externally controlled, yet. However, an appropriate connection to the experiment control would be one of the next steps.

Second, I want to consider the quantum number m_R at low magnetic fields from a theoretical point of view particularly for the rotationally excited state $R = 2$ ($f = 2$, $I = 3$) of the $v = 0$ manifold of the $a^3\Sigma_u^+$ potential. We performed calculations based on the model described in Ref. [122]. Figures 5.5 and 5.6 show the energies of all hyperfine levels as a function of B for low magnetic fields, together with the corresponding expectation values $\langle m_R \rangle$ and $\langle F \rangle$. Please note that one can clearly distinguish between different m_F states as m_F represents a good quantum number for all relevant magnetic fields. The two figures reveal several features:

- In general, the hyperfine levels approach or even cross each other if the magnetic field is decreased. At $B = 0$ G the total hyperfine structure is within about $100\,\text{MHz} \times h$.

- For $B \lesssim 100\,\text{G}$, m_R is mixed up and consequently not a good quantum number anymore.

- In contrast, at vanishing magnetic fields, F represents a good quantum number, which is not the case for significant values of B.

After the STIRAP transfer that takes place at $B = 1000$ G, the molecules have $m_F = 2$ and $m_R = 0$. This state is indicated by the red curves in Fig. 5.5(a). If we follow the energy level down to low values of B, we find that the expectation value $\langle m_R \rangle$ should change from $\langle m_R \rangle = 0$ to 1. But, the measured degrees of alignment at about $B = 10$ G show the best
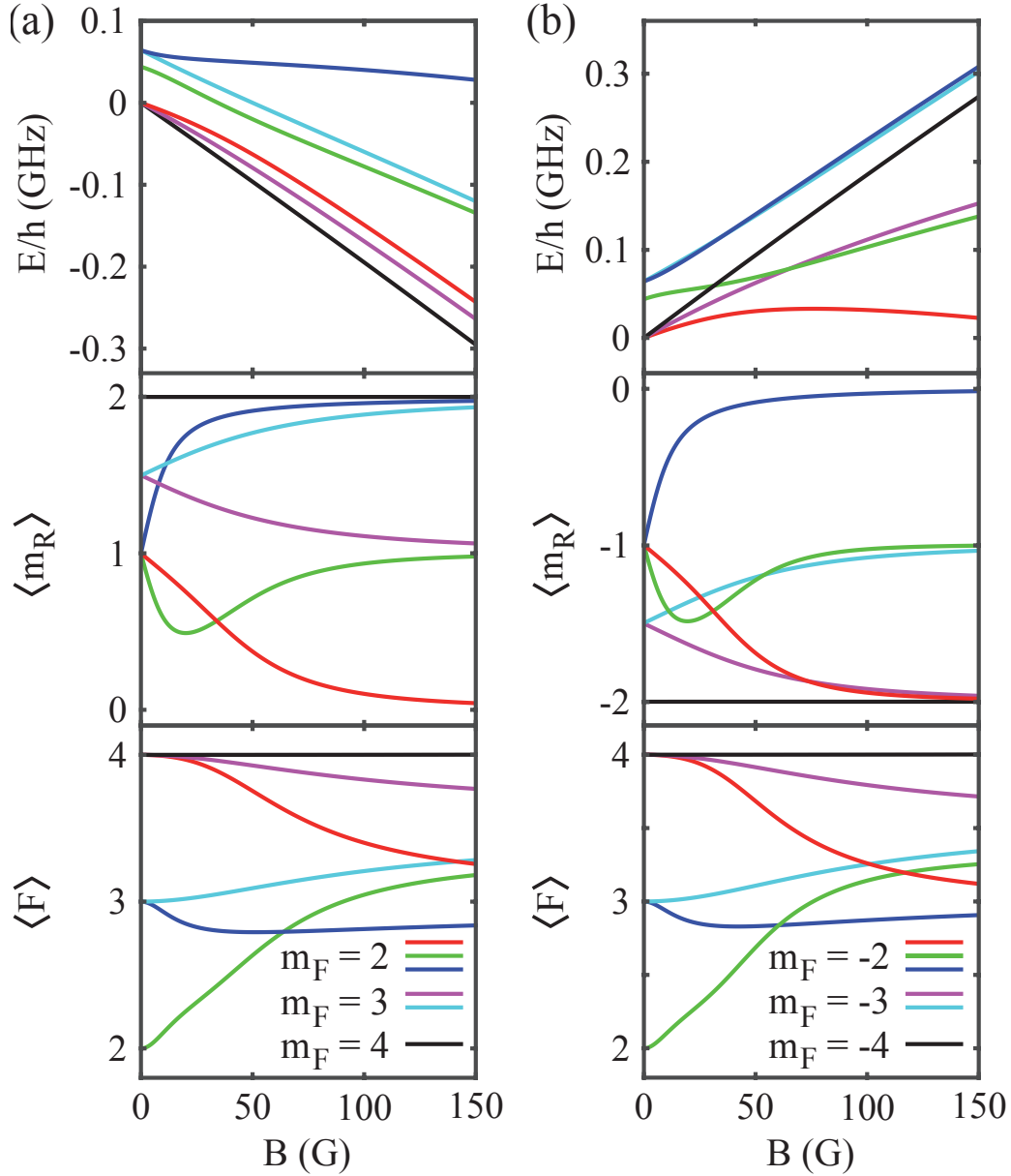
Figure 5.5: Hyperfine levels of the rotationally excited state $R = 2$ within the $v = 0$ manifold of the $a^3\Sigma_u^+$ potential corresponding to $m_F = 2, 3, 4$ (a) and $m_F = -2, -3, -4$ (b). Shown are the energy level structure (upper panel), the expectation values $\langle m_R \rangle$ (middle panel) and the expectation values $\langle F \rangle$ (lower panel) for low magnetic fields B. The energy is given relative to the position of the red curve of (a) at $B = 0$ G. This level is characterized by $m_R = 0$ for high magnetic fields and represents the state in which we initially prepare our molecules. The calculations are based on the model described in Ref. [122].
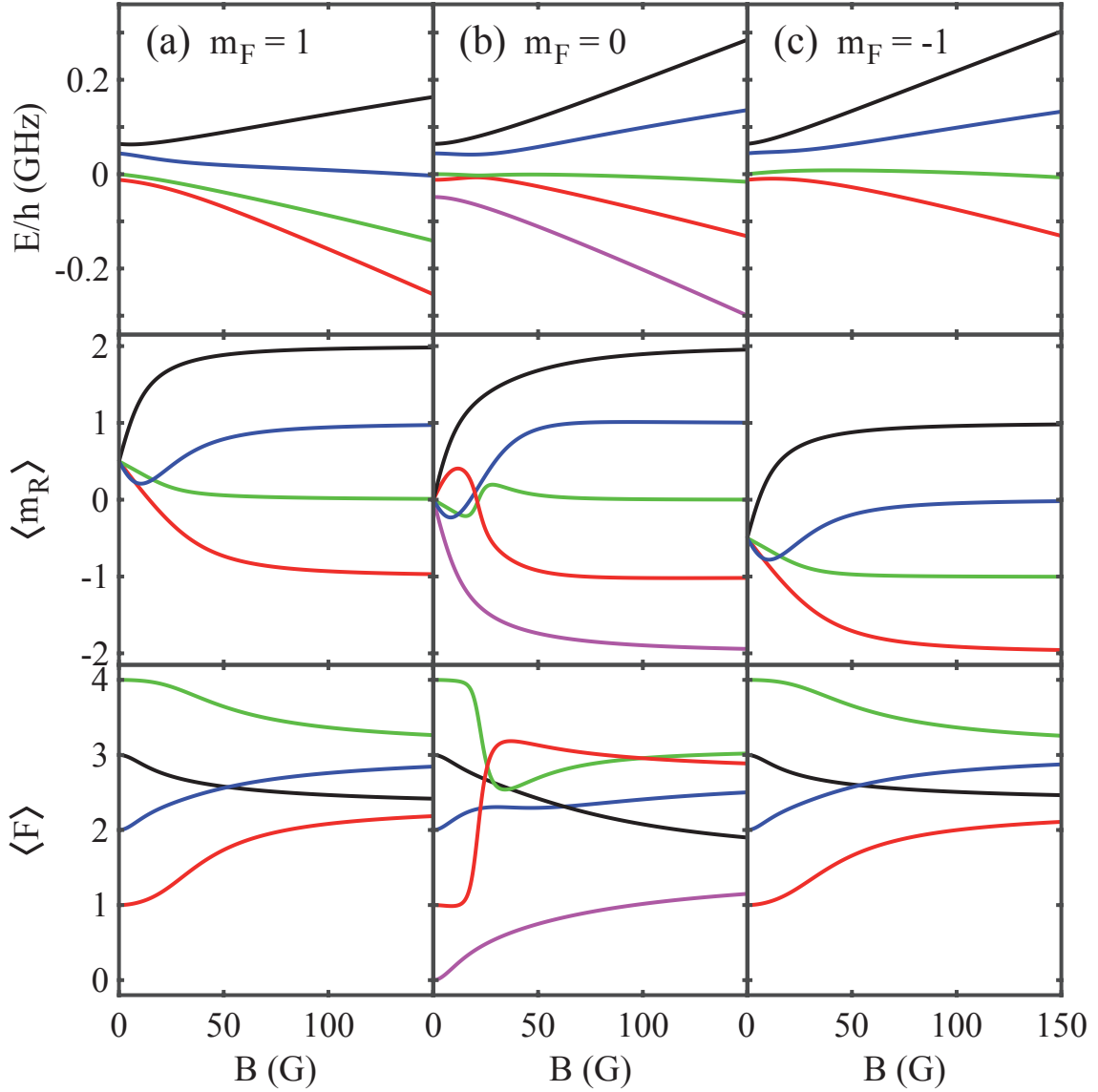
Figure 5.6: Hyperfine levels of the rotationally excited state $R = 2$ within the $v = 0$ manifold of the $a^3\Sigma_u^+$ potential corresponding to $m_F = 1$ (a), $m_F = 0$ (b), and $m_F = -1$ (c). For the parameter denotations and the energy reference see Fig. 5.5. The calculations are based on the model described in Ref. [122].

agreement with the calculated values for states characterized by $m_R = \pm 2$ (see discussion in section 5.5). According to Figs. 5.5 and 5.6, only the energy levels corresponding to ($\langle F \rangle = 4$, $m_F = 4$) and ($\langle F \rangle = -4$, $m_F = -4$) clearly exhibit either $m_R = +2$ or -2 for such low values of B. Therefore, also the quantum number m_F would have to undergo a change as the

dimers are initially prepared in $m_F = 2$. In section 3.10.2, we have discussed that by means of the lattice beams, transfers of molecules between energy levels are possible when ramping the magnetic field. However, a firm statement about the final state of $R = 2$ at about $B = 10$ G and the route towards it is not possible at the moment and necessitates further investigation.

6 Mixing of 0^+ and 0^- Observed in Hyperfine and Zeeman Structure of Ultracold Rb_2 Molecules

arXiv: 1505.00682 (2015)

Markus Deiß, Björn Drews, and Johannes Hecker Denschlag

Institut für Quantenmaterie and Center for Integrated Quantum Science and Technology IQ^{ST}, Universität Ulm, 89069 Ulm, Germany

Eberhard Tiemann

Institut für Quantenoptik, Leibniz Universität Hannover, 30167 Hannover, Germany

We study the combination of hyperfine and Zeeman structure in the spin-orbit coupled $A^1\Sigma_u^+ - b^3\Pi_u$ complex of $^{87}Rb_2$. For this purpose, absorption spectroscopy at a magnetic field around $B = 1000$ G is carried out. We drive optical dipole transitions from the lowest rotational state of an ultracold Feshbach molecule to various vibrational levels with 0^+ symmetry of the $A - b$ complex. In contrast to previous measurements with rotationally excited alkali-dimers, we do not observe equal spacings of the hyperfine levels. In addition, the spectra vary substantially for different vibrational quantum numbers, and exhibit large splittings of up to 160 MHz, unexpected for 0^+ states. The level structure is explained to be a result of the repulsion between the states 0^+ and 0^- of $b^3\Pi_u$, coupled via hyperfine and Zeeman interactions. In general, 0^- and 0^+ have a spin-orbit induced energy spacing Δ, that is different for the individual vibrational states. From each measured spectrum we are able to extract Δ, which otherwise is not easily accessible in conventional spectroscopy schemes. We obtain values of Δ in the range of ± 100 GHz which can be described by coupled channel calculations if a spin-orbit coupling is introduced that is different for 0^- and 0^+ of $b^3\Pi_u$.

6.1 Introduction

The strongly spin-orbit coupled $A^1\Sigma_u^+ - b^3\Pi_u$ complex of alkali-metal dimers has been studied in great detail in recent years, stimulated by the fruitful combination of high-resolution spectroscopy and numerical close-coupled calculations. Various homonuclear (Rb$_2$ [157, 171, 172], Cs$_2$ [173, 174], Na$_2$ [175, 176], K$_2$ [177-180], Li$_2$ [181, 182]) and heteronuclear (NaRb [183, 184], RbCs [185-187], KRb [188], NaCs [189], KCs [190-192], NaK [193-195]) species have been investigated and modeled. Potential energy curves as well as r-dependent spin-orbit-coupling functions were extracted, where r is the internuclear separation. Concerning the hyperfine structure of the $A - b$ state, however, only little experimental data is available so far.

For thermal and thus rotationally excited samples of Na$_2$ and K$_2$ hyperfine structures with line splittings up to hundreds of MHz, characterized by nearly equidistant separations of the energy levels were observed [176, 180]. Such hyperfine structures of the $\Omega = 0$ components of the $A - b$ complex come about owing to the molecular rotation that mixes different Ω components. For the case of low rotational angular momentum J, line splittings of at most a few MHz are expected. Indications of such small hyperfine splittings for $J = 1$ RbCs molecules in state $\Omega = 0$ were reported in Ref. [185], but a detailed analysis was not given.

In this work, we investigate the combined hyperfine and Zeeman pattern of the $A - b$ complex for Rb$_2$ molecules with $J = 1$ observed by exciting an appropriate Feshbach molecular state [see level scheme in Fig.6.1(a)]. Particularly for states, where the main component exhibits $b^3\Pi_u$ 0^+ symmetry, we measure large level spacings of up to 160 MHz. Furthermore, the line pattern is not equally spaced and the overall structure changes strongly from one vibrational level to another. Consequently, our spectra are dominated by a mechanism different from the one discussed previously in the context of fast rotating molecules. In fact, we find that the observed energy level structures corresponding to vibrational states of $b^3\Pi_u$ 0^+ arise from second order hyperfine and Zeeman interaction coupling the 0^+ and 0^- components of $b^3\Pi_u$. More precisely, these two interactions work together in a cooperative way enhancing the effect. By fitting a relatively simple model to our data we extract the initially unknown frequency spacing Δ between 0^- and 0^+ for each vibrational level. This is an important result of our work because the state $b^3\Pi_u$ 0^- is not directly accessible in spectroscopy schemes starting from any singlet or triplet ground state molecular level. Our derived values for Δ systematically deviate by about 90 GHz from predictions of close-coupled channel calculations. We interpret this as a difference in the spin-orbit coupling function for 0^- and 0^+.

This article is organized as follows. In section 6.2, we give an overview of the experimental setup and the spectroscopy scheme. Then, section 6.3 describes the relevant molecular energy states needed for the presentation of our experimental results in section 6.4. In section 6.5 we introduce a simple model that fully explains the characteristics of the observed spectra. Our model calculations are discussed in section 6.6 along with the interpretation of the data and the determination of Δ for the investigated vibrational states of $b^3\Pi_u$. Finally, in section 6.7 we describe the extension of the potential scheme needed for modeling the observations by coupled channel calculations.
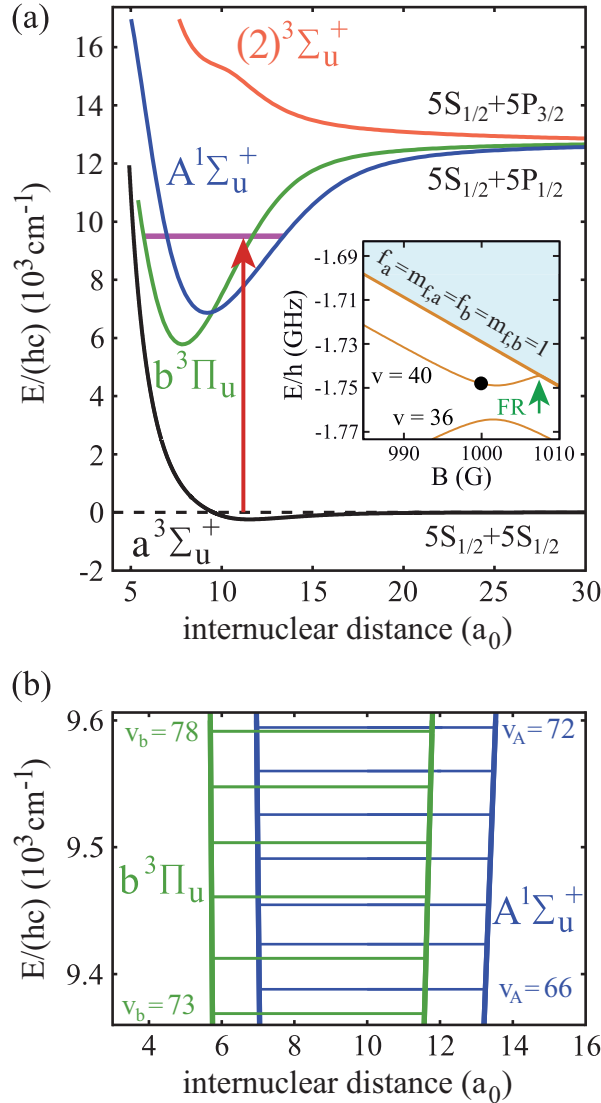
Figure 6.1: (a) Spectroscopy scheme. Weakly bound Feshbach molecules are irradiated by a laser pulse and excited to molecular levels of the $A^1\Sigma_u^+ - b^3\Pi_u$ manifold from where they spontaneously decay to nonobserved states. The potential $(2)^3\Sigma_u^+$ is included because it couples to 0^- of $b^3\Pi_u$ (see text). Furthermore, the inset shows the level structure in the vicinity of the Feshbach resonance (FR). At a magnetic field of $B = 999.9$ G the Feshbach state (indicated by the black circle) is located $1.748\,\mathrm{GHz} \times h$ below the $|f_a = 1, m_{f_a} = 1\rangle + |f_b = 1, m_{f_b} = 1\rangle$ dissociation threshold at $0\,\mathrm{G}$. In (b), the vibrational levels v_A and v_b within the $A^1\Sigma_u^+ - b^3\Pi_u$ 0^+ complex that are relevant for our measurements are depicted. All potential curves are taken from [121], while the energies of v_A and v_b correspond to the calculated values given in [196] (see also tables 6.1 and 6.2).

6.2 Experimental setup

We carry out our experiments with a pure sample of about $N_0 = 3 \times 10^4$ weakly bound $^{87}Rb_2$ Feshbach molecules which have both $X^1\Sigma_g^+$ and $a^3\Sigma_u^+$ character. The setup and the molecule preparation scheme are described in detail in Refs. [53, 124]. Therefore, they are just briefly presented here. Initially a BEC or ultracold thermal cloud of spin-polarized ^{87}Rb atoms with total angular momentum $f = 1$, $m_f = 1$ is loaded into a rectangular, 3D optical lattice at a wavelength of $\lambda = 1064.5$ nm, which is formed by a superposition of three linearly polarized standing light waves with polarizations orthogonal to each other. By slowly crossing the magnetic Feshbach resonance (FR) at 1007.4 G from high to low fields, pairs of atoms in doubly occupied lattice sites are converted into weakly bound molecules. Afterwards, the magnetic field is set to 999.9 ± 0.1 G, where we perform the spectroscopy. In order to get rid of remaining atoms, a combined microwave and light pulse is applied which removes them from the lattice. We end up with a pure ensemble of molecules that resides in the lowest Bloch band of the optical lattice with no more than a single dimer per lattice site. The lattice depth for the molecules with respect to each of the standing light waves of the optical lattice is about $64E_R$ where $E_R = h^2/(2m\lambda^2)$ represents the recoil energy. Here, m denotes the mass of the molecule and h is Planck's constant. Since at these lattice depths the tunneling rate is very low, intermolecular collisions are strongly suppressed, and we measure lifetimes on the order of 1 s.

Figure 6.1(a) shows the spectroscopy scheme. The Feshbach molecule ensemble is irradiated by a rectangular light pulse for a duration τ of typically a few ms. At the location of the molecular sample the beam waist is about 1.1 mm. For the observed spectra, we used laser powers of tens or hundreds of μW. The light propagates orthogonally to the quantization axis which is defined by the applied magnetic field that points in vertical direction. By using a half-wave plate we can choose the light being polarized either in the horizontal plane or in the vertical axis giving rise to σ transitions (i.e., σ^+ and σ^-) or π transitions. Molecules, that are resonantly excited from the Feshbach state to a level of the $A - b$ complex, are in general lost due to subsequent fast decay to nonobserved states. We measure the remaining fraction N/N_0 of Feshbach dimers. For this purpose, we dissociate the molecules by ramping back over the Feshbach resonance and detect the corresponding atom number via absorption imaging.

The spectroscopy is performed at wavelengths between 1042 and 1068 nm (corresponding to about $9360 - 9600$ cm^{-1}) using a grating-stabilized cw diode laser that has a short-term linewidth of ~ 100 kHz. This laser is frequency-stabilized to a Fizeau interferometer wavemeter (High Finesse WS7), with an update rate of about 10 Hz. As the laser frequency drifts between updates, we obtain a frequency stability of $\pm(2 - 5)$MHz. The wavemeter is calibrated to an atomic ^{87}Rb reference signal at 780 nm in intervals of minutes. It has a specified absolute accuracy of 60 MHz, but the accuracy is on the MHz level for difference frequency determinations within several hundred MHz. Furthermore, over a period of several months we checked the frequency readings of the wavemeter for the same molecular transitions and did not find deviations of more than ±10 MHz. This demonstrates the good reproducibility of the wavemeter readings in connection with the calibration mentioned above.

6.3 Relevant states

6.3.1 Feshbach molecules

The Rb_2 Feshbach molecules in our experiment are weakly bound dimers with both singlet and triplet character, i.e., the selected state is a mixture of $X^1\Sigma_g^+$ and $a^3\Sigma_u^+$ ([122, 124]). However, only the $X^1\Sigma_g^+$ component allows to drive transitions to the $A - b$ complex because for an electric dipole transition the u/g symmetry has to change and the $A - b$ complex has u symmetry. According to coupled channel calculations, at a magnetic field of $999.9\,\mathrm{G}$ the singlet component, mainly characterized by $S = L = R = 0$, $I = 2$, $m_I = 2$, $F = 2$, contributes 16% to the Feshbach state which has the exact quantum numbers $m_F = 2$ and parity $+$. Here, S, L, R, I and F ($\vec{F} = \vec{R} + \vec{L} + \vec{S} + \vec{I}$) denote the quantum numbers of the total electronic spin, the total orbital angular momentum, the rotation of the atom pair, the total nuclear spin, and the total molecular angular momentum, respectively. Furthermore, m_I and m_F represent the corresponding projections onto the quantization axis. Consequently, the singlet component of the Feshbach molecules has $J = 0$ ($\vec{J} = \vec{R} + \vec{L} + \vec{S}$).

The inset of Fig. 6.1(a) shows the molecular level structure in the vicinity of the Feshbach resonance. Throughout the present work, all excitation energies are given with respect to the $|f_a = 1, m_{f_a} = 1\rangle + |f_b = 1, m_{f_b} = 1\rangle$ atomic dissociation limit at $0\,\mathrm{G}$. Note, its energy is $8.543\,\mathrm{GHz} \times h$ below the atomic dissociation limit when hyperfine interaction is ignored. At a magnetic field of $999.9\,\mathrm{G}$ the Feshbach state is located at $-1.748\,\mathrm{GHz} \times h$. Here, the main contribution is determined by the Zeeman shift of the atom pair $|f_a = 1, m_{f_a} = 1\rangle + |f_b = 1, m_{f_b} = 1\rangle$. The molecular binding energy is only about $20\,\mathrm{MHz} \times h$ with respect to this threshold.

6.3.2 $A^1\Sigma_u^+ - b^3\Pi_u$ complex

Spin-orbit interaction leads to a mixing of the states $A^1\Sigma_u^+$ and $b^3\Pi_u$ forming the $A - b$ complex. In a simple approach this mixing comes about in two steps. First, due to spin-orbit coupling the state $b^3\Pi_u$ splits up into three components, $\Omega = 0, 1, 2$. The quantum number Ω denotes the projection of the sum of all electronic angular momenta onto the internuclear axis and equals the projection of the molecular angular momentum J on the same axis. For Rb_2 the relative separation of the three terms is about $80\,\mathrm{cm}^{-1}$, as mainly determined by the atomic spin-orbit splitting of Rb in its 5^2P state. At this stage, the $b^3\Pi_u$, $\Omega = 0$ state has two degenerate components, 0^+ and 0^-. Second, spin-orbit coupling mixes $A^1\Sigma_u^+$ (i.e., 0^+ symmetry) and $b^3\Pi_u$ 0^+, whereas the $b^3\Pi_u$ 0^- component couples to $(2)^3\Sigma_u^+$ 0^- [see Fig. 6.1(a)]. As a consequence of the repulsive interactions 0^+ and 0^- of $b^3\Pi_u$ are separated from each other, which is referred to as Λ-type splitting [197]. This effect is crucial for the interpretation of the observations of the present work.

The vibrational levels of the $A - b$ states relevant to our measurements are illustrated in Fig. 6.1(b). The levels with dominant triplet (singlet) character are indicated by vibrational quantum numbers v_b (v_A). Moreover, tables 6.1 and 6.2 list the numerical values for the term energies and the b state admixtures calculated by Drozdova *et al.* [157] and taken from [196].

v_A	p_b [%]	$E_{\mathrm{calc}}/(hc)$ [cm^{-1}]	$E_{\mathrm{exp}}/(hc)$ [cm^{-1}]	ε [10^{-3} cm^{-1}]	δ [MHz]
66	15.60	9388.005	9387.9967	8.3	-2
67	28.50	9423.589	9423.5794	9.6	
68	23.21	9454.571	9454.5652	5.8	
69	7.66	9491.049	9491.0451	3.9	-2
70	10.82	9525.742	9525.7346	7.4	
72	39.36	9594.454	9594.4485	5.5	-22

Table 6.1: Comparison of calculated (E_{calc}) and measured (E_{exp}) level energies for various vibrational levels v_A of the $A^1\Sigma_u^+$ state with $J = 1$. All level energies E_{exp} are observed with π-polarized light. The column $\varepsilon = (E_{\mathrm{calc}} - E_{\mathrm{exp}})/hc$ gives the difference of the measured and predicted values. Furthermore, the parameter p_b denotes the admixture of the $b^3\Pi_u$ potential and δ represents the measured frequency difference between the σ and the π resonance. For the case of $v_A = 67$, 68 and 70 we only performed spectroscopy using π-polarized light and therefore δ was not determined. The values for p_b and E_{calc} are taken from [196].

v_b	p_b [%]	$E_{\mathrm{calc}}/(hc)$ [cm^{-1}]	$E_{\mathrm{exp}}/(hc)$ [cm^{-1}]	ε [10^{-3} cm^{-1}]	Δ [GHz]
73	82.70	9368.758	9368.7480	10.0	$81.8^{+10.6}_{-8.5}$
74	69.59	9412.519	9412.5122	6.8	$104.5^{+23.9}_{-16.4}$
75	73.80	9460.874	9460.8718	2.2	$-19.7^{+0.6}_{-0.6}$
76	88.37	9503.516	9503.5040	12.0	$40.0^{+2.2}_{-2.0}$
78	58.25	9591.479	9591.4721	6.9	$36.4^{+3.4}_{-2.9}$

Table 6.2: Comparison of calculated (E_{calc}) and measured (E_{exp}) level energies for various vibrational levels v_b of the $b^3\Pi_u$ 0^+ state with $J = 1$, analogous to table 6.1. The parameter Δ is the splitting of the $0^\pm$ components as determined by fitting our theoretical model to the measured spectra (see section 6.6).

The calculation is based on a two-potential approach considering $A^1\Sigma_u^+$ and $b^3\Pi_u$ ($\Omega = 0^+, 1, 2$). The mixing is described by the parameter p_b, which represents the probability of finding the vibrational level in the electronic state b. Consequently, for the A state the corresponding parameter is given by $p_A = 1 - p_b$. All other admixtures like $\Delta\Omega = 1$ are negligible in our cases. Our spectroscopy scheme addresses only the A component of a vibrational level of the $A - b$ manifold. Moreover, only states with angular momentum $J = 1$ and negative parity can be observed, because the electronic singlet component of the Feshbach molecule has the quantum number $J = 0$ and positive total parity.

6.4 Experimental observations

6.4.1 Spectra of A levels

We first discuss the data for levels with mainly $A^1\Sigma_u^+$ character. Six different vibrational states ($v_A = 66$ to 70 and 72) have been investigated. The obtained spectra for $v_A = 66$ to 70 look very similar. Figure 6.2(a) shows the recording for $v_A = 66$ as an example. Two resonance dips are visible, one being the π transition ($\Delta m_F = 0$), while the other one is the σ transition
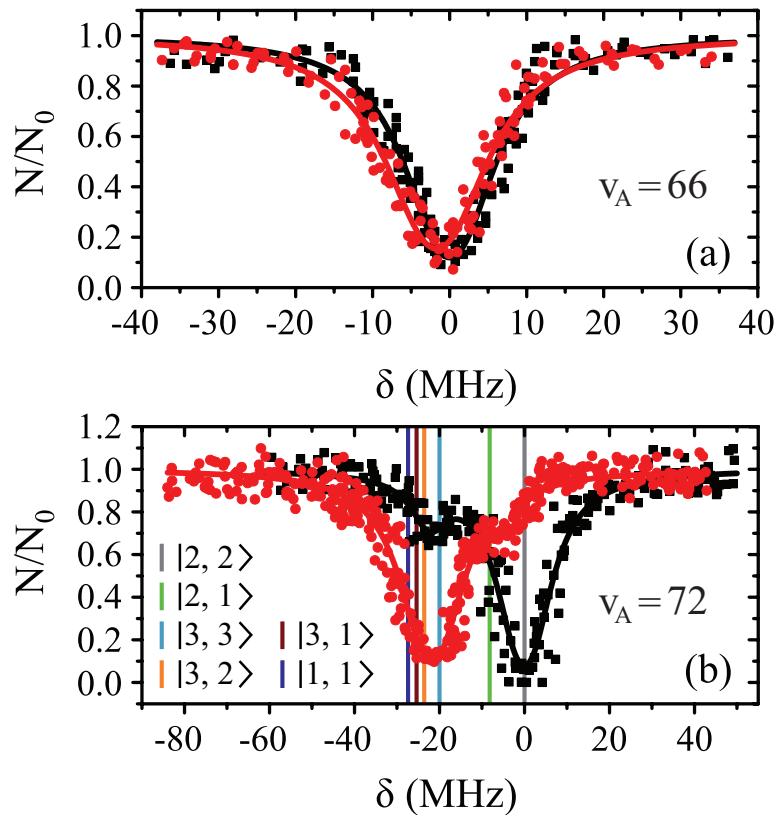

Figure 6.2: Loss resonances for excitation of molecules from the Feshbach state to vibrational levels $v_A = 66$ (a) and $v_A = 72$ (b) of the $A^1\Sigma_u^+$ potential obtained with π-polarized light (black squares) and σ-polarized light (red circles). Shown is the fraction N/N_0 of remaining Feshbach dimers dependent on the detuning δ, where $\delta = 0$ is at the resonance frequency of the strong π transition. The corresponding offset energies are listed in table 6.1. Solid lines are fits of the function e^{-KL} to the data (see section 6.4.1). For a given vibrational quantum number v_A the measurements with π- and σ-polarized light are performed using the same laser intensities and pulse lengths. Colored vertical lines in part (b) indicate the frequency positions of the levels $|F', m_F'\rangle$ resulting from our model calculations (see section 6.6).

($\Delta m_F = \pm 1$). Within the measurement uncertainty of a few MHz both resonances are located on top of each other and Zeeman or hyperfine splitting is not observed. We determine the transition frequencies from fits to the data using the function e^{-KL}, where the amplitude K is a free fitting parameter and L represents a Lorentzian. Typically, the obtained transition linewidths (FWHM) are on the order of $10 - 20\,\mathrm{MHz}$.

In table 6.1 the absolute energies of states v_A derived from the π resonances are summarized and compared to theoretical predictions. The admixing parameter p_b and E_{calc} are taken from Ref. [196]. Since the calculations were originally given with respect to the potential minimum of $X^1\Sigma_g^+$, for the comparison to our experimental results, we added the electronic term energy $T_e^X = -3993.5928(30)\,\mathrm{cm}^{-1}/(hc)$ of $X^1\Sigma_g^+$ [122] and the hyperfine shift of $+8.543\,\mathrm{GHz} \times h/c$, where c is the speed of light. The overall agreement between the theoretical and experimental data is within the uncertainty of the theoretical predictions of $0.01\,\mathrm{cm}^{-1}/(hc)$ (corresponding to $300\,\mathrm{MHz} \times h$). Noticeably, the calculated values are systematically higher by several $10^{-3}\,\mathrm{cm}^{-1}$ compared to our measurements. Besides a possible systematic uncertainty within the theoretical model, these deviations can also arise from the limited accuracy of our wavemeter and the uncertainty of the energy T_e^X.

In contrast to the states $v_A = 66$ and 69, where both, the π and the σ transition occur at the same frequency within the measurement uncertainty, $v_A = 72$ shows a significant splitting [cf. Fig. 6.2(b)]. This is due to the fact that the admixing of the b state is relatively large ($p_b \approx 40\%$, see table 6.1) and a $b^3\Pi_u$ 0^- level is located energetically close-by. The level $v_A = 72$ significantly exhibits the characteristics of $b^3\Pi_u$ 0^+, which will be discussed in the following sections.

6.4.2 Spectra of b levels

Our spectroscopic data on states with mainly triplet character, i.e., $p_b > 50\%$, are shown in Fig. 6.3. For all investigated vibrational quantum numbers $v_b = 73$ to 76 and 78 we only clearly observe a single resonance dip when using π-polarized light. Contrary to that, the scans related to σ polarization reveal 2 or 3 resonance features of which some might have an unresolved substructure. In each spectrum, the σ transitions are well separated from the π transition. We therefore choose the π resonance as a local reference to which we assign the frequency $\delta = 0$ in the figures.

At first sight the spectra for $v_b = 73$ to 76 and 78 might look somewhat irregular. For different vibrational levels v_b the number of transitions, their splittings, and their relative intensities vary. In addition, the splittings for a given v_b are not equidistant as mentioned earlier for high J. However, closer inspection reveals that all these spectra are characterized by a similar pattern. To show this, we arrange the spectra in the order $v_b = 74, 73, 78$ and 76 [Fig. 6.3(a)-(d)] corresponding to their respective splitting magnitude. In each spectrum the σ lines are located at $\delta > 0$. There is always one weak resonance next to the π transition and one strong resonance feature at larger δ. For $v_b = 76$, where the total splitting is very large, the resonance dip at $\delta \sim 90\,\mathrm{MHz}$ seems to split up into two or more lines. Due to the limited resolution of about $5\,\mathrm{MHz}$ in our experiment we cannot clearly resolve the individual resonance
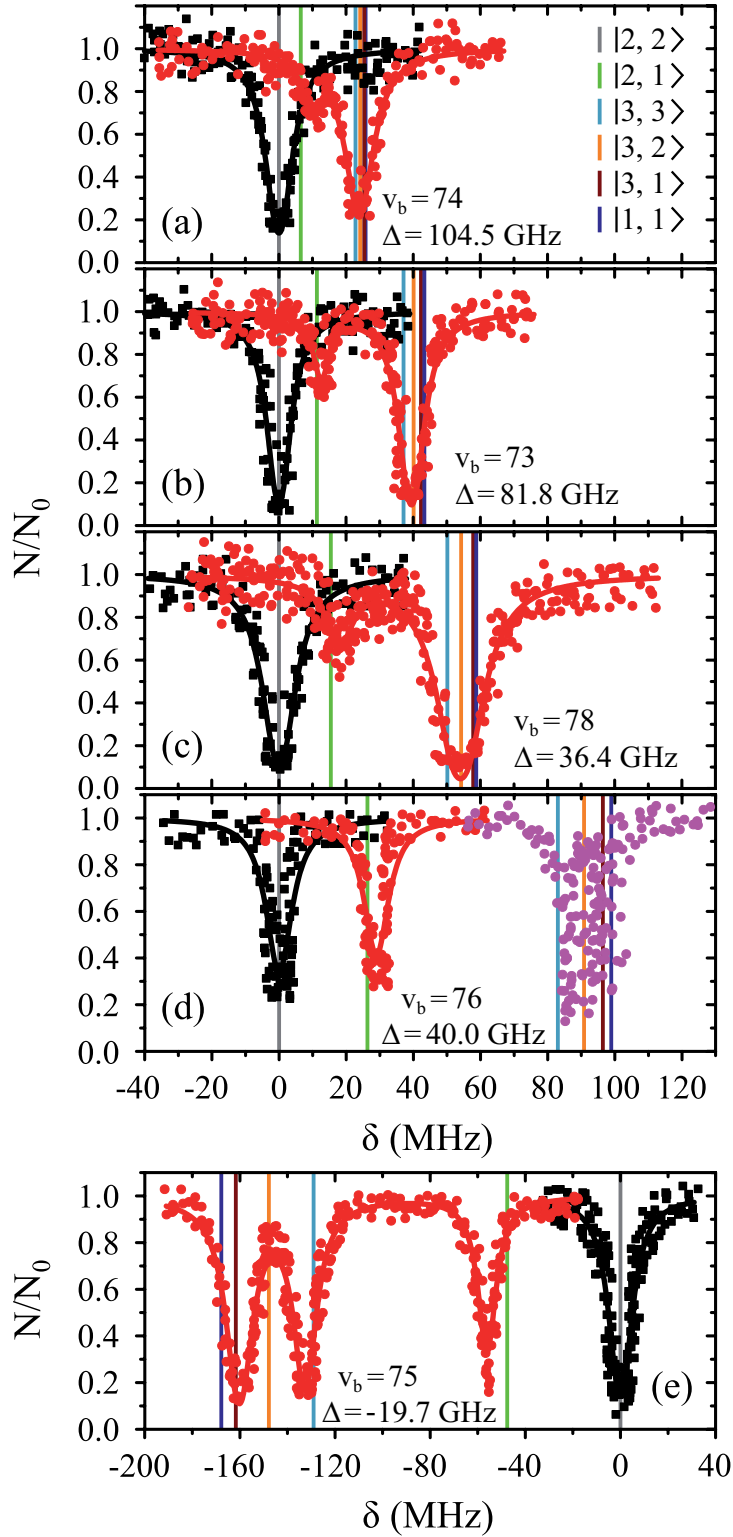
Fig. 6.3: Loss spectra for excitation of molecules from the Feshbach state to vibrational levels $v_b = 74$ (a), $v_b = 73$ (b), $v_b = 78$ (c), $v_b = 76$ (d), and $v_b = 75$ (e) of the $b^3\Pi_u$ potential obtained with π-polarized light (black squares) and σ-polarized light (red circles). All parameter denotations, the fit function and the meanings of the vertical lines are identical to those of Fig. 6.2. The offset energies corresponding to the transitions at $\delta = 0$ are given in table 6.2. For $v_b = 73$ and 74 the intensity and pulse length of the σ-polarized light was the same as for π polarization. The spectra of $v_b = 78$ ($v_b = 75$) were measured with different pulse lengths τ, where the ratio was $\tau_\sigma/\tau_\pi = 5/3$ ($\tau_\sigma/\tau_\pi = 2/1$). Concerning $v_b = 76$, data of two scans with σ-polarized light are shown (magenta and red). Whereas the magenta data points were obtained using the same pulse area as for π polarization, it was by a factor of eight larger when measuring the red data points.

lines, but the observed fluctuations in the number of molecules are a clear indication of an internal structure of this resonance dip.

In contrast, the spectrum of $v_b = 75$ [Fig. 6.3(e)] is inverted compared to the spectra discussed before and exhibits three σ resonances, all of them at $\delta < 0$. As it is spread over an even larger frequency range of about $160\,\mathrm{MHz}$, the resonance dips at $-160\,\mathrm{MHz}$ and $-130\,\mathrm{MHz}$ are clearly separated from each other. The offset energies for the observed lines at $\delta = 0$ are listed in table 6.2 and are compared to the theoretical predictions of Ref. [196]. Again, the agreement is within the theoretical uncertainty. However, we note that the measured π transitions contain shifts due to hyperfine and Zeeman interaction. These shifts of up to $190\,\mathrm{MHz}$ (see section 6.6) would need to be subtracted for a proper comparison of the data with the calculations of Ref. [157].

6.5 Simple model of the molecule

In principle, hyperfine and Zeeman interaction within the $^3\Pi$ state of diatomic molecules has been theoretically investigated in depth (see, e.g., the 4th-order perturbation approach of [198]). However, properly applying such theoretical (and often complex) approaches to interpret measured spectra can still be a challenge because of the large number of parameters for representing the different orders. Therefore, we have developed a simple model which neglects some fundamental properties of a molecule. Nevertheless, it should be adequate to explain semi-quantitatively the Zeeman and hyperfine structure observed in our spectra.

In our model, the Rb_2 molecule is treated as a rigid rotor with fixed internuclear separation. Consequently, there is no vibrational degree of freedom. However, the positions of the nuclei can be interchanged. This is necessary in order to construct fully antisymmetric wave functions for the system of the two nuclei and the two valence electrons owing to the particles' fermionic character. Essentially, we consider the molecule as if it was composed of two unperturbed neutral atoms, of which, however, the angular momenta $\vec{L}$ and $\vec{J}$ are strongly coupled to the rigid rotator axis. In each of the atoms the orbital angular momentum L_i of the local electron i is a good quantum number. Thus, molecules belonging to the atom pair $5S_{1/2}+5P_{1/2}$ have both a p-orbital with $L_i = 1$ and a s-orbital with $L_i = 0$, and the total orbital angular momentum is $L = 1$ ($\vec{L} = \vec{L}_1 + \vec{L}_2$). Therefore, the two valence electrons can never be found in the same orbital. Coupling the electrons to the rotator axis (which corresponds to the internuclear axis) forms the electronic states $^{2S+1}\Lambda_{u/g}$ of the molecule. For simplicity, in the following discussion we restrict the model to those electronic states that are most relevant to describe our observations, i.e., states with u-symmetry and $\Omega = 0$. These are $b^3\Pi_u$ (0^+ as well as 0^-), $A^1\Sigma_u^+$ and $(2)^3\Sigma_u^+$ (see section 6.3.2).

The molecule is described by the Hamiltonian

$$H = H_{\mathrm{Diag}} + H_{\mathrm{SO}} + H_{\mathrm{R}} + H_{\mathrm{HF}} + H_{\mathrm{Z}} \,, \tag{6.1}$$

which, in addition to a diagonal energy matrix, contains spin-orbit coupling, nuclear rotation,

hyperfine and Zeeman interaction. The diagonal energy matrix

$$H_{\text{Diag}} = \sum_{\Lambda, S, 0^\pm} E_{\Lambda, S, 0^\pm} \; P(^{2S+1}\Lambda_u \; 0^\pm) \tag{6.2}$$

sets the initial values for the energies $E_{\Lambda, S, 0^\pm}$ of the electronic levels $^{2S+1}\Lambda_u \; 0^\pm$ before the remaining terms of the Hamiltonian are turned on. Here, $P(^{2S+1}\Lambda_u \; 0^\pm)$ denotes the projector onto the respective state. In order to describe the hyperfine and Zeeman structure for a given vibrational level v' (with symmetry $^{2S'+1}\Lambda'_{u'} \; 0^\pm$), the influence of all surrounding vibronic levels for each symmetry is mimicked by a single, effective energy value $E_{\Lambda, S, 0^\pm}$. As an example, let us assume that we want to describe the hyperfine and Zeeman structure of the vibrational level $v_b = 75$ of the b state. As can be seen in Fig. 6.1(b), $v_b = 75$ is surrounded by several v_A levels in its proximity, with $v_A = 67$, 68 and 69 being the closest ones. All these v_A levels are replaced by a single effective vibrational level with energy $E_{\Sigma, 0, 0^+}$ in our model.

The second term of Eq. (6.1) is the spin-orbit interaction

$$H_{\text{SO}} = C_{\text{SO}}(\vec{S}_1 \cdot \vec{L}_1 + \vec{S}_2 \cdot \vec{L}_2) \; , \tag{6.3}$$

which couples spin $\vec{S}_i$ and orbital angular momentum $\vec{L}_i$ of electron i. Here, C_{SO} denotes the spin-orbit parameter being the corresponding atomic value divided by two because we have only 50% probability for each electron to be in the p-orbital. From the atomic fine structure in ^{87}Rb (see, e.g., [87]) one obtains $C_{\text{SO}} = \left[E(5^2P_{3/2}) - E(5^2P_{1/2})\right]/(3\hbar^2) = 2374\,\text{GHz} \times h/\hbar^2$. We use this value of C_{SO} for the spin-orbit interaction between $(2)^3\Sigma_u^+$ and $b^3\Pi_u \; 0^-$. These states are separated by about 5000cm^{-1} [cf. Fig.6.1(a)]. The corresponding level repulsion shifts the $b^3\Pi_u$ 0^- component to lower energies by several tens of GHz $\times h$ compared to the situation, when spin-orbit interaction is ignored. For the spin-orbit coupling between $A^1\Sigma_u^+$ and $b^3\Pi_u \; 0^+$, we additionally take into account the overlap integral of the relevant vibrational wave functions, which is typically ~ 0.1 for states of the considered frequency range ($9360 - 9600 \text{ cm}^{-1}$). The spin-orbit interaction is responsible for the frequency splitting Δ between the 0^- and 0^+ components of $b^3\Pi_u$ and the mixing of the A and b state which is expressed in terms of the admixing parameter p_b. It turns out that Δ and p_b are the two quantities, which essentially determine the hyperfine and Zeeman structure of a vibrational state. By fine tuning Δ and p_b in our model we can describe the observed spectra. For practical purposes, we vary neither C_{SO} nor the value of the overlap integral ($= 0.1$), instead we use the term energies of the relevant uncoupled states in H_{Diag}. Concretely, we adjust p_b by setting the separation between $A^1\Sigma_u^+$ and $b^3\Pi_u$, while the size of Δ is adjusted by shifting the term energy of the 0^- level relative to the 0^+ level.

The third term of Eq. (6.1),

$$H_{\text{R}} = B_v \vec{R}^2 \; , \tag{6.4}$$

describes the rotation of the atom pair. According to the calculations of Drozdova *et al.* [196], the rotational constant B_v is about 0.54 GHz $\times h/\hbar^2$ for the $A - b$ states with dominant b character and vibrational quantum numbers $v_b \sim 70 - 80$ of ^{87}Rb$_2$. The quantum number

of angular momentum $\vec{R}$ appearing in the atom pair basis determines the total parity of the molecular state according to $-(-1)^R$. But R is not a good quantum number for the molecular eigenstates since $\vec{R}^2$ does not commute with H_{Diag}.

Next, we consider the hyperfine interaction H_{HF}. As mentioned in [173], the Fermi contact term is in general sufficient to characterize the hyperfine interaction of alkali-metal dimers. We use

$$H_{\text{HF}} = b_{\text{F}}(\vec{S} \cdot \vec{I}) , \qquad (6.5)$$

with $\vec{S} = \vec{S}_1 + \vec{S}_2$ and $\vec{I} = \vec{I}_1 + \vec{I}_2$. According to Ref.[173], the effective Fermi contact parameter b_{F} for an atom pair $(s+p)$ is $b_{\text{F}} \sim A_{\text{HF,atom}}/4$, where $A_{\text{HF,atom}} = 3.417\,\text{GHz} \times h/\hbar^2$ denotes the atomic hyperfine parameter for the $5S_{1/2}$ level of ^{87}Rb [199]. We note that Eq. (6.5) is formally identical to the atomic hyperfine interaction of a ground state electron (i.e., s orbital) with its local nuclear spin I_i. The factor $1/4$ normalizes the interaction because at any instant in time only one of the two electrons (i.e., the s electron) interacts with only one of the two nuclei. By using the ansatz of Eq. (6.5) we neglect the nondiagonal part of the hyperfine interaction with respect to S and I and thus there is no mixing of u/g symmetry. However, this approximation should be valid as the energy spacing between possibly coupled u/g states is significantly larger than the $0^-/0^+$ spacing considered in this work.

The last term of Eq. (6.1) characterizes the Zeeman interaction in a homogeneous magnetic field of strength B in z direction

$$H_{\text{Z}} = \mu_{\text{B}}[g_L \; L_z + g_S \; S_z + g_I \; I_z]B , \qquad (6.6)$$

with μ_{B} being Bohr's magneton. Here, we consider the Zeeman interaction due to the orbital angular momenta of the electrons, the electronic spins as well as the nuclear spins, where $g_L = 1$, $g_S = 2.002319$ and $g_I = -0.000995$ for ^{87}Rb [199] are the corresponding g-factors.

The matrix elements are calculated in an uncoupled atom pair basis, being a properly antisymmetrized product of eigenstates of all needed angular momenta and their projection on the space-fixed axis z, and the nuclear positions at both ends of the rotator axis. Table 6.3 gives an overview of the range of quantum numbers for the $\Omega = 0$ states of $b^3\Pi_u$, which are needed to setup the matrix. The total molecular angular momentum J ($\vec{J} = \vec{R} + \vec{L} + \vec{S}$, i.e., without nuclear spins) is a fairly good quantum number, because the hyperfine and Zeeman interaction is small compared to the other interactions.

6.6 Model calculations and interpretation of measured data

In the following we use the model introduced in the previous section to calculate the Zeeman and hyperfine structure for an $A - b$ bound state as a function of the frequency splitting $\Delta = [E(0^-, J = 0) - E(0^+, J = 1)]/h$ of the $0^\pm$ components of $b^3\Pi_u$[35], the degree of mixture p_b between the A and b states, as well as the magnetic field B. We define Δ to be the

---

[35]The different J values are required for obtaining the same parity for the mixed states. In addition to $J = 0$, also the level $J = 2$ of 0^- will couple to $J = 1$ of 0^+. The rotational energy splitting between $J = 0$ and 2 of 0^- is determined by Eq. (6.4).

J	0^+			0^-		
	I	$+/-$	R	I	$+/-$	R
0	1, 3	$+$	1	0, 2	$-$	0, 2
1	0, 2	$-$	0, 2	1, 3	$+$	1, 3
2	1, 3	$+$	1, 3	0, 2	$-$	0, 2, 4
3	0, 2	$-$	2, 4	1, 3	$+$	1, 3, 5
4	1, 3	$+$	3, 5	0, 2	$-$	2, 4, 6
$\vdots$	$\vdots$	$\vdots$	$\vdots$	$\vdots$	$\vdots$	$\vdots$

Table 6.3: Overview of the range of quantum numbers for states 0^+ and 0^- of $b^3\Pi_u$ with low angular momentum J. The $+/-$ columns provide the total parity whereas I represents the total nuclear spin and R is the atom pair rotation. Note that the quantum numbers I and parity alternate with J. This behavior is also found for the even and odd values of R. Furthermore, the molecular rotation increases with J.

splitting between $0^\pm$ after diagonalization of the Hamiltonian H of Eq. (6.1). In order to keep the discussion simple, we restrict ourselves to the range of quantum numbers and parameters directly related to our experiments. As explained in section 6.3.2, starting from Feshbach molecules we can only optically excite $A - b$ bound levels through the $A^1\Sigma_u^+$ 0^+ component with angular momentum $J = 1$ and negative parity. Furthermore, we want to point out that the eigenstates of the Hamiltonian of Eq. (6.1) are eigenstates of the total nuclear spin I. Thus, we can restrict ourselves to bound states with $I = 2$, being equal to the value of the singlet component of the Feshbach state applying the electric dipole selection rule $\Delta I = 0$.

The diagonal Zeeman and hyperfine interactions of the states $0^\pm$ are negligible compared to our measurement uncertainty. However, both the Zeeman interaction H_Z and the hyperfine interaction H_{HF} couple 0^+ and 0^- within $b^3\Pi_u$. In particular, $(J = 1, I = 2)$ of 0^+ couples to $(J = 0, I = 2)$ and $(J = 2, I = 2)$ of 0^- (see table 6.3). This leads to mixing, i.e., to the creation of eigenstates with a net electronic magnetic moment and thus to Zeeman and hyperfine splittings. Interestingly, hyperfine and Zeeman interaction amplify the line splittings in a cooperative way because they have matrix elements for the coupling between 0^+ and 0^- similar in magnitude and equal in sign. Hence, if Zeeman and hyperfine interaction are of the same strength their combined effect increases the line spacings not only by a factor of two but by a factor of four. Our experiments are indeed close to this regime for the selected magnetic field of about 1000 G.

The Zeeman and hyperfine splitting crucially depends on the frequency spacing Δ between the levels 0^- and 0^+ of $b^3\Pi_u$. Using standard perturbation theory, the splitting is estimated to be proportional to $\langle H_Z + H_{HF}\rangle^2/\Delta$. We recall that the spin-orbit couplings to $(2)^3\Sigma_u^+$ and $A^1\Sigma_u^+$ generate the spacing Δ between the levels 0^- and 0^+ of $b^3\Pi_u$ in the restricted Hilbert space.

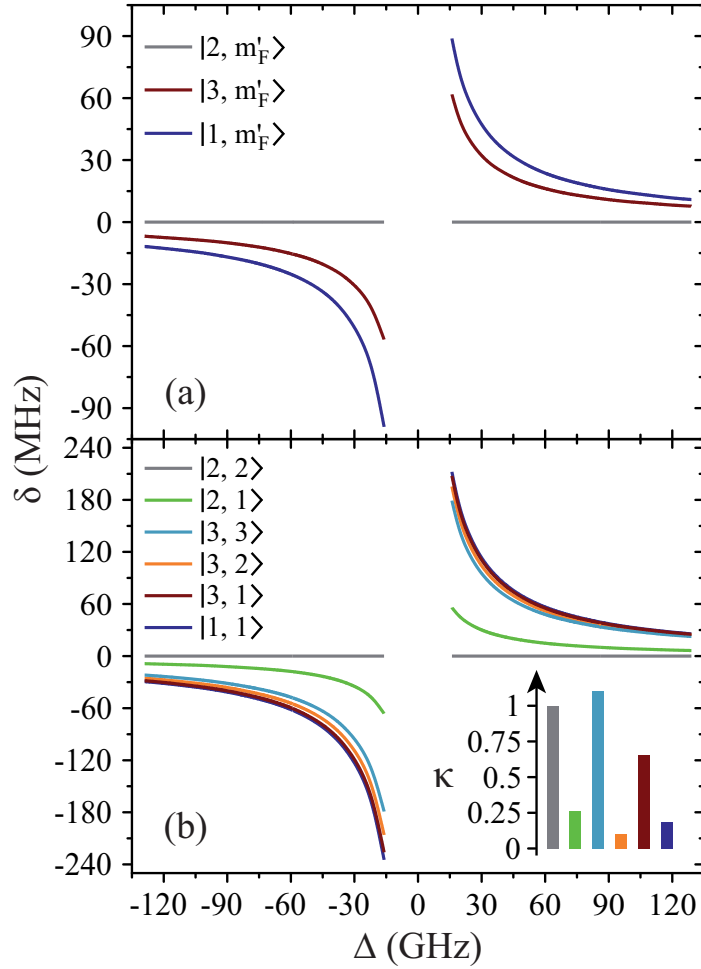Figure 6.4 depicts results of our model calculations for a vibrational level of $A - b$ with

Figure 6.4: Hyperfine level structure for a vibrational state v_b with $p_b = 80\%$ for two magnetic fields, $B = 0$ G (a) and 1000 G (b). Shown are the frequency positions δ of the levels $|F', m_F'\rangle$ relative to the state $|2,2\rangle$, as a function of Δ. The inset in (b) gives the relative strengths κ for the optical dipole transitions from the Feshbach state towards the levels $|F', m_F'\rangle$ of v_b at $B = 1000$ G. For $|2,2\rangle$ we set $\kappa = 1$. For convenience, we have plotted the same data in Fig. 6.7 in terms of $1/\Delta$. This makes it easier to read off the line splittings for small $|\Delta|$.

80% triplet (b) and 20% singlet (A) character. The frequency positions of levels $|F', m_F'\rangle$ are shown as a function of Δ for two magnetic fields, $B = 0$ G and 1000 G. Although the total angular momentum F' is generally not a good quantum number anymore at higher magnetic fields, we refer to the molecular levels by the correlated value of F' at $B = 0$ G. In Fig. 6.4 only those six states $|F', m_F'\rangle$ are plotted that, according to the dipole selection rules, are accessible by our spectroscopy experiment. As the Feshbach molecule has $F = 2$, $m_F = 2$, levels with the

quantum numbers $m'_F = 2$ ($m'_F = 1, 3$) can be observed via π (σ) transitions. We choose the state $|F' = 2, m'_F = 2\rangle$ as energy reference (i.e., $\delta = 0$), because it corresponds to the strong π resonance in Figs. 6.2 and 6.3. This allows for convenient comparison of our calculations to the measured spectra. Note, at $B = 0$ G, no m_F splitting can occur and therefore only three different curves are discernible in Fig. 6.4(a).

In our calculations, Δ is set by adjusting the initial energy spacing between the 0^+ and 0^- components of the b state in H_{Diag} [see Eq. (6.2)]. To a good approximation, within the frequency ranges considered in Fig. 6.4 (i.e., $|\Delta| = 16 - 129$ GHz) the level splittings increase inversely with Δ, just as expected from perturbation theory. This can directly be seen in Fig. 6.7 of section 6.10. For $B = 1000$ G and a small $|\Delta|$ of 16 GHz, the overall spreading of the levels reaches more than 200 MHz, whereas for a large $|\Delta| \geq 60$ GHz it is on the order of a few tens of MHz or less. Furthermore, the ordering of the energy levels is inverted, when the sign of Δ changes. We point out that some level spacings are smaller than the expected linewidths and therefore cannot be resolved in the experiment. The widths of the levels are mainly determined by those of the $A^1\Sigma_u^+$ state (~ 12 MHz) and the admixing parameter p_A, because the width of the pure $b^3\Pi_u$ state is orders of magnitude smaller compared to the one of $A^1\Sigma_u^+$. The basic structure of the calculated levels (see Fig. 6.4) and the level widths let us expect to resolve three resonance features which agrees well with our observations shown in Fig. 6.3.

We now want to assign the experimentally observed resonances to distinct transitions. Besides considering the line positions we also take into account the strength of the lines. For this purpose, we calculate the dipole matrix elements $M_{\text{FS},(F',m'_F)}$ from the initial Feshbach state $|\text{FS}\rangle$ to the final levels $|F', m'_F\rangle$ of the mixed $b^3\Pi_u$ state. As already mentioned, we only have to consider the singlet component of both levels. The inset in Fig. 6.4(b) shows the relative transition strengths $\kappa = M^2_{\text{FS},(F',m'_F)}/M^2_{\text{FS},(2,2)}$ at $B = 1000$ G. We can roughly group the six transitions into three strong ones (by σ light towards final states $|3,1\rangle$ and $|3,3\rangle$, by π light towards $|2,2\rangle$) and three weak transitions (σ: towards $|1,1\rangle$ and $|2,1\rangle$ and π: towards $|3,2\rangle$). Our observed spectra always exhibit only one strong line for π-polarized light (cf. Fig. 6.3). It is therefore assigned to $|2,2\rangle$ and used as reference level. The calculations predict a second resonance for π polarization which should be about one order of magnitude weaker. However, we did not unambiguously observe this line since its signal is easily drowned by the overlaying strong σ lines if the achieved light polarization is not sufficiently pure.

In the following, the σ transitions are discussed in detail using the results shown in Fig. 6.4(b). Although the transition towards $|2,1\rangle$ is weak, we should be able to clearly observe it, since the level $|2,1\rangle$ is well separated from all other levels. The three remaining transitions (towards $|1,1\rangle$, $|3,1\rangle$ and $|3,3\rangle$), however, are quite close to each other. Especially for larger values of $|\Delta|$ ($\gtrsim 40$ GHz) these levels cannot be resolved and only a single resonance should be visible. Among the three transitions, the one towards $|3,3\rangle$ is most dominant. For low values of $|\Delta|$ (< 40 GHz) the strong $|3,3\rangle$ line splits clearly from those corresponding to $|1,1\rangle$ and $|3,1\rangle$ which both barely separate. This explains why our observed spectra for σ-polarized light in Fig. 6.3 exhibit at most three resonance features. At this stage we have shown that the experimental data can be qualitatively explained by our theoretical model and that we already

can assign quantum numbers to the measured resonance lines.

Now, we want to carry out a more quantitative comparison of the measured line splittings in Fig. 6.3 with the model predictions. For this, we study the dependence of the energy level structure on the admixing parameter p_b, i.e., the percentage of the $b^3\Pi_u$ potential in the vibrational state v_b. In the simulations, we set p_b by adjusting the term energy of the bare $A^1\Sigma_u^+$ state in Eq. (6.2). Results for $\Delta = +59$ GHz are shown in Fig. 6.5. To good approximation, within the investigated range from $p_b = 65\%$ to 95% the level frequencies depend linearly on p_b. This makes sense as the discussed hyperfine and Zeeman interaction only appears within the $b^3\Pi_u$ ($\Omega = 0$) state.

In order to carry out the quantitative comparison for each spectrum v_b, we individually fix the splitting of the bare $A^1\Sigma_u^+$ 0^+ and $b^3\Pi_u$ 0^+ levels such that the admixing parameter p_b equals to its literature value [157, 196], as listed in table 6.2. Afterwards, we fit our model to the measured spectrum by adjusting a single parameter, the effective term energy of $b^3\Pi_u$ 0^- in H_{Diag} and thus the splitting Δ between the 0^- and 0^+ components of the b state. All other parameters of the model are kept at the values given in section 6.5. For the fit, we ignore the states $|3, 2\rangle$ and $|1, 1\rangle$ since they cannot be experimentally resolved [see inset of Fig. 6.4(b)]. The resulting spectral positions of the hyperfine levels are shown in Fig. 6.3 as vertical lines together with the measured spectra. The agreement is quite satisfactory as the experimental and calculated line positions do not differ by more than a few MHz. Our fit results for Δ, i.e., the splitting of the $0^\pm$ states after diagonalizing the Hamiltonian H of Eq. (6.1), are listed in Fig. 6.3 as well as in table 6.2. We obtain values ranging from $\Delta = -19.7$ GHz to 104.5 GHz. The error boundaries for Δ in table 6.2 are estimated by simulations shifting the resonance
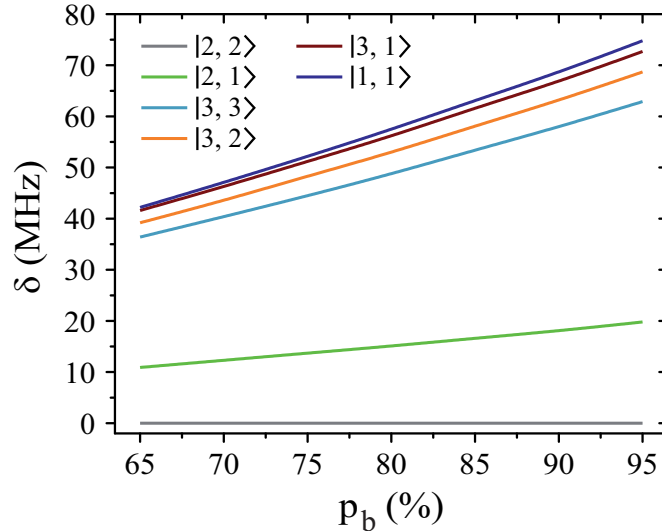

Figure 6.5: Dependence of the hyperfine and Zeeman structure on the admixing parameter p_b for a fixed value of $\Delta = +59$ GHz and a magnetic field of $B = 1000$ G. The frequency δ is given relative to the $|2, 2\rangle$ level.

frequency δ of the strong $|F' = 3, m_F' = 1\rangle$ line by $\pm 5\,\text{MHz}$ relative to the reference $|2, 2\rangle$. Such an approach is reasonable as the frequency stability in our measurements is $\pm(2 - 5)\text{MHz}$.

Next, we investigate the Zeeman and hyperfine structure as a function of the magnetic field. Figures 6.6(a) and (b) depict the model calculations for the vibrational levels $v_b = 75$ and 73, respectively, using the values of p_b and Δ given in table 6.2. For both plots the admixing parameters are similar ($p_b \approx 80\%$), while the respective frequency spacings Δ have different signs and magnitude. We show all the levels accessible in our spectroscopy together with the experimentally derived levels at $B = 999.9$ G. Here, the frequency reference is represented by the level $|2, 2\rangle$ at this magnetic field. We present in Fig. 6.6(c) the full hyperfine and Zeeman structure of a single state v_b for $\Delta = +14.0\,\text{GHz}$, $p_b = 80.00\%$. This graph reveals particularly well the transition from the linear Zeeman effect to a quadratic behavior above a few hundreds of gauss and the enhancement of the splitting by the cooperative effect between Zeeman and hyperfine interaction.

Finally, we want to give a quantitative interpretation of the spectrum corresponding to the vibrational level $v_A = 72$ of $A^1\Sigma_u^+$ [see Fig. 6.2(b)], which has a large b state admixture ($p_b = 39.36\%$) due to the strong coupling of $v_A = 72$ to $v_b = 78$ as these states are fairly close to each other. The separation is only 89.2 GHz according to tables 6.1 and 6.2. For $v_b = 78$, our model determines a spacing of $\Delta = 36.4^{+3.4}_{-2.9}$ GHz between its 0^+ and 0^- components. Consequently, the $b^3\Pi_u\ 0^-$ state is only separated by $-52.8^{+3.4}_{-2.9}$ GHz from the $A^1\Sigma_u^+\ 0^+$ state. From this, we can predict the hyperfine structure for $v_A = 72$ with our model. The results are shown in Fig. 6.2(b). As can be seen, the calculated and measured resonances agree well, which nicely confirms the consistency of our model.

6.7 Splitting between 0^+ and 0^- components in a potential scheme

In the previous section, we have determined the effective splitting $\Delta = [E(0^-, J = 0) - E(0^+, J = 1)]/h$ for the state $b^3\Pi_u$ using our simple model without vibrational degree of freedom. Here, we compare the obtained results to those of coupled channel calculations with a potential scheme, i.e., including the full dynamics of the relative motion within the atom pair. As a first step we follow Ref. [157] and therefore restrict the calculations to the $A - b$ system, such that the spin-orbit interaction and the molecular rotation only couple the A and b states. Thus, the influence of the spin-orbit coupling of $b^3\Pi_u\ 0^-$ to $(2)^3\Sigma_u^+\ 0^-$ is not yet considered. The term values for the $A - b$ complex are listed in table 6.4. For the calculations we take the model potentials and spin-orbit functions reported in Ref. [157]. Columns 3 and 4 show the term values for 0^+, $J = 1$ and 0^-, $J = 0$ in the absence of spin-orbit coupling, respectively. At this stage, the 0^+ and 0^- components of the $b^3\Pi_u$ state are only split due to rotation. Column 5 lists the term energies for 0^+, $J = 1$ if the spin-orbit coupling is included. These are the same values as given in tables 6.1 and 6.2. Column 6 provides the energy difference of each 0^+ state in column 4 relative to the closest 0^- state in column 3. This quantity, which we call Δ_{A-b}, is the prediction for the $0^\pm$ splitting within the $A - b$ system. Noticeably, Δ_{A-b} varies strongly for
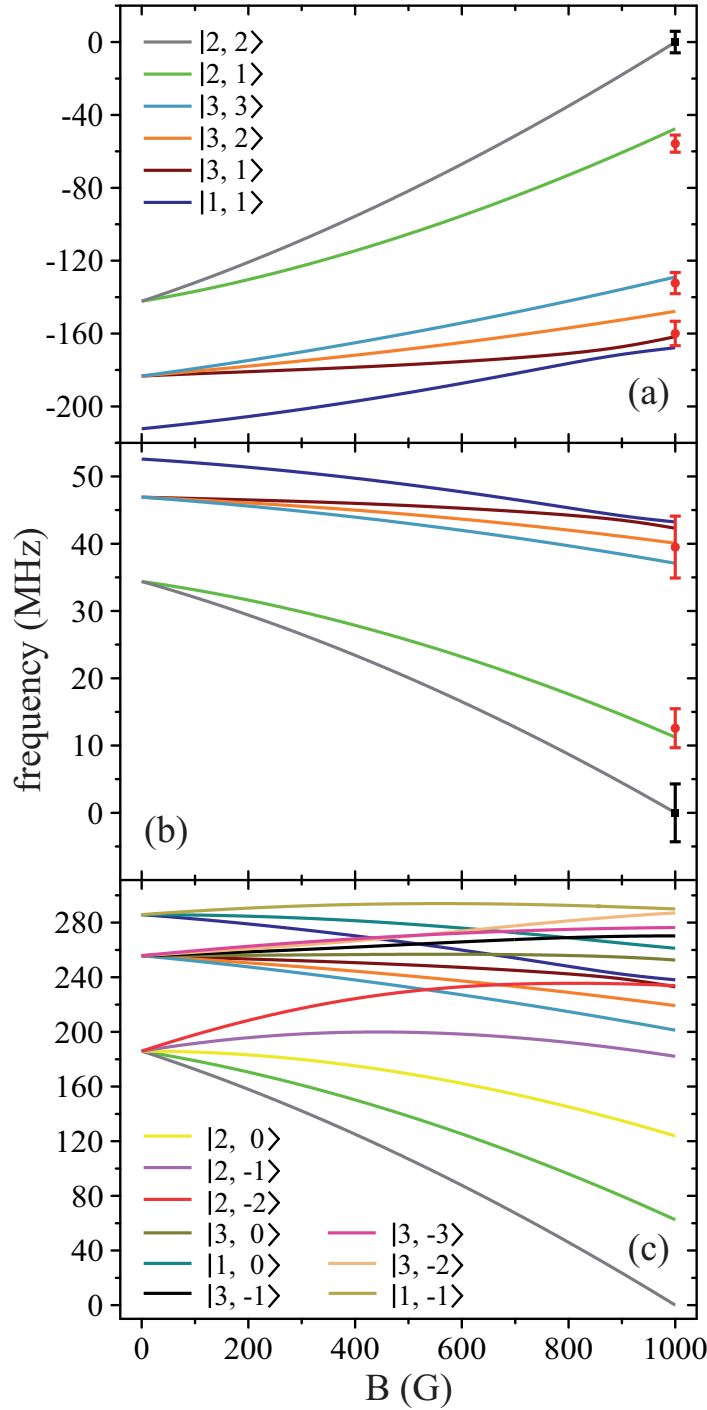
Fig. 6.6: Zeeman structure of the hyperfine levels $|F', m'_F\rangle$ as a function of the magnetic field B. The frequency is referenced to the position of level $|2, 2\rangle$ at $B = 999.9$ G. (a) Simulations for $\Delta = -19.7$ GHz, $p_b = 73.80\%$, (b) for $\Delta = +81.8$ GHz, $p_b = 82.70\%$ and (c) for $\Delta = +14.0$ GHz, $p_b = 80.00\%$. The black square (red dot) plot symbols indicate the experimentally observed resonances obtained with π-polarized (σ-polarized) light corresponding to $v_b = 75$ (a) and 73 (b). The error bars represent the measured transition linewidths (FWHM) determined from our fits to the data [cf. Fig. 6.3(b) and (e)]. In (c), all hyperfine energy levels of the vibrational state v_b ($J = 1$, $I = 2$) are plotted, where the color code is extended for the additional levels compared to (a) and (b).

different vibrational levels, which results from the fact, that the uncoupled vibrational ladders v_A and v_b of $A^1\Sigma_u^+$ and $b^3\Pi_u$ are interwoven with different spacings. Thus, their repulsion

state	v_A, v_b	0^+, $J=1$ (w/o SO) $[hc \times \mathrm{cm}^{-1}]$	0^-, $J=0$ (w/o SO) $[hc \times \mathrm{cm}^{-1}]$	0^+, $J=1$ (w SO) $[hc \times \mathrm{cm}^{-1}]$	$\Delta_{\mathrm{A-b}}$ [GHz]	Δ_{obs} [GHz]	$\Delta_{\mathrm{obs}} - \Delta_{\mathrm{A-b}}$ [GHz]
$A^1\Sigma_u^+$	65	9352.911		9352.078	534.3		
$b^3\Pi_u$	73	9369.939	9369.901	9368.758	34.3	81.8	$47.5^{+10.6}_{-8.5}$
$A^1\Sigma_u^+$	66	9388.026		9388.005	-542.7		
$b^3\Pi_u$	74	9414.679	9414.641	9412.519	63.6	104.5	$40.9^{+23.9}_{-16.4}$
$A^1\Sigma_u^+$	67	9423.000		9423.589	-268.3		
$A^1\Sigma_u^+$	68	9457.834		9454.571	137.9		
$b^3\Pi_u$	75	9459.210	9459.172	9460.874	-51.0	-19.7	$31.3^{+0.6}_{-0.6}$
$A^1\Sigma_u^+$	69	9492.527		9491.049	373.0		
$b^3\Pi_u$	76	9503.529	9503.492	9503.516	-0.7	40.0	$40.7^{+2.2}_{-2.0}$
$A^1\Sigma_u^+$	70	9527.078		9525.742	655.2		
$b^3\Pi_u$	77	9547.635	9547.598	9547.629	-0.9		
$A^1\Sigma_u^+$	71	9561.487		9560.041	-373.0		
$b^3\Pi_u$	78	9591.525	9591.488	9591.479	0.3	36.4	$36.1^{+3.4}_{-2.9}$
$A^1\Sigma_u^+$	72	9595.754		9594.454	-88.9	-52.8	$36.1^{+3.4}_{-2.9}$
$A^1\Sigma_u^+$	73	9629.979		9627.657	224.9		

Table 6.4: Energy levels of the component $\Omega = 0$ of $A^1\Sigma_u^+$ and of $b^3\Pi_u$ without (w/o SO) and with (w SO) spin-orbit coupling. Column 3 shows the calculated energies for 0^+ of the A and b states for $J = 1$, whereas column 4 contains only energy levels for 0^- and $J = 0$. In column 5 the corresponding values for 0^+ and $J = 1$ are provided, obtained with the spin-orbit interaction between states A and b. Column 6 reports the splittings $[E(0^-) - E(0^+)]/h$ calculated for the restricted system $A - b$ and denoted by $\Delta_{\mathrm{A-b}}$, while column 7 lists the results derived from our experiments. (For details see text.)

due to the interaction of different vibrational levels is fairly irregular. Column 7, labeled Δ_{obs}, recalls the findings for Δ inferred from our measurements. There is disagreement between the measurements and the results of the restricted coupled channel model. All values Δ_{obs} are significantly larger than $\Delta_{\mathrm{A-b}}$. However, it is striking that the differences between Δ_{obs} and $\Delta_{\mathrm{A-b}}$ are all close to $40\,\mathrm{GHz}$. The actual values are given in column 8, where the uncertainties are taken from Δ_{obs} (see, e.g., table 6.2). Indeed, all differences (except for $v_b = 75$) are equal within the given uncertainties. Could the spin-orbit coupling to state $(2)^3\Sigma_u^+$ be responsible for this discrepancy of $\approx 40\,\mathrm{GHz}$? No, it cannot. Indeed, the $(2)^3\Sigma_u^+$ state is far up in energy [cf. Fig. 6.1(a)] and therefore all vibrational levels of $b^3\Pi_u$ 0^- experience an almost constant shift, but it has the wrong sign to explain the observations. If *ab initio* calculations for the $(2)^3\Sigma_u^+$ potential energy curve and the corresponding spin-orbit interaction are applied, we

obtain quantitatively that the 0^- component of the $b^3\Pi_u$ state is shifted by about $50\,\text{GHz} \times h$ to lower energies. This increases the deviation of already 40 GHz to about 90 GHz, much beyond experimental uncertainties.

Because the energetic order of the 0^+ components are accurately determined from former spectroscopic work [157], our observation directs clearly to the spin-orbit energy of the 0^- component of state $b^3\Pi_u$. Interestingly, the spin-orbit functions of $b^3\Pi_u$ presented in Fig. 6(a) of [157] are different for $\Omega = 2$ and $\Omega = 0$ by about $1.8\,\text{cm}^{-1}$ as derived from the reported amplitude D_e^{SO} of the spin-orbit function in Table V of Ref. [157]. This difference indicates that $b^3\Pi_u$ is no longer a pure spin-orbit multiplet of a Π state. If we consider that a similar deviation of the multiplet structure also exists for 0^-, then a decrease of about $2.6\,\text{cm}^{-1}$ compared to the spin-orbit function for 0^+ in [157] would be sufficient to model the Δ_{obs} as given in table 6.4. We believe that this is a plausible explanation of our observation.

Finally, in view of the calculated splittings of 0^- and 0^+ we want to recall the measurements for the vibrational levels $v_A = 66$ and 69 of $A^1\Sigma_u^+$ (cf. Fig. 6.2(a) and table 6.1). The absolute values $|\Delta_{\text{A-b}}|$, even when corrected by the above determined shift of 90 GHz, are very large. Therefore, according to the discussion in section 6.6, we do not expect significant hyperfine and Zeeman splittings. Indeed, no hyperfine structure was observed in our spectra for $v_A = 66$ and 69.

6.8 Conclusion

We have investigated the combined hyperfine and Zeeman structure in the spin-orbit coupled $A^1\Sigma_u^+ - b^3\Pi_u$ complex of $^{87}\text{Rb}_2$ dimers. We performed spectroscopy of ultracold Feshbach molecules at a magnetic field of 999.9 G and recorded the spectra for several excited vibrational levels with either dominant $A^1\Sigma_u^+$ character ($v_A = 66 - 70$ and 72) or dominant $b^3\Pi_u$ character ($v_b = 73 - 76$ and 78). We observe large line splittings of up to 160 MHz and find that the Zeeman and hyperfine structure of the 0^+ state of $b^3\Pi_u$ varies strongly for different vibrational levels. Using a simple model, where the molecule is treated as a rigid rotor of two neutral atoms, we can explain the level structures as resulting from nondiagonal hyperfine and Zeeman interactions between the 0^+ and 0^- components of $b^3\Pi_u$. The hyperfine and Zeeman interactions act in a cooperative way, which enhances the level splittings. Furthermore, the level splittings depend linearly on the admixture p_b for the components 0^+ of the complex $b^3\Pi_u$ and $A^1\Sigma_u^+$, and scale inversely with the frequency spacing Δ between 0^- and 0^+. From fits of our model to the data, we find that Δ strongly varies in the range of -53 to 105 GHz within the interval of studied v_b and v_A. Our observed values for Δ systematically deviate by about $90\,\text{GHz}$ from predictions of close-coupled channel calculations of the electronic structure correlated to the atom pair asymptote $5^2S + 5^2P$ using empirical potentials for $A^1\Sigma_u^+$ and $b^3\Pi_u$ and *ab initio* results for $(2)^3\Sigma_u^+$. We can eliminate this deviation by introducing a spin-orbit coupling function that is different by $2.6\,\text{cm}^{-1}$ for 0^- and 0^+.

The fact, that we can extract the frequency spacing Δ from our measurements of the hyperfine and Zeeman structure is a significant result of this work. In ordinary spectroscopy, starting from a ground state molecule only the state 0_u^+ can be addressed, owing to selection

rules. Therefore, very little data on the Λ-type doubling of $\Omega = 0$ is available, so far. Recently, all multiplet components of the $(1)^3\Pi_g$ state were observed in the photoassociation of ultracold ^{85}Rb atoms [139]. The colliding $^2S + ^2S$ atom pair contains a superposition of states with both symmetries $^3\Sigma_u^+$ (0^- and 1) from which $(1)^3\Pi_g$ ($\Omega = 0^\pm, 1, 2$) can be reached by electric dipole transitions. To our knowledge, our method represents the first work to experimentally access Δ by investigating only one of the $0^\pm$ components of $b^3\Pi_u$.

In the simple model only the hyperfine contribution from the s electron was considered. Thus it is unknown, how much the missing contribution by the p electron and the electric quadrupole interaction might influence the determination of the energy splitting between 0^- and 0^+. In this respect and according to the evaluated multiplet structure here, it would be interesting to compare the results of the simple model to full close-coupled channel calculations based on accurate Born-Oppenheimer potential curves including hyperfine and Zeeman interaction with its non-diagonal contributions between the multiplet components. But for this task more experimental data is needed in order to determine the vibrational dependence over a large interval, which allows for deriving r-dependent functional forms of the spin-orbit interaction and probably also of the hyperfine interaction. The latter one was clearly needed in an earlier study on the triplet ground state $a^3\Sigma_u^+$ of Rb$_2$ [122]. We want to emphasize that the strength of the present approach is, that the modeling of all observations on hyperfine and Zeeman splittings are concentrated in an effective single parameter, an average value of the spin-orbit function for 0^-. The hyperfine parameter and the g-factors are kept constant at their atomic values. This will be altered if a wide range of vibrational levels is studied.

In general, the gained information is valuable for a detailed, fundamental understanding of molecular hyperfine and Zeeman level structures. Despite the already existing long tradition (see, e.g., the early paper by Freed [198]) there is still great interest in this field of research as documented by recent experimental studies, for instance with respect to Rb$_2$ [124, 200, 201]. Our results can be exploited for an optimized preparation of ultracold deeply-bound ground state molecules either via photoassociation [202] or a stimulated Raman adiabatic transfer (STIRAP) starting from Feshbach molecules.

6.9 Acknowledgements

6.10 Inverse dependence of the hyperfine structure on the splitting between 0^+ and 0^- components

In figure 6.7 we show the hyperfine level structure for the parameters of Fig. 6.4 but as a function of $1/\Delta$. Figure 6.7 clearly reveals the inverse dependence of the level splittings on
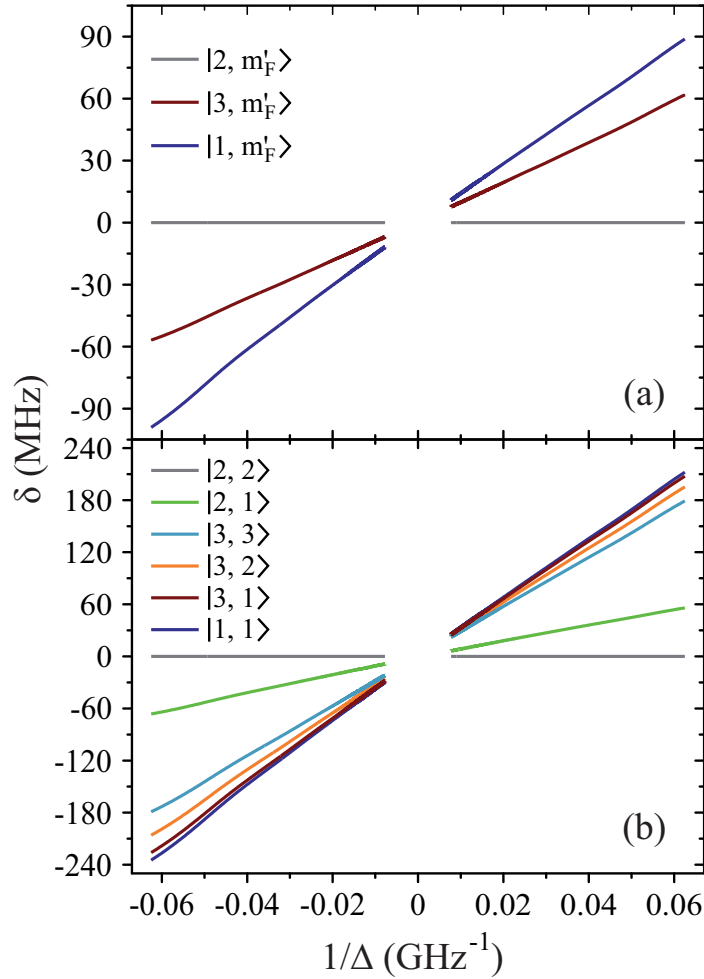
Figure 6.7: Hyperfine level structure for a vibrational state v_b with $p_b = 80\%$ for two magnetic fields, $B = 0$ G (a) and 1000 G (b). Shown are the frequency positions δ of the levels $|F', m'_F\rangle$ relative to the state $|2, 2\rangle$, as a function of $1/\Delta$.

Δ in the investigated range of $|\Delta| = 16 - 129$ GHz. This representation is more convenient for reading off the splitting for small values of Δ. Furthermore, it becomes obvious that the Zeeman effect enhances the splittings since in (b) the frequency separation of the group of levels characterized by $F = 1$ and 3 relative to the group corresponding to $F = 2$ is significantly larger than in (a).

6.11 Additional spectroscopic data concerning the $\mathrm{b}^3\Pi_\mathrm{u}$ state

We also have performed one-photon spectroscopy starting from Feshbach molecules towards

the vibrational levels $v_b = 79$ and 84 of the $b^3\Pi_u$ state. These data are not fully interpreted up to now. Nevertheless, for the sake of completeness and documentation, table 6.5 gives a comparison of the experimentally observed level energies and the values calculated by A. Drozdova *et al.* [196]. In the following, the measurement results and some theoretical considerations are discussed. However, please note, a firm explanation of the spectra is not possible at the moment and necessitates further investigations.

6.11.1 Discussion of data for $\mathbf{v_b = 84}$

Figure 6.8 shows our recording concerning the 0^+ component of the vibrational level $v_b = 84$. This scan has to be considered as preliminary as its details cannot be explained by our theoretical model. Within a range of 100MHz, we clearly observe two resonances for σ-polarized light and three resonances when using π polarization. In the following, we choose the arithmetic mean of the center frequencies of the three π lines as reference. The corresponding value of $E_{\mathrm{exp}}/(hc) = 9852.7094\,\mathrm{cm}^{-1}$ agrees well with the theoretical prediction for $v_b = 84$ (cf. table 6.5). Surprisingly, we measure three resonance features when applying π-polarized light. As discussed in section 6.4.2, the spectra for the 0^+ component with respect to vibrational levels $v_b = 73$ to 76 and 78 exhibit just a single π line and according to selection rules no more than two π transitions are allowed. Noticeably, if one neglects the two π resonances at around $\delta = 0$ and -40 MHz in Fig. 6.8, the general structure of the spectrum is similar to the one observed for $v_b = 73$ to 76 and 78.

Of course, technical problems could lead to artifacts. For example, I want to consider the effect of imperfect polarizations. In Fig. 6.8, there is no resonance dip for σ-polarized light on top of the strong π resonance at around $\delta = +40$ MHz. This indicates that the achieved σ polarization was sufficiently pure. In contrast, concerning π polarization we cannot make such a statement. It might be possible, that at the given frequency range, the π measurement was

v_b	b [%]	$E_{\mathrm{calc}}/(hc)$ [cm^{-1}]	$E_{\mathrm{exp}}/(hc)$ [cm^{-1}]	ε [10^{-3}cm^{-1}]
84	90.42	9852.710	9852.7094	0.6
79	89.80	9636.230	9636.1486	81.4
			9636.2079	22.1
			9636.2419	−11.9
			9636.3145	−84.5
			9636.4127	−182.7

Table 6.5: Comparison of calculated E_{calc} and measured E_{exp} level energies with respect to vibrational states $v_b = 84$ and 79 of the $b^3\Pi_u$ potential. The energy reference is given by the $|f_a = 1, m_{f_a} = 1\rangle + |f_b = 1, m_{f_b} = 1\rangle$ atomic dissociation limit at zero magnetic field (see section 6.3.1). In analogy to tables 6.1 and 6.2, $\varepsilon = (E_{\mathrm{calc}} - E_{\mathrm{exp}})/(hc)$ and p_b denotes the admixture of the $b^3\Pi_u$ potential. The values for E_{calc} and p_b are taken from [196].
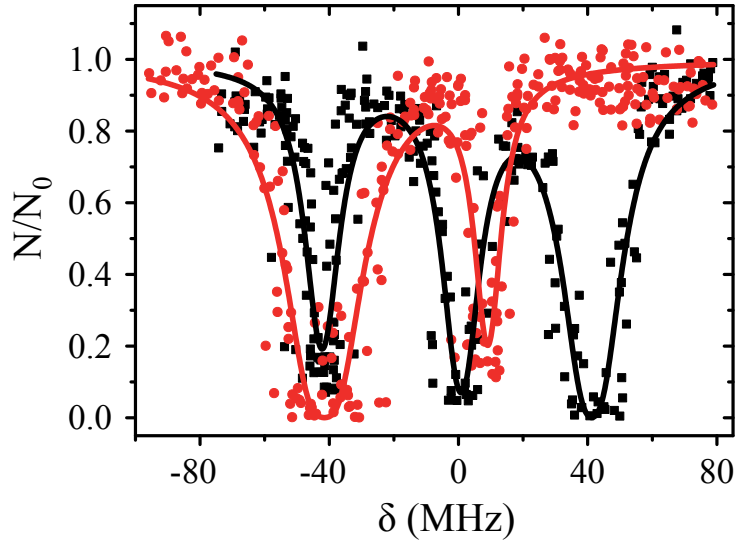
Figure 6.8: Loss resonances for excitation of molecules from the Feshbach state towards the vibrational level $v_b = 84$ of the $b^3\Pi_u$ potential obtained with π-polarized light (squares) and σ-polarized light (circles). Here, the offset energy corresponding to $\delta = 0$ and given in table 6.5 represents the arithmetic mean of the three frequencies related to the π resonances. In analogy to Figs. 6.2 and 6.3, N/N_0 denotes the remaining fraction of Feshbach dimers and solid lines are fits to the data applying the function e^{-KL}. The measurements with π- and σ-polarized light were performed for the same laser intensities and pulse lengths.

compromised due to imperfect polarization, which would influence the signals at around $\delta = 0$ and -40 MHz. In order to exclude a potential technical problem, a new measurement of the $v_b = 84$ spectrum should be performed.

6.11.2 Discussion of data for $v_b = 79$

Here, only measurements for π-polarized light were performed. We observed five resonances, which are separated by about a few GHz from each other (see Fig. 6.9). Among them, the resonance at $E_{\exp}/(hc) = 9636.2419 \, \text{cm}^{-1}$ shows the best agreement with the calculated value corresponding to $v_b = 78$ (cf. table 6.5). How this structure comes about is not clear at the moment. Possibly, similar to the mechanism reported for RbCs molecules in Ref. [185], it is related to the fact that a $\Omega = 1$ state of $b^3\Pi_u$ is close-by. In table 6.6, calculated level energies of $\Omega = 0$, 1, and 2 states of $b^3\Pi_u$ for all relevant frequency ranges are listed. In general, the spacing between the $\Omega = 0$ and $\Omega = 1$ components is on the order of a few cm^{-1}. However, as the spacing is very similar for the different vibrational states, it is surprising that the particular level structure of Fig. 6.9 was only observed at around $9636 \, \text{cm}^{-1}$. Therefore, a firm statement about the influence of the $\Omega = 1$ state is not possible at the moment and necessitates further
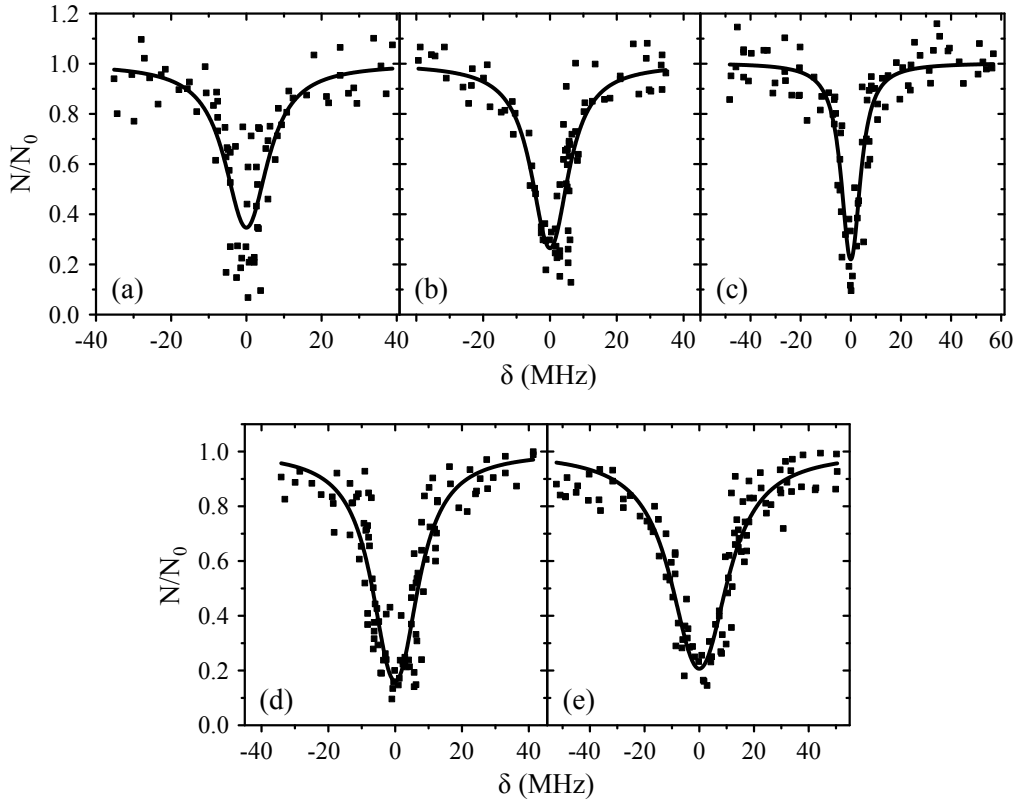
Figure 6.9: Loss resonances for excitation of Feshbach molecules at around $9636\,\mathrm{cm}^{-1}$ observed with π-polarized light. The frequency $\delta = 0$ corresponds to $9636.1486\,\mathrm{cm}^{-1}$ (a), $9636.3145\,\mathrm{cm}^{-1}$ (b), $9636.4127\,\mathrm{cm}^{-1}$ (c), $9636.2079\,\mathrm{cm}^{-1}$ (d), and $9636.2419\,\mathrm{cm}^{-1}$ (e) (cf. table 6.5).

theoretical and experimental investigation.

6.11.3 States corresponding to $(1)^3\Sigma_\mathbf{g}^+$ and $(2)^1\Sigma_\mathbf{g}^+$

In this section, I want to consider some states of the $(1)^3\Sigma_g^+$ and $(2)^1\Sigma_g^+$ potentials as they are close to the investigated frequency ranges.

- $(1)^3\Sigma_g^+$: According to the data corresponding to Fig. 3 of Ref. [124], the observed resonances at $\sim 9636\,\mathrm{cm}^{-1}$ ($\sim 9853\,\mathrm{cm}^{-1}$) given in table 6.5 are located between the $(1)^3\Sigma_g^+$ vibrational levels $v_{(1)} = 7$ at about $9624\mathrm{cm}^{-1}$ and $v_{(1)} = 8$ at about $9659\mathrm{cm}^{-1}$ ($v_{(1)} = 13$ at about $9828\mathrm{cm}^{-1}$ and $v_{(1)} = 14$ at about $9862\mathrm{cm}^{-1}$). Please note, each vibrational level $v_{(1)}$ is a doublet of 0_g^- and 1_g substructures of which the barycenters exhibit a splitting of more than 40 GHz [124]. However, the separation of adjacent states of $b^3\Pi_u$ and $(1)^3\Sigma_g^+$ is still on the order of at least several cm^{-1}. Thus, for the spectra shown in Figs. 6.8 and

$E_{\mathrm{calc}}^{\Omega=0}/(hc)$ [cm^{-1}]	$E_{\mathrm{calc}}^{\Omega=1}/(hc)$ [cm^{-1}]	$E_{\mathrm{calc}}^{\Omega=2}/(hc)$ [cm^{-1}]
9368.758	9365.693	9354.493
9412.519	9410.754	9399.921
9460.874	9455.609	9445.146
9503.516	9500.256	9490.167
9591.479	9588.918	9579.587
9636.230	9632.930	9623.984
9852.710	9849.711	9842.750

Table 6.6: Comparison of calculated level energies for adjacent $\Omega = 0$, 1, and 2 components of the $b^3\Pi_u$ state taken from Ref. [196]. Only those energy regions are considered that are relevant with respect to the spectroscopy results presented in this chapter (i.e., the values of the first column are identical to those given in tables 6.2 and 6.5, respectively).

6.9 none of the resonance lines can be assigned to $(1)^3\Sigma_g^+$.

- $(2)^1\Sigma_g^+$: Information about the level structure of $(2)^1\Sigma_g^+$ can be gained from the set of parameters for ^{85}Rb$_2$ molecules listed in Ref. [203]. The provided term value T_e for the minimum of the $(2)^1\Sigma_g^+$ potential curve is 13601.57 cm^{-1} with respect to the minimum of the $X^1\Sigma_g^+$ potential. Using the offset energies given in section 6.4.1 this value corresponds to 9608.26 cm^{-1} when taking the $|f_a = 1, m_{f_a} = 1\rangle + |f_b = 1, m_{f_b} = 1\rangle$ atomic dissociation limit at zero magnetic field as energy reference. Within a potential, the term values $T(v)$ of vibrational states can be calculated by means of the Dunham expansion (for more details, see, e.g., [204]), which reads

$$T(v) \approx T_e + \omega_e \left(v + \frac{1}{2}\right) - \omega_e x_e \left(v + \frac{1}{2}\right)^2 , \qquad (6.7)$$

if it is truncated after the second order and rotational terms are neglected. For ^{85}Rb$_2$, according to Ref. [203], $\omega_{e85} = 31.488$ cm^{-1} and $\omega_e x_{e85} = -0.0114$ cm^{-1}. Now, we have to calculate the corresponding parameters for ^{87}Rb$_2$. Accounting for the isotope shift leads to $\omega_{e87} = \omega_{e85}\sqrt{\mu_{85}/\mu_{87}}$ and $\omega_e x_{e87} = \omega_e x_{e85}(\mu_{85}/\mu_{87})$ [204], where μ_{85} and μ_{87} are the reduced masses of the ^{85}Rb$_2$ and the ^{87}Rb$_2$ molecules, respectively. Inserting $T_e = 9608.26$ cm^{-1}, $\omega_{e87} = \sqrt{(85/87)} \times 31.488$ cm^{-1} and $\omega_e x_{e87} = (85/87) \times -0.0114$ cm^{-1} in Eq. (6.7) yields the term values listed in table 6.7. As can be seen, no vibrational state $v_{(2)}$ of $(2)^1\Sigma_g^+$ is in the direct vicinity of the measured transition lines around 9636 cm^{-1} and 9853 cm^{-1}. However, I want to emphasize that the estimation of the term values concerning $v_{(2)}$ is somewhat poor since higher order terms in the Dunham expansion are neglected as the corresponding coefficients are not available. Please note, an electric dipole transition from the Feshbach state towards $(2)^1\Sigma_g^+$ is not possible owing to selection

$v_{(2)}$	T [cm^{-1}]
0	9623.82
1	9654.97
2	9686.14
3	9717.33
4	9748.54
5	9779.78
6	9811.04
7	9842.32
8	9873.62
9	9904.94
10	9936.29

Table 6.7: Term values $T(v_{(2)})$ of vibrational states $v_{(2)} = 0$ to 10 corresponding to the $(2)^1\Sigma_g^+$ potential of Rb$_2$ estimated using the Dunham coefficients provided in Ref. [203].

rules. Thus, any influence of $(2)^1\Sigma_g^+$ on the spectra shown in Figs. 6.8 and 6.9 would be related to coupling mechanisms between potentials shifting the energies of relevant states.

7 Population Distribution of Product States Following Three-Body Recombination in an Ultracold Atomic Gas

Arne Härter, Artjom Krükow, Markus Deiß, Björn Drews, and Johannes Hecker Denschlag

Institut für Quantenmaterie and Center for Integrated Quantum Science and Technology IQST, Universität Ulm, 89069 Ulm, Germany

Eberhard Tiemann

Institut für Quantenoptik, Leibniz Universität Hannover, 30167 Hannover, Germany

Three-body recombination is a collision between three atoms where two atoms combine to form a molecule and the third atom carries away part of the released reaction energy. Here, we experimentally determine for the first time the population distribution of the molecular reaction products after a three-body recombination for non-resonant particle interactions. The key to our measurements is a sensitive detection scheme that combines the photoionization of the molecules with subsequent ion trapping. Using an ultracold ^{87}Rb gas at very low kinetic energy below $h \times 20$ kHz, we find a broad population of final states with binding energies of up to $h \times 750$ GHz. This is in contrast with previous experiments, performed in the resonant interaction regime, that found a dominant population of only the most weakly bound molecular state or the occurrence of Efimov resonances. This work may contribute to the development of an in-depth model that can qualitatively and quantitatively predict the reaction products of three-body recombination.

7.1 Introduction

Whereas cold collisions of two atoms are well understood, the addition of a third collision partner markedly complicates the interaction dynamics. In the context of Bose-Einstein condensation in atomic gases, three-body recombination plays a crucial role [205-208] and it constitutes a present frontier of few-body physics [209-211]. Until now, recombination events were mainly investigated by measuring atom loss rates. Discussions of the final states populated in the recombination process were restricted to the special case of resonant interactions [212, 213] and culminated in the observations of Efimov resonances [214-216] and of molecules in the most weakly bound states [217, 218]. However, in the more general case of non-resonant interaction, that is, a modulus of the scattering length smaller than or comparable to the van der Waals radius, the recombination products might depend on details of the interaction potential. In fact, ongoing theoretical studies using simplified models indicate that recombination does not necessarily always favour the most weakly bound state (J. d'Incao, private communication; see also Ref. [219]). In general, recombination processes are of fundamental interest in various physical systems [205, 220, 221]. The control and tunability of ultracold atomic systems provide an experimental testbed for a detailed understanding of the nature of these processes.

Here, we demonstrate the probing of molecules with binding energies up to $h \times 750\,\text{GHz}$ (where h is Planck's constant) generated through three-body recombination of ultracold thermal ^{87}Rb atoms. We produce the atomic sample in an optical dipole trap located within a linear Paul trap. The recombination and detection process is illustrated in Fig. 7.1(a)-(d). Following a recombination event, the created Rb_2 molecule can undergo resonance-enhanced multi-photon ionization (REMPI) by absorbing photons from the dipole trap laser at a wavelength of around 1064.5 nm. The ion is then captured in the Paul trap and detected essentially background-free with very high sensitivity on the single-particle level. Fig. 7.1(e) shows a simplified scheme of the Rb_2 and Rb_2^+ potential energy curves. From weakly bound molecular states, three photons suffice to reach the molecular ionization threshold. An additional photon may dissociate the molecular ion. By scanning the frequency of the dipole trap laser by more than 60 GHz we obtained a high-resolution spectrum featuring more than 100 resonance peaks. This dense and complex spectrum contains information concerning which vibrational, rotational and hyperfine levels of the Rb_2 molecule are populated. We present an analysis of these data and make a first assignment of the most prominent resonances. This assignment indicates that in the recombination events a broad range of levels is populated in terms of vibrational, rotational, electronic and nuclear spin quantum numbers.

7.2 Experimental scheme

Our experimental scheme to detect cold molecules makes use of the generally excellent detection efficiencies attainable for trapped ions. It is related to proven techniques where cold molecules in magneto-optical traps were photoionized from the singlet and triplet ground states [121, 222-226] (see also Ref.[227]). Our method is unique as it introduces the use of a hybrid atom-ion trap that significantly improves the detection sensitivity. We perform the following experimental
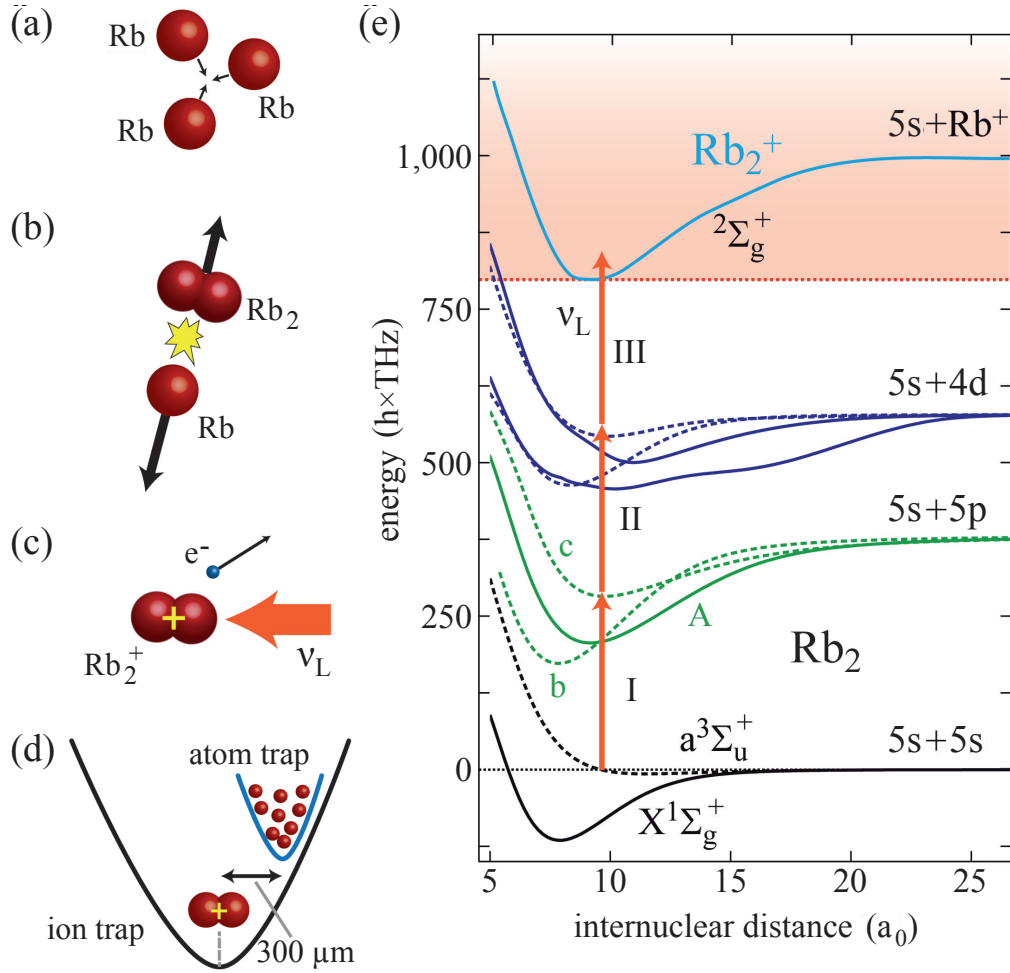
Figure 7.1: Illustration of recombination and ionization in the atom-ion trap. (a,b) A three-body collision in the ultracold gas of ^{87}Rb atoms (a) leads to a recombination event in which a Rb$_2$ molecule is formed with high kinetic energy (b). (c) While the atom is lost from the trap, the molecule can be photoionized in a REMPI process and trapped in the Paul trap. (d) The relative positions of the atom and ion trap centers are shifted by about 300 μm to avoid atom–ion collisions. (e) Potential energy curves of the Rb$_2$ and Rb$_2^+$ molecule adapted from Refs. [121, 228]. The curves A, b, c are $A^1\Sigma_u^+$, $b^3\Pi_u$, $c^3\Sigma_u^+$. The internuclear distance is given in units of Bohr radii a_0. A REMPI path with three photons is shown. It can create Rb$_2^+$ ions in vibrational states up to $v \approx 17$.

sequence. A thermal atomic sample typically containing $N_{\text{at}} \approx 5 \times 10^5$ spin-polarized ^{87}Rb atoms in the $|F = 1, m_F = -1\rangle$ hyperfine state is prepared in a crossed optical dipole trap at a magnetic field of about 5 G. The trap is positioned onto the nodal line of the radiofrequency

field of a linear Paul trap. Along the axis of the Paul trap the centers of the atom and ion trap are separated by about $300\,\mu\mathrm{m}$ to avoid unwanted atom-ion collisions [Fig. 7.1(d)]. At atomic temperatures of about $700\,\mathrm{nK}$ and peak densities $n_0 \approx 5 \times 10^{13}\,\mathrm{cm}^{-3}$ the total three-body recombination rate in the gas is $\Gamma_{\mathrm{rec}} = L_3 n_0^2 N_{\mathrm{at}}/3^{5/2} \approx 10\,\mathrm{kHz}$. Here, the three-body loss rate coefficient L_3 was taken from Ref. [207]. At the rate Γ_{rec}, pairs of Rb_2 molecules and Rb atoms are formed as final products of the reactions. Both the atom and molecule would generally be lost from the shallow neutral particle trap owing to the comparatively large kinetic energy they gain in the recombination event (in our case typically of the order of a few $\mathrm{K} \times k_{\mathrm{B}}$, where k_{B} is the Boltzmann constant). The molecule, however, can be state-selectively ionized in a REMPI process driven by the dipole trap laser. All of these molecular ions remain trapped in the deep Paul trap and are detected with single-particle sensitivity (Methods). In each experimental run, we hold the atomic sample for a time $\tau \approx 10\,\mathrm{s}$. After this time we measure the number of produced ions in the trap from which we derive (after averaging over tens of runs) the ion production rate Γ_{ion} normalized to a cloud atom number of 10^6 atoms.

As a consistency check of our assumption that Rb_2 molecules are ionized in the REMPI process, we verify the production of Rb_2^+ molecules. For this, we perform ion mass spectrometry in the Paul trap (Methods). We detect primarily molecular Rb_2^+ ions, a good fraction of atomic Rb^+ ions but no Rb_3^+ ions. Our experiments show that Rb^+ ions are produced in light-assisted collisions of Rb_2^+ ions with Rb atoms on timescales below a few milliseconds. Details of this dissociation mechanism are under investigation and will be discussed elsewhere.

7.3 Dependence of the ion production on atomic density, laser frequency and laser intensity

In the following, we analyze the dependence of the ion production rate on atomic density as well as on laser frequency and intensity. This will ultimately help to understand the three-body recombination process.

7.3.1 Density dependence

Two pathways for the production of our neutral Rb_2 molecules come immediately to mind. One pathway is far-off-resonant photoassociation of two colliding Rb atoms (here with a detuning of about $500\,\mathrm{GHz} \times h$). This pathway can be ruled out using several arguments, the background of which will be discussed in more depth later. For one, we observe molecules with a parity that is incompatible with photoassociation of totally spin-polarized ensembles. Furthermore, we observe a dependence of the ion production rate on light intensity that is too weak to explain photoassociation.

The second pathway is three-body recombination of Rb atoms. Indeed, by investigating the dependence of the ion production rate Γ_{ion} (which is normalized to a cloud atom number of 10^6 atoms) on atomic density, we find the expected quadratic dependence (Fig. 7.2). For this measurement the density was adjusted by varying the cloud atom number while keeping the light intensity of the dipole trap constant.
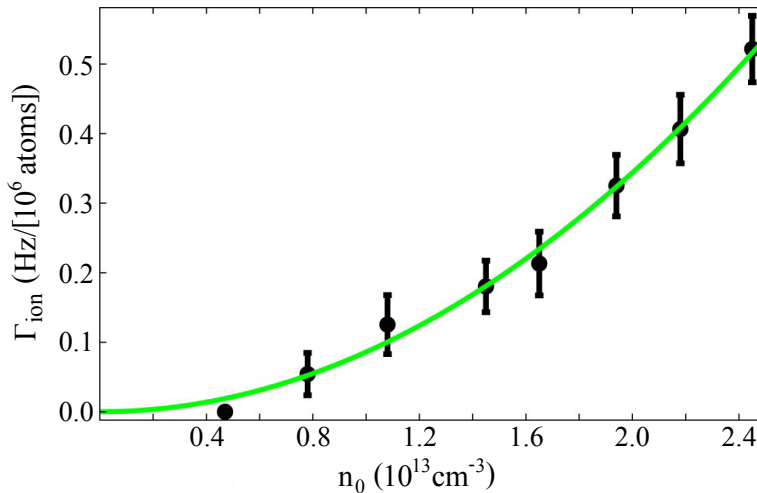
Figure 7.2: Dependence of the ion production rate Γ_{ion} on atomic density. Γ_{ion} is normalized to a cloud atom number of 10^6 atoms. The data are well described by a quadratic fit (solid green line). They were taken at a constant dipole trap laser intensity $I_L = 36\,\mathrm{kWcm^{-2}}$ and a laser frequency of $\nu_L = 281,630\,\mathrm{GHz}$. The error bars indicate statistical uncertainties and represent one standard deviation from the mean.

7.3.2 Dependence on laser frequency - REMPI spectrum

Next, we investigate the dependence of the ion production rate on the wavelength of the narrow-linewidth dipole trap laser (Methods). We scan the wavelength over a range of about $0.3\,\mathrm{nm}$ around $1064.5\,\mathrm{nm}$, corresponding to a frequency range of about $60\,\mathrm{GHz}$. Typical frequency step sizes are 50 or $100\,\mathrm{MHz}$. We obtain a rich spectrum of resonance lines that is shown in Fig. 7.3(a). The quantity $\bar{\Gamma}_{ion}$ denotes the ion production rate normalized to the atom number of the cloud and to the square of the atomic peak density. We find strongly varying resonance strengths and at first sight fairly irregular frequency spacings. In the following we will argue that most resonance lines can be attributed to respective well-defined molecular levels (resolving vibrational, rotational and often even hyperfine structure) that have been populated in the recombination process. These levels are located in the triplet or singlet ground state, $a^3\Sigma_u^+$ and $X^1\Sigma_g^+$, respectively. The relatively dense distribution of these lines reflects that a fairly broad range of states is populated. A direct assignment of the observed resonances is challenging, as it hinges on the precise knowledge of the level structure of all the relevant ground and excited states. In the following we will access and understand the data step by step.

One feature of the spectrum that stands out is the narrow linewidth of many lines. For example, Fig. 7.3(b) shows a resonance of which the substructures have typical half-widths $\Delta\nu_r \approx 50\mathrm{MHz}$. This allows us to roughly estimate the maximal binding energy of the molecules involved. As the velocity of the colliding ultracold atoms is extremely low, the kinetics of the
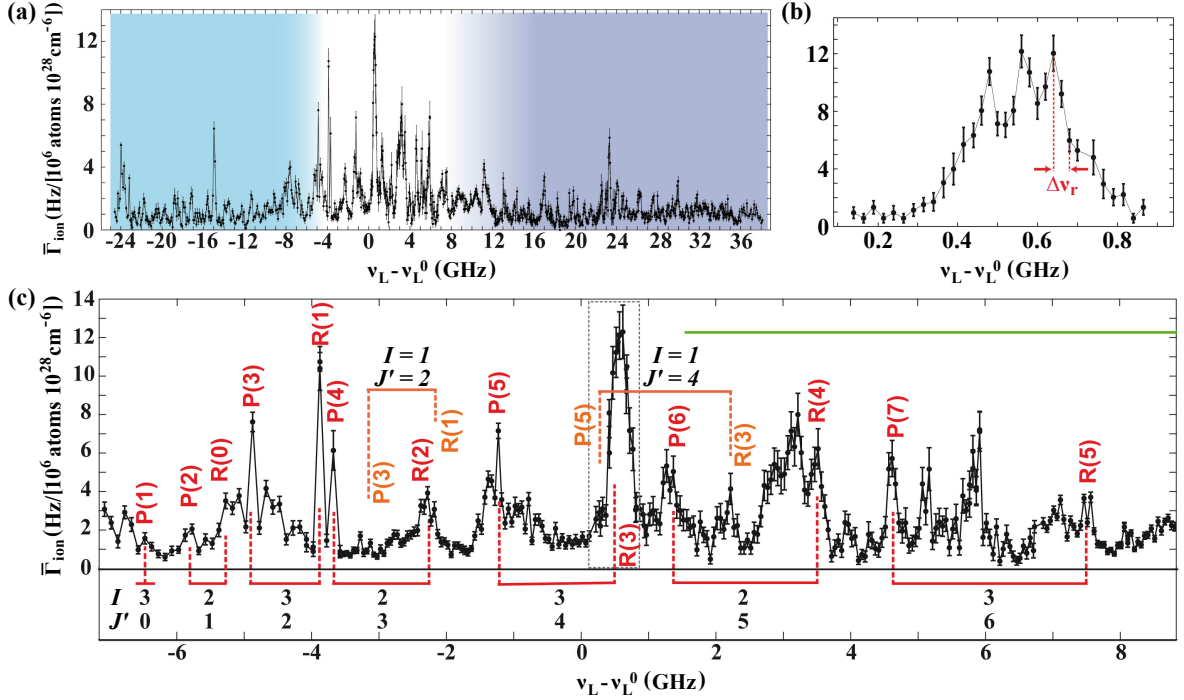
Figure 7.3: REMPI spectrum. (a) A scan of the dipole trap laser frequency ν_L over more than 60 GHz around an offset frequency $\nu_L^0 = 281.610$ THz shows a multitude of resonance lines. Each data point is the result of 30-60 repetitions of the experiment with ion detection on the single-particle level. The total spectrum was obtained over a time span of 2 months. Checks of the long-term consistency of resonance positions and strengths were performed. Spectral regions dominated by transitions to $c^3\Sigma_g^+$ are indicated by the shaded areas in dark and light blue (0_g^- and 1_g component, respectively). (b) High-resolution scan of the strong resonance at $\nu_L - \nu_L^0 \approx 0.5$ GHz. (c) Central spectral region with assigned P/R branches of the transition $X^1\Sigma_g^+(v = 115) \rightarrow A^1\Sigma_u^+(v' = 66)$. The corresponding quantum numbers I and J' are given. $P(J)$ marks the transition $J \rightarrow J+1$; $R(J)$ marks the transition $J \rightarrow J-1$. These lines can be grouped into pairs sharing the same J' of the excited state and I quantum number. The region where also transitions to $b^3\Pi_u$ appear is marked by a green horizontal bar. The error bars indicate statistical uncertainties and represent one standard deviation from the mean.

recombination products is dominated by the released molecular binding energy E_b. Owing to energy and momentum conservation the molecules will be expelled from the reaction with a molecular velocity $v_{Rb_2} = \sqrt{2E_b/(3m_{Rb_2})}$ where m_{Rb_2} is the molecular mass. The molecular resonance frequency ν_0 will then be Doppler-broadened with a half-width $\Delta\nu_D = \sqrt{3}\nu_0 v_{Rb_2}/2c$. Here, c is the speed of light. By comparing $\Delta\nu_D$ to the observed values of $\Delta\nu_r$ we estimate a

maximal binding energy of the order of $E_{\text{b,max}} \approx h \times 2.5\,\text{THz}$. This simple analysis overestimates the value $E_{\text{b,max}}$ because it neglects the natural linewidth of the transition and possible saturation broadening. Still, it already strongly constrains the possibly populated molecular levels that are observed in our experiment.

7.3.3 Dependence on laser intensity

Next, we investigate the dependence of the ion production rate on laser intensity I_{L}. In our experimental setup, this measurement is rather involved because the laser driving the REMPI process also confines the atomic cloud. Thus, simply changing only the laser intensity would undesirably also change the density n_0 of the atoms. To prevent this from happening we keep n_0 constant ($n_0 \approx 5 \times 10^{13}\,\text{cm}^{-3}$) by adjusting the atom number and temperature appropriately. Owing to these experimental complications we can vary I_{L} only roughly by a factor of 2 [Fig. 7.4(a)]. We set the laser frequency to the value of $\nu_{\text{L}} = \nu_{\text{L}}^0 \equiv 281,610\,\text{GHz}$, on the tail of a large resonance (Fig. 7.3). The atomic temperatures in this measurement range between $500\,\text{nK}$ and $1.1\,\mu\text{K}$, well above the critical temperatures for Bose-Einstein condensation. The atomic densities can therefore be described using a Maxwell-Boltzmann distribution. Assuming a simple power-law dependence of the form $\bar{\Gamma}_{\text{ion}} \propto I_{\text{L}}^\alpha$ we obtain the best fit using an exponent $\alpha = 1.5(1)$ [solid green line in Fig. 7.4(a)]. This fit is between a linear and a quadratic intensity dependence (dashed red and blue lines, respectively). Thus, at least two of the three transitions composing the ionization process are partially saturated at the typical intensities used.

To better circumvent possible density variations of the atomic cloud induced by changes in laser intensity, we employ a further method that enables us to vary the intensity with negligible effects on the atomic sample. We achieve this by keeping the time-averaged intensity $\langle I_{\text{L}} \rangle$ constant and comparing the ion production rates within a continuous dipole trap and a chopped dipole trap in which the intensity is rapidly switched between 0 and $2I_{\text{L}}$. In both cases the trap is operated at an intensity $\langle I_{\text{L}} \rangle \approx 15\,\text{kWcm}^{-2}$. In the chopped configuration the intensity is switched at a frequency of 100 kHz so that the atoms are exposed to the light for $5\,\mu\text{s}$ followed by $5\,\mu\text{s}$ without light. It should be noted that molecules formed in the dark period with sufficiently high kinetic energies may leave the central trapping region before the laser light is switched back on. They are then lost for our REMPI detection. Taking into account the molecular velocity and the transverse extensions of the laser beams we can estimate that this potential loss mechanism leads to errors of less than 30%, even at the highest binding energies relevant to this work ($E_{\text{b}} \approx h \times 750\,\text{GHz}$, see below). We did not observe evidence of such losses experimentally. Investigations were made by changing the chopping frequency. We define R as the ratio of the ion production rates in the chopped and the continuous trap configuration. Figure 7.4(b) shows the results of these measurements for various laser frequencies ν_{L}. We find a value $R \approx 1.5$ for off-resonant frequency settings $\nu_{\text{L}} - \nu_{\text{L}}^0 < 0.4\,\text{GHz}$, in good agreement with the result presented in Fig. 7.4(a). When scanning the laser onto resonance at $\nu_{\text{L}} - \nu_{\text{L}}^0 \approx 0.45\,\text{GHz}$ [Fig. 7.3(b)] we obtain $R \approx 1$. This result indicates a linear intensity dependence of the REMPI process in the resonant case, which is explained by the saturation of two of the three molecular transitions involved. It is known that transitions into the ionization continuum [photon III,
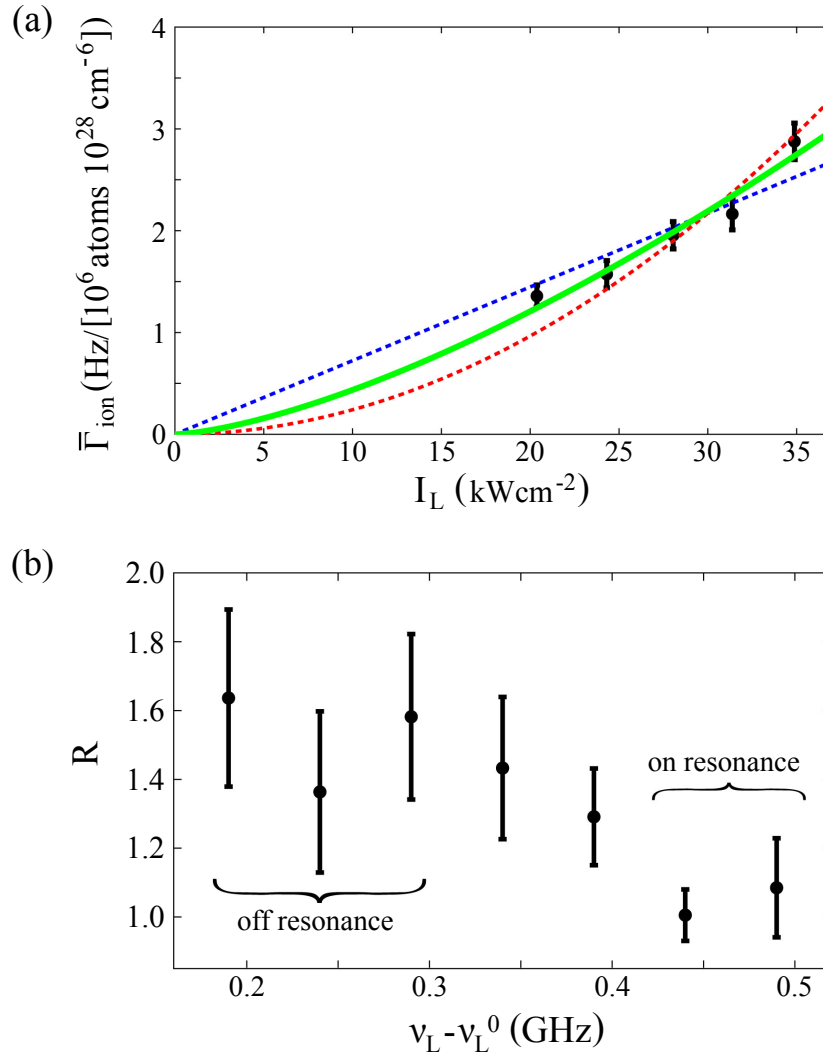
Figure 7.4: Dependence of the ion production rate on the intensity of the dipole trap laser. (a) Assuming a power-law dependence $\bar{\Gamma}_{\mathrm{ion}} \propto I_{\mathrm{L}}^{\alpha}$, the best fit to the data is achieved for $\alpha \approx 1.5$ (solid green line). Linear and quadratic fits are also given (blue and red dashed lines, respectively). (b) Measurement of the intensity dependence using a chopped dipole trap. The ratio $R \approx 1$ on resonance indicates saturation of both transitions I and II. The error bars indicate statistical uncertainties and represent one standard deviation from the mean.

Fig. 7.1(e)] will not saturate under the present experimental conditions. This means that the excitation pathway through photon I and II must be saturated and therefore both are close to resonance.

7.4 Assignment of observed resonances to molecular transitions

Given the wavelength range of about $1,064.5 \pm 0.15$ nm, an inspection of the level structure shows that photon I can only resonantly drive three different transitions that connect vibrational levels in states X and a to vibrational levels in states A, b and c [Fig. 7.1(e)]. Spectroscopic details for these transitions and the corresponding vibrational levels are given in the Methods and in Fig. 7.5[36]. From recent spectroscopic studies [122, 124, 229] and further measurements in our laboratory the level structure of all relevant levels of the X, a, A, b, and c states is well known. The absolute precision of most of the level energies is far better than 1 GHz for low rotational quantum numbers J.

In the experimental data [Fig. 7.3(a)] the central region from $\nu_{\mathrm{L}} - \nu_{\mathrm{L}}^0 = -6$ to 7 GHz is marked by several prominent resonances that are significantly stronger than those observed throughout the rest of the spectrum. These resonance peaks can be assigned to transitions from the X ground state to A and b states. The prominence of these singlet transitions is explained by the near degeneracy of levels due to small hyperfine splittings. Indeed, by analyzing these strong resonances with regard to line splittings and intensities it was possible to consistently assign rotational ladders for total nuclear spin quantum numbers $I = 1, 2, 3$ for the transition $X\,(v = 115) \to A\,(v' = 66)$. The starting point of the rotational ladder for $I = 2$ was fixed by spectroscopic measurements in our laboratory. At frequencies $\nu_{\mathrm{L}} - \nu_{\mathrm{L}}^0 \gtrsim 2$ GHz additional strong lines appear that we attribute to the $X\,(v = 109) \to b\,(v' = 73)$ transition. The fact that we observe X state molecules with $I = 1$, 2, 3 is interesting because for $I = 1$, 3 the total parity of the molecule is negative, whereas for $I = 0$, 2 it is positive. However, a two-body collision state of our spin-polarized Rb atoms necessarily has positive total parity due to symmetry arguments and a photoassociation pathway would lead to ground-state levels with positive parity. The observed production of molecules with negative total parity must then be a three-body collision effect.

We now consider the role of secondary atom-molecule collisions that would change the product distribution owing to molecular relaxation. Two aspects are of importance: depopulation of detected molecular levels, and population of detected molecular levels through relaxation from more weakly bound states. In our experiments reported here we detect molecules that are formed in states with binding energies of the order of hundreds of GHz $\times h$. These molecules leave the reaction with kinetic energies of several K $\times k_{\mathrm{B}}$. At these energies the rate coefficients for depopulating atom-molecule collisions are small (see for example Ref.[219]) and the collision probability before the molecule is either ionized or has left the trap is below 1%.

For the population processes, we can estimate an upper bound for rate coefficients by assuming recombination to occur only into the most weakly bound state with a binding energy of $24\,\mathrm{MHz} \times h$. In this case subsequent atom-molecule collision rates will be roughly comparable to those expected in the ultracold limit. At typical rate coefficients of $10^{-10}\,\mathrm{cm}^3\mathrm{s}^{-1}$ (Refs.[230-

---

[36]Please note that in the original publication of A. Härter *et al.* [36] the relevant excitation energies with respect to $A^1\Sigma_u^+$ and $b^3\Pi_u$ were assigned to the vibrational levels $v'_A = 68$ and $v'_b = 72$. Later it turned out that actually these energies correspond to $v'_A = 66$ and $v'_b = 73$, respectively. Therefore, I changed the numbering accordingly in the present reprint.
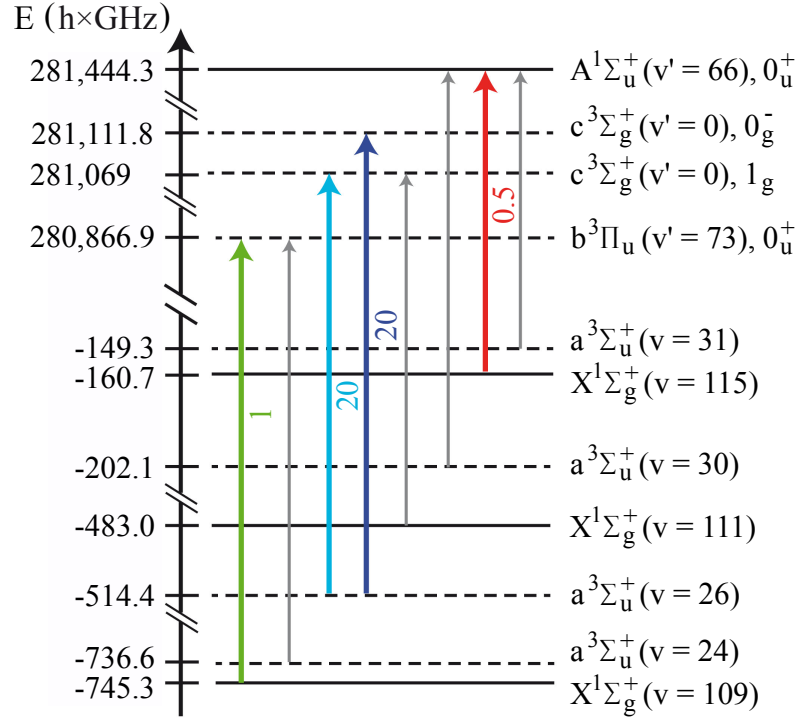
Figure 7.5: Overview over relevant molecular levels and transitions. The vertical axis denotes the energy E_{b} of the energetically lowest levels of each vibrational manifold with respect to the $5S + 5S$ asymptote. Colored thick arrows represent molecular transitions relevant to the spectrum of Fig. 7.3. The expected relative strengths of these transitions are also given. Grey arrows mark transitions that occur in the relevant spectral region but are so weak that they can be neglected (for further spectroscopic details, see Methods). We identify three main molecular transitions for the initial step of the REMPI process. The blue arrows indicate molecules in the $v = 26$ vibrational level of the $a^3\Sigma_u^+$ potential that are excited to the $v' = 0$ level of the $c^3\Sigma_g^+$ potential. This level is split into a 1_g and a 0_g^- component. The red arrow is an excitation from $X^1\Sigma_g^+$ ($v = 115$) to $A^1\Sigma_u^+$ ($v' = 66$). The green arrow is an excitation from $X^1\Sigma_g^+$ ($v = 109$) to $b^3\Pi_u$ ($v' = 73$). This transition becomes possible through the strong spin-orbit coupling of the A and b states.

233]) and the atomic densities $n_0 \sim 1 \times 10^{13}\,\mathrm{cm}^{-3}$ used in the measurement shown in Fig. 7.2, the collision probability before the molecule leaves the atom cloud is around 5%. This small probability grows linearly with density so that the density dependence of the ion production rate should show a significant cubic contribution if secondary collisions were involved (as expected for this effective four-body process). This is inconsistent with the data and thus indicates that the population that we detect is not significantly altered by secondary collisions.

We can roughly estimate the range of molecular rotation J of the populated levels in the

ground state. The strong, isolated lines that we have assigned to the $X(v=115) \rightarrow A(v'=66)$ transition are all contained within a relatively small spectral region ($|\nu_{\rm L} - \nu_{\rm L}^0| < 6$ GHz) and are explained by rotational quantum numbers $J \leq 7$. Population of higher rotational quantum numbers would result in a continuation of the strong resonance lines stretching to transition frequencies beyond $\nu_{\rm L} - \nu_{\rm L}^0 = 10$ GHz, which we do not observe. Similarly, if only rotational quantum numbers $J \leq 5$ were populated, a spectrum would result that does not have enough lines to explain the data. Thus, we can roughly set the limits on the molecular rotation to $J \leq 7$, a value that is also consistent with our observations of the spread of the transitions $X \rightarrow b$ and $a \rightarrow c$ (Fig. 7.5). Finding quantum numbers as high as $J = 7$ is remarkable because the three-body collisions at microkelvin temperatures clearly take place in a s-wave regime, that is, at vanishing rotational angular momentum. Hence, one could expect to produce X state molecules dominantly at $J = 0$, which, however, we do not observe.

Despite the limited spectral range covered by our measurements, we can already estimate the number of molecular vibrational levels populated in the recombination events. From the three states $X(v=109)$, $a(v=26)$ and $X(v=115)$ that we can observe within our wavelength range, all deliver comparable signals in the spectrum of Fig. 7.3. This suggests that at least all vibrational states more weakly bound than $X(v=109)$ should be populated, a total of 38 vibrational levels (counting both singlet and triplet states). This is a significant fraction of the 169 existing levels of the X and a states, although restricted to a comparatively small range of binding energies.

7.5 Conclusion

In conclusion, our work represents a first experimental step towards a detailed understanding on how the reaction channels in three-body recombination are populated. A full understanding will clearly require further experimental and theoretical efforts. On the experimental side the scanning range has to be increased and it could be advantageous to switch to a two-color REMPI scheme in the future. Such studies may finally pave the way to a comprehensive understanding of three-body recombination, which includes the details of the final products.

Reaching beyond the scope of three-body recombination, the great sensitivity of our detection scheme has enabled us to state-selectively probe single molecules that are produced at rates of only a few hertz. We thereby demonstrate a new scheme for precision molecular spectroscopy in extremely dilute ensembles.

7.6 Methods

7.6.1 Dipole trap and REMPI configuration

The crossed dipole trap is composed of a horizontal and a vertical beam focused to beam waists of $\sim 90\mu$m and $\sim 150\mu$m, respectively. It is positioned onto the nodal line of the radiofrequency field of the linear Paul trap with micrometer precision. The two trap centers are separated by about $300\,\mu$m along the axis of the Paul trap [Fig. 7.1(d)]. In a typical configuration, the

trap frequencies of the dipole trap are $(175, 230, 80)$ Hz resulting in atom cloud radii of about $(6, 7, 16)$ µm. The short-term frequency stability of the dipole trap laser source is of the order of 1 kHz and it is stabilized against thermal drifts to achieve long-term stability of a few megahertz. The two beams of the dipole trap are mutually detuned by 160 MHz to avoid interference effects in the optical trap. Consequently, two frequencies are in principle available to drive the REMPI process. However, the intensity of the horizontal beam is 4 times larger than the one of the vertical beam and we have not directly observed a corresponding doubling of lines. Further details on the atom-ion apparatus are given in Ref. [234].

7.6.2 Paul trap configuration

The linear Paul trap is driven at a radiofrequency of 4.17 MHz and an amplitude of about 500 V resulting in radial confinement with trap frequencies of $(\omega_{x,Ba}, \omega_{y,Ba}) = 2\pi \times (220, 230)$ kHz for a $^{138}\mathrm{Ba}^+$ ion. Axial confinement is achieved by applying static voltages to two endcap electrodes yielding $\omega_{z,Ba} = 2\pi \times 40.2$ kHz. The trap frequencies for dark Rb_2^+ and Rb^+ ions produced in the REMPI processes are $(m_{Ba}/m_{dark} \times \omega_{x,Ba},\ m_{Ba}/m_{dark} \times \omega_{y,Ba},\ \sqrt{m_{Ba}/m_{dark}} \times \omega_{z,Ba})$, where m_{Ba} and m_{dark} denote the mass of the Ba^+ ion and the dark ion, respectively. The depth of the Paul trap depends on the ionic mass and exceeds 2 eV for all ionic species relevant to this work.

7.6.3 Ion detection methods

We employ two methods to detect Rb_2^+ and Rb^+ ions, both of which are not amenable to fluorescence detection. In the first of these methods we use a single trapped and laser-cooled $^{138}\mathrm{Ba}^+$ ion as a probe. By recording its position and trapping frequencies in small ion strings with up to 4 ions we detect both the number and the masses of the ions following each REMPI process (see also Ref. [235]). The second method is based on measuring the number of ions in the Paul trap by immersing them into an atom cloud and recording the ion-induced atom loss after a hold time of 2 s (see also Ref. [236]). During this detection scheme, we take care to suppress further generation of ions by working with small and dilute atomic clouds and by detuning the REMPI laser from resonance. Both methods are background-free in the sense that no ions are captured on timescales of days in the absence of the atom cloud. Further information on both detection methods is given in the Supplementary Information of Ref. [36] given in section 7.8[37].

7.6.4 Spectroscopic details

Spin-orbit and effective spin-spin coupling in the A, b, and c states lead to Hund's case (c) coupling where the relevant levels of states A and b have 0_u^+ symmetry whereas the levels of state $c^3\Sigma_g^+$ are grouped into 0_g^- and 1_g components. The level structure of the 0_u^+ states is quite simple as it is dominated by rotational splittings. Typical rotational constants for the

---

[37]Also available at `http://www.nature.com/nphys/journal/v9/n8/extref/nphys2661-s1.pdf`.

electronically excited states are of the order of $400\,\mathrm{MHz}$; for the weakly bound X and a states they are around $100 - 150\,\mathrm{MHz}$.

Figure 7.5 shows the relevant optical transitions between the X, a states and the A, b, c states in our experiment. For the given expected relative strengths of these transitions, we consider only Franck-Condon factors and the mixing of singlet and triplet states, and electronic transition moments are ignored. The colored arrows correspond to transitions with large enough Franck-Condon factors (typically $10^{-2}-10^{-3}$) so that at laser powers of $\approx 10^4\,\mathrm{Wcm^{-2}}$ resonant transitions can be well saturated. Transitions marked with grey arrows can be neglected owing to weak transition strengths, being forbidden in first order by dipole selection rules.

7.7 Acknowledgements and author contributions

7.8 Supplementary Information

In this Supplementary Information we describe two methods that we employ to detect small numbers of $\mathrm{Rb_2^+}$ and $\mathrm{Rb^+}$ ions in our linear Paul trap.

7.8.1 Ion detection method 1

To implement our first ion detection method allowing mass-sensitive detection of "dark" ions we rely on the presence of a single "bright" ion in the trap. Information on additional ions can be extracted from its fluorescence position. When using this method, our experimental procedure begins with the loading of a single $^{138}\mathrm{Ba^+}$ ion into our linear Paul trap. We laser-cool the ion and image its fluorescence light onto an electron-multiplying charge-coupled device camera. This enables us to determine the position of the trap center to better than $100\,\mathrm{nm}$. The ion is confined at radial and axial trapping frequencies $\omega_{\mathrm{r,Ba}} \approx 2\pi\times220\mathrm{kHz}$ and $\omega_{\mathrm{ax,Ba}} \approx 2\pi\times40.2\mathrm{kHz}$ and typically remains trapped on timescales of days. Next, we prepare an ultracold atomic sample in the crossed dipole trap. At typical atomic temperatures of about $700\,\mathrm{nK}$ the atom cloud has radial and axial extensions of about $7\,\mathrm{\mu m}$ and $15\,\mathrm{\mu m}$ and is thus much smaller than the trapping volume of our Paul trap. To avoid atom-ion collisions we shift the $\mathrm{Ba^+}$ ion by about $300\,\mathrm{\mu m}$ with respect to the atom cloud before the atomic sample arrives in the Paul trap. The shifting is performed along the axis of the trap by lowering the voltage on one of the endcap electrodes. Additionally, we completely extinguish all resonant laser light so that the atoms are only subjected to the light of the dipole trap. The atomic sample is moved into the

center of the radial trapping potential of the Paul trap and is typically held at this position for a time $\tau_{\text{hold}} \approx 10\,\text{s}$. Despite the axial offset from the center of the Paul trap, the atom cloud at this position is fully localized within the trapping volume of the Paul trap. After the hold time the sample is detected using absorption imaging. Subsequently, the ion cooling beams are switched back on for fluorescence detection of the Ba^+ ion.

The presence of a second ion in the trap leads to positional shifts of the $^{138}\text{Ba}^+$ ion by distances on the order of $10\,\text{µm}$ (see Fig. 7.6). We make use of the mass-dependent trap frequencies of the Paul trap to gain information on the ion species trapped. In a two-ion Coulomb crystal composed of a Ba^+ ion and a dark ion, the axial center-of-mass frequency $\omega_{\text{ax,2ion}}$ shifts with respect to $\omega_{\text{ax,Ba}}$ depending on the mass of the dark ion m_{dark} [237]. We measure $\omega_{\text{ax,2ion}}$ by modulating the trap drive at frequencies ω_{mod} and by monitoring the induced axial oscillation of the Ba^+ ion, visible as a blurring of the fluorescence signal. In this way, after each ion trapping event, we identify a resonance either at $\omega_{\text{mod}} \approx 2\pi \times 44\,\text{kHz}$ or $\omega_{\text{mod}} \approx 2\pi \times 38\,\text{kHz}$ corresponding to $m_{\text{dark}} = 87\,\text{u}$ and $m_{\text{dark}} = 174\,\text{u}$, respectively (see table 7.1).

We have expanded this method for ion strings with up to four ions including the Ba^+ ion. For this purpose, we perform the following step-by-step analysis.

1. The position x of the Ba^+ ion with respect to the trap center is detected. If $x \neq 0$, the value of x allows us to directly determine the total number of ions in the string.

2. If $x = 0$ we need to distinguish between a single Ba^+ ion and a three-ion string with Ba^+ at its center. This is done by modulating the trap drive at $\omega_{\text{ax,Ba}}$, thereby only exciting the Ba^+ ion if no further ions are present.

3. We destructively detect the Rb^+ ions by modulating the trap drive on a $5\,\text{kHz}$ wide band
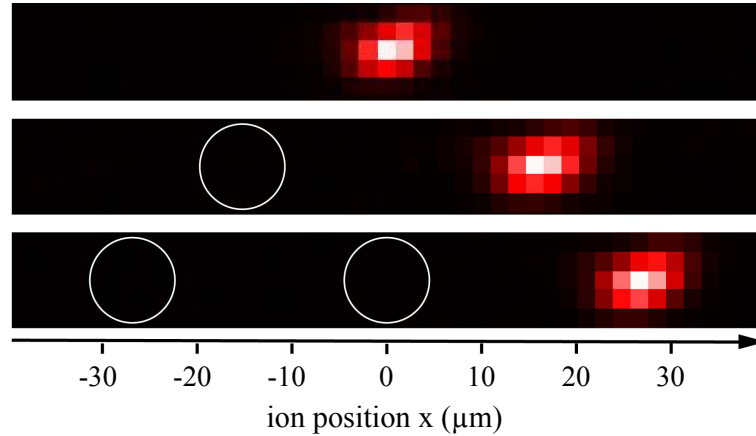
Figure 7.6: Ion detection using a $^{138}\text{Ba}^+$ ion. Positional shifts of the fluorescence of the Ba^+ ion and measurements of the trap oscillation frequencies allow us to perform mass-sensitive detection of up to three "dark" ions in the trap.

ion species	$\omega_{\mathrm{ax,2ion}}/2\pi$ [kHz]	$\omega_{\mathrm{r}}/2\pi$ [kHz]
$^{138}\mathrm{Ba}^+$ and $^{138}\mathrm{Ba}^+$	40.2	220.0
$^{138}\mathrm{Ba}^+$ and $^{87}\mathrm{Rb}^+$	44.0	345.3
$^{138}\mathrm{Ba}^+$ and $^{87}\mathrm{Rb}_2^+$	37.7	170.7

Table 7.1: Trap oscillation frequencies of two-ion crystals.

around $2 \times \omega_{\mathrm{r,Rb}}/(2\pi) = 691\,\mathrm{kHz}$. This selectively removes only Rb^+ ions from the string making use of the relatively weak interionic coupling when exciting the ions radially.

4. Steps 1. and 2. are repeated to detect the number of remaining ions.

5. The Rb_2^+ ions are destructively detected via modulation around $2 \times \omega_{\mathrm{r,Rb_2}}/(2\pi) = 341\mathrm{kHz}$.

7.8.2 Ion detection method 2

We have also developed a second ion detection method that does not require an ion fluorescence
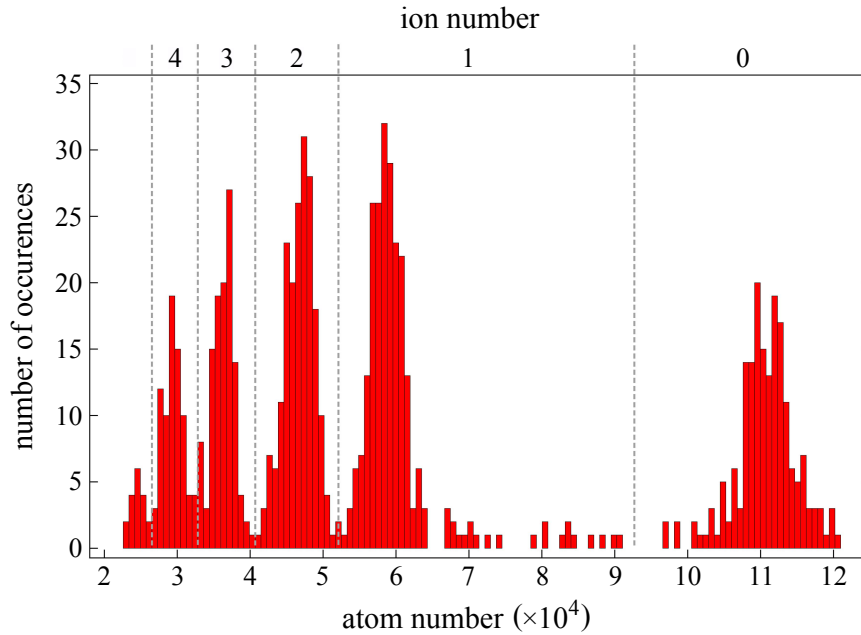
Figure 7.7: Ion detection method based on ion-induced atom loss. We overlap an ultracold atom cloud containing approximately 110,000 atoms with the center of the Paul trap. After an interaction time $\tau = 2\,\mathrm{s}$ we detect the ion-induced atom loss via absorption imaging of the atom cloud. The discrete number of trapped ions is clearly reflected in the displayed histogram of atom numbers.

signal. Instead, the trapped ions are detected via their interaction with an atomic sample. For this purpose, we produce a comparatively small atom cloud containing about 1×10^5 atoms at a density of a few $10^{12}\,\mathrm{cm}^{-3}$. In addition, we set the frequency of the dipole trap laser to an off-resonant value so that the production of additional ions during the ion probing procedure becomes extremely unlikely. We now fully overlap the ion and atom traps for an interaction time $\tau_\mathrm{int} = 2\,\mathrm{s}$. By applying an external electric field of several V/m we set the ion excess micromotion energy to values on the order of tens of $k_\mathrm{B} \times \mathrm{mK}$ [236, 238]. Consequently, if ions are present in the trap, strong atom losses occur due to elastic atom-ion collisions. Fig. 7.7 shows a histogram of the atom numbers of the probe atom samples consisting of the outcome of about 1,000 experimental runs. The histogram displays several peaks which can be assigned to the discrete number of ions in the trap. Up to five ions were trapped simultaneously and detected with high fidelity. The atom loss rate increases nonlinearly with ion number mainly because the interionic repulsion prevents the ions from all occupying the trap center where the atomic density is maximal. While ion detection method 2 does not distinguish ionic masses, it has advantages in terms of experimental stability and does not require the trapping of ions amenable to laser cooling or other fluorescence based detection techniques.

8 Concluding Remarks

In the following, I want to briefly summarize the main results of the thesis and discuss possible future investigations and further prospects of the setup.

8.1 Summary

At the moment, Rb_2 is one of the few nonpolar molecular species with which experiments at temperatures in the µK or even nK regime can be performed. In this thesis, I reported on results, where these dimers were controlled on the quantum level by means of laser pulse sequences and magnetic ramps. We investigated various precisely defined states within the vibrational ground state manifold ($v = 0$) of the lowest triplet potential, $a^3\Sigma_u^+$, as well as the hyperfine structure of $\Omega = 0^+$ levels of the spin-orbit coupled $A^1\Sigma_u^+ - b^3\Pi_u$ complex.

For this purpose, the molecules were held in a 3D optical lattice that allows to isolate them from each other. The corresponding potential depths for the three standing light waves depend on the state- and frequency-dependent, in general anisotropic, dynamical polarizability $\alpha(\omega)$ of the dimers. We demonstrated how this fact can be exploited to measure the degrees of alignment of the molecular axis with respect to each direction of space. The underlying method was applied to different states of $v = 0$ within $a^3\Sigma_u^+$. In order to access these energy levels we employed STIRAP transfer starting with weakly bound Feshbach dimers. Our studies show that the alignment of the molecular axis can be engineered by preparing an appropriate rotational state. Furthermore, we derived the dynamical polarizabilities parallel and orthogonal to the molecular axis of the Rb_2 dimer, $\alpha_\parallel = (8.9 \pm 0.9) \times 10^3$ a.u. and $\alpha_\perp = (0.9 \pm 0.4) \times 10^3$ a.u., respectively. Focusing on the isotropic, nonrotating case, a theoretical analysis of $\alpha(\omega)$ with respect to all vibrational levels of the $a^3\Sigma_u^+$ and $X^1\Sigma_g^+$ potentials was provided.

From the obtained spectroscopic results on the $A^1\Sigma_u^+ - b^3\Pi_u$ complex in Rb_2 we learned that interesting interactions can occur in strongly perturbed systems. The mixing of the singlet and triplet states and level shifts, both owing to spin-orbit couplings, have a significant influence on hyperfine structures in the $A-b$ manifold. This was revealed by our measurements for states with 0^+ symmetry and $J = 1$. Noticeably, the observed splittings of hyperfine levels can reach values which are orders of magnitude larger than expected. In addition, the spectra exhibit nonequal level spacings and a strong dependence on the vibrational quantum number. Using a simple model, we could explain the recorded combined hyperfine and Zeeman structures and extract quantitative information from the data.

8.2 Outlook

In view of the results discussed in this work I want to give an outline of several experiments that might be performed in the future.

- **Coherent superposition of molecular states:** Until now, we have performed experiments individually for various well-defined molecular quantum states of the $v_a = 0$ manifold of $a^3\Sigma_u^+$. Here, the high resolution achieved in our STIRAP transfer guaranteed the unambiguous population of the desired final energy level. A consequent next step would be the creation of superpositions of states. For the case of heteronuclear KRb, couplings between different rotational levels ($R = 0$ and 1) [59] as well as between different $R = 0$ hyperfine levels [45] of $v_X = 0$ within $X^1\Sigma_g^+$ were demonstrated using microwaves. In Ref. [59] dipolar spin-exchange interactions were observed in interferometry experiments with the superposition state of $R = 0$ and 1 applying the Ramsey technique. The fringe contrast as a function of the interrogation time showed oscillations in addition to an overall decay. With respect to Rb_2 and the lowest vibrational level of $a^3\Sigma_u^+$ the rotational states $R = 0$ and 2 might be used to encode a spin. However, according to selection rules there is no obvious route to create a superposition of $R = 0$ and 2 employing microwave techniques. Instead, an optical Raman scheme would be feasible and easy to realize since the relevant level energies are precisely known from our studies. It would be very interesting to measure the dephasing of the spin-coherence dependent on the tunneling rates of the molecules in the optical lattice and due to collisions. Please note, Rb_2 is nonpolar and we work with triplet molecules. A comparison of the results to those obtained with polar dimers in their singlet ground state could lead to new insights.

- **$A - b$ spectroscopy:** In the present thesis we experimentally investigated the hyperfine structure within the $A^1\Sigma_u^+ - b^3\Pi_u$ complex for states with 0^+ symmetry and $J = 1$ ($\vec{J} = \vec{R} + \vec{L} + \vec{S}$). It would be interesting to extend these studies to levels of higher angular momentum J. According to selection rules this is not possible in a direct way, when starting from the nonrotating Feshbach state at $B \sim 1000$ G. However, rotationally excited, weakly bound molecules can be prepared by tuning the magnetic field and bridging avoided crossings via adiabatic population transfer with radiofrequency fields [125]. Thereby, higher J levels of the $A - b$ complex could in principle be addressed in single optical dipole transitions. Furthermore, in order to measure the splittings between the 0^+ and 0^- components of $b^3\Pi_u$ the ability to spectroscopically observe 0^- levels is required. As already mentioned in chapter 6, an excitation of molecules from the lowest singlet or triplet electronic state towards $b^3\Pi_u$ 0^- in a one-photon process is not allowed. Instead, a two-photon Raman scheme, i.e., dark state spectroscopy might be promising. For this purpose, the $(1)^3\Pi_g$ potential (cf. Fig. 3.12) possibly provides an appropriate intermediate level. But please note, both states $b^3\Pi_u$ as well as $(1)^3\Pi_g$ belong to the $5s + 5p$ atomic asymptote and consequently the Franck-Condon factors for transitions between levels of these potentials are in general very low. Therefore, a theoretical estimation of this quantity should be performed in order to identify the most adequate intermediate

states.

- **Scattering experiments with rotating molecules:** Recently, a theoretical investigation of the scattering of a particle with internal structure from a single slit was reported. In Refs. [239] and [240], Wolfgang P. Schleich and collaborators considered a rigid rotor, e.g., a diatomic molecule, slowly approaching a slit, which is comparable in size to the rotor dimension. In a quantum mechanical treatment they calculated the transmission of the particle through the aperture. It turned out that, as a result of the rotational motion, it can be trapped briefly within the slit. Here, I want to discuss some aspects concerning the feasibility of such studies in ultracold-molecule setups using optical lattices. First of all, applying Feshbach resonances, very weakly bound dimers can be produced that have a remarkable internuclear distance of more than 100 nm. This is close to the typical widths of optical potential wells and therefore light fields represent a promising tool to create an appropriate slit. Furthermore, it is possible to prepare the molecules either in rotating or nonrotating states dependent on the species and the employed Feshbach resonance. Now, one might imagine the following experimental scenario: The molecule formation takes place in a deep 3D optical lattice. Subsequently, one of the lattice beams is turned off giving rise to an array of parallel quasi-1D traps. After a short time, these tubes will be occupied by at most a single detectable molecule, if inelastic collisions occur. By applying magnetic field gradients the trapping potential can be tilted such that the molecules will move towards one edge of the individual traps. Next, a slit is produced at the center of each trap. For instance, this can be realized by means of a standing light wave in the transverse direction which has half the wavelength of the optical lattice. A different approach relies on imprinting light sheets by utilizing a phase plate or a digital micromirror device (DMD) with subsequent focusing via a lens characterized by a high numerical aperture. Then, the tilt of the trapping potential is reversed in order to accelerate the molecules towards the slit. Finally, the number of transmitted dimers is measured as a function of time.

The following, last issue addresses a rather technical aspect related to our setup.

- **Optical dipole trap:** We intend to implement an optical dipole trap in order to replace the QUIC setup. An optical dipole trap would significantly simplify the experimental sequence as the transfer of the atomic cloud within the glass cell (cf. section 3.5) would be obsolete. Furthermore, it could be advantageous regarding the production of a larger absolute number of molecules. As mentioned in section 3.8.2, when starting with about 4×10^5 atoms, we can produce only about $2.5 - 3 \times 10^4$ Feshbach dimers at the moment, although the conversion efficiency for the doubly occupied potential wells is $\sim 90\%$. Therefore, the low number of molecules is directly related to a low number of lattice sites that are filled with exactly two atoms. This is a result of the potential created by the QUIC trap. In principle, it would be necessary to adjust the trapping frequencies, i.e., the density of the atom cloud before it is loaded into the optical lattice. Unfortunately, the corresponding magnetic fields cannot be changed significantly without facing different

problems. For the realization of an optical dipole trap a laser[38] at a wavelength of 1570 nm with a maximum output power of 10 W is available in our laboratory. All parameters relevant for the desired application have been checked and the necessary intensity stabilization has already been built up (see Ref. [241]).

I want to conclude the present thesis by pointing out that until now, several molecular species were prepared in the rovibrational ground state of either the lowest singlet or triplet potential. However, in terms of alignment or orientation, we have seen that rotationally excited molecules are very interesting. In principle, the methods to control and probe the alignment of the molecular axis, demonstrated for the case of nonpolar Rb_2 in this work, can be readily implemented in a wide range of ultracold-molecule setups. Therefore, besides the already mentioned possible applications, e.g., concerning superpositions of states, further research in this direction will lead to new insights that might not even be envisioned at the moment.

---

[38]CEFL-KILO-10-LP-W10-G5-WT1-FM1-ST1-OM0-B301-FA from Keopsys SA, Lannion, France.

A Appendix

A.1 Effective parameters for analytical representations of dynamical polarizabilities

As described in section 4.8, Eq. (4.8) can be used to reproduce the numerical results for the real part of the dynamical polarizability with respect to all vibrational levels of the triplet and singlet electronic ground state of Rb_2. In the following, the corresponding effective parameters (tables A.1, A.2 and A.3) and the off-resonant frequency regimes (figures A.1 and A.2), where the analytical expression is valid, are given. These results are provided by our collaborators Olivier Dulieu, Romain Vexiau and Nadia Bouloufa-Maafa, and presented in Ref. [131]. Please note, here we always consider molecules that do not rotate, i.e., $N = 0$.
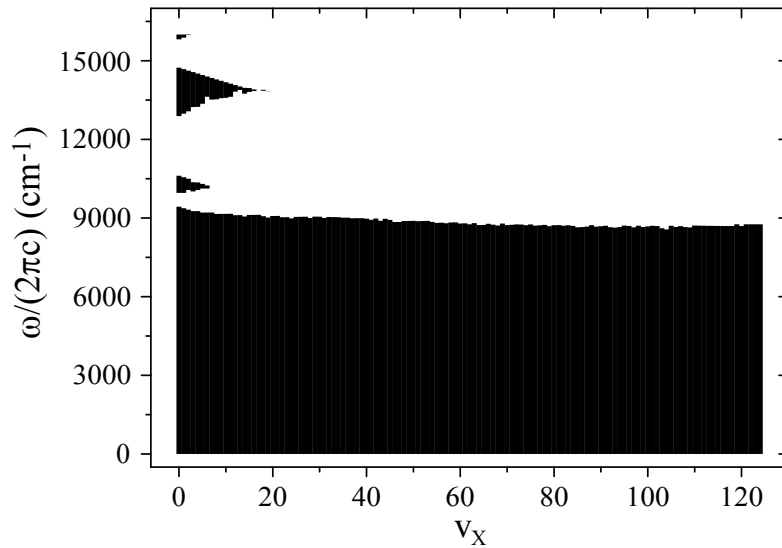
A.1.1 Vibrational states of $a^3\Sigma_u^+$
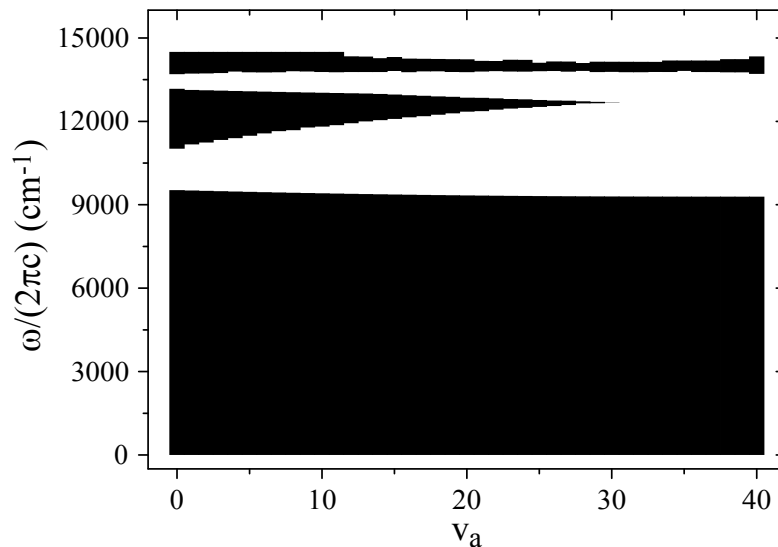
Figure A.1: Frequency regions indicated by the black areas, where the real part of $\alpha(\omega)$ of the $a^3\Sigma_u^+$ vibrational states v_a can be represented using two or three effective transitions.

v_a	$\widetilde{\omega}_{\text{eff},1}$ [cm^{-1}]	$d_{\text{eff},1}$ [a.u.]	$\widetilde{\omega}_{\text{eff},2}$ [cm^{-1}]	$d_{\text{eff},2}$ [a.u.]	rRMS [%]
0	10112.33	2.792881	13481.32	3.211023	0.976
1	10124.48	2.806632	13462.41	3.186648	2.402
2	10138.02	2.819581	13442.32	3.161026	4.702
3	10149.23	2.826924	13422.63	3.136275	7.265
4	10165.60	2.836308	13403.04	3.113487	9.453
5	10178.56	2.839702	13384.04	3.092283	11.806
6	10193.00	2.841532	13365.39	3.073084	13.520
7	10209.01	2.842671	13346.88	3.055347	13.608
8	10241.94	2.856396	13327.47	3.038251	15.856
9	10255.95	2.850516	13309.78	3.024335	12.723
10	10297.71	2.865961	13290.31	3.009602	13.416
11	10337.01	2.875559	13271.41	2.997182	14.456
12	10649.49	2.912128	13315.06	3.254995	14.369
13	10743.27	2.917850	13297.31	3.267539	10.163
14	10856.18	2.925106	13279.06	3.281925	9.215
15	10952.70	2.930383	13257.34	3.281501	8.486
16	11067.05	2.919322	13243.23	3.309404	7.851
17	11171.55	2.918061	13220.90	3.312712	7.547
18	11272.00	2.907345	13201.39	3.324143	7.232
19	11385.70	2.889403	13182.66	3.345595	7.046
20	11474.75	2.868762	13164.56	3.358371	6.764
21	11589.59	2.857391	13139.36	3.366384	6.569
22	11676.27	2.840077	13117.14	3.371518	6.251
23	11768.03	2.814790	13096.43	3.383873	5.906
24	11863.93	2.790719	13073.29	3.395242	5.583
25	11948.75	2.764104	13051.38	3.406065	5.242
26	12023.87	2.743002	13027.71	3.407386	4.795
27	12106.93	2.707386	13005.36	3.423806	4.397
28	11037.87	2.367592	13099.24	3.476488	1.415
29	11080.24	2.345712	13089.80	3.479831	1.210
30	11079.21	2.253547	13062.51	3.533553	1.059
31	9911.65	0.936293	12846.40	4.140226	0.408
32	9907.44	0.841004	12826.29	4.160146	0.335
33	9862.64	0.714259	12804.07	4.184604	0.241
34	10003.28	0.707082	12794.13	4.180198	0.256
35	9790.85	0.486185	12768.17	4.215499	0.120
36	9965.93	0.471244	12762.26	4.213153	0.134
37	11626.80	1.191479	12795.94	4.060964	0.159
38	12195.85	1.533889	12794.74	3.947516	0.091
39	12670.01	3.586949	12874.37	2.258576	0.090
40	11672.87	0.000000	12733.75	4.236863	0.069

Table A.1: Parameters for reproducing the real part of $\alpha(\omega)$ for the $a^3\Sigma_u^+$ vibrational states v_a using two effective transitions. Given are the relevant transition frequencies ω_{eff} in units of wavenumbers $[\widetilde{\omega}_{\text{eff}} = \omega_{\text{eff}}/(2\pi c)]$ and the corresponding dipole moments d_{eff}. The relative root mean square (rRMS) values are calculated according to Eq. (4.9) and represent the errors of the simplified model compared to the numerical results (see also Fig. 4.9).

v_a	$\widetilde{\omega}_{\text{eff},1}$ [cm^{-1}]	$d_{\text{eff},1}$ [a.u.]	$\widetilde{\omega}_{\text{eff},2}$ [cm^{-1}]	$d_{\text{eff},2}$ [a.u.]	$\widetilde{\omega}_{\text{eff},3}$ [cm^{-1}]	$d_{\text{eff},3}$ [a.u.]	rRMS [%]
0	9590.41	0.185198	10120.66	2.785057	13482.52	3.215639	1.071
1	9737.73	0.904303	10217.37	2.641512	13471.82	3.220395	0.830
2	9763.22	1.257521	10333.45	2.488387	13459.98	3.224902	0.860
3	9751.48	1.364655	10430.64	2.426252	13447.38	3.228257	0.860
4	9736.83	1.413862	10524.00	2.391762	13434.65	3.232971	0.917
5	9717.63	1.414144	10602.93	2.386689	13420.99	3.236433	1.019
6	9699.59	1.401748	10677.32	2.389227	13406.69	3.239517	1.163
7	9683.02	1.382871	10748.52	2.395828	13391.70	3.242234	1.162
8	9672.13	1.378077	10831.95	2.391468	13376.86	3.248165	1.366
9	9655.95	1.341866	10891.17	2.410047	13359.86	3.247776	0.911
10	9647.39	1.330426	10972.00	2.409608	13343.58	3.253083	0.921
11	9637.84	1.308216	11044.01	2.417081	13326.02	3.255710	1.123
12	9641.33	1.333716	11171.09	2.368223	13317.41	3.292024	0.711
13	9630.35	1.300184	11251.03	2.376126	13300.81	3.305618	0.650
14	9619.82	1.264942	11330.84	2.383139	13284.29	3.320739	0.717
15	9611.72	1.230969	11398.49	2.394595	13264.85	3.324882	0.672
16	9611.41	1.220352	11494.21	2.371852	13250.66	3.349338	0.794
17	9602.28	1.178701	11560.85	2.385153	13230.57	3.356448	0.760
18	9600.19	1.154154	11638.84	2.378668	13212.05	3.369833	0.746
19	9599.30	1.130792	11723.85	2.363649	13193.91	3.390178	0.815
20	9611.89	1.132451	11808.64	2.330800	13176.30	3.406338	0.698
21	9589.93	1.055503	11864.09	2.362846	13153.04	3.416474	0.760
22	9593.22	1.030744	11936.50	2.352384	13131.44	3.427758	0.661
23	9610.59	1.028859	12011.99	2.318529	13111.74	3.443508	0.578
24	9608.67	0.986896	12075.04	2.314174	13089.46	3.457836	0.571
25	9611.16	0.949278	12136.81	2.302735	13068.36	3.474313	0.444
26	9630.08	0.932263	12196.63	2.283813	13045.34	3.483366	0.363
27	9652.31	0.914930	12265.06	2.248322	13022.47	3.505861	0.348
28	9664.11	0.875433	12323.33	2.239643	12997.09	3.517888	0.244
29	9713.59	0.873735	12370.71	2.194975	12977.59	3.537408	0.326
30	9462.31	0.438363	11672.79	2.320231	13035.17	3.508957	0.213
31	9549.01	0.536731	12413.74	3.394454	13188.14	2.485224	0.029
32	9549.37	0.485334	12477.46	3.502939	13180.90	2.340804	0.025
33	9549.31	0.431667	12537.24	3.627132	13177.05	2.154360	0.021
34	9547.69	0.375099	12592.55	3.771700	13182.21	1.901211	0.018
35	9546.97	0.318713	12648.01	3.952470	13215.83	1.501938	0.016
36	9267.78	0.000000	11274.59	1.182139	12810.47	4.060789	0.240
37	9515.30	0.188211	12709.74	4.169399	13316.67	0.743190	0.018
38	9386.63	0.082332	12648.45	3.652151	12944.33	2.146721	0.045
39	9193.98	0.000000	12724.88	4.221117	13355.56	0.374808	0.043
40	9596.83	0.000000	12731.90	4.235114	13550.10	0.110491	0.071

Table A.2: Parameters for reproducing the real part of $\alpha(\omega)$ for the $a^3\Sigma_u^+$ vibrational states v_a using three effective transitions. Given are the relevant transition frequencies ω_{eff} in units of wavenumbers [$\widetilde{\omega}_{\text{eff}} = \omega_{\text{eff}}/(2\pi c)$] and the corresponding dipole moments d_{eff}. The relative root mean square (rRMS) values are calculated according to Eq. (4.9) and represent the errors of the simplified model compared to the numerical results. As can be seen from Fig. 4.9, the rRMS values are significantly decreased by adding a third transition in Eq. (4.8).

A.1.2 Vibrational states of $\mathbf{X^1\Sigma_g^+}$

Figure A.2: Frequency regions indicated by the black areas, where the real part of $\alpha(\omega)$ of the $X^1\Sigma_g^+$ vibrational states v_X can be represented using two effective transitions.

v_X	$\widetilde{\omega}_{\mathrm{eff},1}$ [cm^{-1}]	$d_{\mathrm{eff},1}$ [a.u.]	$\widetilde{\omega}_{\mathrm{eff},2}$ [cm^{-1}]	$d_{\mathrm{eff},2}$ [a.u.]	rRMS [%]
0	11450.31	2.647731	15019.57	2.965774	0.518
1	11383.24	2.689551	14963.22	2.929415	1.962
2	11263.16	2.707908	14893.80	2.828507	2.175
3	11192.67	2.726587	14841.26	2.774923	1.770
4	11084.86	2.738700	14793.77	2.724816	2.423
5	10988.23	2.746025	14752.23	2.688516	2.736
6	10896.90	2.743087	14716.89	2.665019	3.174
7	11177.30	2.815120	14700.93	2.730883	0.827
8	11147.88	2.830717	14669.19	2.716210	0.776
9	11106.07	2.845253	14637.00	2.696263	0.816
10	11059.13	2.858737	14604.95	2.675684	0.889
11	11010.69	2.871102	14573.62	2.654337	0.986
12	10970.15	2.878189	14547.88	2.646632	1.012
13	10838.51	2.793461	14587.80	2.757705	1.008
14	10881.05	2.890135	14500.45	2.627477	1.117
15	10727.35	2.799699	14543.51	2.741307	1.213
16	10208.21	2.257552	14978.89	3.404092	0.226
17	10002.85	1.947713	13849.09	3.524078	0.024
18	10100.47	2.224233	14911.39	3.438765	0.160
19	10061.69	2.225589	14922.86	3.445085	0.122
20	9882.99	1.945188	13777.83	3.534547	0.027
21	9843.10	1.941773	13738.67	3.538702	0.030
22	9813.35	1.953855	13746.87	3.537403	0.028
23	9777.20	1.948963	13708.85	3.541736	0.031
24	9750.04	1.960652	13717.97	3.540422	0.028
25	9708.16	1.942813	13630.49	3.548562	0.038
26	9676.11	1.939030	13590.00	3.551851	0.042
27	9645.62	1.935171	13549.82	3.554939	0.047
28	9624.18	1.952327	13569.55	3.551978	0.042
29	9588.19	1.934617	13470.93	3.558445	0.057
30	9562.35	1.934546	13435.34	3.559923	0.062
31	9545.37	1.953333	13466.08	3.556637	0.054
32	9515.47	1.940706	13378.95	3.560743	0.069
33	9493.89	1.943129	13349.76	3.561133	0.073
34	9473.56	1.945944	13322.16	3.561295	0.078
35	9456.33	1.956178	13318.38	3.559747	0.077
36	9437.75	1.960584	13288.73	3.559217	0.082
37	9424.53	1.972904	13301.55	3.557346	0.078
38	9407.51	1.976326	13267.29	3.556797	0.084
39	9392.40	1.983139	13243.85	3.555443	0.088
40	9381.54	1.996441	13253.11	3.553087	0.085
41	9375.86	2.021790	13313.92	3.548456	0.070
42	9356.73	2.009166	13209.66	3.550194	0.093
43	9358.74	2.052830	13346.77	3.542223	0.062
44	9338.83	2.029753	13201.80	3.545753	0.094
45	9336.82	2.058367	13275.94	3.540565	0.075
46	9339.36	2.096092	13393.08	3.533154	0.052
47	9333.18	2.106903	13392.40	3.530663	0.051
48	9323.64	2.103332	13337.80	3.531068	0.062

49	9318.98	2.116007	13338.47	3.527961	0.062
50	9315.02	2.125330	13333.24	3.525646	0.063
51	9314.11	2.141766	13357.85	3.521955	0.058
52	9311.93	2.151245	13356.64	3.519599	0.058
53	9310.18	2.163034	13354.05	3.516491	0.059
54	9314.05	2.185063	13415.45	3.511925	0.048
55	9317.92	2.205836	13467.32	3.507238	0.039
56	9318.38	2.215597	13465.81	3.504802	0.039
57	9321.95	2.231658	13494.15	3.500965	0.035
58	9322.50	2.236386	13472.81	3.499704	0.038
59	9325.20	2.246586	13474.43	3.497270	0.038
60	9332.11	2.265347	13521.61	3.492997	0.031
61	9335.86	2.272377	13517.88	3.491465	0.031
62	9342.86	2.287969	13551.11	3.487904	0.026
63	9345.01	2.287936	13512.58	3.488343	0.031
64	9355.62	2.306927	13573.27	3.483989	0.023
65	9361.08	2.313513	13564.84	3.483078	0.023
66	9364.38	2.310490	13521.05	3.485027	0.028
67	9373.19	2.320842	13540.44	3.483386	0.024
68	9382.32	2.330355	13554.17	3.482087	0.021
69	9383.40	2.317073	13471.50	3.487990	0.030
70	9395.20	2.329938	13508.42	3.486106	0.024
71	9401.64	2.326841	13477.73	3.489506	0.025
72	9407.54	2.321753	13440.51	3.493896	0.028
73	9415.13	2.318271	13418.38	3.498014	0.028
74	9425.64	2.320938	13419.16	3.500383	0.025
75	9429.20	2.305132	13355.00	3.509545	0.030
76	9442.08	2.309778	13371.57	3.511674	0.025
77	9447.61	2.295936	13322.42	3.520967	0.028
78	9452.64	2.279567	13271.63	3.531566	0.030
79	9466.62	2.281567	13287.09	3.535311	0.025
80	9468.05	2.254515	13211.08	3.550865	0.030
81	9473.88	2.235088	13166.77	3.563714	0.032
82	9484.27	2.224975	13157.22	3.572906	0.029
83	9487.26	2.196832	13098.00	3.589895	0.032
84	9497.46	2.183098	13087.81	3.600874	0.030
85	9513.36	2.179872	13105.63	3.607725	0.024
86	9517.28	2.149908	13059.28	3.625901	0.025
87	9519.21	2.113937	13006.38	3.646556	0.027
88	9511.69	2.057523	12915.59	3.675471	0.034
89	9529.57	2.051950	12941.50	3.683968	0.027
90	9529.37	2.009042	12894.41	3.707103	0.029
91	9528.63	1.962363	12846.68	3.731797	0.031
92	9545.70	1.950943	12869.57	3.742245	0.025
93	9553.80	1.918367	12856.44	3.761154	0.023
94	9551.50	1.866579	12816.63	3.786906	0.024
95	9537.66	1.792444	12748.78	3.820251	0.029
96	9544.41	1.753703	12742.39	3.840335	0.027
97	9561.03	1.732331	12763.41	3.853660	0.022
98	9544.53	1.650799	12706.31	3.887472	0.026

99	9561.88	1.625137	12727.86	3.901814	0.021
100	9555.12	1.559982	12702.97	3.928275	0.022
101	9548.67	1.492998	12681.93	3.954403	0.023
102	9553.27	1.441929	12683.00	3.974922	0.021
103	9580.44	1.420738	12716.85	3.986278	0.015
104	9595.33	1.378012	12729.22	4.003254	0.012
105	9552.23	1.259510	12675.30	4.039337	0.017
106	9568.39	1.215614	12693.19	4.054950	0.014
107	9558.89	1.139750	12685.56	4.077061	0.014
108	9572.52	1.088815	12699.79	4.092563	0.011
109	9577.94	1.026769	12706.26	4.109467	0.010
110	9554.84	0.936267	12695.11	4.130496	0.011
111	9557.79	0.871677	12702.17	4.145328	0.009
112	9561.12	0.806703	12709.11	4.159077	0.008
113	9564.72	0.741371	12715.78	4.171734	0.007
114	9568.55	0.676546	12722.10	4.183155	0.006
115	9573.17	0.612471	12728.23	4.193373	0.005
116	9578.47	0.549063	12734.02	4.202418	0.004
117	9584.65	0.486356	12739.48	4.210336	0.003
118	9594.62	0.425485	12744.70	4.217095	0.003
119	9577.09	0.354456	12746.11	4.223570	0.003
120	9636.94	0.310253	12752.36	4.227532	0.002
121	9655.62	0.251670	12753.80	4.232437	0.002
122	9806.04	0.220488	12756.29	4.235328	0.001
123	10319.14	0.248531	12761.67	4.234457	0.001
124	12073.63	1.115818	12809.17	4.092981	0.003

Table A.3: Parameters for reproducing the real part of $\alpha(\omega)$ for the $X^1\Sigma_g^+$ vibrational states v_X using two effective transitions. Given are the relevant transition frequencies ω_{eff} in units of wavenumbers $[\widetilde{\omega}_{\text{eff}} = \omega_{\text{eff}}/(2\pi c)]$ and the corresponding dipole moments d_{eff}. The relative root mean square (rRMS) values are calculated according to Eq. (4.9) and represent the errors of the simplified model compared to the numerical results (see also Fig. 4.9).

A.2 Ultrakalte Moleküle in Reih und Glied

Physik in unserer Zeit 46 (2), 60 (2015)[39]

Markus Deiß und Johannes Hecker Denschlag

Universität Ulm

Chemische Reaktionen können stattfinden, wenn Atome oder Moleküle miteinander stoßen. Die Reaktionsdynamik ist dabei abhängig von verschiedenen Parametern, insbesondere auch der relativen Orientierung der Kollisionspartner zueinander. Vor kurzem ist es an der Universität Ulm gelungen, ultrakalte Moleküle innerhalb eines optischen Gitters durch Rotationsanregung auszurichten und diese Ausrichtung mit einer neuartigen Methode zu vermessen [46]. Dies ermöglicht zukünftig die Untersuchung von stereochemischen Reaktionsprozessen bei Temperaturen von unter 1 µK in einem Modellsystem, das sich durch ein Höchstmaß an Kontrolle auszeichnet.

Ein homonukleares, zweiatomiges Molekül ähnelt einer Hantel, deren Achse im Raum rotieren kann. Für solch einen Rotator sind die Energieeigenzustände durch die Quantenzahlen des Drehimpulses R und m_R festgelegt. Die dazugehörige Wellenfunktion, die Kugelflächenfunktion $Y_{R,m_R}(\theta, \phi)$, beschreibt die Winkelverteilung der Hantelachse. Abbildung A.3(a) zeigt Polardiagramme von $|Y_{R,m_R}(\theta, \phi)|^2$ für zwei Rotationseigenfunktionen. Im Fall von $R = 0$ und $m_R = 0$ erhält man eine isotrope Verteilung, das heißt die Molekülachse zeigt zufällig in eine beliebige Richtung des Raumes. Hingegen ist für $R = 2$, $m_R = 0$ das Molekül hauptsächlich entlang der z-Achse ausgerichtet.

In unserem Experiment [46] werden zunächst aus Atomen ultrakalte Rb_2-Moleküle erzeugt [242], die keine Rotation aufweisen, das heißt $R = 0$. Mit Hilfe eines stimulierten Zwei-Photon-Übergangs auf der Basis zweier Laserpulse kann man nun sehr effizient beispielsweise den Zustand $R = 2$, $m_R = 0$ präparieren. Der dazu nötige Drehimpuls stammt aus dem Eigendrehimpuls der Photonen. Ein Magnetfeld in z-Richtung definiert die Quantisierungsachse und stabilisiert den Rotationszustand der Moleküle sowie die Ausrichtung ihrer Achse.

Die Moleküle sind in einem dreidimensionalen optischen Gitter gefangen, das durch stehende Lichtwellen in allen drei Raumrichtungen mit zueinander orthogonalen Polarisationen generiert wird. Daraus resultiert eine periodische Potentialstruktur, eine Art Eierkarton in 3D, wobei in unserem Fall jeder Gitterplatz mit höchstens einem Molekül besetzt wird [Abbildung A.3(b)]. Wie lässt sich nun die Ausrichtung der Moleküle messen?

---

[39]Copyright Wiley-VCH Verlag GmbH & Co. KGaA. Reproduced with permission.
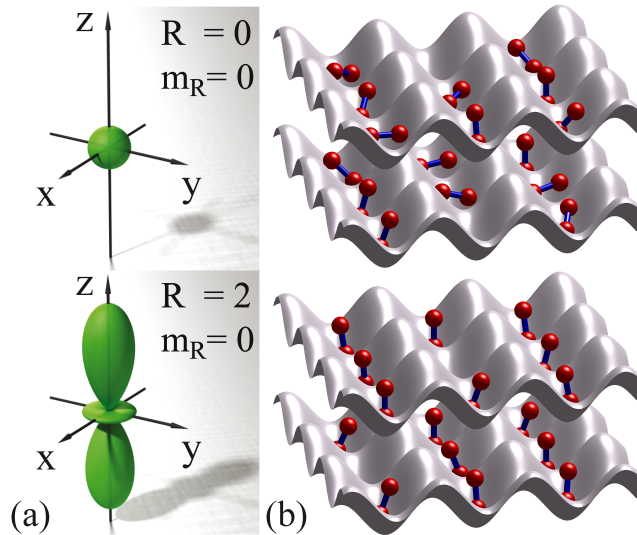
Abbildung A.3: Molekülausrichtung. (a) Polare Darstellung des Betragsquadrats der Rotationswellenfunktionen für $R = 0$ und $m_R = 0$ (oben) und $R = 2$, $m_R = 0$ (unten). Je weiter ein Punkt auf der Kurvenoberfläche vom Koordinatenursprung entfernt ist, desto größer ist die Wahrscheinlichkeit, dass die Molekülachse vom Ursprung ausgehend dorthin zeigt. (b) Verteilung der Moleküle innerhalb des dreidimensionalen optischen Gitters. Für $R = 2$, $m_R = 0$ (unten) erhält man im Mittel eine teilweise Ausrichtung entlang der z-Achse, während im Fall von $R = 0$, $m_R = 0$ (oben) die Richtungen der Molekülachsen gleichverteilt sind.

Die Tiefe der Potentialmulde, die von einer stehenden Lichtwelle hervorgerufen wird, hängt vom relativen Winkel zwischen der Polarisation des Lichtfeldes und der Molekülachse ab. Es werden nun die Gittertiefen für die Polarisationen in x-, y- und z-Richtung gemessen. Im Fall des kugelsymmetrischen Molekülzustands $R = 0$ finden wir gleiche Gittertiefen, unabhängig von der Polarisationsrichtung. Verwenden wir jedoch den Zustand $R = 2$, $m_R = 0$, so ist das Gitter für Polarisation in z-Richtung fast doppelt so tief wie für Polarisationen orthogonal dazu.

Zur Bestimmung der Potentialtiefe wird diese moduliert. Eine resonante Modulation erzeugt eine Anregung des Bewegungszustandes des Moleküls, wodurch es aus dem Gitter verloren geht. Der Grund dafür ist, dass Moleküle in einem optischen Gitter, ähnlich wie Elektronen im Festkörper, eine Energie-Bandstruktur aufweisen, die von der Gittertiefe abhängt. Da die Bandstruktur genau bekannt ist, kann man aus den beobachteten Resonanzfrequenzen auf die Gittertiefe rückschließen und somit die relative Orientierung der Moleküle zur verwendeten Polarisationsrichtung ermitteln.

Diese Methode ermöglicht interessante Kollisionsexperimente mit den teilweise ausgerichteten, ultrakalten Molekülen. Wie anfangs erwähnt, sollten Reaktionsprozesse von Molekülen abhängig davon sein, wie ihre Achsen zueinander stehen. Folglich könnten etwa Reaktionen
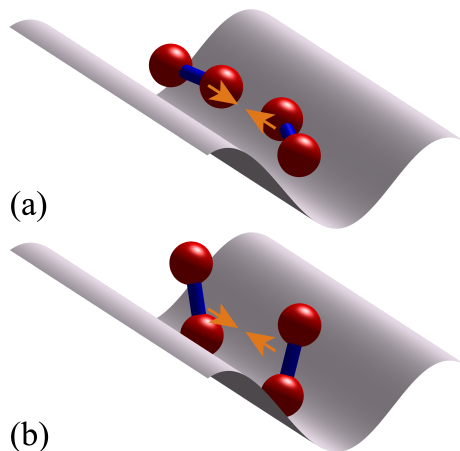
Abbildung A.4: Stereochemie. Kollision zweier Moleküle in einer eindimensionalen Potential-
röhre für verschiedene relative Ausrichtungen (a) und (b) der Molekülachsen.

zwischen Molekülen mit $R = 0$ beziehungsweise $R = 2$ verschiedene Raten aufweisen oder gar unterschiedliche Produkte erzeugen.

In unserem Aufbau sind solche Experimente einfach zu realisieren. Nach der Präparation der Moleküle im dreidimensionalen optischen Gitter kann beispielsweise eine der drei stehenden Wellen ausgeschaltet werden. Das Gitter verwandelt sich dann in ein System von parallelen Potentialröhren, in denen sich die ausgerichteten Moleküle frei bewegen und kollidieren können (Abbildung A.4). Solche Experimente werden zu einem tieferen Verständnis fundamentaler chemischer Prozesse führen.

Erklärung

Hiermit erkläre ich, Markus Johannes Deiß, geboren am 01.05.1983 in Ehingen (Donau), dass ich die vorliegende Dissertation mit dem Titel

"Alignment and Spectroscopy of Ultracold Rb_2 Molecules"

selbständig angefertigt und keine anderen als die angegebenen Quellen und Hilfsmittel benutzt sowie die wörtlich oder inhaltlich übernommenen Stellen als solche kenntlich gemacht und die Satzung der Universität Ulm zur Sicherung guter wissenschaftlicher Praxis beachtet habe.

Ulm, den 27. Mai 2015   ....

                                        Markus Johannes Deiß

Erklärung über individuellen Beitrag zur Dissertation

Die kumulative Dissertation mit dem Titel *"Alignment and Spectroscopy of Ultracold Rb₂ Molecules"*, angefertigt von Markus Johannes Deiß, geboren am 01.05.1983 in Ehingen (Donau), ist in Teilen in Ko-Autorenschaft mit anderen Wissenschaftlern entstanden. Dies bezieht sich auf die Kapitel 4 bis 7 sowie Anhang A.2, welche (ausgenommen der Abschnitte 5.9 und 6.11) deckungsgleich mit den an entsprechender Stelle aufgeführten wissenschaftlichen Publikationen sind.

- Kapitel 4: Ich war bei der Ausarbeitung der Messmethoden sowie der Aufnahme der gezeigten Messdaten in hauptverantwortlichem Maße in enger Kooperation mit dem Zweitautor, Björn Drews, beteiligt. Ich habe Teile der Datenanalyse übernommen und war hauptverantwortlich für das Schreiben der Publikation.

- Kapitel 5: Ich war bei der Ausarbeitung der Messmethoden sowie der Aufnahme der gezeigten Messdaten in hauptverantwortlichem Maße in enger Kooperation mit dem Zweitautor, Björn Drews, beteiligt. Ich habe Teile der Datenanalyse übernommen und war hauptverantwortlich für das Schreiben der Publikation.

- Kapitel 6: Ich war bei der Ausarbeitung der Messmethoden sowie der Aufnahme der gezeigten Messdaten in hauptverantwortlichem Maße in enger Kooperation mit dem Zweitautor, Björn Drews, beteiligt. Ferner war ich hauptverantwortlich für die Datenanalyse, die Durchführung der Simulationen und das Schreiben der Publikation.

- Kapitel 7: Ich habe spektroskopische Messungen mit Rb₂ Molekülen durchgeführt. Diese Daten waren wesentlich, um die Besetzungsverteilung der molekularen Endzustände nach Drei-Körper-Rekombination von neutralen Rb Atomen, welche in entsprechenden Experimenten innerhalb des BaRbI Projekts in unserem Institut beobachtet wurde, zu erklären.

- Anhang A.2: Dieser Artikel beschreibt Messresultate und Inhalte aus Kapitel 5 (für den individuellen Beitrag hierzu, siehe oben). Ich war hauptverantwortlich für das Schreiben der Publikation.

Ulm, den 27. Mai 2015 ....

Markus Johannes Deiß

Bestätigung der Richtigkeit der Angaben durch den Betreuer der Dissertation:

Ulm, den 27. Mai 2015 ....

Prof. Dr. Johannes Hecker Denschlag

157

Der Inhalt dieser Seite wurde aus Gründen des Datenschutzes entfernt.

Der Inhalt dieser Seite wurde aus Gründen des Datenschutzes entfernt.

List of Figures

List of Tables

Bibliography

[1] C. S. ADAMS and E. RIIS: *Laser cooling and trapping of neutral atoms.* Prog. Quant. Electr. 21 (1), 1 (1997).

[2] E. S. SHUMAN, J. F. BARRY, and D. DEMILLE: *Laser cooling of a diatomic molecule.* Nature 467, 820 (2010).

[3] J. F. BARRY, D. J. MCCARRON, E. B. NORRGARD, M. H. STEINECKER, and D. DEMILLE: *Magneto-optical trapping of a diatomic molecule.* Nature 512, 286 (2014).

[4] M. T. HUMMON, M. YEO, B. K. STUHL, A. L. COLLOPY, Y. XIA, and J. YE: *2D magneto-optical trapping of diatomic molecules.* Phys. Rev. Lett. 110, 143001 (2013).

[5] J. D. WEINSTEIN, R. DECARVALHO, T. GUILLET, B. FRIEDRICH, and J. M. DOYLE: *Magnetic trapping of calcium monohydride molecules at millikelvin temperatures.* Nature 395, 148 (1998).

[6] M. ZEPPENFELD, M. MOTSCH, P. W. H. PINKSE, and G. REMPE: *Optoelectrical cooling of polar molecules.* Phys. Rev. A 80, 041401(R) (2009).

[7] M. ZEPPENFELD, B. G. U. ENGLERT, R. GLÖCKNER, A. PREHN, M. MIELENZ, C. SOMMER, L. D. VAN BUUREN, M. MOTSCH, and G. REMPE: *Sisyphus cooling of electrically trapped polyatomic molecules.* Nature 491, 570 (2012).

[8] H. L. BETHLEM, G. BERDEN, and G. MEIJER: *Decelerating neutral dipolar molecules.* Phys. Rev. Lett. 83, 1558 (1999).

[9] K. MØLHAVE and M. DREWSEN: *Formation of translationally cold MgH^+ and MgD^+ molecules in an ion trap.* Phys. Rev. A 62, 011401(R) (2000).

[10] P. F. STAANUM, K. HØJBJERRE, P. S. SKYT, A. K. HANSE, and M. DREWSEN: *Rotational laser cooling of vibrationally and translationally cold molecular ions.* Nat. Phys. 6, 271 (2010).

[11] T. SCHNEIDER, B. ROTH, H. DUNCKER, I. ERNSTING, and S. SCHILLER: *All-optical preparation of molecular ions in the rovibrational ground state.* Nat. Phys. 6, 275 (2010).

[12] M. H. ANDERSON, J. R. ENSHER, M. R. MATTHEWS, C. E. WIEMAN, and E. A. CORNELL: *Observation of Bose-Einstein condensation in a dilute atomic vapor.* Science 269, 198 (1995).

[13] K. B. DAVIS, M.-O. MEWES, M. R. ANDREWS, N. J. VAN DRUTEN, D. S. DURFEE, D. M. KURN, and W. KETTERLE: *Bose-Einstein condensation in a gas of sodium atoms.* Phys. Rev. Lett. 75, 3969 (1995).

[14] K. M. JONES, E. TIESINGA, P. D. LETT, and P. S. JULIENNE: *Ultracold photoassociation spectroscopy: Long-range molecules and atomic scattering.* Rev. Mod. Phys. 78, 483 (2006).

[15] J. M. SAGE, S. SAINIS, T. BERGEMAN, and D. DEMILLE: *Optical production of ultracold polar molecules.* Phys. Rev. Lett. 94, 203001 (2005).

[16] M. VITEAU, A. CHOTIA, M. ALLEGRINI, N. BOULOUFA, O. DULIEU, D. COMPARAT, and P. PILLET: *Optical pumping and vibrational cooling of molecules.* Science 321, 232 (2008).

[17] J. DEIGLMAYR, A. GROCHOLA, M. REPP, K. MÖRTLBAUER, C. GLÜCK, J. LANGE, O. DULIEU, R. WESTER, and M. WEIDEMÜLLER: *Formation of ultracold polar molecules in the rovibrational ground state.* Phys. Rev. Lett. 101, 133004 (2008).

[18] K. AIKAWA, D. AKAMATSU, M. HAYASHI, K. OASA, J. KOBAYASHI, P. NAIDON, T. KISHIMOTO, M. UEDA, and S. INOUYE: *Coherent transfer of photoassociated molecules into the rovibrational ground state.* Phys. Rev. Lett. 105, 203001 (2010).

[19] T. KÖHLER, K. GÓRAL, and P. S. JULIENNE: *Production of cold molecules via magnetically tunable Feshbach resonances.* Rev. Mod. Phys. 78, 1311 (2006).

[20] C. CHIN, R. GRIMM, P. JULIENNE, and E. TIESINGA: *Feshbach resonances in ultracold gases.* Rev. Mod. Phys. 82, 1225 (2010).

[21] S. INOUYE, M. R. ANDREWS, J. STENGER, H.-J. MIESNER, D. M. STAMPER-KURN, and W. KETTERLE: *Observation of Feshbach resonances in a Bose-Einstein condensate.* Nature 392, 151 (1998).

[22] P. COURTEILLE, R. S. FREELAND, D. J. HEINZEN, F. A. VAN ABEELEN, and B. J. VERHAAR: *Observation of a Feshbach resonance in cold atom scattering.* Phys. Rev. Lett. 81, 69 (1998).

[23] J. L. ROBERTS, N. R. CLAUSSEN, J. P. BURKE JR., C. H. GREENE, E. A. CORNELL, and C. E. WIEMAN: *Resonant magnetic field control of elastic scattering in cold ^{85}Rb.* Phys. Rev. Lett. 81, 5109 (1998).

[24] C. A. REGAL, C. TICKNOR, J. L. BOHN, and D. S. JIN: *Creation of ultracold molecules from a Fermi gas of atoms.* Nature 424, 47 (2003).

[25] J. HERBIG, T. KRAEMER, M. MARK, T. WEBER, C. CHIN, H.-C. NÄGERL, and R. GRIMM: *Preparation of a pure molecular quantum gas.* Science 301, 1510 (2003).

[26] K. E. STRECKER, G. B. PARTRIDGE, and R. G. HULET: *Conversion of an atomic Fermi gas to a long-lived molecular Bose gas.* Phys. Rev. Lett. 91, 080406 (2003).

[27] K. XU, T. MUKAIYAMA, J. R. ABO-SHAEER, J. K. CHIN, D. E. MILLER, and W. KETTERLE: *Formation of quantum-degenerate sodium molecules.* Phys. Rev. Lett. 91, 210402 (2003).

[28] J. CUBIZOLLES, T. BOURDEL, S. J. J. M. F. KOKKELMANS, G. V. SHLYAPNIKOV, and C. SALOMON: *Production of long-lived ultracold Li_2 molecules from a Fermi gas.* Phys. Rev. Lett. 91, 240401 (2003).

[29] S. JOCHIM, M. BARTENSTEIN, A. ALTMEYER, G. HENDL, C. CHIN, J. HECKER DENSCHLAG, and R. GRIMM: *Pure gas of optically trapped molecules created from fermionic atoms.* Phys. Rev. Lett. 240402 (2003).

[30] S. DÜRR, T. VOLZ, A. MARTE, and G. REMPE: *Observation of molecules produced from a Bose-Einstein condensate.* Phys. Rev. Lett. 92, 020406 (2004).

[31] E. A. DONLEY, N. R. CLAUSSEN, S. T. THOMPSON, and C. E. WIEMAN: *Atom–molecule coherence in a Bose–Einstein condensate.* Nature 417, 529 (2002).

[32] S. JOCHIM, M. BARTENSTEIN, A. ALTMEYER, G. HENDL, S. RIEDL, C. CHIN, J. HECKER DENSCHLAG, and R. GRIMM: *Bose-Einstein condensation of molecules.* Science 302, 2101 (2003).

[33] M. GREINER, C. A. REGAL, and D. S. JIN: *Emergence of a molecular Bose–Einstein condensate from a Fermi gas.* Nature 426, 537 (2003).

[34] M. W. ZWIERLEIN, C. A. STAN, C. H. SCHUNCK, S. M. F. RAUPACH, S. GUPTA, Z. HADZIBABIC, and W. KETTERLE: *Observation of Bose-Einstein condensation of molecules.* Phys. Rev. Lett. 91, 250401 (2003).

[35] M. DEIß, B. DREWS, J. HECKER DENSCHLAG, and E. TIEMANN: *Mixing of 0^+ and 0^- observed in hyperfine and Zeeman structure of ultracold Rb_2 molecules.* arXiv: 1505.00682 (2015).

[36] A. HÄRTER, A. KRÜKOW, M. DEIß, B. DREWS, E. TIEMANN, and J. HECKER DENSCHLAG: *Population distribution of product states following three-body recombination in an ultracold atomic gas.* Nat. Phys. 9, 512 (2013).

[37] U. GAUBATZ, P. RUDECKI, M. BECKER, S. SCHIEMANN, M. KÜLZ, and K. BERGMANN: *Population switching between vibrational levels in molecular beams.* Chem. Phys. Lett. 149, 463 (1988).

[38] K. BERGMANN, H. THEURER, and B. W. SHORE: *Coherent population transfer among quantum states of atoms and molecules.* Rev. Mod. Phys. 70, 1003 (1998).

[39] K.-K. NI, S. OSPELKAUS, M. H. G. DE MIRANDA, A. PE'ER, B. NEYENHUIS, J. J. ZIRBEL, S. KOTOCHIGOVA, P. S. JULIENNE, D. S. JIN, and J. YE: *A high phase-space-density gas of polar molecules.* Science 322, 231 (2008).

[40] J. G. DANZL, M. J. MARK, E. HALLER, M. GUSTAVSSON, R. HART, J. ALDEGUNDE, J. M. HUTSON, and H.-C. NÄGERL: *An ultracold high-density sample of rovibronic ground-state molecules in an optical lattice.* Nat. Phys. 6, 265 (2010).

[41] T. TAKEKOSHI, L. REICHSÖLLNER, A. SCHINDEWOLF, J. M. HUTSON, C. RUTH LE SUEUR, O. DULIEU, F. FERLAINO, R. GRIMM, and H.-C. NÄGERL: *Ultracold dense samples of dipolar RbCs molecules in the rovibrational and hyperfine ground state.* Phys. Rev. Lett. 113, 205301 (2014).

[42] P. K. MOLONY, P. D. GREGORY, Z. JI, B. LU, M. P. KÖPPINGER, C. RUTH LE SUEUR, C. L. BLACKLEY, J. M. HUTSON, and S. L. CORNISH: *Creation of ultracold $^{87}Rb^{133}Cs$ molecules in the rovibrational ground state.* Phys. Rev. Lett. 113, 255301 (2014).

[43] J. W. PARK, S. A. WILL, and M. W. ZWIERLEIN: *Ultracold dipolar gas of fermionic $^{23}Na^{40}K$ molecules in their absolute ground state.* Phys. Rev. Lett. 114, 205302 (2015).

[44] F. LANG, K. WINKLER, C. STRAUSS, R. GRIMM, and J. HECKER DENSCHLAG: *Ultracold triplet molecules in the rovibrational ground state.* Phys. Rev. Lett. 101, 133005 (2008).

[45] S. OSPELKAUS, K.-K. NI, G. QUÉMÉNER, B. NEYENHUIS, D. WANG, M. H. G. DE MIRANDA, J. L. BOHN, J. YE, and D. S. JIN: *Controlling the hyperfine state of rovibronic ground-state polar molecules.* Phys. Rev. Lett. 104, 030402 (2010).

[46] M. DEIß, B. DREWS, B. DEISSLER, and J. HECKER DENSCHLAG: *Probing the axis alignment of an ultracold spin-polarized Rb_2 molecule.* Phys. Rev. Lett. 113, 233004 (2014).

[47] H. L. BETHLEM, G. BERDEN, F. M. H. CROMPVOETS, R. T. JONGMA, A. J. A. VAN ROIJ, and G. MEIJER: *Electrostatic trapping of ammonia molecules.* Nature 406, 491 (2000).

[48] B. G. U. ENGLERT, M. MIELENZ, C. SOMMER, J. BAYERL, M. MOTSCH, P. W. H. PINKSE, G. REMPE, and M. ZEPPENFELD: *Storage and adiabatic cooling of polar molecules in a microstructured trap.* Phys. Rev. Lett. 107, 263003 (2011).

[49] H.-I LU, I. KOZYRYEV, B. HEMMERLING, J. PISKORSKI, and J. M. DOYLE: *Magnetic trapping of molecules via optical loading and magnetic slowing.* Phys. Rev. Lett. 112, 113006 (2014).

[50] M. GREINER, O. MANDEL, T. ESSLINGER, T. W. HÄNSCH, and I. BLOCH: *Quantum phase transition from a superfluid to a Mott insulator in a gas of ultracold atoms.* Nature 415, 39 (2002).

[51] B. PAREDES, A. WIDERA, V. MURG, O. MANDEL, S. FÖLLING, I. CIRAC, G. V. SHLYAPNIKOV, T. W. HÄNSCH, and I. BLOCH: *Tonks–Girardeau gas of ultracold atoms in an optical lattice.* Nature 429, 277 (2004).

[52] T. KINOSHITA, T. WENGER, and D. S. WEISS: *Observation of a one-dimensional Tonks-Girardeau gas.* Science 305, 1125 (2004).

[53] G. THALHAMMER, K. WINKLER, F. LANG, S. SCHMID, R. GRIMM, and J. HECKER DENSCHLAG: *Long-lived Feshbach molecules in a three-dimensional optical lattice.* Phys. Rev. Lett. 96, 050402 (2006).

[54] T. VOLZ, N. SYASSEN, D. M. BAUER, E. HANSIS, S. DÜRR, and G. REMPE: *Preparation of a quantum state with one molecule at each site of an optical lattice.* Nat. Phys. 2, 692 (2006).

[55] A. CHOTIA, B. NEYENHUIS, S. A. MOSES, B. YAN, J. P. COVEY, M. FOSS-FEIG, A. M. REY, D. S. JIN, and J. YE: *Long-lived dipolar molecules and Feshbach molecules in a 3D optical lattice.* Phys. Rev. Lett. 108, 080405 (2012).

[56] M. DEIß, B. DREWS, J. HECKER DENSCHLAG, N. BOULOUFA-MAAFA, R. VEXIAU, and O. DULIEU: *Polarizability of ultracold Rb_2 molecules in the rovibrational ground state of $a\,{}^3\Sigma_u^+$.* arXiv: 1501.03793 (2015). Accepted for publication in New Journal of Physics.

[57] K.-K. NI, S. OSPELKAUS, D. WANG, G. QUÉMÉNER, B. NEYENHUIS, M. H. G. DE MIRANDA, J. L. BOHN, J. YE, and D. S. JIN: *Dipolar collisions of polar molecules in the quantum regime.* Nature 464, 1324 (2010).

[58] S. OSPELKAUS, K.-K. NI, D. WANG, M. H. G. DE MIRANDA, B. NEYENHUIS, G. QUÉMÉNER, P. S. JULIENNE, J. L. BOHN, D. S. JIN, and J. YE: *Quantum-state controlled chemical reactions of ultracold potassium-rubidium molecules.* Science 327, 853 (2010).

[59] B. YAN, S. A. MOSES, B. GADWAY, J. P. COVEY, K. R. A. HAZZARD, A. M. REY, D. S. JIN, and J. YE: *Observation of dipolar spin-exchange interactions with lattice-confined polar molecules.* Nature 501, 521 (2013).

[60] B. ZHU, B. GADWAY, M. FOSS-FEIG, J. SCHACHENMAYER, M. L. WALL, K. R. A. HAZZARD, B. YAN, S. A. MOSES, J. P. COVEY, D. S. JIN, J. YE, M. HOLLAND, and A. M. REY: *Suppressing the loss of ultracold molecules via the continuous quantum Zeno effect.* Phys. Rev. Lett. 112, 070404 (2014).

[61] N. SYASSEN, D. M. BAUER, M. LETTNER, T. VOLZ, D. DIETZE, J. J. GARCIA-RIPOLL, J. I. CIRAC, G. REMPE, and S. DÜRR: *Strong dissipation inhibits losses and induces correlations in cold molecular gases.* Science 320, 1329 (2008).

[62] M. H. G. DE MIRANDA, A. CHOTIA, B. NEYENHUIS, D. WANG, G. QUÉMÉNER, S. OSPELKAUS, J. L. BOHN, J. YE, and D. S. JIN: *Controlling the quantum stereodynamics of ultracold bimolecular reactions.* Nat. Phys. 7, 502 (2011).

[63] M. DEIß und J. HECKER DENSCHLAG: *Ultrakalte Moleküle in Reih und Glied.* Physik in unserer Zeit 46 (2), 60 (2015).

[64] L. D. CARR, D. DEMILLE, R. V. KREMS, and J. YE: *Cold and ultracold molecules: science, technology and applications.* New J. Phys. 11, 055049 (2009).

[65] O. DULIEU and C. GABBANINI: *The formation and interactions of cold and ultracold molecules: new challenges for interdisciplinary physics.* Rep. Prog. Phys. 72, 086401 (2009).

[66] R. V. KREMS: *Cold controlled chemistry.* Phys. Chem. Chem. Phys. 10, 4079 (2008).

[67] G. QUÉMÉNER and P. S. JULIENNE: *Ultracold molecules under control!* Chem. Rev. 112, 4949 (2012).

[68] D. JAKSCH, V. VENTURI, J. I. CIRAC, C. J. WILLIAMS, and P. ZOLLER: *Creation of a molecular condensate by dynamically melting a Mott insulator.* Phys. Rev. Lett. 89, 040402 (2002).

[69] H. P. BÜCHLER, E. DEMLER, M. LUKIN, A. MICHELI, N. PROKOF'EV, G. PUPILLO, and P. ZOLLER: *Strongly correlated 2D quantum phases with cold polar molecules: Controlling the shape of the interaction potential.* Phys. Rev. Lett. 98, 060404 (2007).

[70] B. H. MCGUYER, M. MCDONALD, G. Z. IWATA, M. G. TARALLO, W. SKOMOROWSKI, R. MOSZYNSKI, and T. ZELEVINSKY: *Precise study of asymptotic physics with subradiant ultracold molecules.* Nat. Phys. 11, 32 (2015).

[71] C. CHIN, V. V. FLAMBAUM, and M. G. KOZLOV: *Ultracold molecules: new probes on the variation of fundamental constants.* New J. Phys. 11, 055048 (2009).

[72] T. ZELEVINSKY, S. KOTOCHIGOVA, and J. YE: *Precision test of mass-ratio variations with lattice-confined ultracold molecules.* Phys. Rev. Lett. 100, 043201 (2008).

[73] D. DEMILLE, S. SAINIS, J. SAGE, T. BERGEMAN, S. KOTOCHIGOVA, and E. TIESINGA: *Enhanced sensitivity to variation of m_e/m_p in molecular spectra.* Phys. Rev. Lett. 100, 043202 (2008).

[74] V. V. FLAMBAUM and M. G. KOZLOV: *Enhanced sensitivity to the time variation of the fine-structure constant and m_p/m_e in diatomic molecules.* Phys. Rev. Lett. 99, 150801 (2007).

[75] A. MICHELI, G. K. BRENNEN, and P. ZOLLER: *A toolbox for lattice-spin models with polar molecules.* Nat. Phys. 2, 341 (2006).

[76] M. L. Wall, K. R. A. Hazzard, and A. M. Rey: *Quantum magnetism with ultracold molecules.* arXiv: 1406.4758 (2014).

[77] D. DeMille: *Quantum computation with trapped polar molecules.* Phys. Rev. Lett. 88, 067901 (2002).

[78] D. Yelin, K. Kirby, and R. Côté: *Schemes for robust quantum computation with polar molecules.* Phys. Rev. A 74, 050301(R) (2006).

[79] P. Rabl, D. DeMille, J. M. Doyle, M. D. Lukin, R. J. Schoelkopf, and P. Zoller: *Hybrid quantum processors: Molecular ensembles as quantum memory for solid state circuits.* Phys. Rev. Lett. 97, 033003 (2006).

[80] A. Härter: *Two-body and three-body dynamics in atom-ion experiments.* PhD thesis, Universität Ulm (2013).

[81] M. Theis: *Optical Feshbach resonances in a Bose-Einstein condensate.* PhD thesis, Leopold-Franzens-Universität Innsbruck (2005).

[82] K. Winkler: *Ultracold molecules and atom pairs in optical lattice potentials.* PhD thesis, Leopold-Franzens-Universität Innsbruck (2007).

[83] K. Winkler: *Aufbau einer magnetischen Transportapparatur für ultrakalte Atome.* Master's thesis, Leopold-Franzens-Universität Innsbruck (2002).

[84] G. Thalhammer: *Ultrakalte gepaarte Atome in kohärenten Lichtfeldern.* PhD thesis, Leopold-Franzens-Universität Innsbruck (2007).

[85] M. Greiner, I. Bloch, T. W. Hänsch, and T. Esslinger: *Magnetic transport of trapped cold atoms over a large distance.* Phys. Rev. A 63, 031401(R) (2001).

[86] T. Lupfer: *Aufbau eines weitdurchstimmbaren Diodenlasers.* Bachelor's thesis, Universität Ulm (2011).

[87] D. A. Steck: *Rubidium 87 D line data.* Revision 2.1.4 (2010). Available at `http://steck.us/alkalidata`.

[88] G. Camy, C. J. Bordé, and M. Ducloy: *Heterodyne saturation spectroscopy through frequency modulation of the saturating beam.* Optics Communications 41 (5), 325 (1982).

[89] R. K. Raj, D. Bloch, J. J. Snyder, G. Camy, and M. Ducloy: *High-frequency optically heterodyned saturation spectroscopy via resonant degenerate four-wave mixing.* Phys. Rev. Lett. 44, 1251 (1980).

[90] U. Schünemann, H. Engler, R. Grimm, M. Weidemüller, and M. Zielonkowski: *Simple scheme for tunable frequency offset locking of two lasers.* Rev. Sci. Instrum. 70, 242 (1999).

[91] G. C. BJORKLUND, M. D. LEVENSON, W. LENTH, and C. ORTIZ: *Frequency modulation (FM) spectroscopy: Theory of lineshapes and signal-to-noise analysis.* Appl. Phys. B 32, 145 (1983).

[92] K. SINGER, S. JOCHIM, M. MUDRICH, A. MOSK, and M. WEIDEMÜLLER: *Low-cost mechanical shutter for light beams.* Rev. Sci. Instrum. 73, 4402 (2002).

[93] R. W. P. DREVER, J. L. HALL, F. V. KOMALSKI, J. HOUGH, G. M. FORD, A. J. MUNLEY, and H. WARD: *Laser phase and frequency stabilization using an optical resonator.* Appl. Phys. B 31, 97 (1983).

[94] E. D. BLACK: *An introduction to Pound-Drever-Hall laser frequency stabilization.* Am. J. Phys. 69, 79 (2001).

[95] I. KINSKI: *Magnetic trapping apparatus and frequency stabilization of a ring cavity laser for Bose-Einstein condensation experiments.* Master's thesis, Freie Universität Berlin (2005).

[96] T. OKOSHI, K. KIKUCHI, and A. NAKAYAMA: *Novel method for high resolution measurement of laser output spectrum.* Electronics Letters 16, 630 (1980).

[97] J. BALEWSKI: *Hochauflösende Photoassoziationsspektroskopie von Rydberg-Dimeren und Trimeren.* Master's thesis, Universität Stuttgart (2009).

[98] T. KLOSS: *Messung der Laserlinienbreite anhand des Selbst-Heterodyn-Verfahrens.* Bachelor's thesis, Universität Ulm (2012).

[99] T. UDEM, R. HOLZWARTH, and T. W. HÄNSCH: *Optical frequency metrology.* Nature 416, 233 (2002).

[100] M. THOMA: *Stabilisierung und Charakterisierung eines Frequenzkamms.* Master's thesis, Universität Ulm (2012).

[101] W. KETTERLE, D. S. DURFEE, and D. M. STAMPER-KURN: *Making, probing and understanding Bose-Einstein condensates.* In: Bose-Einstein condensation in atomic gases, Proceedings of the International School of Physics "Enrico Fermi", Course CXL (edited by M. Inguscio, S. Stringari and C. E. Wieman), pp. 67-176, IOS press (1999).

[102] F. DALFOVO, S. GIORGINI, L. PITAEVSKII, and S. STRINGARI: *Theory of Bose-Einstein condensation in trapped gases.* Rev. Mod. Phys. 71, 463 (1999).

[103] C. J. PETHICK and H. SMITH: *Bose-Einstein condensation in dilute gases.* Second Edition, Cambridge University Press (2008).

[104] T. ESSLINGER, I. BLOCH, and T. W. HÄNSCH: *Bose-Einstein condensation in a quadrupole-Ioffe-configuration trap.* Phys. Rev. A 58, 2664(R) (1998).

[105] O. J. LUITEN, M. W. REYNOLDS, and J. T. M. WALRAVEN: *Kinetic theory of the evaporative cooling of a trapped gas.* Phys. Rev. A 53, 381 (1996).

[106] I. BLOCH: *Ultracold quantum gases in optical lattices.* Nat. Phys. 1, 23 (2005).

[107] R. GRIMM, M. WEIDEMÜLLER, and Y. B. OVCHINNIKOV: *Optical dipole traps for neutral atoms.* Adv. At. Mol. Opt. Phys. 42, 95 (2000).

[108] Y. B. OVCHINNIKOV, J. H. MÜLLER, M. R. DOERY, E. J. D. VREDENBREGT, K. HELMERSON, S. L. ROLSTON, and W. D. PHILLIPS: *Diffraction of a released Bose-Einstein condensate by a pulsed standing light wave.* Phys. Rev. Lett. 83, 284 (1999).

[109] J. HECKER DENSCHLAG, H. HÄFFNER, C. MCKENZIE, A. BROWAEYS, D. CHO, K. HELMERSON, S. ROLSTON, and W. D. PHILLIPS: *A Bose-Einstein condensate in an optical lattice.* J. Phys. B: At. Mol. Opt. Phys. 35, 3095 (2002).

[110] M. GREINER, I. BLOCH, O. MANDEL, T. W. HÄNSCH, and T. ESSLINGER: *Exploring phase coherence in a 2D lattice of Bose-Einstein condensates.* Phys. Rev. Lett. 87, 160405 (2001).

[111] M. P. A. FISHER, P. B. WEICHMAN, G. GRINSTEIN, and D. S. FISHER: *Boson localization and the superfluid-insulator transition.* Phys. Rev. B 40, 546 (1989).

[112] D. JAKSCH, C. BRUDER, J. I. CIRAC, C. W. GARDINER, and P. ZOLLER: *Cold bosonic atoms in optical lattices.* Phys. Rev. Lett. 81, 3108 (1998).

[113] T. VOLZ, S. DÜRR, S. ERNST, A. MARTE, and G. REMPE: *Characterization of elastic scattering near a Feshbach resonance in ^{87}Rb.* Phys. Rev. A 68, 010702(R) (2003).

[114] A. J. MOERDIJK, B. J. VERHAAR, and A. AXELSSON: *Resonances in ultracold collisions of ^6Li, ^7Li, and ^{23}Na.* Phys. Rev. A 51, 4852 (1995).

[115] P. O. FEDICHEV, YU. KAGAN, G. V. SHLYAPNIKOV, and J. T. M. WALRAVEN: *Influence of nearly resonant light on the scattering length in low-temperature atomic gases.* Phys. Rev. Lett. 77, 2913 (1996).

[116] M. THEIS, G. THALHAMMER, K. WINKLER, M. HELLWIG, G. RUFF, R. GRIMM, and J. HECKER DENSCHLAG: *Tuning the scattering length with an optically induced Feshbach resonance.* Phys. Rev. Lett. 93, 123001 (2004).

[117] G. THALHAMMER, M. THEIS, K. WINKLER, R. GRIMM, and J. HECKER DENSCHLAG: *Inducing an optical Feshbach resonance via stimulated Raman coupling.* Phys. Rev. A 71, 033403 (2005).

[118] A. MARTE, T. VOLZ, J. SCHUSTER, S. DÜRR, G. REMPE, E. G. M. VAN KEMPEN, and B. J. VERHAAR: *Feshbach resonances in rubidium 87: Precision measurement and analysis.* Phys. Rev. Lett. 89, 283202 (2002).

[119] P. S. JULIENNE, E. TIESINGA, and T. KÖHLER: *Making cold molecules with time dependent Feshbach resonances.* J. Mod. Opt. 51, 1787 (2004).

[120] R. VEXIAU, N. BOULOUFA, M. AYMAR, J. G. DANZL, M. J. MARK, H.-C. NÄGERL, and O. DULIEU: *Optimal trapping wavelengths of Cs₂ molecules in an optical lattice.* Eur. Phys. J. D 65, 243 (2011).

[121] J. LOZEILLE, A. FIORETTI, C. GABBANINI, Y. HUANG, H. K. PECHKIS, D. WANG, P. L. GOULD, E. E. EYLER, W. C. STWALLEY, M. AYMAR, and O. DULIEU: *Detection by two-photon ionization and magnetic trapping of cold Rb₂ triplet state molecules.* Eur. Phys. J. D 39, 261 (2006).

[122] C. STRAUSS, T. TAKEKOSHI, F. LANG, K. WINKLER, R. GRIMM, J. HECKER DENSCHLAG, and E. TIEMANN: *Hyperfine, rotational, and vibrational structure of the $a\,^3\Sigma_u^+$ state of $^{87}Rb_2$.* Phys. Rev. A 82, 052514 (2010).

[123] C. STRAUSS: *Precision spectroscopy with ultracold $^{87}Rb_2$ triplet molecules.* PhD thesis, Universität Ulm (2011).

[124] T. TAKEKOSHI, C. STRAUSS, F. LANG, J. HECKER DENSCHLAG, M. LYSEBO, and L. VESETH: *Hyperfine, rotational, and Zeeman structure of the lowest vibrational levels of the $^{87}Rb_2$ $(1)\,^3\Sigma_g^+$ state.* Phys. Rev. A 83, 062504 (2011).

[125] F. LANG, P. V. D. STRATEN, B. BRANDSTÄTTER, G. THALHAMMER, K. WINKLER, P. S. JULIENNE, R. GRIMM, and J. HECKER DENSCHLAG: *Cruising through molecular bound-state manifolds with radiofrequency.* Nat. Phys. 4, 223 (2008).

[126] K. WINKLER, G. THALHAMMER, F. LANG, R. GRIMM, J. HECKER DENSCHLAG, A. J. DALEY, A. KANTIAN, H. P. BÜCHLER, and P. ZOLLER: *Repulsively bound atom pairs in an optical lattice.* Nature 441, 853 (2006).

[127] K. WINKLER, F. LANG, G. THALHAMMER, P. V. D. STRATEN, R. GRIMM, and J. HECKER DENSCHLAG: *Coherent optical transfer of Feshbach molecules to a lower vibrational state.* Phys. Rev. Lett. 98, 043201 (2007).

[128] F. LANG, C. STRAUSS, K. WINKLER, T. TAKEKOSHI, R. GRIMM, and J. HECKER DENSCHLAG: *Dark state experiments with ultracold, deeply-bound triplet molecules.* Faraday Discuss. 142, 271 (2009).

[129] F. LANG: *Coherent transfer of ultracold molecules: From weakly to deeply bound.* PhD thesis, Leopold-Franzens-Universität Innsbruck (2009).

[130] B. DREWS *et al.* (in preparation).

[131] See Supplemental Material of Ref. [56] available at `http://arxiv.org/pdf/1501.03793.pdf` for the results of the analytical fits to the calculated polarizabilities corresponding to

different vibrational levels v_a (v_X) of $a^3\Sigma_u^+$ ($X^1\Sigma_g^+$) using two or three effective transitions and for the numerical values of the transition electric dipole moments starting from either the lowest triplet state ($a^3\Sigma_u^+$) or singlet state ($X^1\Sigma_g^+$) towards the most relevant excited potentials.

[132] A. DEREVIANKO, S. G. PORSEV, and J. F. BABB: *Electric dipole polarizabilities at imaginary frequencies for hydrogen, the alkali–metal, alkaline–earth, and noble gas atoms.* At. Data Nucl. Data Tables 96, 323 (2010).

[133] Y. GUAN, X. HAN, J. YANG, Z. ZHOU, X. DAI, E. H. AHMED, A. M. LYYRA, S. MAGNIER, V. S. IVANOV, A. S. SKUBLOV, and V. B. SOVKOV: *Updated potential energy function of the Rb_2 $a^3\Sigma_u^+$ state in the attractive and repulsive regions determined from its joint analysis with the $2\,^3\Pi_{0g}$ state.* J. Chem. Phys. 139, 144303 (2013).

[134] R. BEUC, M. MOVRE, V. HORVATIC, C. VADLA, O. DULIEU, and M. AYMAR: *Absorption spectroscopy of the rubidium dimer in an overheated vapor: An accurate check of molecular structure and dynamics.* Phys. Rev. A 75, 032512 (2007).

[135] M. AYMAR and O. DULIEU: *Calculation of accurate permanent dipole moments of the lowest $^{1,3}\Sigma^+$ states of heteronuclear alkali dimers using extended basis sets.* J. Chem. Phys. 122, 204302 (2005).

[136] M. FOUCRAULT, P. MILLIE, and J. P. DAUDEY: *Nonperturbative method for core–valence correlation in pseudopotential calculations: Application to the Rb_2 and Cs_2 molecules.* J. Chem. Phys. 96, 1257 (1992).

[137] W. MÜLLER, J. FLESCH, and W. MEYER: *Treatment of intershell correlation effects in ab initio calculations by use of core polarization potentials. Method and application to alkali and alkaline earth atoms.* J. Chem. Phys. 80, 3297 (1984).

[138] M. AYMAR and O. DULIEU: *Comment on "Calculation of accurate permanent dipole moments of the lowest $^{1,3}\Sigma^+$ states of heteronuclear alkali dimers using extended basis sets" [J. Chem. Phys. 122, 204302 (2005)].* J. Chem. Phys. 125, 047101 (2006).

[139] M. A. BELLOS, D. RAHMLOW, R. CAROLLO, J. BANERJEE, O. DULIEU, A. GERDES, E. E. EYLER, P. L. GOULD, and W. C. STWALLEY: *Formation of ultracold Rb_2 molecules in the $v'' = 0$ level of the $a^3\Sigma_u^+$ state via blue-detuned photoassociation to the $1\,^3\Pi_g$ state.* Phys. Chem. Chem. Phys. 13, 18880 (2011).

[140] O. DULIEU and P. S. JULIENNE: *Coupled channel bound states calculations for alkali dimers using the Fourier grid method.* J. Chem. Phys. 103, 60 (1995).

[141] V. KOKOOULINE, O. DULIEU, R. KOSLOFF, and F. MASNOU-SEEUWS: *Mapped Fourier methods for long-range molecules: Application to perturbations in the Rb_2 (0_u^+) photoassociation spectrum.* J. Chem. Phys. 110, 9865 (1999).

[142] R. VEXIAU, D. BORSALINO, M. AYMAR, O. DULIEU, and N. BOULOUFA-MAAFA: *Optimal frequencies to control heteronuclear alkali dimers in optical lattices.* Submitted (2015).

[143] J. T. KIM, Y. LEE, and A. V. STOLYAROV: *Quasi-relativistic treatment of the low-lying KCs states.* J. Mol. Spectrosc. 256, 57 (2009).

[144] M. AYMAR and O. DULIEU: *Calculations of transition and permanent dipole moments of heteronuclear alkali dimers NaK, NaRb and NaCs.* Mol. Phys. 105, 1733 (2007).

[145] S. FRIEBEL, C. D'ANDREA, J. WALZ, M. WEITZ, and T. W. HÄNSCH: CO_2*-laser optical lattice with cold rubidium atoms.* Phys. Rev. A 57, R20(R) (1998).

[146] R. JÁUREGUI, N. POLI, G. ROATI, and G. MODUGNO: *Anharmonic parametric excitation in optical lattices.* Phys. Rev. A 64, 033403 (2001).

[147] M. GREINER: *Ultracold quantum gases in three-dimensional optical lattice potentials.* PhD thesis, Ludwig-Maximilians-Universität München (2003).

[148] J. E. SANSONETTI, W. C. MARTIN, and S. L. YOUNG: *Handbook of basic atomic spectroscopic data* (version 1.1.3). National Institute of Standards and Technology, Gaithersburg, MD (2005). Available at `http://physics.nist.gov/Handbook`.

[149] M. S. SAFRONOVA, C. J. WILLIAMS, and C. W. CLARK: *Optimizing the fast Rydberg quantum gate.* Phys. Rev. A 67, 040303(R) (2003).

[150] M. S. SAFRONOVA, C. J. WILLIAMS, and C. W. CLARK: *Relativistic many-body calculations of electric-dipole matrix elements, lifetimes, and polarizabilities in rubidium.* Phys. Rev. A 69, 022509 (2004).

[151] J. DEIGLMAYR, M. AYMAR, R. WESTER, M. WEIDEMÜLLER, and O. DULIEU: *Calculations of static dipole polarizabilities of alkali dimers: Prospects for alignment of ultracold molecules.* J. Chem. Phys. 129, 064309 (2008).

[152] M. S. SAFRONOVA, W. R. JOHNSON, and A. DEREVIANKO: *Relativistic many-body calculations of energy levels, hyperfine constants, electric-dipole matrix elements, and static polarizabilities for alkali-metal atoms.* Phys. Rev. A 60, 4476 (1999).

[153] M. TOMZA and R. MOSZYŃSKI: *Private communication.* The given value is calculated using the method described in [154].

[154] M. TOMZA, W. SKOMOROWSKI, M. MUSIAŁ, R. GONZÁLEZ-FÉREZ, C. P. KOCH, and R. MOSZYNSKI: *Interatomic potentials, electric properties and spectroscopy of the ground and excited states of the Rb_2 molecule: ab initio calculations and effect of a non-resonant field.* Mol. Phys. 111, 1781 (2013).

[155] A. DEREVIANKO, W. R. JOHNSON, M. S. SAFRONOVA, and J. F. BABB: *High-precision calculations of dispersion coefficients, static dipole polarizabilities, and atom-wall interaction constants for alkali-metal atoms.* Phys. Rev. Lett. 82, 3589 (1999).

[156] T. ROM, T. BEST, O. MANDEL, A. WIDERA, M. GREINER, T. W. HÄNSCH, and I. BLOCH: *State selective production of molecules in optical lattices.* Phys. Rev. Lett. 93, 073002 (2004).

[157] A. N. DROZDOVA, A. V. STOLYAROV, M. TAMANIS, R. FERBER, P. CROZET, and A. J. ROSS: *Fourier transform spectroscopy and extended deperturbation treatment of the spin-orbit-coupled $A\,^1\Sigma_u^+$ and $b\,^3\Pi_u$ states of the Rb_2 molecule.* Phys. Rev. A 88, 022504 (2013).

[158] M. LEPERS, R. VEXIAU, M. AYMAR, N. BOULOUFA-MAAFA, and O. DULIEU: *Long-range interactions between polar alkali-metal diatoms in external electric fields.* Phys. Rev. A 88, 032709 (2013).

[159] H. STAPELFELDT and T. SEIDEMAN: *Colloquium: Aligning molecules with strong laser pulses.* Rev. Mod. Phys. 75, 543 (2003).

[160] R. N. ZARE: *Laser control of chemical reactions.* Science 279, 1875 (1998).

[161] A. GIJSBERTSEN, W. SIU, M. F. KLING, P. JOHNSSON, P. JANSEN, S. STOLTE, and M. J. J. VRAKKING: *Direct determination of the sign of the NO dipole moment.* Phys. Rev. Lett. 99, 213003 (2007).

[162] Z. NING and J. C. POLANYI: *Surface aligned reaction.* J. Chem. Phys. 137, 091706 (2012).

[163] F. KRAUSZ and M. IVANOV: *Attosecond physics.* Rev. Mod. Phys. 81, 163 (2009).

[164] D. A. BAUGH, D. Y. KIM, V. A. CHO, L. C. PIPES, J. C. PETTEWAY, and C. D. FUGLESANG: *Production of a pure, single ro-vibrational quantum-state molecular beam.* Chem. Phys. Lett. 219, 207 (1994).

[165] N. MUKHERJEE and R. N. ZARE: *Stark-induced adiabatic Raman passage for preparing polarized molecules.* J. Chem. Phys. 135, 024201 (2011).

[166] B. FRIEDRICH and D. R. HERSCHBACH: *On the possibility of aligning paramagnetic molecules and ions in a magnetic field.* Z. Phys. D 24, 25 (1992).

[167] M. LEMESHKO, R. V. KREMS, J. M. DOYLE, and S. KAIS: *Manipulation of molecules with electromagnetic fields.* Mol. Phys. 111, 1648 (2013).

[168] B. NEYENHUIS, B. YAN, S. A. MOSES, P. J. COVEY, A. CHOTIA, A. PETROV, S. KOTOCHIGOVA, J. YE, and D. S. JIN: *Anisotropic polarizability of ultracold polar $^{40}K^{87}Rb$ molecules.* Phys. Rev. Lett. 109, 230403 (2012).

[169] M. RUTKOWSKI and H. ZACHARIAS: *Depolarisation of the spatial alignment of the rotational angular momentum vector by hyperfine interaction.* Chem. Phys. 301, 189 (2004) and Corrigendum to [Chem. Phys. 301, 189 (2004)] ibid. 310, 321 (2005).

[170] N. C.-M. BARTLETT, J. JANKUNAS, R. N. ZARE, and J. A. HARRISON: *Time-dependent depolarization of aligned D_2 caused by hyperfine coupling.* Phys. Chem. Chem. Phys. 12, 15689 (2010).

[171] H. SALAMI, T. BERGEMAN, B. BESER, J. BAI, E. H. AHMED, S. KOTOCHIGOVA, A. M. LYYRA, J. HUENNEKENS, C. LISDAT, A. V. STOLYAROV, O. DULIEU, P. CROZET, and A. J. ROSS: *Spectroscopic observations, spin-orbit functions, and coupled-channel deperturbation analysis of data on the $A\,^1\Sigma_u^+$ and $b\,^3\Pi_u$ states of Rb_2.* Phys. Rev. A 80, 022515 (2009).

[172] C. AMIOT, O. DULIEU, and J. VERGÈS: *Resolution of the apparent disorder of the Rb_2 $A\,^1\Sigma_u^+\,(0_u^+)$ and $b\,^3\Pi_u\,(0_u^+)$ spectra: A case of fully coupled electronic states.* Phys. Rev. Lett. 83, 2316 (1999).

[173] J. BAI, E. H. AHMED, B. BESER, Y. GUAN, S. KOTOCHIGOVA, A. M. LYYRA, S. ASHMAN, C. M. WOLFE, J. HUENNEKENS, F. XIE, D. LI, L. LI, M. TAMANIS, R. FERBER, A. DROZDOVA, E. PAZYUK, A. V. STOLYAROV, J. G. DANZL, H.-C. NÄGERL, N. BOULOUFA, O. DULIEU, C. AMIOT, H. SALAMI, and T. BERGEMAN: *Global analysis of data on the spin-orbit-coupled $A\,^1\Sigma_u^+$ and $b\,^3\Pi_u$ states of Cs_2.* Phys. Rev. A 83, 032514 (2011).

[174] J. G. DANZL, M. J. MARK, E. HALLER, M. GUSTAVSSON, N. BOULOUFA, O. DULIEU, H. RITSCH, R. HART, and H.-C. NÄGERL: *Precision molecular spectroscopy for ground state transfer of molecular quantum gases.* Faraday Discuss. 142, 283 (2009).

[175] P. QI, J. BAI, E. AHMED, A. M. LYYRA, S. KOTOCHIGOVA, A. J. ROSS, C. EFFANTIN, P. ZALICKI, J. VIGUÉ, G. CHAWLA, R. W. FIELD, T.-J. WHANG, W. C. STWALLEY, H. KNÖCKEL, E. TIEMANN, J. SHANG, L. LI, and T. BERGEMAN: *New spectroscopic data, spin-orbit functions, and global analysis of data on the $A\,^1\Sigma_u^+$ and $b\,^3\Pi_u$ states of Na_2.* J. Chem. Phys. 127, 044301 (2007).

[176] J. B. ATKINSON, J. BECKER, and W. DEMTRÖDER: *Hyperfine structure of the 625 nm band in the $a\,^3\Pi_u \leftarrow X\,^1\Sigma_g$ transitions of Na_2.* Chem. Phys. Lett. 87, 128 (1982).

[177] S. FALKE, I. SHERSTOV, E. TIEMANN, and C. LISDAT: *The $A\,^1\Sigma_u^+$ state of K_2 up to the dissociation limit.* J. Chem. Phys. 125, 224303 (2006).

[178] M. R. MANAA, J. BAI, A. J. ROSS, F. MARTIN, B. CROZET, A. M. LYYRA, L. LI, C. AMIOT, and T. BERGEMAN: *Spin-orbit interactions, new spectral data, and deperturbation of the coupled $b\,^3\Pi_u$ and $A\,^1\Sigma_u^+$ states of K_2.* J. Chem. Phys. 117, 11208 (2002).

182

[179] C. LISDAT, O. DULIEU, H. KNÖCKEL, and E. TIEMANN: *Inversion analysis of K_2 coupled electronic states with the Fourier grid method.* Eur. Phys. J. D 17, 319 (2001).

[180] C. LISDAT, H. KNÖCKEL, and E. TIEMANN: *First observation of hyperfine structure in K_2.* J. Mol. Spectrosc. 199, 81 (2000).

[181] K. URBANSKI, S. ANTONOVA, A. YIANNAPOULOU, A. M. LYYRA, L. LI, and W. C. STWALLEY: *All optical triple resonance spectroscopy of the $A\,^1\Sigma_u^+$ state of $^7Li_2$.* J. Chem. Phys. 104, 2813 (1996).

[182] C. LINTON, F. MARTIN, I. RUSSIER, A. J. ROSS, P. CROZET, S. CHURASSY, and R. BACIS: *Observation and analysis of the $A\,^1\Sigma_u^+$ state of $^6Li_2$ from $v = 0$ to the dissociation limit.* J. Mol. Spectrosc. 175, 340 (1996).

[183] O. DOCENKO, M. TAMANIS, R. FERBER, E. A. PAZYUK, A. ZAITSEVSKII, A. V. STOLYAROV, A. PASHOV, H. KNÖCKEL, and E. TIEMANN: *Deperturbation treatment of the $A\,^1\Sigma^+ - b\,^3\Pi$ complex of NaRb and prospects for ultracold molecule formation in $X\,^1\Sigma^+\,(v = 0; J = 0)$.* Phys. Rev. A 75, 042503 (2007).

[184] M. TAMANIS, R. FERBER, A. ZAITSEVSKII, E. A. PAZYUK, A. V. STOLYAROV, H. CHEN, J. QI, H. WANG, and W. C. STWALLEY: *High resolution spectroscopy and channel-coupling treatment of the $A\,^1\Sigma^+ - b\,^3\Pi$ complex of NaRb.* J. Chem. Phys. 117, 7980 (2002).

[185] M. DEBATIN, T. TAKEKOSHI, R. RAMESHAN, L. REICHSÖLLNER, F. FERLAINO, R. GRIMM, R. VEXIAU, N. BOULOUFA, O. DULIEU, and H.-C. NÄGERL: *Molecular spectroscopy for ground-state transfer of ultracold RbCs molecules.* Phys. Chem. Chem. Phys. 13, 18926 (2011).

[186] O. DOCENKO, M. TAMANIS, R. FERBER, T. BERGEMAN, S. KOTOCHIGOVA, A. V. STOLYAROV, A. D. DE FARIA NOGUEIRA, and C. E. FELLOWS: *Spectroscopic data, spin-orbit functions, and revised analysis of strong perturbative interactions for the $A\,^1\Sigma^+$ and $b\,^3\Pi$ states of RbCs.* Phys. Rev. A 81, 042511 (2010).

[187] T. BERGEMAN, C. E. FELLOWS, R. F. GUTTERRES, and C. AMIOT: *Analysis of strongly coupled electronic states in diatomic molecules: Low-lying states of RbCs.* Phys. Rev. A 67, 050501(R) (2003).

[188] J.-T. KIM, Y. LEE, B. KIM, D. WANG, W. C. STWALLEY, P. L. GOULD, and E. E. EYLER: *Spectroscopic analysis of the coupled $1\,^1\Pi$, $2\,^3\Sigma^+$ ($\Omega = 0^-, 1$), and $b\,^3\Pi$ ($\Omega = 0^\pm, 1, 2$) states of the KRb molecule using both ultracold molecules and molecular beam experiments.* Phys. Chem. Chem. Phys. 13, 18755 (2011).

[189] J. ZAHAROVA, M. TAMANIS, R. FERBER, A. N. DROZDOVA, E. A. PAZYUK, and A. V. STOLYAROV: *Solution of the fully-mixed-state problem: Direct deperturbation analysis of the $A\,^1\Sigma^+ - b\,^3\Pi$ complex in a NaCs dimer.* Phys. Rev. A 79, 012508 (2009).

[190] A. KRUZINS, O. NIKOLAYEVA, J. KLINCARE, M. TAMANIS, R. FERBER, E. A. PAZYUK, and A. V. STOLYAROV: *Fourier-transform spectroscopy of $(4)\,^1\Sigma^+ \to A\,^1\Sigma^+ - b\,^3\Pi$, $A\,^1\Sigma^+ - b\,^3\Pi \to X\,^1\Sigma^+$, and $(1)\,^3\Delta_1 \to b\,^3\Pi_{0\pm}$ transitions in KCs and deperturbation treatment of $A\,^1\Sigma^+$ and $b\,^3\Pi$ states.* J. Chem. Phys. 139, 244301 (2013).

[191] A. KRUZINS, J. KLINCARE, O. NIKOLAYEVA, M. TAMANIS, R. FERBER, E. A. PAZYUK, and A. V. STOLYAROV: *Fourier-transform spectroscopy and coupled-channels deperturbation treatment of the $A\,^1\Sigma^+ - b\,^3\Pi$ complex of KCs.* Phys. Rev. A 81, 042509 (2010).

[192] M. TAMANIS, J. KLINCARE, A. KRUZINS, O. NIKOLAYEVA, R. FERBER, E. A. PAZYUK, and A. V. STOLYAROV: *Direct excitation of the "dark" $b\,^3\Pi$ state predicted by deperturbation analysis of the $A\,^1\Sigma^+ - b\,^3\Pi$ complex in KCs.* Phys. Rev. A 82, 032506 (2010).

[193] R. FERBER, E. A. PAZYUK, A. V. STOLYAROV, A. ZAITSEVSKII, P. KOWALCZYK, H. CHEN, H. WANG, and W. C. STWALLEY: *The $c\,^3\Sigma^+$, $b\,^3\Pi$, and $a\,^3\Sigma^+$ states of NaK revisited.* J. Chem. Phys. 112, 5740 (2000).

[194] H. SUN and J. HUENNEKENS: *Spin-orbit perturbations between the $A\,(2)\,^1\Sigma^+$ and $b\,(1)\,^3\Pi_0$ states of NaK.* J. Chem. Phys. 97, 4714 (1992).

[195] A. J. ROSS, C. EFFANTIN, J. D'INCAN, and R. F. BARROW: *Laser-induced fluorescence of NaK: the $b\,(1)\,^3\Pi$ state.* J. Phys. B: At. Mol. Phys. 19, 1449 (1986).

[196] See Supplemental Material of [157] given at `http://link.aps.org/supplemental/10.1103/PhysRevA.88.022504`.

[197] J. M. BROWN and A. J. MERER: *Lambda-type doubling parameters for molecules in Π electronic states of triplet and higher multiplicity.* J. Mol. Spectrosc. 74, 488 (1979).

[198] K. F. FREED: *Theory of the hyperfine structure of molecules: Application to $^3\Pi$ states of diatomic molecules intermediate between Hund's cases (a) and (b).* J. Chem. Phys. 45, 4214 (1966).

[199] E. ARIMONDO, M. INGUSCIO, and P. VIOLINO: *Experimental determinations of the hyperfine structure in the alkali atoms.* Rev. Mod. Phys. 49, 31 (1977).

[200] C.-C. TSAI, T. BERGEMAN, E. TIESINGA, P. S. JULIENNE, and D. J. HEINZEN: *Hyperfine and vibrational structure of weakly bound levels of the lowest 1_g state of molecular $^{87}Rb_2$.* Phys. Rev. A 88, 052509 (2013).

[201] A. N. DROZDOVA, X. HAN, X. DAI, G. WANNOUS, P. CROZET, and A. J. ROSS: *On the $2\,^1\Pi_g$ state of the rubidium dimer.* J. Mol. Spectrosc. 299, 25 (2014).

[202] M. TOMZA, M. H. GOERZ, M. MUSIAŁ, R. MOSZYNSKI, and C. P. KOCH: *Optimized production of ultracold ground-state molecules: Stabilization employing potentials with ion-pair character and strong spin-orbit coupling.* Phys. Rev. A 86, 043424 (2012).

[203] C. AMIOT: *Laser-induced fluorescence of Rb_2: The (1) $^1\Sigma_g^+$ (X), (2) $^1\Sigma_g^+$, (1) $^1\Pi_u$ (B), (1) $^1\Pi_g$, and (2) $^1\Pi_u$ (C) electronic states.* J. Chem. Phys. 93, 8591 (1990).

[204] W. DEMTRÖDER: *Molekülphysik.* 2. Auflage, Oldenbourg Verlag (2013).

[205] H. F. HESS, D. A. BELL, G. P. KOCHANSKI, R. W. CLINE, D. KLEPPNER, and T. J. GREYTAK: *Observation of three-body recombination in spin-polarized hydrogen.* Phys. Rev. Lett. 51, 483 (1983).

[206] E. A. BURT, R. W. GHRIST, C. J. MYATT, M. J. HOLLAND, E. A. CORNELL, and C. E. WIEMAN: *Coherence, correlations, and collisions: What one learns about Bose-Einstein condensates from their decay.* Phys. Rev. Lett. 79, 337 (1997).

[207] J. SÖDING, D. GUÉRY-ODELIN, P. DESBIOLLES, F. CHEVY, H. INAMORI, and J. DALIBARD: *Three-body decay of a rubidium Bose-Einstein condensate.* Appl. Phys. B 69, 257 (1999).

[208] B. D. ESRY, C. H. GREENE, and J. P. BURKE: *Recombination of three atoms in the ultracold limit.* Phys. Rev. Lett. 83, 1751 (1999).

[209] H. SUNO and B. D. ESRY: *Three-body recombination in cold helium-helium-alkali-metal-atom collisions.* Phys. Rev. A 80, 062702 (2009).

[210] Y. WANG, J. P. D'INCAO, and B. D. ESRY: *Cold three-body collisions in hydrogen-hydrogen-alkali-metal atomic systems.* Phys. Rev. A 83, 032703 (2011).

[211] N. L. GUEVARA, Y. WANG, and B. D. ESRY: *New class of three-body states.* Phys. Rev. Lett. 108, 213202 (2012).

[212] P. O. FEDICHEV, M. W. REYNOLDS, and G. V. SHLYAPNIKOV: *Three-body recombination of ultracold atoms to a weakly bound s level.* Phys. Rev. Lett. 77, 2921 (1996).

[213] P. F. BEDAQUE, E. BRAATEN, and H.-W. HAMMER: *Three-body recombination in Bose gases with large scattering length.* Phys. Rev. Lett. 85, 908 (2000).

[214] V. EFIMOV: *Energy levels arising from resonant two-body forces in a three-body system.* Phys. Lett. B 33, 563 (1970).

[215] E. BRAATEN and H.-W. HAMMER: *Three-body recombination into deep bound states in a Bose gas with large scattering length.* Phys. Rev. Lett. 87, 160407 (2001).

[216] T. KRAEMER, M. MARK, P. WALDBURGER, J. DANZL, C. CHIN, B. ENGESER, A. LANGE, K. PILCH, A. JAAKOLA, H.-C. NÄGERL, and R. GRIMM: *Evidence for Efimov quantum states in an ultracold gas of caesium atoms.* Nature 440, 315 (2006).

[217] T. WEBER, J. HERBIG, M. MARK, H.-C. NÄGERL, and R. GRIMM: *Three-body recombination at large scattering lengths in an ultracold atomic gas.* Phys. Rev. Lett. 91, 123201 (2003).

[218] S. JOCHIM, M. BARTENSTEIN, A. ALTMEYER, G. HENDL, C. CHIN, J. HECKER DENSCHLAG, and R. GRIMM: *Pure gas of optically trapped molecules created from fermionic atoms.* Phys. Rev. Lett. 91, 240402 (2003).

[219] A. SIMONI and J.-M. LAUNAY: *Ultracold atom-molecule collisions with hyperfine coupling.* Laser Phys. 16, 707 (2006).

[220] D. R. BATES, A. E. KINGSTON, and R. W. P. MCWHIRTER: *Recombination between electrons and atomic ions. I. Optically thin plasmas.* Proceedings of the Royal Society of London. Series A. Mathematical and Physical Sciences 267, 297 (1962).

[221] D. R. FLOWER and G. J. HARRIS: *Three-body recombination of hydrogen during primordial star formation.* Monthly Notices of the Royal Astronomical Society 377, 705 (2007).

[222] A. FIORETTI, D. COMPARAT, A. CRUBELLIER, O. DULIEU, F. MASNOU-SEEUWS, and P. PILLET: *Formation of cold Cs_2 molecules through photoassociation.* Phys. Rev. Lett. 80, 4402 (1998).

[223] C. GABBANINI, A. FIORETTI, A. LUCCHESINI, S. GOZZINI, and M. MAZZONI: *Cold rubidium molecules formed in a magneto-optical trap.* Phys. Rev. Lett. 84, 2814 (2000).

[224] Y. HUANG, J. QI, H. K. PECHKIS, D. WANG, E. E. EYLER, P. L. GOULD, and W. C. STWALLEY: *Formation, detection and spectroscopy of ultracold Rb_2 in the ground $X\,^1\Sigma_g^+$ state.* J. Phys. B: At. Mol. Opt. Phys. 39, 857 (2006).

[225] W. SALZMANN, T. MULLINS, J. ENG, M. ALBERT, R. WESTER, M. WEIDEMÜLLER, A. MERLI, S. M. WEBER, F. SAUER, M. PLEWICKI, F. WEISE, L. WÖSTE, and A. LINDINGER: *Coherent transients in the femtosecond photoassociation of ultracold molecules.* Phys. Rev. Lett. 100, 233003 (2008).

[226] S. T. SULLIVAN, W. G. RELLERGERT, S. KOTOCHIGOVA, K. CHEN, S. J. SCHOWALTER, and E. R. HUDSON: *Trapping molecular ions formed via photo-associative ionization of ultracold atoms.* Phys. Chem. Chem. Phys. 13, 18859 (2011).

[227] M. MUDRICH, P. HEISTER, T. HIPPLER, C. GIESE, O. DULIEU, and F. STIENKEMEIER: *Spectroscopy of triplet states of Rb_2 by femtosecond pump-probe photoionization of doped helium nanodroplets.* Phys. Rev. A 80, 042512 (2009).

[228] M. AYMAR, S. AZIZI, and O. DULIEU: *Model-potential calculations for ground and excited Σ states of Rb_2^+, Cs_2^+ and $RbCs^+$ ions.* J. Phys. B: At. Mol. Opt. Phys. 36, 4799 (2003).

[229] A. DROZDOVA: *Study of spin-orbit coupled electronic states of Rb_2, NaCs and NaK molecules. Laser spectroscopy and accurate coupled-channel deperturbation analysis.* PhD thesis, Univ. de Lyon and Lomonosov Moscow State Univ. (2012).

[230] T. MUKAIYAMA, J. R. ABO-SHAEER, K. XU, J. K. CHIN, and W. KETTERLE: *Dissociation and decay of ultracold sodium molecules.* Phys. Rev. Lett. 92, 180402 (2004).

[231] P. STAANUM, S. D. KRAFT, J. LANGE, R. WESTER, and M. WEIDEMÜLLER: *Experimental investigation of ultracold atom-molecule collisions.* Phys. Rev. Lett. 96, 023201 (2006).

[232] N. ZAHZAM, T. VOGT, M. MUDRICH, D. COMPARAT, and P. PILLET: *Atom-molecule collisions in an optically trapped gas.* Phys. Rev. Lett. 96, 023202 (2006).

[233] G. QUÉMÉNER, J.-M. LAUNAY, and P. HONVAULT: *Ultracold collisions between Li atoms and Li_2 diatoms in high vibrational states.* Phys. Rev. A 75, 050701 (2007).

[234] S. SCHMID, A. HÄRTER, A. FRISCH, S. HOINKA, and J. HECKER DENSCHLAG: *An apparatus for immersing trapped ions into an ultracold gas of neutral atoms.* Rev. Sci. Instrum. 83, 053108 (2012).

[235] S. SCHMID, A. HÄRTER, and J. HECKER DENSCHLAG: *Dynamics of a cold trapped ion in a Bose-Einstein condensate.* Phys. Rev. Lett. 105, 133202 (2010).

[236] A. HÄRTER, A. KRÜKOW, A. BRUNNER, W. SCHNITZLER, S. SCHMID, and J. HECKER DENSCHLAG: *Single ion as a three-body reaction center in an ultracold atomic gas.* Phys. Rev. Lett. 109, 123201 (2012).

[237] G. MORIGI and H. WALTHER: *Two-species Coulomb chains for quantum information.* Eur. Phys. J. D 13, 261 (2001).

[238] D. J. BERKELAND, J. D. MILLER, J. C. BERGQUIST, W. M. ITANO, and D. J. WINELAND: *Minimization of ion micromotion in a Paul trap.* J. Appl. Phys. 83, 5025 (1998).

[239] B. W. SHORE, P. DÖMÖTÖR, E. SADURNI, G. SÜSSMANN, and W. P. SCHLEICH: *Scattering of a particle with internal structure from a slit.* New J. Phys. 17, 013046 (2015).

[240] P. DÖMÖTÖR, P. FÖLDI, M. G. BENEDICT, B. W. SHORE, and W. P. SCHLEICH: *Scattering of a particle with internal structure from a slit: exact numerical solutions.* New J. Phys. 17, 023044 (2015).

[241] A.-L. MAREK: *Intensitätsstabilisierung und Entwurf einer Dipolfalle für ^{87}Rb-Atome.* Wissenschaftliche Arbeit im Rahmen des Lehramtsstudiums (2014).

[242] G. REMPE: *Moleküle eiskalt geordnet.* Physik in unserer Zeit 38 (1), 6 (2007).